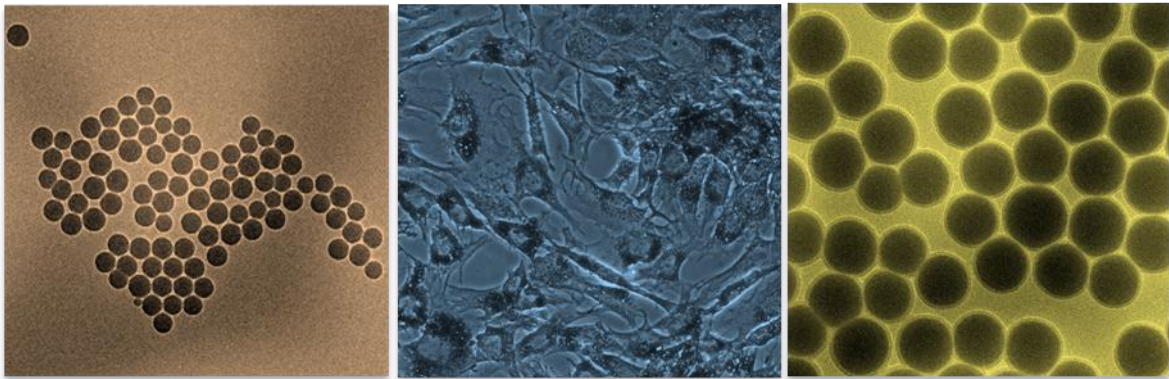


**DESIGN AND STUDY OF
MULTIFUNCTIONAL SYSTEMS BASED
ON MAGNETIC NANOPARTICLES FOR
BIOMEDICAL APPLICATIONS**



Noelia Guldris Pensado

PROGRAMA DE DOCTORADO EN NANOMEDICINA

Facultad de Física

SANTIAGO DE COMPOSTELA

2017





TESIS DOCTORAL

**DESIGN AND STUDY OF
MULTIFUNCTIONAL
SYSTEMS BASED ON
MAGNETIC NANOPARTICLES
FOR BIOMEDICAL
APPLICATIONS**

Noelia Guldris Pensado

DEPARTAMENTO DE FÍSICA APLICADA

PROGRAMA DE DOCTORADO EN NANOMEDICINA

Facultad de Física

SANTIAGO DE COMPOSTELA

2017



José Rivas Rey, Catedrático del Departamento de Física Aplicada de la Universidad de Santiago de Compostela, como director y tutor de esta tesis, y **Manuel Bañobre** y **Laura Salonen** investigadores del International Iberian Nanotechnology Laboratory (INL), Braga, (Portugal), como directores de esta tesis:

CERTIFICAN

que el trabajo titulado “**DESIGN AND STUDY OF MULTIFUNCTIONAL SYSTEMS BASED ON MAGNETIC NANOPARTICLES FOR BIOMEDICAL APPLICATIONS**” realizado por Noelia Guldris Pensado, ha sido revisado y reúne todos los requisitos exigidos en el artículo 34 del reglamento de los Estudios de Doctorado, y que como no incurre en las causas de abstención establecidas en la ley 30/1992, autorizan su presentación para optar al título de Doctora en la Universidad de Santiago de Compostela por el Programa de Doctorado en Nanomedicina.

Santiago de Compostela, 25 Enero 2017

José Rivas Rey

Manuel Bañobre López

Laura Salonen

Director y Tutor

Director

Directora





This Ph.D. thesis has been carried out at the International Iberian Nanotechnology Laboratory (INL) in collaboration with the University of Santiago de Compostela (USC). The work was funded by POCTEP (Operational Program for Cross-border Cooperation Spain-Portugal) through the 'InveNNta' project, a joint initiative between the INL and the Health Research Institute of Santiago de Compostela (IDIS), managed through the Ramón Domínguez Foundation, and co-financed by the ERDF (European Regional Development Fund), by the P.O. Norte CCDR-N/ON.2 program, and by GAIN, Xunta de Galicia.



***'I declare after all there is no enjoyment like reading!
How much sooner one tires of any thing than of a book!
When I have a house of my own, I shall be miserable if I
have not an excellent library.'***

Caroline Bingley, *Pride and Prejudice*





ACKNOWLEDGMENTS

First, I would like to thank Prof. José Rivas for giving me the opportunity to work in his group and for the support given in these years. In addition, my co-supervisors Dr. Manuel Bañobre and Dr. Laura Salonen also played a very important role in supporting the development of this PhD thesis, and I am very grateful for the fruitful discussions, the time investment, and the patience they always gave me.

From Osaka University, I would like to thank Prof. Kikuchi for accepting me in his lab for four months. I learnt valuable scientific and personal skills in Japan. I would also like to thank especially to Minoshima-sensei for his help in all the practical issues. This internship could not be possible without the help of 'Fundación Barrié de la Maza', I would like to thank the Foundation for the financial support.

From the Hospital of Santiago de Compostela, I would like to thank Prof. José Castillo for the fruitful collaboration we have had these years. Barbara Argibay, Francisco Campos, Ramón Iglesias, and Tomás Sobrino thank you so much for the *in vitro* and *in vivo* experiments.

I would like to thank all my colleagues at INL from the Nanomaterials Group, especially Dr. Carlos Abreu-Rodriguez for welcoming me into his group; Dr. Yury Kolen'ko for the help with nanoparticle synthesis and many other things; Dr. Juan Gallo for the aid with nanoparticle functionalization, MRI measurements, etc.; Enrique Carbo for the TEM acquisitions; but most of all, thank you all for the time outside the lab.

Also from INL, I would like to thank Dr. Dmitri Petrovykh for his help with the IR measurements, and Dr. Begoña Espiña for measurements on the UV-Vis microplate reader; they were always willing to help me with these and other issues.

From the University of Minho, I especially thank Elisa Pinto for her availability for the NMR measurements, and Dr. Manuel Martin from the University of Santiago de Compostela for his help with the NMR of nanoparticles.

From the CACTI in Vigo, I would like to thank to the Mass Spectrometry and the elemental analysis units for the measurements performed.

To my favorite PhD students at INL: Tareq, Jose and Noel for many lunches, for the laughs and the fun together. Even if sometimes I felt lost in the middle of physical debates, I always enjoyed your company so much.

To my dearest colleagues in Osaka: Nishiura-san, Miyata-san, Camille-chan, Suzuki-kun, Arizono-kun, Yamasaki-kun, Sowa-kun, Omori-kun, and Watabe-kun. Many many thanks for the time that we spent together and that I will never forget.

To the best neighbor in the world: Charles, not only for teaching me practical things such as how to run a washing machine in Japanese, but also for spending your time with me. For sure, I will meet you again in Germany.

To the most exigent friend ever: Ren. I hope that these lines are well written so you cannot complain about my English, again. Anyway, I really enjoyed our lunches together, the fireworks, the walks, etc. I know we will meet again somewhere in Europe.

A Manuel Bañobre por empezar este proyecto juntos y apoyarme en los momentos difíciles.

A Laura S. por ser la jefa perfecta y una amiga al mismo tiempo, no creo que nadie más podría haberlo hecho tan bien.

A Jose Blanco por ser el compañero de laboratorio más desorganizado del mundo, pero estar siempre dispuesto a teorizar sobre nuestros pequeños fracasos con los experimentos. Eso hizo el sufrimiento mucho más ameno durante estos años.

A mis compañeros del CIQUS, quienes formaron parte de mi nacimiento como científica, al Prof. Riguera, a Juan Correa, Marcos Fernández, Sandra Amaral, Luiz Pinto, Silvia Porto y Ramón Novoa. Especialmente a Marcos, gracias por tu tiempo y generosidad enseñándome casi todo lo que sé; y a Juan por ser el compañero ideal en las clases de baile donde tan bien lo hemos pasado tantas veces!

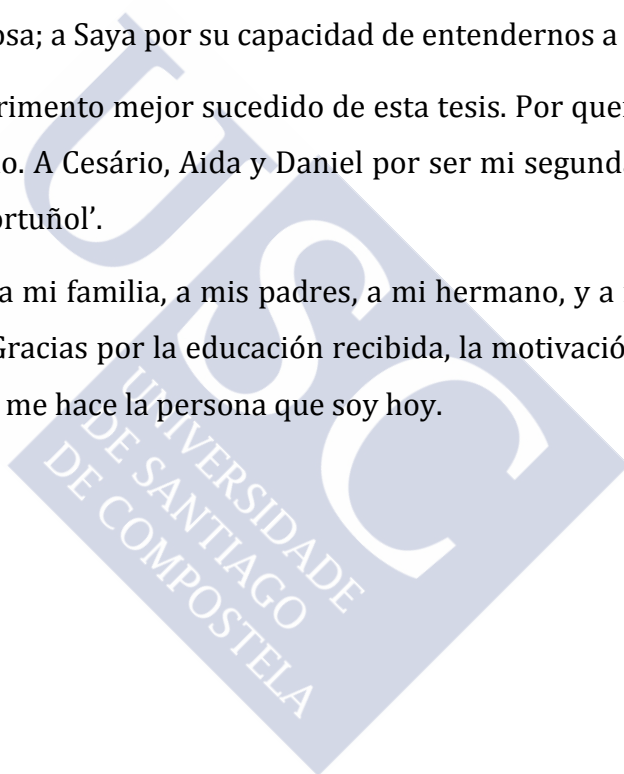
A mis súper amigos de la carrera Fátima, Miguel, Juan Fafián, Alba, Eva, Víctor por taaaaaantas cosas que no podría nunca escribirlas aquí, primero porque son secretas y segundo porque darían otras 200 paginas!! A Fati por el tiempo vivido en UK, la Pint of Cider y tantas otras cosas; a Miguel por ser un encanto y cuidar de Fati; a Juanchi

por sus críticas, por no ser nunca, nunca constructivas, y aun así hacerse querer; a Alba por enseñarme a bailar reggaeton como nadie; a Víctor por sus ataques pe...n; a Eva por su humor y su arte en el fútbolín. Todos estos momentos sin duda han hecho que los experimentos fallidos no importaran en el fin de semana, gracias por eso.

A mis amigas de siempre, Carol, Laura B., Ana, Nati y Saya, porque no saben que es una nanopartícula, pero me han escuchado hablar de ellas innumerables veces y nunca me han mandado callar. A Carol por el pato o pingüino; a Laura por el verano más largo de la historia juntas; a Ana por su sonrisa y ejemplo; a Nati por ser la compi de clase más tranquila, sabia y generosa; a Saya por su capacidad de entendernos a todas.

A Diogo, por ser el experimento mejor sucedido de esta tesis. Por quererme y decidir caminar la vida a mi lado. A Cesário, Aida y Daniel por ser mi segunda familia aquí y entender siempre mi 'portuñol'.

Y por supuesto, gracias a mi familia, a mis padres, a mi hermano, y a mi sobrina, por ser lo más importante. Gracias por la educación recibida, la motivación, la fuerza y el cariño interminable que me hace la persona que soy hoy.





MOTIVATION

Iron oxide nanoparticles have long showed promising properties for their successful application in both diagnosis and therapy, for example as carriers in drug delivery, contrast agents for magnetic resonance imaging, and heat generating sources in magnetic hyperthermia. To date, the use of magnetic nanoparticles in the clinic is not widespread due to various hindrances related with the synthesis, such as scale-up, reproducibility, and the cost of production, the characterization of polydisperse samples, and the unpredictable interactions between produced materials and biomolecules. The aim of this thesis was to address three fundamental aspects that hamper the eventual use of iron oxide nanoparticles in the clinic. First, the development of synthesis and purification procedures to obtain at low-cost iron oxide nanoparticles with tunable properties, high biocompatibility, and great magnetic response. The synthesis of nanoparticles must be efficient, reproducible and up-scalable to provide profitable formulations. Second, the study of the physicochemical properties of magnetic nanoparticles after interaction with biomolecules in order to shed light on phenomena such as particle aggregation, protein adsorption, and cell internalization. The understanding of these interactions is of fundamental importance, as they govern the biodistribution and targeting ability of the nanoparticles *in vivo*. And third, new possibilities of chemical functionalization of naked iron oxide nanoparticles need to be explored in order to achieve multifunctional and theranostic performance with high yields, simplicity, and high reproducibility. With the aim of translational research, these studies were driven towards three areas of remarkable relevance in medicine: i) contrast agents in magnetic resonance imaging, ii) magnetic labels of stem cells for cell tracking applications, and iii) stimuli-responsive delivery systems.

Only with a complete understanding of biointerfaces, personalized medicine with tailored nanoparticles will become a reality. In that sense, this thesis contributes to the knowledge required to move forward from benchtop to end-user application.



SUMMARY

Nanomedicine is a new field employing nanotechnology tools for biomedical applications. Nanomaterials feature sizes between 1 and 100 hundred nanometers, and therefore they fill the gap between single molecules and bulk materials. They open the possibility to access biological processes on the same size scale. Nanoparticles have shown great potential to achieve the goal of personalized medicine due to the possibilities to modify their surface with proteins, targeting molecules, or imaging probes. Particularly, iron oxide nanoparticles show promising properties for successful application in biomedicine due to their low-cost production, high biocompatibility, and great magnetic response. Strategies for the functionalization of inorganic cores have been developed over the past years, and efforts have been devoted to engineering nanoparticles with multifunctional ligands on the surface to enable active tumor targeting, detection over different imaging modalities, and stimulus-driven cargo release. During this Ph.D. thesis, three main aspects of iron oxide nanoparticles have been evaluated. First, the stability of nanoparticles has been addressed in biological fluids. Second, the uptake of nanoparticles by stem cells for cell tracking applications was studied with nanoparticles of different sizes and bearing different organic coatings. Third, new possibilities of chemical functionalization of naked iron oxide nanoparticles by orthogonal processes have been explored, in order to achieve high yields, simplicity and high reproducibility.

KEYWORDS: nanoparticles, iron oxide, MRI, cell tracking, click chemistry, Diels–Alder, CuAAC, hyperthermia.

RESUMEN (ESPAÑOL)

La nanomedicina es una nueva área de conocimiento que utiliza las herramientas de la nanotecnología para aplicaciones biomédicas. Los materiales nanoestructurados con tamaños de 1 a 100 nm se encuentran en el rango intermedio entre las pequeñas moléculas y los materiales macroscópicos, y por tanto, ofrecen la posibilidad de interactuar con procesos biológicos en la misma escala. Las nanopartículas poseen características prometedoras para lograr la 'medicina personalizada', gracias a la posibilidad de modificar su superficie con moléculas de interés biológico, como proteínas, ligandos receptores, o sondas de imagen. Las nanopartículas compuestas por óxidos de hierro son particularmente prometedoras por poseer buena respuesta magnética, excelente biocompatibilidad, y bajos costes de producción. En los últimos años se han desarrollado nuevas estrategias para la modificación de nanopartículas de óxidos de hierro, intentando diseñar nanopartículas con propiedades diana que se dirijan a tumores, que además sean detectables mediante varias técnicas de imagen, y que adicionalmente consigan liberar un fármaco mediante estímulos externos. En esta tesis de doctorado se han evaluado tres aspectos fundamentales de nanopartículas de óxidos de hierro para su aplicación en biomedicina. Primero, se ha estudiado el proceso de síntesis y de purificación de nanopartículas de óxido de hierro, así como su interacción con biomoléculas. Segundo, se ha evaluado las diferencias en

internalización en células madre de nanopartículas de óxidos de hierro con varios recubrimientos orgánicos. Tercero, se han explorado nuevos métodos de funcionalización de nanopartículas mediante química 'click' que ofrece ventajas como simplicidad, altos rendimientos, y buena reproducibilidad.

PALABRAS CLAVE: nanopartículas, óxidos de hierro, MRI, seguimiento de células madre, química click, Diels–Alder, CuAAC, hipertermia.

RESUMO (GALEGO)

A nanomedicina é unha nova área de coñecemento que emprega as ferramentas da nanotecnoloxía para aplicacións biomédicas. Os materiais nanoestruturados con tamaños de 1 a 100 nanómetros encóntranse no rango intermedio entre as pequenas moléculas e os materiais macroscópicos, e polo tanto, ofrecen a posibilidade de interaccionar con procesos biolóxicos na mesma escala. As nanopartículas posúen características prometedoras para lograr a 'medicina personalizada', grazas á posibilidade de modificar a súa superficie con moléculas de interese biolóxico, como proteínas, ligandos receptores, ou sondas de imaxe. As nanopartículas compostas por óxidos de ferro son particularmente prometedoras por posuír excelente biocompatibilidade, baixos custos de produción, e resposta magnética. Novas estratexias para a modificación de nanopartículas de óxidos de ferro desenvolvéronse nos últimos anos, tentando deseñar nanopartículas con propiedades diana en tumores, detectables mediante varias técnicas de imaxe, e tamén para externamente inducir á liberación dun fármaco. Nesta tese de doutoramento evaluáronse tres aspectos fundamentais de nanopartículas de óxidos de ferro para a súa aplicación en biomedicina. Primeiro, estudouse o proceso de síntese e de purificación de nanopartículas de óxido de ferro, así como a súa interacción con biomoléculas. Segundo, evaluáronse as diferenzas en internalización en células nai de nanopartículas de óxidos de ferro con diferentes recubrimientos orgánicos. Terceiro, exploráronse novos métodos de funcionalización de nanopartículas mediante química 'click' que ofrece vantaxes como simplicidade, altos rendementos, e alta reproducibilidade.

PALABRAS CHAVE: nanopartículas, óxidos de ferro, MRI, cell tracking, química click, Diels–Alder, CuAAC, hipertermia.

TABLE OF CONTENTS

ABBREVIATIONS	5
CHAPTER 1	9
1 Introduction.....	9
1.1 Nanomedicine.....	10
1.2 Magnetic Nanoparticles.....	11
1.2.1 Synthesis Method	12
1.2.2 Surface Functionalization	14
1.2.3 NP Functionalization: Click Chemistry.....	18
1.2.4 1,3-Dipolar Cycloaddition.....	20
1.2.5 Diels–Alder Reaction	21
1.3 Biomedical Applications	24
1.3.1 MRI: T_1 , T_2 , and Dual Contrast Agents.....	24
1.3.2 Cell Tracking.....	28
1.3.3 Labeling Procedures	28
1.3.4 Limitations of IONs for Cell Tracking.....	30
1.3.5 Hyperthermia.....	31
1.3.6 Magnetic Hyperthermia.....	32
1.3.7 Drug Delivery.....	36
1.3.8 Magnetic Nanohybrids	36
1.3.9 Drug Loading.....	37
1.3.10 IONs in the Clinic	44
1.4 Biointerface	45
1.4.1 Protein Corona	46
1.4.2 Uptake by Cells.....	48
CHAPTER 2	53

2	Ultrasmall Magnetic Nanoparticles: MRI performance and <i>in vitro</i> stability	53
2.1	Introduction	54
2.2	Synthesis of IONs	55
2.3	USPIO Stability	63
2.3.1	Chemical Stability.....	63
2.3.2	USPIOs Protein Adsorption.....	65
2.3.3	<i>In vitro</i> Studies.....	66
2.4	MRI Measurements	68
2.5	Conclusions.....	72
2.6	Experimental	73
2.6.1	Chemicals.....	73
2.6.2	USPIOs Synthesis Procedure	73
2.6.3	Characterization	74
2.6.4	Nanoparticle Functionalization.....	75
2.6.5	Chemical Stability.....	76
2.6.6	USPIO Stability in Biological Medium.....	76
2.6.7	Viability Assay	77
2.6.8	Cell Count.....	77
2.6.9	MRI Measurements.....	77
CHAPTER 3	79
3	Magnetite Nanoparticles for Stem Cell Labeling	79
3.1	Introduction	80
3.2	Synthesis of IONs	81
3.3	Coating Modification.....	84
3.4	Fe Content in MSCs.....	87
3.5	Cell Health.....	90
3.6	<i>In vivo</i> Studies.....	91

3.7	Conclusions.....	94
3.8	Experimental	95
3.8.1	Materials and Methods.....	95
3.8.2	IONs Synthesis Procedure	97
3.8.3	Glucosamine Modification	97
3.8.4	<i>In vitro</i> Experiments.....	98
3.8.5	Incubation between PLL and USPIO-PAA-GlcN	98
3.8.6	ICP of Labeled MSC.....	99
3.8.7	PB Staining.....	99
3.8.8	LDH Assay.....	99
3.8.9	Cell Count.....	99
3.8.10	<i>In vivo</i> Experiments.....	100
3.8.11	MRI Studies.....	100
3.8.12	Agar Phantoms.....	100
3.8.13	<i>In vivo</i> MRI.....	101
CHAPTER 4	103
4	Clickable Iron Oxide Nanoparticles.....	103
4.1	Introduction.....	104
4.2	Allyl-Functionalized IONs.....	105
4.3	Naked ION Synthesis	108
4.4	Isocyanates for ION Functionalization.....	110
4.4.1	Synthesis of Isocyanate Ligands.....	110
4.4.2	ION Functionalization with Isocyanates.....	112
4.4.3	Model Reactions.....	119
4.5	Click Reactions on the NP Surface.....	122
4.6	Conclusions.....	131
4.7	Experimental	133

4.7.1 Synthetic Procedures.....	135
CHAPTER 5	155
5 General Conclusions	155
6 Bibliography.....	159



ABBREVIATIONS

Abs	absorbance
Ac ₂ O	acetic anhydride
AMF	alternating magnetic field
Aq	aqueous
BCA	bicinchoninic acid
BSA	bovine serum album
CA	contrast agent
calcd	calculated
CC	column chromatography
CPMG	Carr Purcell Meiboom Gill
CuAAC	Cu(I)-catalyzed azide–alkyne cycloaddition
Cy3-NH ₂	cyanine3 amine
d	days
DBU	8-diazabicyclo[5.4.0]undec-7-ene
D _h	hydrodynamic diameter
DLS	dynamic light scattering
DMA	<i>N,N</i> -dimethylacetamide
DMF	<i>N,N</i> -dimethylformamide
doxo	doxorubicin
EDC	1-ethyl-3-(3-dimethylaminopropyl)carbodiimide
EDG	electron-donating groups
EDX	energy-dispersive X-ray spectroscopy

EGFR	epidermal growth factor receptor
EI	electron impact ionization
ESI	electrospray ionization
eq	equivalent
EtOAc	ethyl acetate
EtOH	ethanol
EWG	electron-withdrawing groups
FA	flip angle
FDA	food and drug administration
FOV	field of view
FSE	fast spin echo
FT-IR	Fourier transform infrared spectroscopy
GlcN	D-glucosamine
h	hours
HAADF	high-angle annular dark-field
H_c	coercive force
HPF	heparin-protamine-Ferumoxytol
ICP-OES	inductively coupled plasma optical emission spectroscopy
IMDM	Iscove's Modified Dulbecco's Medium
ION	iron oxide nanoparticle
IR	infrared
LDH	lactate dehydrogenase
MeCN	acetonitrile
MEG	multi-gradient echo

MEMS	multi-echo-multi-sliced
MeOH	methanol
MH	magnetic hyperthermia
min	minutes
MRI	magnetic resonance imaging
MS	mass spectrometry
M_s	saturation magnetization
MSC	mesenchymal stem cell
MSME	multi-slice multi-spin-echo sequence
MW	molecular weight
NaOAc	sodium acetate
NMR	nuclear magnetic resonance
NP	nanoparticle
OPA	<i>o</i> -phthalaldehyde
PAA	polyacrylic acid
PEG	polyethylene glycol
PB	Prussian blue
PBS	phosphate buffer saline
PC	protein corona
PI	polydispersity index
PLA	polylactic acid
PLL	poly-lysine
PMMA	poly(methyl methacrylate)
PTFE	poly(tetrafluoroethylene)

<i>r</i>	relaxivity
RES	reticular endothelial system
RGD	arginine-glycine-aspartate
rMSCs	rat mesenchymal stem cells
rpm	revolutions per minute
RSD	relative standard deviation
rt	room temperature
SAR	specific absorption rate
SD	standard deviation
SPIOs	superparamagnetic iron oxide nanoparticle
STEM	scanning transmission electron microscopy
<i>t</i>	time
TEM	transmission electron microscopy
TGA	thermogravimetric assay
TLC	thin-layer chromatography
USPIO	ultrasmall superparamagnetic iron oxide nanoparticle
VSM	vibrating sample magnetometry
XRD	powder X-ray diffraction
XPS	X-ray photoelectron spectroscopy

CHAPTER 1

1 Introduction



1.1 NANOMEDICINE

In December 1959, Richard Feynman gave a talk titled "*There's Plenty of Room at the Bottom*" at the annual meeting of the American Physical Society at Caltech (USA), where he foresaw the potential of miniaturization. Nanotechnology refers to materials with size within the nanometer range, 1 to 100 nm, that display unique physicochemical characteristics such as large surface area, superparamagnetism, or surface plasmon resonance. Nanoscale materials fill the gap between single molecules and bulk materials, and therefore open the possibility to access biological processes on the same size scale.

The application of nanotechnology in biomedicine is an emerging field known as nanomedicine.¹ Magnetic nanoparticles (NPs) among others have shown great potential as carriers in drug delivery, as contrast agents for magnetic resonance imaging (MRI), and as heat generating sources in hyperthermia treatment.² One of the challenges for nanomedicine is to achieve personalized nanocarriers with targeting capabilities that diminish the side effects of aggressive therapies.³

Particularly, iron oxide nanoparticles (IONs) have promising properties for successful application in biomedicine due to their low-cost production, high biocompatibility, and great magnetic response.⁴ The performance of IONs depends on their composition, morphology and size of the inorganic core, and on the nature and coverage rate of the organic coating.⁵ Strategies for the functionalization of inorganic cores have been developed over the past years,⁶ and efforts have been devoted to engineering NPs with multifunctional ligands on the surface to enable active tumor targeting, detection over different imaging modalities, and stimulus-driven cargo release. The use of nanomaterials has the potential to enhance the selective therapeutic efficacy, to tune biodistribution and pharmacokinetic of drugs, and to achieve prompter diagnosis.

In the following Chapters of this Ph.D. thesis, the synthesis and properties of iron oxide nanoparticles will be discussed, as well as their role in biomedical applications. Additionally, the biointerface between the produced materials and the biological

milieu will be discussed in terms of protein corona formation and internalization processes by cells.

1.2 MAGNETIC NANOPARTICLES

Magnetic NPs have been used in several biomedical applications^{7,8} despite the highly demanding requirements regarding chemical stability, toxicity, and magnetic performance. As mentioned, IONs are considered as the most promising NPs for biomedical applications, and different types of IONs exist depending on their structure, composition, and properties.⁹ Among others, the three most studied IONs are hematite or α -Fe₂O₃, maghemite or γ -Fe₂O₃, and magnetite or Fe₃O₄.⁷ Hematite is highly stable towards corrosion because it is fully oxidized and entirely composed of Fe³⁺. It is inexpensive to produce, highly stable in water, and its band gap enables the absorption of visible light. Therefore, it is usually employed as a catalyst or gas sensor.¹⁰

Magnetite or Fe₃O₄ is composed of both divalent and trivalent Fe in a cubic inverse spinel. The stoichiometric ratio between Fe²⁺ and Fe³⁺ is 1:2, where Fe²⁺ occupies half of the octahedral positions while Fe³⁺ splits between the remaining octahedral and all the tetrahedral positions. Maghemite or Fe₂O₃ is composed of Fe³⁺ ions organized in a cubic structure, and it is the full oxidation product of magnetite. Since properties of magnetite and maghemite are similar and the differentiation between them is difficult by routine characterization techniques, most of the reported literature regarding biomedical applications does not differentiate between these forms. They are both ferromagnetic and exhibit superparamagnetism under a certain core size.¹⁰

The properties of IONs depend mainly on the core size, morphology, composition, and organic coating.⁷ The core size is a crucial parameter for magnetic behavior: under a certain value, NPs become a single domain and show superparamagnetism. In this situation, NPs show no remanence, i.e. no residual magnetism when B_0 is removed, and null coercivity, which refer to the field required to bring the magnetization back to zero. In IONs, the single-to-multi domain transition occurs at a particle size of 20 ~nm.¹¹ Superparamagnetism is a fundamental property for biomedical

applications in order to avoid the formation of NP agglomerates. Therefore, the improvement of magnetic properties should be addressed while avoiding the increase in NP size.

The doping with magnetic and non-magnetic ions is a common strategy to enhance the magnetic performance without increasing the core size. Cheon¹² and coworkers developed a synthesis method of magnetite doped with Mn²⁺ and Zn²⁺, where an optimal stoichiometry was found to display saturation magnetization (M_s) of 175 emu · g⁻¹, significantly higher than the 127 emu · g⁻¹ found for undoped magnetite. The basis for the increase of M_s is related to the preferential location of Zn²⁺ at the octahedral positions, avoiding the spin cancellation of Fe³⁺ in the original antiferromagnetic arrangement.

1.2.1 Synthesis Method

IONs have been synthesized by different methods to control key physicochemical features such as particle core size, particle size distribution, particle morphology, and colloidal stability.¹³ In addition, new methods are continuously emerging towards more environmentally friendly and cost-efficient experimental procedures. The main synthesis methods of IONs are co-precipitation, microemulsion, hydrothermal, and thermal decomposition.

The co-precipitation method can be considered as the simplest method to synthesize IONs.¹⁴ The reaction involves two stages: first the burst of nucleation, and second the crystal growth.¹⁵ The development of these processes dictates the final particle core size distribution. The chemical transformation occurs in an aqueous solution of Fe³⁺/Fe²⁺ salts with the addition of a base, such as sodium hydroxide, ammonium, or hydrazine, in a temperature range from 20 to 90 °C.



The morphology, particle size and distribution are among the most important parameters that determine the final physicochemical properties of magnetic NPs, and they have been found to be strongly dependent on experimental conditions such as the ionic strength of the medium, temperature, ratio and concentration of iron salts, pH,

etc.¹⁶ The M_s values obtained by this method are around 30–50 $\text{emu}\cdot\text{g}^{-1}$. The main drawback of the co-precipitation method is the polydisperse size distribution of the synthesized NPs, which greatly affects the magnetic properties. However, this methodology has the advantages of being environmentally friendly, simple, scalable, and fast.¹⁶

Thermal decomposition is the synthesis method offering the best control in crystallinity, size distribution, and morphology.¹⁷ It is based on the decomposition of organometallic compounds in high-boiling organic solvents (200–300 °C) containing stabilizing surfactants, such as oleic acid or oleylamine. The experimental ratios between the organometallic precursor, the surfactant, and the solvent together with time and temperature are the parameters governing the structural and morphological properties of the prepared NPs.¹³ The reaction conditions of this technique are very demanding and an inert atmosphere is required during the synthesis (Figure 1A). Thermal decomposition leads to NPs dispersed in organic solvents. Therefore, ligand-exchange strategies are needed in order to obtain water-dispersible NPs.

The hydrothermal method is based on maintaining the reaction mixture at high pressure by employing autoclave reactors (Figure 1B).¹³ This method was reported by Li and coworkers¹⁸ and it is based on the formation of a liquid-solid-solution system, where the metal salts are transferred from the interface of the solution to the solid phase to form the nanocrystals. The solvents employed are normally water or ethanol and the temperatures are in the range of 100–200 °C, with higher temperatures favoring the nucleation step leading to NPs with smaller core sizes. On the other hand, longer reaction times promote the grain growth giving access to larger core sizes.¹⁴ Other reaction conditions such as nature of the solvent, salt precursors, and addition of seeds, have also an impact on the size and the morphology of the NPs. The yields obtained are fair and the reaction time can vary from hours to days. The particle size distribution is usually narrow due to the high temperatures employed.

The microemulsion method consists of the formation of microdroplets of water-in-oil or vice versa (Figure 1C), oil-in-water, based on the different hydrophobic and hydrophilic properties of two solvents and mediated by the presence of a surfactant

that stabilizes the isotropic dispersion.⁷ In particular, water-in-oil microemulsions are the most used to synthesize magnetic NPs, in which the microdroplets act as small nanoreactors. This method offers a relatively good control of the core size and morphology by modifying the organic/aqueous ratio of the solvent mixture.¹⁹ However, the yield of the reaction is the lowest compared to the aforementioned methods.

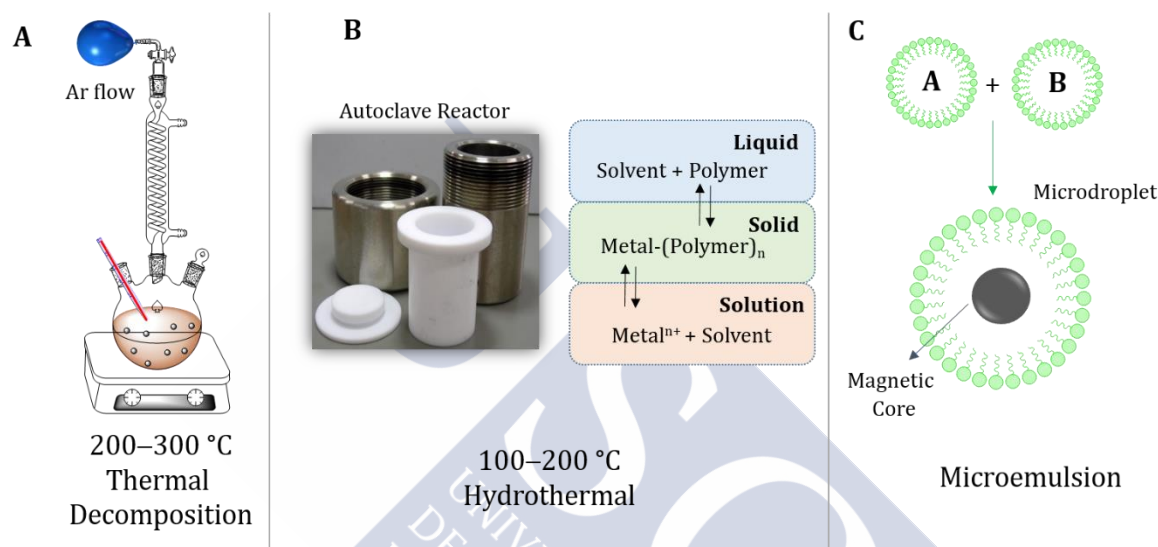


Figure 1: A) Experimental set up for thermal decomposition synthesis of IONs, B) Picture of autoclave reactor for hydrothermal synthesis and scheme of the liquid-solid-solution phases, C) Reaction between microdroplets showing the material transfer in order to obtain IONs by microemulsion method.

Each of the methods presented above display advantages and disadvantages. The current challenge in NP synthesis²⁰ is the scale-up to obtain NPs with high crystallinity, size monodispersity, controlled morphology, and reproducible organic coverage content. The production of NPs with desirable properties on a high scale is still a milestone that prevents the advance of magnetic NPs for biomedical applications.

1.2.2 Surface Functionalization

The surface of naked IONs is composed of Fe and O atoms, where Fe act as a Lewis acid and coordinates water molecules in an aqueous medium.^{21,22} Therefore, the surface charge, or ζ -potential, in naked IONs is pH-dependent: at basic pH it is negative, at acidic pH positive, and at a neutral pH around zero.

The prevention of agglomeration of IONs in aqueous medium can be accomplished by steric and/or electrostatic stabilization.²³ On one hand, the steric stabilization is adequate to stabilize NPs in solutions with high salt concentration and in a wide range of pH. The strategy relies on the use of polymer shells that maintain the NPs apart due to an increase in the entropy of the polymers when they approach. On the other hand, the electrostatic stabilization relies on the electrostatic repulsion between the NPs, and is thus highly dependent on the salt concentration and pH. The force of electrostatic repulsion can become greater than van der Waals attraction forces when NPs are charged, and lead to stabilization of individual NPs. Both stabilization modes can play a role at the same time in the colloidal stability of the NPs.

Therefore, either organic or inorganic coating of IONs is needed for them to be stable at physiological pH,²³ to enhance chemical stability, to reduce cytotoxicity, and to confer antifouling properties against biomolecules.⁸ There are two main approaches to functionalize IONs: *in situ* functionalization and post-synthesis surface modification.²³ *In situ* functionalization refers to a one-pot synthesis of the inorganic core and the shell at the same time. In this procedure, the chemicals are added together to the reaction mixture. This strategy is simple and time-efficient. Post-synthesis surface modification implies a two-step procedure: first, the inorganic core is synthesized, and second, the addition of molecules with binding affinities to the inorganic core is performed. This strategy offers versatility as there is a broad commercially available catalogue of chelating molecules.

Within post-synthesis protocols, the chemical surface modification of IONs can be achieved by ligand addition, ligand exchange, or encapsulation.²⁴ The ligand addition consists of adding the ligand of interest to the prepared NPs, with no removal of other ligands. Contrarily, ligand exchange usually implies the substitution of hydrophobic ligands with hydrophilic ones governed by equilibrium reactions. Third, the IONs can be also efficiently encapsulated in a polymer matrix with hydrophilic/hydrophobic properties. All these functionalization strategies result in different structures and morphological conformations, such as core-shell, mosaic, shell-core, matrix disperse, and shell-core-shell structures (Figure 2).²³

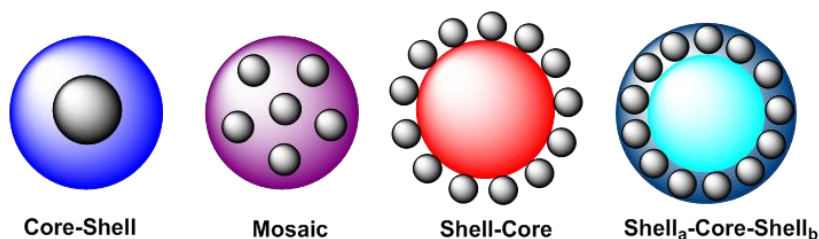


Figure 2: Structure of core-shell, mosaic, shell-core, and shell_a-core-shell_b NPs.

As mentioned, a vast variety of materials also exists for the coating of IONs (Table 1).²⁵ The materials can be classified into two main categories by the nature of their composition: inorganic and organic compounds. Different coating materials affect the colloidal stability, adsorption of molecules, chemical degradability, and magnetic properties of the synthesized NPs. Therefore, the selection of coating must be done bearing in mind the future application of the IONs.

Table 1: Classification of materials for surface modification of IONs.

Inorganic compounds	Organic compounds
Silica	Small molecules: silanes citrates, phosphates
Metals: gold, rare-earth elements	Polymers: natural and synthetic
Metal oxides: zinc, cobalt ferrites	Macromolecules: liposomes, dendrimers

One of the most used inorganic coating for IONs is silica, since it gives high colloidal stability, excellent water dispersion, and protection against photodegradation and oxidation.²⁶ The most common methodology uses the Stöber process,²⁷ i.e. the condensation at basic pH of hydroxylic groups at ION surface with orthosilicates. The thickness of the silica layer can be controlled through reaction conditions such as time, pH, or amount of catalyst. The functionalization of the silica coating involves straightforward and well-known chemistry, which gives access to IONs with functional moieties for further attachment of drugs, antibodies, or imaging probes.

On the other hand, gold is among the most used metals as coating for IONs due to its ability to be post-functionalized through thiol-gold chemistry.²³ Moreover, gold offers a protective layer with relatively low reactivity or chemical inertness. There are

several examples in the literature for Au-coated IONs. For example, Sun and coworkers²⁸ reported a method in which HAuCl_4 seeds were reduced on the surface of IONs, yielding core-shell nanostructured Au-coated magnetite NPs and preserving the original magnetic properties of IONs. However, when transition metal oxides are used as coating, the magnetic properties may change depending on the magnetic nature of the metal oxides phase formed.²⁹ For example, Cheon and coworkers³⁰ reported a heterostructure composed of a core of Fe_3O_4 coated with cobalt ferrite shell with higher M_s and coercive forces.

The main concerns about inorganic coatings are their degradability and toxicity, as opposed to organic materials.^{23,31} Organic molecules that are able to interact with the IONs' surface can be divided into small molecules, polymers, and macromolecules (Table 1). Unlike polymers, small molecules are able to enhance the colloidal stability of IONs with little to no increase in the hydrodynamic diameter.²³ This characteristic is important when IONs are designed to diffuse to the extravascular space, as particle size plays a fundamental role in NP biodistribution.²⁴ There are several functional groups with high affinity to anchor to the surface of IONs: carboxylates, phosphonates, aminosilanes, and alcohols are the most commonly used.^{23,26,32} Ligands with multiple functional groups are especially interesting because they interact through multiple bonds.³³ Examples of molecules with multiple functional groups are citric acid,³⁴ dimercaptosuccinic acids,³⁵ and dopamine (Figure 3).³⁶

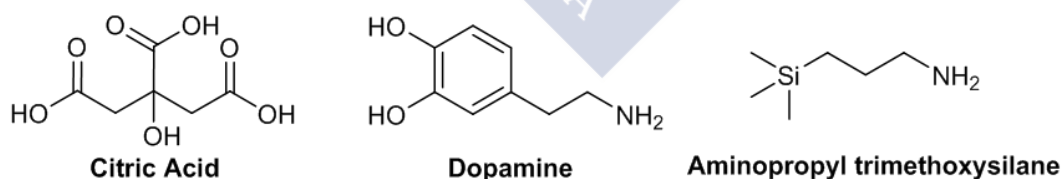


Figure 3: Examples of small molecules for the functionalization of IONs.

Oppositely, polymers offer a shell protection with the consequent increase in hydrodynamic diameter. Polymers used in NP coating can be of natural or synthetic nature. Dextran and chitosan are natural polymers based on polysaccharides often used as coating agents due to their high biocompatibility. The large amount of hydroxyl groups in these polymers enables multiple effective interactions by hydrogen bonding between the polymers and the IONs leading to stable nanocolloids.²³ For example,

Feridex is a dextran-coated ION that successfully obtained the food and drug administration (FDA) approval and made it into the clinic.

In order to obtain new features, synthetic polymers emerged to bring distinctive properties than those offered by natural polymers. For example, polyethylene glycol (PEG) coating provides NPs with high water solubility, improved biocompatibility, and enhanced blood circulation time (Figure 4).^{37,38} Polylactic acid (PLA) coating contributes to enhancing the biocompatibility and biodegradability of the NPs and exhibits low toxicity.³⁸ Polyacrylic acid (PAA) coating is also commonly used because it offers great possibilities for bioconjugation due to the large amount of carboxylic groups available for further functionalization.

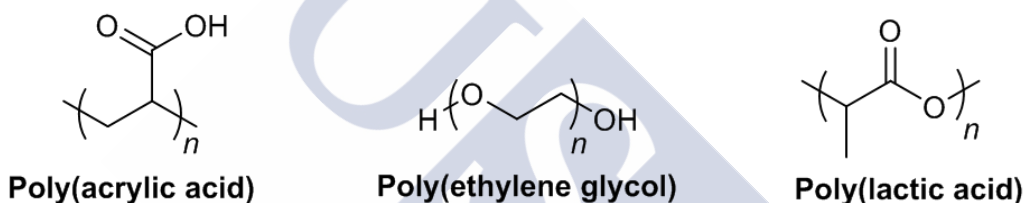


Figure 4: Examples of polymers use for the coating of IONs.

Among macromolecules, liposomes are useful assemblies to encapsulate NPs when the loading of NPs need to be increased, for example, to achieve better contrast in MRI or higher temperatures in magnetic hyperthermia.²³ The bilayer structure can encapsulate hydrophobic and hydrophilic substances, such as IONs, drugs, or imaging probes. In general, the structures composed of magnetic NPs encapsulated within liposomes are usually referred to in the literature as magnetoliposomes.³⁹

1.2.3 NP Functionalization: Click Chemistry

Apart from enhancing biocompatibility and achieving water dispersions of IONs, coating molecules can offer 'anchors' available for further functionalization.⁴⁰ The current challenges of nanomedicine requires nanomaterials with sophisticated structures that bear targeting molecules, multimaging probes, and cargo release with stimulus-driven mechanisms.⁴¹ Therefore, it is of fundamental importance to develop chemistry strategies that enable complex surface modifications such as the attachment of biomolecules to NPs.

NPs display polydispersity in size, morphology, and coating coverage, resulting in a high variability of physicochemical properties that hampers the homogeneous conjugation across the NP population. Moreover, the reaction between the NPs and the molecules of interest is interfacial in nature and is affected by factors such as density of ligands on the NP surface, loss of colloidal stability during reaction, and charge repulsions, resulting in low yields of conjugates.⁴²

Additionally, characterization of hybrid inorganic–organic conjugates may be difficult,^{20,42} and therefore it is essential to employ synthetic procedures that are easy to control, reproducible, and with a broad scope. In 2001, Sharpless introduced the new concept of ‘click chemistry’,⁴³ the main philosophy of which relies on focusing the synthetic effort on the functionalities with desired properties rather than achieving complex structures. In order to provide an adequate toolbox of chemical transformations, criteria was established for a reaction to be considered as click:⁴³

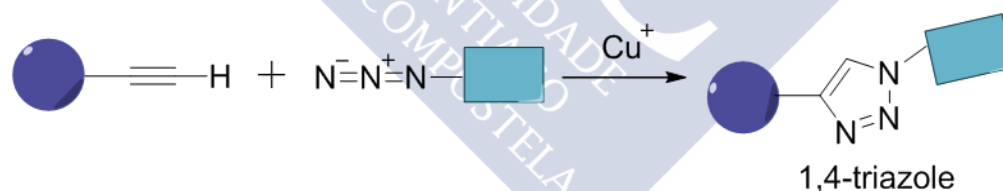
“[to] be modular, wide in scope, give very high yields, generate only inoffensive byproducts that can be removed by nonchromatographic methods, and be stereospecific (but not necessarily enantioselective)...include simple reaction conditions (ideally, the process should be insensitive to oxygen and water), readily available starting materials and reagents, the use of no solvent or a solvent that is benign (such as water) or easily removed, and simple product isolation. Purification, if required, must be by nonchromatographic methods, such as crystallization or distillation, and the product must be stable under physiological conditions.”

These very stringent criteria are actually fulfilled only by some chemical transformations:⁴³ additions to carbon–carbon multiple bonds, such as epoxidation, dihydroxylation, aziridination, sulfenyl halide addition, and Michael addition chemistry, nucleophilic substitution chemistry, such as ring-opening reactions of strained cycles, cycloadditions of unsaturated species (1,3-dipolar cycloadditions) and Diels–Alder reactions, and carbonyl chemistry of the “non-aldol” type, such as formation of ureas, thioureas, aromatic heterocycles, oxime ethers, hydrazones, and amides.

1.2.4 1,3-Dipolar Cycloaddition

Cu(I)-catalyzed azide–alkyne cycloaddition (CuAAC)⁴⁴ is a variation of the thermic reaction known as azide–alkyne cycloaddition. Among those considered as click reactions, CuAAC is the most popular and commonly employed and it is sometimes referred solely as the click reaction.⁴² The Huisgen 1,3-dipolar cycloaddition between azides and alkynes leads to 1,2,3-triazoles in quantitative yields, and if catalyzed by Cu(I), the reaction proceeds $\sim 10^8$ -fold faster at room temperature, and forms regioselectively 1,4-disubstituted triazoles (Scheme 1).

The triazole ring possesses high stability towards hydrolysis, redox reactions, and temperature, and it can be considered an artificial analog of the amide bond,⁴⁵ as it forms hydrogen bonds with water molecules similarly to amide linkages. The CuAAC is not affected by changes in temperature, solvents, and pH. Therefore, it has shown great scope in bioconjugation.⁴⁶ The reaction is neither oxygen- nor water sensitive, since Cu(I) is generated *in situ* with reductant species such as ascorbic acid. CuAAC has been successfully employed for the functionalization of carbohydrates, peptides, nucleosides, and non-natural molecules, such as dendrimers.^{47–49}



Scheme 1: CuAAC reaction between an alkyne and an azide moiety to give access to 1,4-triazole.

Due to its attractive features, the CuAAC has been employed for the functionalization of IONs. For example, Mathur and coworkers⁵⁰ functionalized the surface of magnetite with biotin and a cysteine protease inhibitor by CuAAC, and showed the promise of these nanohybrids for the caption and detection of proteases. In another study, Brougham and coworkers⁵¹ reported for the first time the grafting of a glycopeptide on the surface of IONs by CuAAC. Kjems and coworkers⁵² developed IONs coated with PEG and a specific targeting peptide using CuAAC and showed promising results of receptor-mediated endocytosis in *in vitro* experiments.

1.2.5 Diels–Alder Reaction

One of the most interesting click reactions is the Diels–Alder cycloaddition because it offers thermal reversibility.⁴³ Diels–Alder reaction was first described by Otto Diels and Kurt Alder in 1928,⁵³ for which they were awarded the Nobel Prize in Chemistry in 1950. The reaction is a [4+2] cycloaddition between a conjugated diene and a dienophile to form a substituted six-membered ring. If there is a non-carbon atom present in either the diene or the dienophile, the reaction is called a hetero-Diels–Alder reaction.⁵⁴

The mechanism of the reaction is assumed to proceed via a single cyclic transition state. A variety of dienes can be employed in the Diels–Alder reaction (Figure 5), for which the major requirement is a *cis* conformation within the double bond. Regarding the electron requirements, the normal electron-demand Diels–Alder reaction is a reaction between an electron-rich diene, such as cyclopentadiene, and an electron-deficient dienophile, such as maleic anhydride. However, if the diene has electron-withdrawing groups (EWGs) as substituents, and the dienophile bears electron-donating groups (EDGs), an inverse electron-demand Diels–Alder reaction can take place.

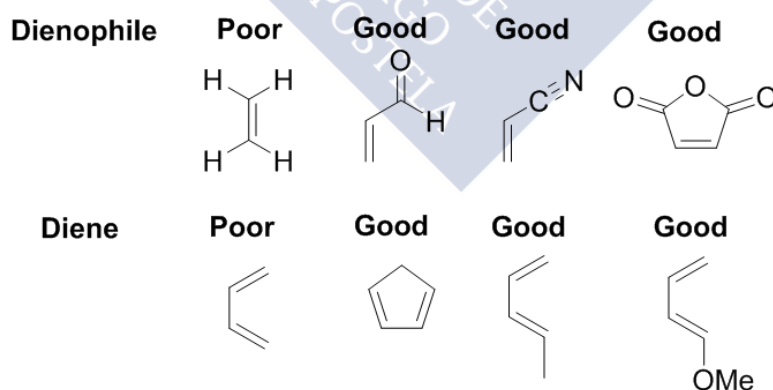
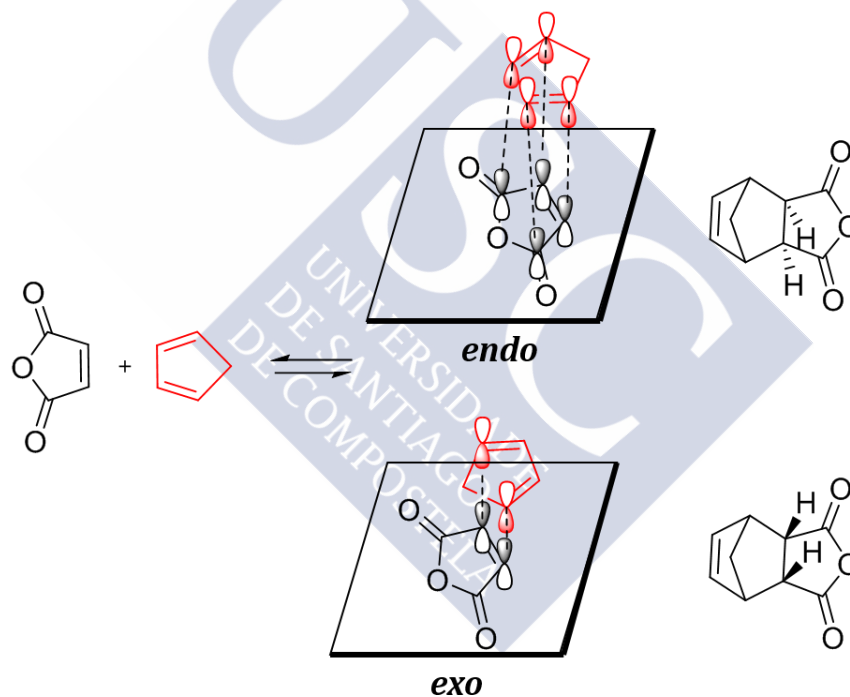


Figure 5: Examples of good and poor dienophiles and dienes in the Diels–Alder reaction.

When an unsymmetrical diene and dienophile react, two different regioisomers can be formed depending on the positions of the substituents. Because Diels–Alder reactions are concerted cycloadditions, the stereochemical information of the reactants is retained within the products, i.e. if the dienophile employed has substituents with *Z*

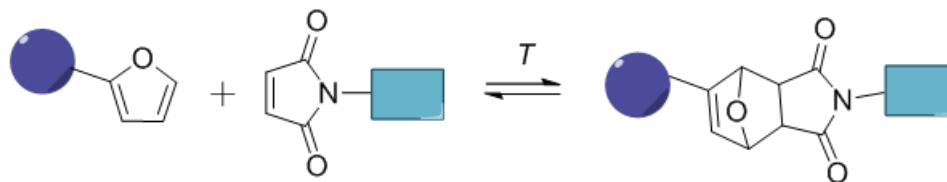
conformation, the adduct product will have the substituents with *anti* stereochemistry. Moreover, if the dienophile is unsymmetrical, two transition states are possible: the *endo* and *exo* transition state, each leading to adducts of different stereochemistry. In the *endo* transition state, the substituent on the dienophile is oriented towards the diene, whereas in *exo* it is oriented away from it. For normal electron-demand Diels–Alder scenarios, with electron-withdrawing substituents such as carbonyls attached to the dienophile, the *endo* transition state is typically preferred, despite often being the more sterically hindered one (Scheme 2). This preference is known as the Alder rule, and it is based on the secondary orbital interactions and the overlap of π orbitals.⁵⁴



Scheme 2: Diels–Alder reaction with the formation of *exo* and *endo* products.

For biomedical applications, the Diels–Alder reaction of furan as the diene with maleimide as the dienophile is the most popular (Scheme 3).⁵⁵ The reason is related to the low temperature that this adduct requires for undergoing the retro-Diels–Alder reaction, although this is dependent on the substituents on both moieties.⁵⁶ This characteristic offers the possibility to obtain temperature-responsive materials.

Different molecules containing furan and maleimide moieties have been extensively used in polymer chemistry, as demonstrated in the vast literature on this topic.⁵⁷⁻⁵⁹



Scheme 3: Diels–Alder reaction between a furan and a maleimide moiety to give access to a 6-membered ring adduct.

The application of the furan–maleimide reactions to IONs is a much more recent strategy. IONs offer the possibility of triggering the retro-Diels–Alder reaction taking advantage of the magnetic properties to initiate the increase in temperature. The temperature needed to produce the retrocyclization is dependent on the particular characteristics of the formed adduct, for example, usually *endo* products require lower temperatures of 30 to 50 °C than the *exo* isomer to undergo the reaction.⁵⁵ Moreover, the electronic characteristics and the position of the substituents on the furan and maleimide moieties also affect the adduct stability. Theoretical and experimental studies have shown that furan dienes substituted with EDGs in the second position are the most promising in obtaining reversibility, while EDG substituents on the fourth position in the furan ring usually give access to high energy adducts that cannot undergo the retrocyclization.⁵⁶

Two different examples are found in the literature that employ furan and maleimide moieties and IONs.^{60,61} Kirschning and coworkers⁶¹ reported on the preparation of IONs with maleimide functional groups. In this work, commercially available magnetite NPs were reacted with maleimide-containing silane ligands, followed by a Diels–Alder reaction with furan-modified coumarin molecules as a model system for the quantification of the maleimide functional groups. Moreover, the maleimide-NPs were functionalized with a furan-modified Ansamitocin, a drug with antitumoral activity. The authors studied the release of the drug by conventional heating in an oil bath and by magnetic hyperthermia. The results showed a higher release rate under magnetic hyperthermia than with conventional heating, and the proposed reason

relied on the hypothesis that a higher temperature is achieved on the surface of IONs with magnetic hyperthermia.

The second example was reported by N'Guyen et al.,⁶⁰ where they performed the double functionalization of IONs with combined click reactions by the synthesis of a phosphonic acid with both alkyne and furan functional groups. In this work, the alkyne was functionalized with hydrophilic polymers to get access to biocompatible and water-dispersible NPs. On the other hand, the furan was reacted with a maleimide-containing fluorophore Rhodamine as a model system. The release of Rhodamine was detected by fluorescence after the treatment of NPs with magnetic hyperthermia. Such systems have great potential for the delivery of molecules on command, and therefore offering reduced toxicity. The next generation of drug delivery nanocarriers is expected to compile theranostic tools and controlled-release responses.

1.3 BIOMEDICAL APPLICATIONS

IONs are considered low in toxicity because Fe is an intrinsic element in the human body with its corresponding metabolic routes. Therefore, IONs are used in several biomedical applications such as MRI, hyperthermia, and drug delivery. Lewis and coworkers⁶² studied the fate of IONs with radioactive Fe in dogs and mice. Their results showed a tolerance of 3000 mmol of Fe per kg of body weight, which corresponds to 150 times more dosage than recommended as a contrast agent in MRI. After 1 h of the injection Fe was concentrated in the liver (82.6%) and spleen (6.2%), but gradually decreased, and radioactive Fe was found in hemoglobin of erythrocytes. Therefore, IONs are generally considered safe for biomedical applications.

1.3.1 MRI: T_1 , T_2 , and Dual Contrast Agents

Magnetic resonance imaging (MRI) is a technique used in the clinical field for the diagnosis of diverse diseases, such as stroke or cancer. It allows the visualization of internal tissues and organs concerning the different water content within the human body. MRI displays remarkable characteristics such as high spatial resolution,

noninvasiveness and the absence of ionizing radiation. However, the sensitivity of MRI is sometimes too low to distinguish between adjacent healthy and damaged tissues, and contrast agents (CAs) are used to enhance resolution, i.e. the relative difference in signal between two adjoining tissues.

In the acquisition of an MRI image, the protons' nuclei spins are aligned with an external magnetic field, and then a radiofrequency pulse of 90° at the Larmor frequency is applied to flip the spins (Figure 6). Two different relaxation processes appear in the different axes (z and xy) in order to restore the initial magnetization (restoration of Boltzmann equilibrium).⁶³ The contrast observed in an acquired MRI image corresponds to a distribution of different relaxation times of protons' nuclei spins. Consequently, CAs enhance the sensitivity by shortening the relaxation times of surrounding protons' nuclei.

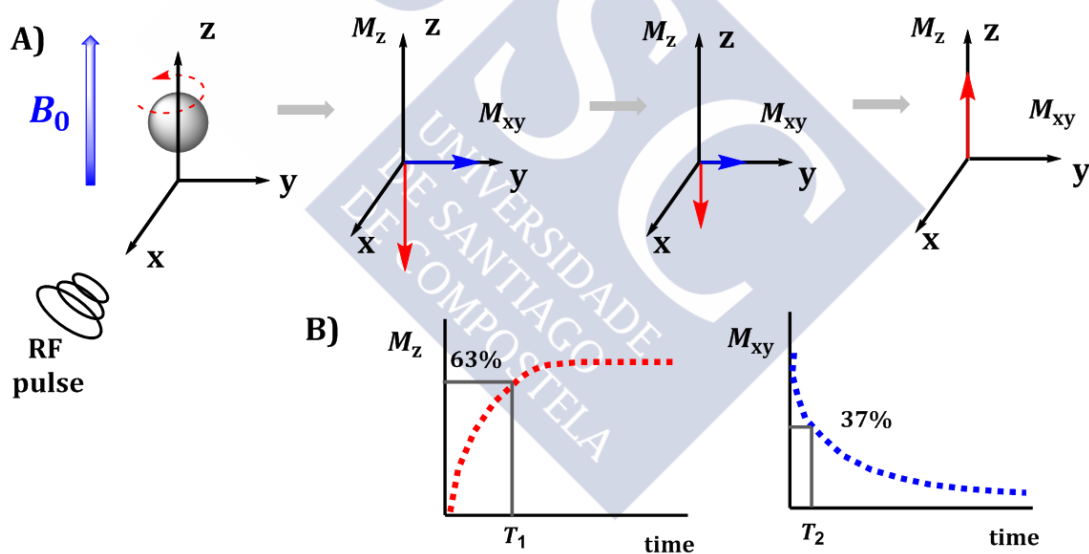


Figure 6. Proton spins relaxation processes defined in MRI in the z and xy axes. RF refers to a radio frequency pulse.

CAs can affect the relaxation time of water protons' nuclei by two different processes: the longitudinal relaxation or T_1 , where the proton signal is enhanced and therefore the contrast obtained is bright or positive; and transversal relaxation or T_2 , where the proton signal is reduced and the contrast obtained is dark or negative. Commonly, CAs are helpful for the reduction of either T_1 or T_2 , e.g. gadolinium chelates function as bright CAs and IONs as dark CAs (Figure 7).

The longitudinal relaxation or lattice-spin mechanism refers to the transfer rate of energy from the nuclear spin system to the neighboring molecules (the lattice) in the z-direction. CAs shortening the T_1 need to fulfill energy transfer requirements to accelerate the motion of the surrounding molecules and achieve the relaxation process faster. The most common source of the local fluctuating field for a proton spin is a direct dipolar interaction. The mechanism of longitudinal relaxation depends on the rate of molecular motion and is therefore dependent on temperature. CAs employed to shorten the T_1 are paramagnetic species (Table 2). The most widely used T_1 CAs in the clinic are based on gadolinium salts, i.e. Dotarem, due to the seven unpaired electrons of the gadolinium ion.

Table 2: Electronic configuration and magnetic moment of metal ions.

	Ion	Electronic configuration	Magnetic Moment (μ_B)
Transition metal ion	Mn ²⁺	↑ ↑ ↑ ↑ ↑	5.9
	Fe ³⁺	↑ ↑ ↑ ↑ ↑	5.9
Lanthanide metal ion	Eu ³⁺	↑↓ ↑ ↑ ↑ ↑ ↑	3.4
	Gd ³⁺	↑ ↑ ↑ ↑ ↑ ↑ ↑	7.9

The transversal or spin-spin relaxation mechanism refers to the rate of decay of the magnetization within the xy plane. After the 90° pulse, the nuclear spins flip and are aligned in one direction, but with time the spins dephase due to field inhomogeneities and/or direct interactions between the spins without energy transfer to the lattice. The spin-spin relaxation is proportional to spin-lattice relaxation, since an increase in z-magnetization is not possible without a decrease in magnetization in the xy plane. The static dipolar fields created by neighboring dipoles are very large in solids. Thus, the spin-spin mechanism is very efficient in NPs.⁶⁴

CAs acting in the T_2 reduce the transverse relaxation time leading to a negative contrast in the acquired image. IONs are currently the most used in this modality.

There are several products approved by FDA in which the common feature is an iron oxide core with different polymeric coatings: Feridex, Resovist, Lumirem.

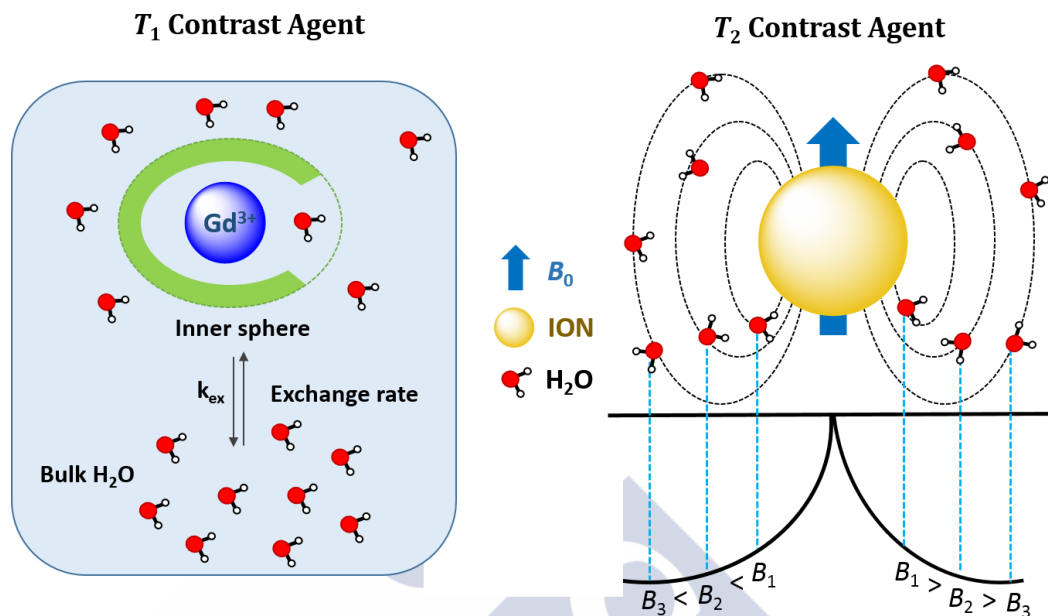


Figure 7: *T₁ and T₂ mechanisms involved in the CAs actuation. For T₁ the mechanism is based on the coordination of water molecules to Gd³⁺. For T₂ CAs the proximity to IONs determines the magnetic field that the water molecules sense.*

The efficiency of CAs to reduce the relaxation time of water protons' nuclei is known as relaxivity (r), and it represents the inverse of the amount of the CA needed to reduce proton relaxation time by one second. Therefore, the higher r is, the more efficient the CA acts, and less CA is needed to reduce the proton relaxation time. The inverse of relaxation time, either T_1 or T_2 , is known as the relaxation rate (s^{-1}), and it is denoted as R_1 or R_2 . Relaxivity is calculated from the slope of the linear fitting $R_{1,2}$ against different CA concentrations, and r is dependent on temperature, magnetic field, and solvent.⁶⁵ For clinical applications, the standard conditions involve field strengths up to 3 T and the temperature of 37 °C.

The clinical diagnosis is sometimes limited by image interferences, such as hemorrhagic regions, bond calcification, metal deposits, and susceptibility artifacts.⁶⁶ The combination of multiple imaging modalities can yield complementary information to identify these interferences. The use of different imaging techniques is an option for that purpose, but it entails coordination of different penetration depths, time scales,

and equipments. Therefore, the dual behavior of a single CA platform within the same technique is preferred as it simplifies the acquisition due to identical penetration depths and time scale in both imaging modes. Dual T_1 – T_2 CAs have attracted attention in the recent years, and complex nanostructures from coupled materials have emerged in order to fulfill both T_1 and T_2 requirements, for example, IONs attached to gadolinium compounds.^{67–69}

1.3.2 Cell Tracking

Stem cells possess two unique properties: self-renewal and differentiation potency.⁷⁰ Self-renewal is the capability of stem cells to undergo numerous cell cycle divisions, and differentiation potency refers to the ability of cells to develop into mature cell types. Cell therapy is based on the administration of stem cells, relying on their ability to self-renew and differentiate into other cell types to replace damaged cells. Stem cells show promise for the treatment of various diseases, such as glioma, ischemic brain injury, and cardiovascular disease,^{71–73} as demonstrated by their involvement in more than 360 clinical trials.⁷⁴

The understanding of the cell dose required, administration route, and biodistribution of these transplanted stem cells is of fundamental importance in order to develop safe and controlled cell therapies. Non-invasive cell tracking and specific imaging along the time of labeled stem cells *in vivo* is an ideal methodology to follow the migration and grafting of transplanted cells, and to evaluate their fate and therapeutic effect.⁷⁵ The magnetic properties that dictate IONs' good performance as CAs can be exploited to magnetically label stem cells. IONs combined with MRI are a common approach for non-invasive cell tracking due to the biocompatibility and efficiency of IONs, and the high spatial resolution, penetration depth, and the lack of ionizing radiations provided by MRI.⁷⁶

1.3.3 Labeling Procedures

The transplanted stem cells are not distinguishable from the host cells of the living organism, and therefore need to be labeled *in vitro* with exogenous materials

(Figure 8). The labeling procedures are based on incubation of stem cells in cell culture medium containing IONs. Important aspects of the procedure are the dose of IONs and the incubation time. The health of the stem cells after magnetic labeling must be unchanged in order to maintain the therapeutic effect and cell migration *in vivo*.

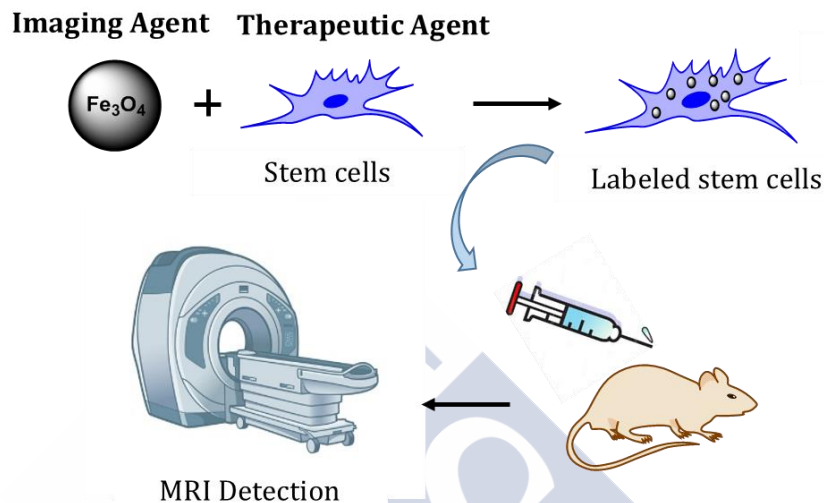


Figure 8: Representation of the labeling procedure of stem cells with IONs for cell tracking applications.

When IONs are used for the co-culturing, the dose term can be split into three: exposure, delivered, and cellular dose (Figure 9).⁷⁷ The exposure dose, also known as the gravimetric dose, is the amount of IONs used in the cell culture medium, normally expressed as $\mu\text{g mL}^{-1}$. The delivered dose refers to the actual mass or number of IONs that come in contact and interact with the cells, and it is, therefore, difficult to quantify. The cellular dose can be considered the most important parameter in cell tracking, as it refers to the amount of IONs that actually access the intracellular compartments, i.e. the uptake of IONs. Thus, cellular dose is a key parameter that determines the detectability of the labeled cells *in vivo*.

Another important parameter in cell labeling procedures is the uniformity and homogeneity of the label across the cell population, and it is usually known as the labeling efficiency. The labeling efficiency refers to the Fe dose on a cell-to-cell basis.⁷⁷ Especially when the IONs have low colloidal stability in the cell culture medium, the formation of large aggregates can lead to Fe incorporation through a sedimentation-driven process resulting in an inhomogeneous distribution of the label through the cell

population.⁷⁸ The labeling efficiency can be assessed quantitatively by Fe staining, i.e. Prussian blue (PB) assay, photothermal microscopy, or flow cytometry (if a fluorophore is employed), in order to confirm the cellular dose.

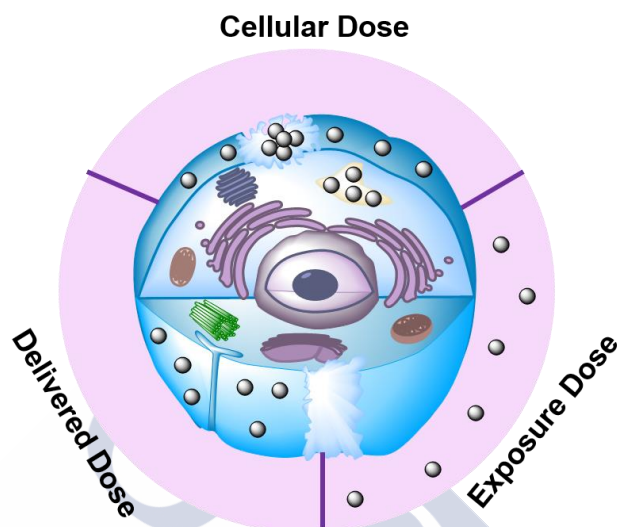


Figure 9: Different dose concepts for cell tracking applications: cellular, delivered, and exposure dose.

The amount of internalized Fe depends on the particular physicochemical properties of the NPs and on the cell type employed, but they are generally in the range of 3–30 pg Fe/cell.⁷⁷ As a reference, Park reported uptake values of 18 pg Fe/cell employing Resovist (FDA approved ION) and PLL.⁷⁹ However, new formulations of IONs have been recently reported in the literature to achieve a higher cellular dose⁷⁷ and, consequently, long-term detectability by MRI. IONs coated with pullulan and ethylenediamine reported by Tabata⁸⁰ showed 65 pg Fe/cell, a very high uptake value also reported by Ni⁸¹ and coworkers with IONs coated with PLL.

1.3.4 Limitations of IONs for Cell Tracking

Despite IONs offering a great opportunity to label stem cells, they also suffer from certain limitations.⁷⁵ The first issue is related to the MRI detection: when the cells proliferate the ION cargo divides into the daughter cells, and therefore the detection may be compromised. Moreover, the cell migration *in vivo* leads to a low density of labeled cells in the area of interest that can be below the detection limit, since detecting a single stem cell is not yet possible. The second limitation concerns the lack of

functional information of the cell from the IONs. On one hand, IONs result in no different MRI signal if the stem cell differentiates into other cell types, and thus the use of complementary techniques, such as immunohistochemistry or confocal chemistry, is needed to access that information. In the case of cell death, the situation is equivalent: IONs will give no distinguishable MRI signal from living cells. Furthermore, when the dead cells are cleared off, they are incorporated by macrophages, thus resulting in a risk of misinterpretation of the MRI signal.

The need for multimodal probes and techniques is mandatory for cell tracking, as there is complex information that needs to be addressed. Cell tracking is still in the early stages and current efforts are focused on multimodality detection of transplanted stem cells to enhance the reliability of the obtained data.⁸²

1.3.5 Hyperthermia

Hyperthermia treatment is based on a temperature increase to cure a medical condition, nowadays mainly investigated for cancer treatment. The belief of heat as a medical tool for therapy dates to many centuries ago to the time of Greeks, Egyptians, and Romans. Parmenides stated in 500 BC:⁸³

Give me a chance to create fever and I will cure any disease.

It was in 1898 when F. Westermarck conducted the first clinical trial to treat cervical cancer by raising local body temperature by the application of hot water. The Swedish gynecologist noted excellent response in seven patients.⁸⁴ Since then, many clinical trials on hyperthermia have been conducted for the treatment of different types of cancer, such as glioblastoma multiforme,⁸⁵ sarcoma, or breast cancer.⁸⁵

The specific mechanisms behind hyperthermic cell damage are still unknown, though it is believed that the key step is protein denaturation.^{86,87} Cell death pathways are different depending on the temperature. When the temperature rises to around 41–45 °C, cells are involved in the apoptosis pathway. Apoptosis is a type of cell death present in normal tissue homeostasis that does not result in an inflammatory response.⁸⁸ Investigations are undergoing to accelerate the apoptosis rate in tumors through treatment with heat,³ radiation,⁸⁹ or chemotherapy.⁹⁰ On the contrary, when

the temperature rises above 46 °C, cells suffer necrosis and the treatment is known as thermal ablation. Necrosis is a premature cell death pathway and therefore result in an inflammatory response.⁸⁸ Thermal ablation is harmful and presents more side effects when compared to mild hyperthermia treatment, and therefore the latter is preferred.

Tumor cells have shown greater sensitivity to heat when compared to healthy cells.⁸³ There are two main aspects that contribute to the higher vulnerability of tumors cells to thermotherapy. First, cancer cells are dividing faster in mitose phase and therefore protein denaturation deeply affects the synthesis and repair of the DNA.⁸⁷ Second, the tumor architecture is characterized by low vessel density as a consequence of rapid growth, which results in low blood flow with less heat dissipation capability.⁹¹

The resistance of tumors to chemo and radio therapies frequently cause failure in the treatment. Hyperthermia has been proven to have a synergic effect with either chemotherapy or radiotherapy,⁹² being more effective than those therapies alone. The therapeutic effect of the delivery of radiation and/or drugs was found to be enhanced with increasing temperature.⁸⁶ As a consequence of hyperthermia, the oxygenation of tumors rises and the penetration of radiation is increased. On the other hand, the blood flow is also increased by heat, improving the delivery of drugs into the tumor.

Hyperthermia treatment is classified into three types according to the treated area: whole body hyperthermia; regional hyperthermia, for advanced cancer treatment by perfusion or microwaves; and local hyperthermia, mainly used for volumes smaller than organs. The latest is the least invasive technique.

1.3.6 Magnetic Hyperthermia

Local hyperthermia uses heat mediators known as antennas that can emit microwaves, ultrasounds, or radio waves.^{93,94} Magnetic hyperthermia (MH), or magnetic fluid hyperthermia, uses magnetic materials, mainly iron oxide NPs, as antennas to transform electromagnetic energy into heat when placed under an alternating magnetic field (AMF).⁹⁵ The radiation employed in MH must be set in the range of radio-frequency within a few kHz to one MHz.⁹⁶ These frequencies guarantee that no

harmful effects occur while ensuring sufficient penetration depths to access internal organs and tissues, in contrast to other radiation techniques such as microwave or photothermal. MH is mainly applied to the treatment of solid tumors (Figure 10),⁹⁵ and this research field has grown exponentially in the last ten years (Figure 11).

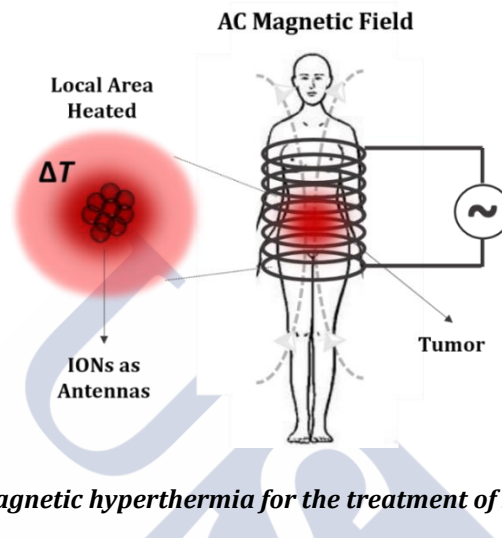


Figure 10: ION-mediated magnetic hyperthermia for the treatment of solid tumors.

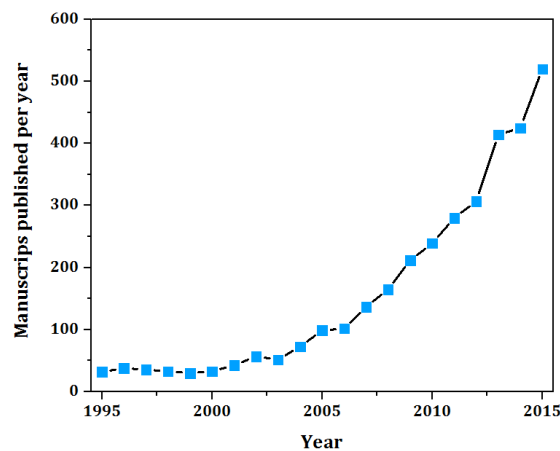


Figure 11. Scientific articles published in the last ten years using 'magnetic hyperthermia' as search term. Web of Knowledge 15.08.16.

The conversion of magnetic into thermal energy in MH can be explained by different mechanisms regarding the magnetic material and experimental conditions employed.^{3,95} If the magnetic material is multi-domain, such as either ferri- or ferromagnetic NPs, the mechanism is governed by hysteresis losses. If the magnetic material is single-domain, e.g. superparamagnetic IONs, the dissipation of heat is promoted through relaxation losses of different nature: Néel and Brownian relaxation. Both relaxation modes depend on the alignment of the particle's magnetic moment in

the direction of the applied magnetic field, and with the reorientation to the equilibrium once the magnetic field ceases. However, Néel relaxation is related with the reorientation of the magnetic moment while the particle itself remains fixed, while Brownian is caused by the friction of the particle with the embedded medium as consequence of the torque provoked when the magnetic moment aligns with the applied magnetic field. On one hand, Néel relaxation is highly size-dependent, as by decreasing the particle size the energy barrier for the magnetization reversal also decreases. On the other hand, Brownian relaxation is also size-dependent but it is mainly governed by the viscosity of the dispersant solution. Both Néel and Brownian mechanisms contribute simultaneously to the thermal energy production. The heating capability of NPs in MH can be defined by several terms, the most common one is known as specific absorption rate (SAR),⁹⁷ expressed in $W g^{-1}$:

$$SAR = \frac{c\Delta T}{mFe \Delta t} \quad (1)$$

where c is the heat capacity, and ΔT is the temperature increment in a certain time (Δt), and mFe is the mass of Fe. SAR depends on the intrinsic physicochemical characteristics of the magnetic material, but also on the parameters of the measurement, such as frequency and amplitude of the applied magnetic field or concentration of the magnetic fluid. Comparisons from different materials in the literature can be challenging due to diverse measuring parameters, and there is a need for standardization protocols.⁹⁵ Alternative expressions for the characterization of heat production have been proposed, such as intrinsic loss power⁹⁸ or effective specific absorption rate.⁹⁹

The magnetic performance of the fluid in MH governs the dosage needed in order to achieve a desirable increase in temperature. Recently, significant efforts have been devoted to the synthesis and design of nanomaterials for MH applications.⁴¹ The most studied composition is the superparamagnetic iron oxide due to the high biocompatibility, low-cost production, and magnetic response.¹⁰⁰ Other formulations have been studied in order to increase the heat generation, for example substituted ferrite NPs with zinc, nickel, cobalt, and manganese.^{66,100-102} However, safety concerns about exogenous ions are high, and iron-based NPs are often preferred.¹⁰³

The physicochemical properties of nanomaterials that affect the heat production are mainly chemical composition, particle size, and core morphology.¹⁰⁴ The particle size determines the magnitude of the magnetic moment and the saturation magnetization of the NPs, and a direct relationship has been found in the literature between the particle size and SAR within the superparamagnetic range.^{95,105} Hergt and coworkers showed the optimal particle size at the transition between superparamagnetic and ferrimagnetic behavior.¹⁰⁶ In IONs, this region corresponds to sizes around 20 nm.¹⁰⁵ As an example, MagForce™ is a company working in clinical trials for the treatment of glioblastoma by the administration of dextran-coated IONs with sizes of 15 nm followed by the application of MH.

As mentioned, the morphology of NPs also plays an important role, as magnetic anisotropy is a key factor on MH.⁹⁵ Shape anisotropy can enhance the heat production of NPs composed by the same chemical identities but with different geometries. Recently, Srikanth and coworkers found great differences in heat production of spheres and octopods of iron oxides.¹⁰⁷ Pellegrino and coworkers¹⁰⁸ also showed an increased heat production for nanocubes composed of iron oxides.

The heat production of IONs is usually evaluated as the macroscopic temperature increase. However, several studies have shown that the local temperature surrounding the ION's surface is higher than that observed on a global scale.^{109,110} Pellegrino and coworkers¹¹⁰ designed a system based on IONs stabilized with PEG polymer chains of different lengths bound to a fluorophore through a heat-sensitive azo group. The amount release of the fluorophore was found to be dependent on its distance from ION surface, suggesting that the vicinity of IONs experienced the highest temperature increase when located under AMF. Moreover, the authors found that the local heat production decreases exponentially with distance from ION surface. These findings shed light on the use of IONs for drug delivery triggered by MH, as the release of molecules can be tuned with designed NPs.

1.3.7 Drug Delivery

Nano-sized materials have emerged as promising vehicles for drug delivery applications.¹¹¹ Nanomaterials have the potential to reduce side effects, by increasing the selectivity to the target tissues, of drug candidates that exhibit good therapeutic efficacy but fail in systemic toxicity. Moreover, nanomaterials can increase the lifetime of drugs in the bloodstream due to the protection they give to the drug against hydrolysis. Requirements for drug delivery systems are known as LADME, standing for liberation, adsorption, distribution, metabolism, and excretion (Figure 12).

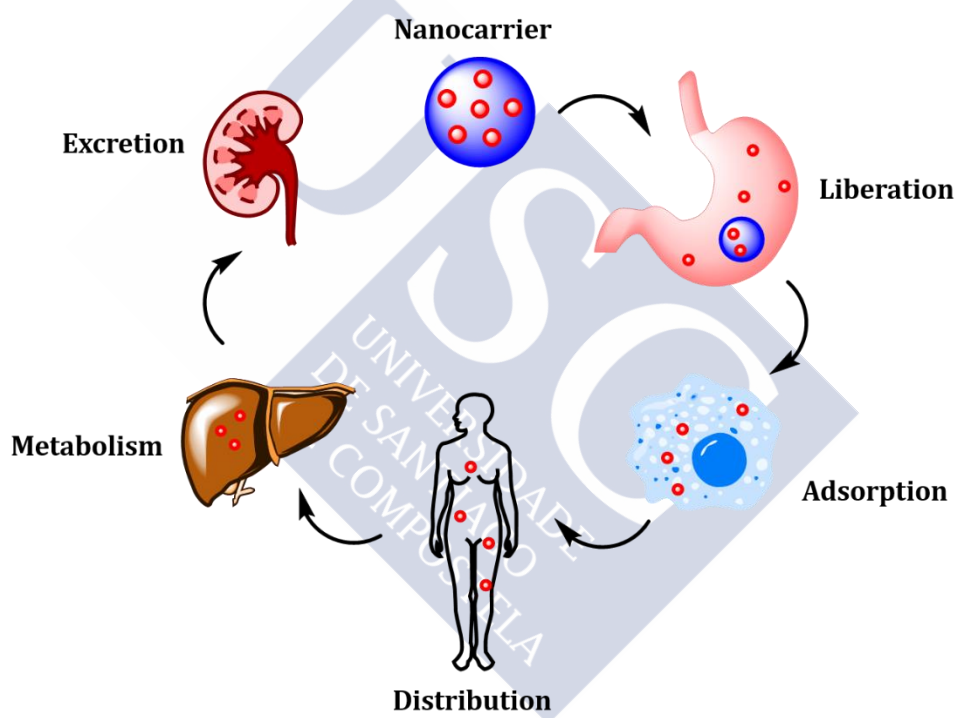


Figure 12: LADME processes that nanocarriers undergo after administration to a host organism.

1.3.8 Magnetic Nanohybrids

Magnetic systems that have emerged as carriers for drug delivery applications include single and cluster functionalized IONs, and secondary supramolecular structures such as magnetoliposomes, magnetic polymersomes, and magnetomicelles.^{2,112} Magnetic nanocomposites have different architectures with embedded NPs either in the core or at the surface of the system depending on the interaction, covalent or non-covalent, between the inorganic NPs and the organic materials.

The magnetic response of the NPs opens the possibility of detection by MRI, guidance to the desired location by application of magnetic fields, temperature increase by hyperthermia, and drug release on command triggered by heat production.^{2,41,66} Therefore, magnetic NPs can act as theranostic probes, providing assistance in both therapy and diagnosis simultaneously.⁴¹

The strategy of clustering individual NPs in supramolecular assemblies allows increasing the magnetic response while maintaining the superparamagnetic behavior. However, hydrodynamic sizes below 200 nm are optimal in order to avoid opsonization and subsequent elimination by the reticular endothelial system (RES).¹¹³

Synthesis methods of IONs were discussed in the previous Section. The hybridization of inorganic NPs with polymeric materials can be performed one-pot or in a further functionalization step after magnetic core formation. The main synthesis methods of organic–inorganic hybrid nanocomposites containing magnetic NPs consist of emulsion, solvothermal, and sol-gel techniques.¹¹

For drug delivery applications, the physicochemical properties of the resulting supramolecular hybrids dictate the pharmacokinetic profile, and special attention must be paid to magnetic loading, biodegradation of organic and inorganic counterparts, polydispersity index, particle size distribution, and surface charge.

1.3.9 Drug Loading

The incorporation of the selected drug into the nanohybrids can be accomplished by several approaches including covalent and non-covalent linkages between the drug and the nanocarrier (Table 3).

Table 3. Interaction-driven forces for the non-covalent incorporation of drugs into magnetic nanocarriers and stimuli-responsive bonds most used in covalent drug functionalization.

Non-covalent	Covalent
Hydrophobic interactions	Thermodegradable bonds
Coordination chemistry	pH degradable bonds
Physically trapped in pores	Enzymatically cleavable bonds

1.3.9.1. Non-Covalent Conjugation

The non-covalent approach for drug loading in nanocarriers relies on low-energy interactions, such as hydrogen bonding, dipole interaction, the hydrophobic effect, and coordination chemistry.² Nature is the best example of creating sophisticated structures based on supramolecular chemistry. The major advantage of this strategy is that there is no need to chemically modify the drug, which could lead to loss of the therapeutic effect. Consequently, the synthetic effort is considerably low in comparison with covalent modifications.

The conjugation between a drug, magnetic NPs, and organic polymers can be very complex, and engineering systems with time-controlled release, i.e. no premature drug release, can be very challenging. For example, Chourpa and coworkers¹¹⁴ showed recently IONs loaded with a complex of iron and doxorubicin (doxo). Fe²⁺ acted as a bridge between doxo and the NPs. However, the drug-release profile reached 60% after 2 h, and when administered *in vivo*, the therapeutic performance was equivalent to that of the free drug. The premature release of a drug loaded into nanocarriers implies obtaining the same therapeutic and toxic effects as when administering the free drug. This is one of the major challenges to be overcome for the success of nanosystems in drug delivery.

However, some examples in the literature have already shown promising results as magnetic drug delivery systems with the non-covalent approach. An example of a successful nanocarrier with doxo was reported by Yang and coworkers.¹¹⁵ The NPs displayed hydrodynamic diameters in the range of 140–180 nm and were prepared by the interaction of negatively charged IONs with positively charged doxo and silk fibroin. The authors stated that the particle formation is driven by electrostatic and/or hydrophobic interactions between the three components, and that there is an optimal doxo/NP ratio. The synthesized nanocarrier showed good internalization in *in vitro* experiments with drug-resistant cell lines and very high rates of tumor regression in *in vivo* experiments.

Non-commercial IONs coated with dextran were also tested after addition of positively charged doxo.¹¹⁶ The doxo release only reached 10% over the first hours at neutral pH,

while at the acidic pH of 6, the released increased to 45%. This is an example of pH-responsive drug release. The NPs were tested in rabbits and showed a better therapeutic performance than free doxo.

Recently, nanosystems that trigger the release by MH have been actively studied.¹¹⁷⁻¹¹⁹ AMF is much less absorbed by human tissues than other radiations such as light or microwaves. A greater penetration depth is therefore possible with AMF, offering a suitable therapy for *in vivo* applications.¹¹⁷

The heating by AMF of non-covalently bound systems is believed to enhance the diffusion rate of the encapsulated drugs, resulting in a notable increment in the release of the drug after AMF irradiation. These systems are still at an early stage, and model molecules such as fluorophores are sometimes employed for the sake of simplifying the quantification of the released amount.

For example, Parak and coworkers¹¹⁷ recently proposed a system of microcapsules with a mean size of 4.6 μm prepared by layer-by-layer methodology. Magnetic nanocubes were placed in the shell of the structure, while the core was loaded with dextran cascade blue, a fluorophore, as a model molecule. The technology used was based on the assembly of polyelectrolytes with opposite charges, and the authors showed that after irradiation with AMF the outer shell was partially disrupted due to the effect of the magnetic NPs, but the release of the cargo from the microcapsule was only partial.

Another example of MH-induced drug delivery was recently reported by Ménager and coworkers.¹¹⁹ In this study, magnetic NPs were used as individual cores with molecularly imprinted polymers, onto which doxo was loaded by hydrogen bonds in the binding sites. After AMF treatment, the NPs showed a doxo released of 60% while control NPs (no AMF irradiation) released at 15%. Moreover, *in vitro* studies with cancer cells showed a reduction in the viability after AMF that caused the release of doxo.

An example with *in vivo* data was reported by Tseng and coworkers, who prepared nanohybrids with sizes varying from 70 to 160 nm.¹²⁰ The supramolecular structures were composed of Zn-doped magnetite coated with adamantane-modified

polyamidoamine and cyclodextrin-modified polyethylenimine that self-assemble entrapping doxo by π - π interactions and hydrogen bonding. The system released doxo on command after hyperthermia treatment due to destabilization of the structure upon heating and exhibited tumor remission with a very low doxo dosage of 2.8 $\mu\text{g}/\text{kg}$.¹²¹

A very sophisticated nanohybrid was recently proposed by Ding and coworkers.¹¹⁸ In this example, the hybrid was composed of small NPs of magnetite and Gd_2O_3 located at the core and embedded with zeolitic imidazolate framework-90, and loaded with anticancer drug 5-fluorouracil. The system showed a 50% of drug release after 7 h while after AMF irradiation at very low frequencies (20 Hz) displayed 50% release after 1.5 h. Moreover, these nanohybrids displayed r_1 of 4.7 and r_2 of 133.7 at 7 T, which offers the possibility of real-time monitoring of the nanohybrids by MRI. This nanohybrid provides therapeutic molecules, an imaging probe, and a stimuli-driven response all in one system.

1.3.9.2. Covalent Conjugation

Another approach for the attachment of drugs to nanosystems is the covalent modification. This strategy may hinder the liberation of the drug, resulting in null therapeutic effect. In order to avoid this, a prerequisite is to employ either biodegradable or cleavable bonds on demand between the magnetic NPs and the drug. If the bond linkage works ideally, it would enable the stabilization of the drug conjugate in the bloodstream and offer the possibility to induce the delivery once the nanoconjugate reaches the desired target. Systemic toxicity of such systems may be remarkably low in comparison with free drugs.

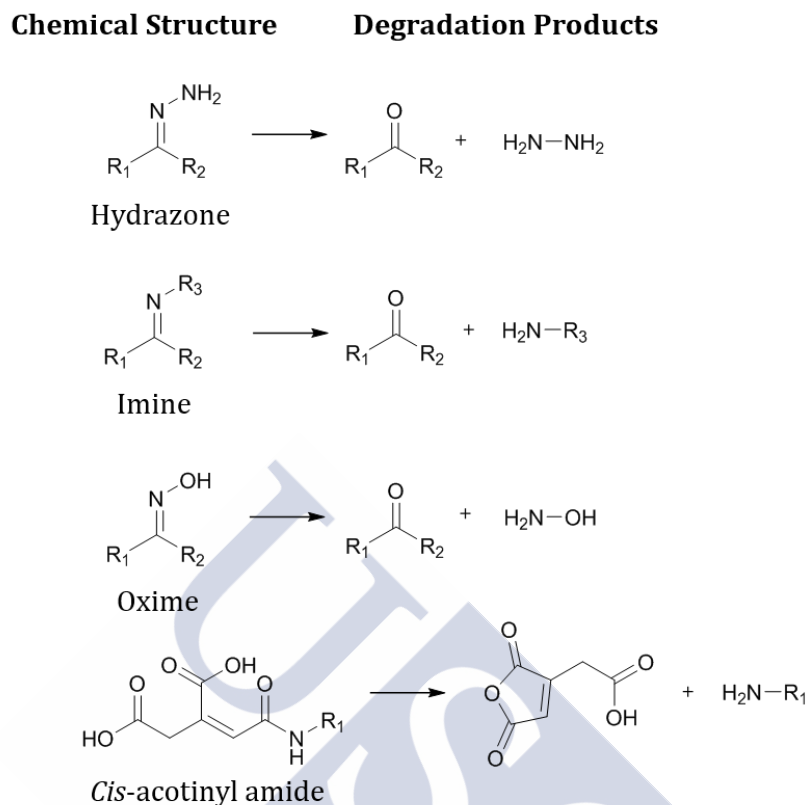
The examples of the literature based on a covalent modification of nanosystems in drug delivery are relatively reduced when compared to non-covalent strategies,² probably due to the more complex synthetic procedures required for this approach.

One of the most studied stimuli sensitive for smart drug nanocarriers is acidic pH.¹²² The reason is related to the biological significance of pH values of 6.5–7, which are present in tumors and inflamed regions.¹²³ Additionally, late endosome and lysosome

organelles in mammalian cells also feature highly acidic pH values of 4.5–5.¹²⁴ Therefore, pH-cleavable bonds can serve to deliver the cargo in the aforementioned biological environments.

The number of functional groups that undergo cleavages under acidic conditions in drug delivery is large, e.g. hydrazones, imines, oximes, acetals, and labile amides (known as a *cis*-aconityl group) (Scheme 4).¹²² There are many drug delivery systems based on pH-sensitive magnetic NPs with different organic polymers, drug loading efficacy, kinetics of drug delivery, etc. For example, Yan and coworkers¹²⁵ reported a system with magnetite core, doxo loaded through hydrazone linkages and with PEG as the organic coating. The system showed 40 wt % of drug release after 20 h at pH 5, localization in the tumor area in *in vivo* experiments, and MRI enhanced contrast in T_2 -weighted images. Another example with magnetite nanocubes was recently reported by Cai and coworkers.¹²⁶ The nanomaterial was coated with poly(methyl methacrylate) (PMMA) and doxo was attached through hydrazone bonds. The kinetics of the drug release were faster in comparison with the previous example, and after 4 h at pH 5 60 wt% of the drug was released. The nanohybrid showed tumor regression and reduced toxicological effects *in vivo* when compared with free doxo.

In addition to acidic pH, there are other biomolecules, such as enzymes, that are overexpressed in pathological conditions, for example, metalloproteinases are related to metastasis and angiogenesis.¹²⁷ Several nanosystems have incorporated enzyme-sensitive bonds, especially to enzymatic hydrolysis, to target malignant tissues and promote localized toxicity. For example, Yang and coworkers¹²⁸ presented IONs loaded with gemcitabine, an anticancer drug, through a tetrapeptide linker sensitive to lysosomal enzymes, and with urokinase receptors for targeting. In this study, the authors showed a 30% decrease in tumor growth when compared with the free drug, and more importantly, the NPs actively targeted human pancreatic cancer, as evaluated by MRI images.



Scheme 4: Reactions of degradation at acidic pH of common functional groups used in covalent conjugation of nanomaterials in drug delivery.

The literature on thermodegradable stimuli-responsive IONs is much more limited as compared with the previously mentioned classes of cleavable bonds. However, some examples with proof-of-concept experiments are available. To date, three different NP conjugates have shown promise for release induced by MH employing the Diels–Alder reaction,⁶⁰ intramolecular lactamization,¹²⁹ and nitrogen release.¹³⁰ Fontaine and coworkers⁶⁰ reported IONs stabilized with phosphonic ligands bearing alkyne and furan moieties. The nanoconjugate offered the possibilities of functionalization through thermoreversible Diels–Alder reaction and 1,3-dipolar cycloaddition. PEG was chosen as a hydrophilic polymer to enhance colloidal dispersability in water and maleimide-bearing Rhodamine B was employed as a model system for a drug. The authors showed that Rhodamine B was released from the NPs after the application of AMF. Recently, Nantz and Knipp¹²⁹ filed a patent about IONs functionalized with a linker bearing a silicon anchor group and an ester-bound drug that respond to heat by lactamization (Figure 13). This system shows a broad scope because the drug can

virtually be of any nature with the only requirement of the presence of either a hydroxyl or an amine group for attachment to the linker.

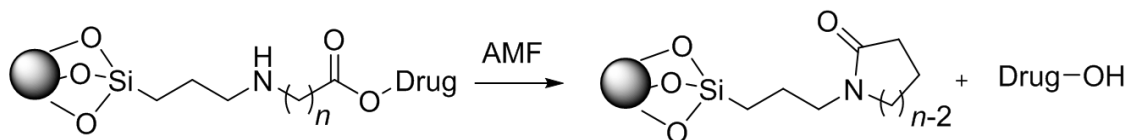


Figure 13: IONs functionalized with a ester-bound drug that undergo lactamization under an AMF.

Another interesting study was reported by Kasko and coworkers.¹³⁰ In this study, the drug is physically sequestered inside the nanochannels of the silica matrix, and coated with an azo-containing polymer. The proposed mechanism of release relies on the breaking of the azo bond, which broke the polymer exposing the pores of the nanomaterials and liberating the drug. The temperature of the solution did not increase significantly, and therefore this work is a great example of the generation of high temperatures responsible for the breaking of the azo-polymer in the vicinity of IONs due to MH.

A similar strategy was recently reported by Zink and coworkers,¹³¹ but in this example, the porous silica shell was loaded with fluorescein as a model. The model drug was trapped inside the porous of the silica shell and closed by a supramolecular complex of cyclodextrin-adamantane (Figure 14). The furan modified with adamantane was released upon treatment with AMF that induced the retro-Diels–Alder, exposing the porous of the silica shell and provoking the release of the cargo.

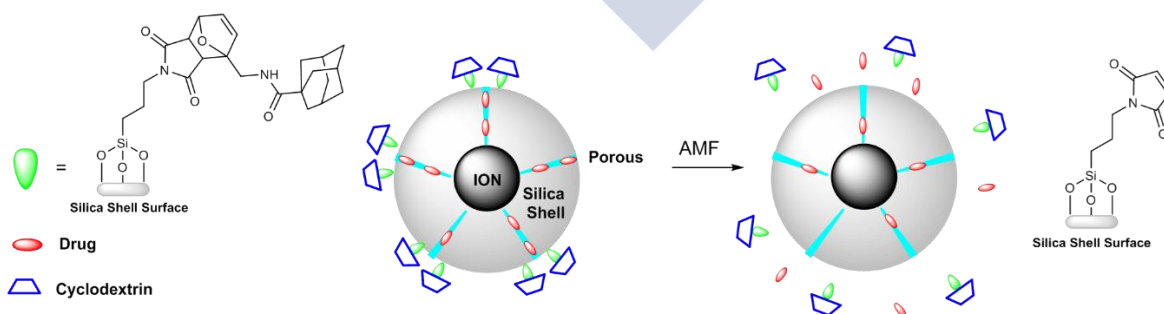


Figure 14: Representation of the nanosystem used in Zink and coworkers work.¹³¹ The structure is composed by a magnetic core with mesoporous silica shell where drug molecules are loaded. The surface of the silica shell is modified with a cycloadduct containing adamantane that interacts with cyclodextrin molecules obstructing the release of the drug. When AMF is applied, the cycloadduct is broken and the pores are opened to release the drug.

All the aforementioned examples, both with covalent and non-covalent approaches, have shown great potential for cancer therapy. However, more studies are needed on the biodistribution of nanohybrids with information of NP mass location, the understanding of transport of nanosystems through biological barriers, and their interaction with biomolecules.²⁰ Additionally, the treatment of cancer is very challenging and requires exhaustive control over the therapy. Friberg and Nyström¹³² recently stated in their review about nanomedicine in cancer treatment:

'The key is to position the right drug at the right time at the right place and at the right concentration.'

1.3.10 IONs in the Clinic

Several formulations based on IONs have been used in clinics.¹³³ The use of IONs in the medical field can be divided into two sections: diagnosis and therapy. In diagnosis, MRI is the biomedical application with the highest number of formulations approved by FDA as CAs and commercialized.¹³³ However, low market interest due to the competition with bright CAs caused their discontinuation despite of the excellent biocompatibility and low toxicity profile.²

Ferumoxtran-10, Combidex or Sinerem is a formulation based on ultrasmall iron oxide nanoparticles with a hydrodynamic diameter of 30 nm and coated with dextran and studied as CAs in lymphography. The studies about this CA started at the beginning of the 1990s¹³⁴ and many others came after supporting the safety profile, and it was included in clinical trials with 1777 patients.¹³⁵

A similar formulation based on superparamagnetic IONs coated with dextran, named as Sienna+,¹¹¹ was successfully approved by the FDA for the detection of lymph nodes, although the administration is performed locally and the detection is carried out by magnetic susceptometry with a Sentimag probe. The agent is nowadays on the market, and it competes with ⁹⁹Tc-based agents that expose the patients to invasive radiation.

Several superparamagnetic ION-based products have been in clinical trials as CAs for MRI,¹¹¹ and two formulations Feridex and Resovist achieved the approval of the FDA. Nevertheless, the radiologists' preference for positive CAs based on gadolinium

chelates caused the withdrawal of these products from the market despite their lower toxicity as compared to gadolinium products. Currently, there is no commercially available CA for MRI based on IONs for intravenous injection.

Conversely, Ferumoxytol or Feraheme,¹³³ an ultrasmall ION coated with polyglucose sorbitol carboxymethyl ether was first studied in phase IV clinical trials as a CA for intravenous administration, but it was found that ultrasmall IONs were incorporated into transferrin or into intracellular stores after RES recognition. However, Ferumoxytol was granted the FDA approval and it is commercially available as a therapy tool for anemia.

Regarding therapy, another formulation for treatment based on the use of superparamagnetic IONs is commercialized in Europe by MagForce AG.² The therapy uses IONs as antennas in MH and it is used in patients with glioblastoma multiform. The solution of IONs is directly injected into the brain tumor and thermoablation is performed as treatment, generally in combination with radiotherapy.

Several ION-based formulations are in clinical trials as positive CAs for MRI and as magnetic drug delivery systems. Despite the withdrawal of superparamagnetic IONs as negative CAs, they show excellent safety profiles and low toxicity that is very promising for their involvement in new nanomaterials for biomedical applications.

1.4 BIOINTERFACE

Biointerface comprises the physicochemical interactions between the surface of produced materials and biological components, such as phospholipid membranes, endocytic vesicles, DNA, proteins, and organelles.¹³⁶ The understanding of these interactions is key for the success of the nanomedicine field since the integrity, biodistribution, and the fate of NPs are affected once they are administered into a living organism.¹³⁷ The physicochemical character of a NP changes upon interactions with biomolecules,¹³⁸ such as proteins,¹³⁹ lipids, and glycosides, due to the formation of a biological corona. In order to approach the goal of personalized nanomedicine, it

is fundamental to consider not only the given inorganic core and organic/inorganic coating, but also the composition and stability of the formed biological corona.

The NPs after production are referred to as 'synthetic entities', while after interaction with biological fluids, and thus formation of a protein corona (PC), NPs are considered as 'biological entities' (Figure 15).¹⁴⁰ Therefore, it is important to consider the composition of the biological corona in the early design of NPs to obtain the expected properties and performance of the NPs.

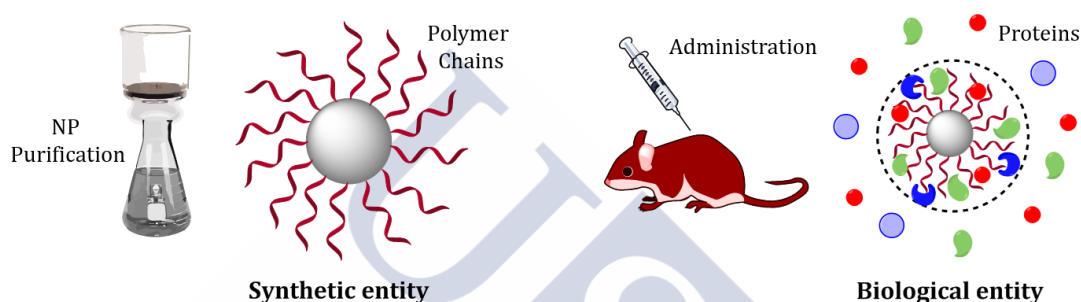


Figure 15: Synthetic entity of NPs after synthesis and purification (left), and biological entity after the administration of NPs to a living organism (right).

It is still not possible to predict the PC of NPs. The complexity of the NPs together with the intrinsic complexity of biological fluids hamper the use of traditional characterization techniques for *in situ* detection. The development of new methods are crucial, and will be discussed in the following.^{20,137} The most studied type of biomolecules in interaction with NPs are proteins, and other non-protein coronas such as those formed by lipids of natural organic matter are far less understood.^{141,142}

1.4.1 Protein Corona

The magnetic performance of IONs is mainly governed by the inorganic core, with physicochemical parameters such as core size, doping ions, and crystallinity playing the most important roles. However, once the NPs are within a living organism, such properties may be jeopardized due to dissolution, aggregation, or degradation of the NPs. Their performance in the required application, e.g. as contrast agents in MRI or as antennas for MH, may be compromised depending on the NP environment.¹⁴³ The outer layer composed either of organic or inorganic materials is responsible for the

colloidal stability of the NPs and it also offers possibilities for anchoring diverse molecules such as imaging probes, polymers, and receptors. The synthetic coating is in direct contact with the medium and therefore constitutes the first point of contact for the biomolecules to interact.

The so-called PC is formed when proteins interact with NPs.¹⁴¹ The definition of PC often refers to two different coronas, depending on the strength of the protein binding to the NP surface. The protein layer bound the closest to the NP, known as hard corona, is the most stable and it is in a long-lived equilibrium state. The hard corona represents a fingerprint of the NP fate.¹⁴⁴ The outermost protein shell, known as soft corona or protein cloud, is constituted by proteins loosely bound to the hard corona, which are in a rapid equilibrium exchange with the molecules in the medium.¹⁴⁴

Cedervall and colleagues¹³⁹ introduced the PC to the NP community in 2007, suggesting size exclusion chromatography, surface plasmon resonance, and isothermal titration calorimetry as the characterization techniques to study the binding affinities between NPs and proteins. However, due to the weak interaction between the hard and the soft corona, the characterization and the relevance of the latter remains not fully confirmed, and sometimes both terms are merged in the general concept of PC.¹⁴¹

Stauber¹⁴¹ and coworkers published a review in 2015, where they affirmed:

'...nanoparticle corona represents a still unresolved hot topic, with high scientific and economic relevance'.

The phenomenon of the PC is still not predictable and the majority of the studies were made in simplistic scenarios such as culture medium or blood plasma,¹⁴⁵⁻¹⁴⁷ with studies in biological fluids from lung or brain now emerging.^{147,148}

The PC formation is related with the physicochemical properties of the synthetic NP but is also influenced by external factors such as temperature,¹⁴⁹ time of exposure between the NPs and the biomolecules,¹⁵⁰ and the concentration of NPs in the physiological media.¹⁴⁰ Additionally, intrinsic chemical characteristics of the NPs also play a fundamental role governing protein adhesion: the hydrophobicity of the coating

has an impact on the PC, with the general assumption that the more hydrophobic the surface, the less protein interaction occurs.^{139,151,152} The surface functionalization¹³⁹ and charge,¹⁵⁰ and the size of the NPs¹⁵³ also have an impact on the final composition of the PC.

Although several studies point out the role of the aforementioned factors governing the PC, there is still not enough knowledge to predict the particular protein corona composition for a given NP.^{141,144,150,154,155} The PC has a high impact on the NPs' blood circulation time, cell uptake,¹⁴⁴ and also on the cell-targeting efficacy,^{156,157} thus its prediction would assist in the design of new nanomaterials. There are some examples in the literature of guiding the PC formation in order to target diverse diseases and/or organs.¹⁵⁸ For example, Hoshino et al.¹⁵⁹ showed that imprinted polymeric nanoparticles were able to capture specific peptides present in the blood stream, and therefore acted *in vivo* as synthetic nanoparticles with antibody-like affinity and selectivity. Wentworth and coworkers¹⁶⁰ modified quantum dots with small molecules, oxysterols, that induced a controlled protein misfolding, resulting in nanomaterials with *in vitro* targeting properties.

1.4.2 Uptake by Cells

After the formation of the biological entity, the biomedical application of the NPs may require internalization within the population of cells of interest in order to accomplish the desired effect. For example, in drug delivery or in cell tracking applications the NPs must be internalized to release the therapeutic molecules and to label the cells, respectively. Together the physicochemical characteristics of the NPs (size, shape, surface charge and hydrophobicity, and surface functionalization)^{161,162} and specific cell properties (cell type, cycle phase, lipid membrane, etc.) govern the NP–cell interactions (Figure 16).¹⁶³

Engineered NPs have to overcome several barriers in order to be internalized by cells. The cell membrane is the first physical barrier that separates the NPs from the cell, and it hinders the diffusion of complexes larger than 1 kDa.¹⁶⁴ There are two different modes for crossing the cell membrane: direct translocation and endocytosis.¹⁶⁵ The

first involves the direct transfer of extracellular molecules into the cytosol without the formation of vesicles. On the other hand, the endocytosis process is employed by large polar molecules that cannot simply pass through the hydrophobic cell membrane. These processes are subdivided into specific categories: phagocytosis, macropinocytosis, caveolar-mediated endocytosis, clathrin-mediated endocytosis, etc., regarding the different biomolecules involved in the signaling and engulfing of the cell membrane. It is important to consider for engineered NPs that endocytosed materials are trafficked into the cytosol by endosomes and lysosomes, which subject NPs to an acidic pH (4.8–6.2) and the presence of hydrolytic enzymes.¹⁶⁶

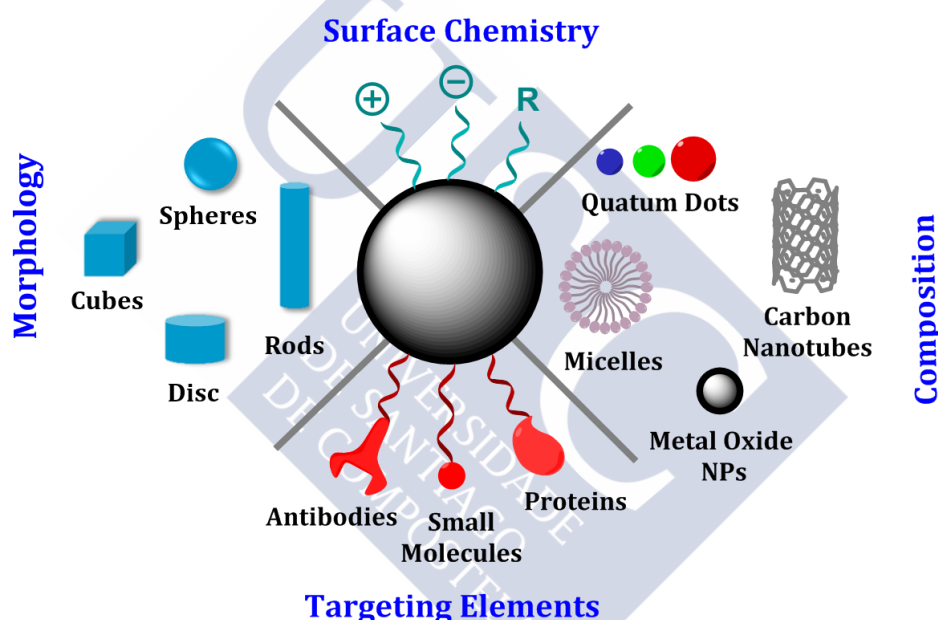


Figure 16: Physicochemical characteristics of NPs that affect the internalization processes in cells.

The size and shape of the NPs dictate the rate and mode of the endocytosis process. Champion and Mitragotri¹⁶⁷ studied the influence of the size and shape of polystyrene NPs on the phagocytosis process. For example, in the case of elliptical disc NPs, if the contact between the cells and the NPs was formed by the short axis, the phagocytosis process was completed in minutes, whereas if the interaction was accomplished by the long axis, the phagocytosis did not occur. These findings shed light on the effect of the geometric anisotropy in nanomaterials in phagocytic processes. Chithrani et al.¹⁶⁸ studied spherical and rod-shaped gold nanoparticles of sizes varying from 14 to 100 nm. They found that with spherical NPs the maximum uptake was achieved with 50 nm

NPs, and that the rod-shaped NPs were less efficiently internalized by Hela cells than their counterparts with spherical morphology. A maximum internalization rate was also found at 50 nm for other compositions of NPs such as silica¹⁶⁹ and single-walled carbon nanotubes.¹⁷⁰

Apart from size, the surface charge also plays a role in internalization. In general, cationic NPs are internalized with higher rates in comparison to negatively charged or neutral NPs.¹⁶⁵ This is due to favorable electrostatic interactions between the positive charges on the NPs and the negatively charged species on the cell membrane.¹⁷¹ However, depending on the cells and the endocytic mechanism negatively charged NPs can also be successfully internalized.¹⁷²

NPs can be functionalized with ligands including antibodies, aptamers, peptides, and small molecules in order to target a desired cell population.¹⁶⁴ This strategy consists of targeting a membrane-bound protein or a carbohydrate, and it is mainly used for oncology treatment. The accumulation of nanomaterials to a certain location because of ligand–receptor interactions is known as active targeting.⁴ Apart from the increase in selective toxicity, the study of NPs with functionalized ligands in oncology gives information about the expression and activity of specific molecules in tumors, and therefore brings knowledge of biological processes to help in the prognosis of the disease.¹⁷³ The tumor cells overexpress biomarkers on their surface known as receptors that have high affinity for some ligands, such as antibodies, aptamers, and small peptides.¹⁷⁴ The expression levels of these receptors vary depending on the tumor type but they are also present in healthy tissues. Therefore, the success of this strategy relies on the appropriate selection of the ligand.

Taking advantage of the high affinity and selectivity of antibodies, IONs were encapsulated in micelles functionalized with epidermal growth factor receptor (EGFR), which accumulated in glioblastoma as detected by MRI.¹⁷⁵ However, antibody functionalization tends to increase the overall particle size, sometimes preventing effective accumulation in the tumor tissue, and its use may be not cost effective.¹⁷⁶ On the contrary, small ligands display the advantages of higher stability, low cost, and nonimmunogenicity.¹⁷⁶ The most commonly used are folic acid¹⁷⁷ and

arginine–glycine–aspartate (RGD) peptide.¹⁷⁸ The conjugation of IONs and folic acid was employed to target diverse cancer cell lines, such as human cervical carcinoma (Hela),¹⁷⁹ mouse melanoma (B16F0),¹⁸⁰ and human epidermoid carcinoma (KB cells).¹⁸¹ Aptamers¹⁸² are single strands of either DNA or RNA with analog binding properties to antibodies but with simple structures, and they were used in combination with IONs to target prostate and colon cancer.^{183,184}

The spacing and density of a given ligand on the surface of NPs affect the internalization process,¹⁶⁶ and they directly depend on the NP size.^{165,185} Small NPs possess low surface area and high curvature that restricts the amount of possible attached ligands. Additionally, the binding affinities of these ligands to the receptors are different depending on their density on NP surface. For low density of ligands on the NPs, the binding affinity is close to the values of the free ligands, and therefore the binding capacity can be too low, leading to inefficient uptake.¹⁶⁸ On the other hand, large NPs have a higher surface area available to allocate more ligands, and the binding affinities become high due to multivalence, which may limit the membrane wrapping, also leading to low uptake.¹⁸⁵ Chan and coworkers¹⁸⁵ employed gold NPs to study the size dependency on receptor-mediated endocytosis, and the authors claim 40–50 nm NPs as the ideal size range to achieved active targeting.

The field of targeting NPs has grown considerably due to the promise of personalized medicine.¹⁸⁶ Studies suggest that ligand-functionalized NPs do not accumulate more in malignant tissues, such as tumors, than non-functionalized NPs, but they are more effectively internalized by tumor cells.¹⁸⁷ Despite the great potential of targeting, only a few nanomaterials have progressed into clinical trials. This slow progress is the consequence of high production costs and small therapeutic gains in comparison with bare nanomaterials.¹⁸⁸ Events such as the formation of the PC in NPs need to be better controlled in order to avoid hiding the ligand from the cell's receptor. More studies are needed to point out the relations between the PC formation and the characteristics of NPs in order to predict the events at the biointerface of produced NPs with biological systems.



CHAPTER 2

2 Ultrasmall Magnetic Nanoparticles: MRI performance and *in vitro* stability



2.1 INTRODUCTION

Ultrasmall superparamagnetic iron oxide nanoparticles (USPIOs), with a mean hydrodynamic diameter below 50 nm, possess characteristics such as biocompatibility, long plasma half-life, and interesting magnetic properties, which make them suitable for a wide range of biomedical applications in both therapy and diagnosis.¹⁸⁹ MRI is one of the most used techniques in the medical field for the diagnosis of diverse diseases due to its high spatial resolution, rapid acquisition times, and the absence of exposure to ionizing radiation. However, CAs are frequently employed to distinguish between adjacent tissues, for example to enhance the visualization of tumor morphology or coronary angiography.

CAs affect the relaxation time of water protons' nuclei by two different processes: the longitudinal relaxation or T_1 , where the contrast obtained is bright or positive, and transversal relaxation or T_2 , with dark or negative contrast. Commonly, CAs are helpful for the reduction of either T_1 or T_2 . Dual T_1 – T_2 CAs would help to distinguish interferences, such as hemorrhagic regions, bone calcification, metal deposits, and susceptibility artifacts,¹⁹⁰ leading to a more accurate and early diagnosis.¹⁹¹ Additionally, dual behavior of a single CA platform within the same technique simplifies the acquisition due to identical penetration depths and time scale in both imaging modes. Consequently, dual T_1 – T_2 systems have attracted attention in the recent years, and complex nanostructures from coupled materials have emerged in order to fulfill both T_2 and T_1 requirements, for example iron oxide NPs attached to gadolinium compounds.^{68,69,192,193} Despite the success of these structures in possessing attractive MRI properties, questions remain that need to be addressed before the clinical application of dual CAs can become a reality.¹⁹⁴ Some of such concerns are the requirement of facile synthesis procedures to obtain crystalline material on a sufficiently large scale with the desired magnetic properties. Additionally, interactions between the NPs and biomolecules should be addressed to assess the suitability of the nanomaterial for biomedical applications.^{195,196} The chemical stability and the behavior of NPs in a biological environment are key factors in biodistribution, toxicity, and their eventual efficiency as imaging probes.¹⁹⁷

In this chapter, a straightforward gram-scale synthesis of water-dispersed USPIOs is presented. Moreover, the protein adsorption on the nanoparticle surface and the aggregation of nanoparticles was evaluated with two samples of different sizes in biological media. The MRI properties of these samples will be also discussed.

2.2 SYNTHESIS OF IONS

In order to gain access to NPs in sufficient quantity with a procedure that refrains from the use of both organic solvents and phase-transfer procedures, USPIOs were prepared using a one-step hydrothermal method.¹⁹⁸ The magnetite structure was chosen to dope with divalent transition metal ions Zn^{2+} and Mn^{2+} to maximize the saturation magnetization.¹⁴ Additionally, Mn^{2+} is known to shorten the T_1 , mainly through magnetic dipole–dipole interactions due to its five unpaired electrons, and thus its incorporation has been shown to lead to dual CAs in some cases.^{199–201}

A mixture of $FeCl_3 \cdot 6H_2O$, $ZnCl_2$, and $MnCl_2 \cdot 4H_2O$ was kept at 200 °C during 24 h with ammonia as the precipitation agent and water as solvent. PAA was the coating of choice due to its hydrophilic nature and the great affinity of carboxylic acid groups for Fe, giving access to water-dispersed NPs in one pot without the need of phase-transfer procedures.

The USPIOs were purified twice by magnetic separation using water as solvent to yield sample **NP-bc** (before centrifugation). In order to decrease NP size and increase monodispersity, sample **NP-bc** was subjected to an additional centrifugation step at 4000 rpm for 12 h, and the collected supernatant gave sample **NP-ac** (after centrifugation). Notably, although the additional separation step reduces the nanoparticle yield, **NP-ac** was obtained on a gram scale (Figure 17).

In order to shed light on the influence of the separation step on the properties of the nanoparticles, the samples before (**NP-bc**) and after (**NP-ac**) the centrifugation were studied in parallel. To gain insight into the composition of the NPs, stoichiometry of both samples was estimated by inductively coupled plasma optical emission spectroscopy (ICP-OES) as $Zn_{0.07}Mn_{0.77}Fe_{2.16}O_4$ for **NP-bc** and $Zn_{0.07}Mn_{0.86}Fe_{2.07}O_4$ for

NP-ac (Table 4). The composition of both samples is very similar, although interestingly the Zn^{2+} content in both samples is very low, suggesting that these experimental conditions, possibly the precipitation agent,²⁰² do not favor the incorporation of Zn^{2+} into the structure.

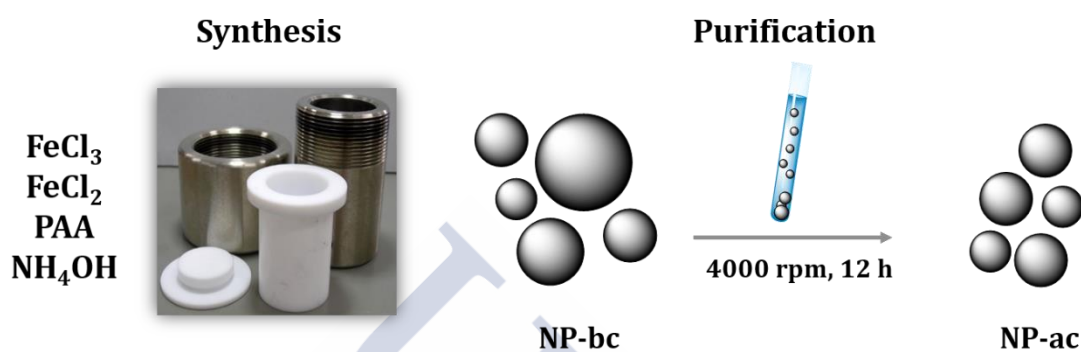


Figure 17: Representation of the ION synthesis by the hydrothermal method, and the separation by centrifugation of the two samples

Table 4: ICP-OES results for NP-bc and NP-ac samples obtained from the calibration curves of Zn, Mn, and Fe. Relative standard deviation express as % in brackets for each element.

Sample	Zn (ppm)	Mn (ppm)	Fe (ppm)	Stoichiometry
NP-bc	0.432 (2%)	0.393 (0.56%)	11.2 (0.67%)	$Zn_{0.07}Mn_{0.77}Fe_{2.16}O_4$
NP-ac	0.256 (0.99%)	0.267 (0.33%)	6.58 (0.215%)	$Zn_{0.07}Mn_{0.86}Fe_{2.07}O_4$

The composition was also studied by powder X-ray diffraction (XRD) (Figure 18). The XRD analysis of **NP-bc** and **NP-ac** displayed one single phase with an inverse spinel crystallographic structure (COD 96-900-2318), identical to pure magnetite, confirming the presence of a doped structure rather than the separate formation of Zn and Mn oxides. In agreement with XRD, energy-dispersive X-ray spectroscopy (EDX) showed the elements homogeneously distributed throughout the NPs (Figure 19).

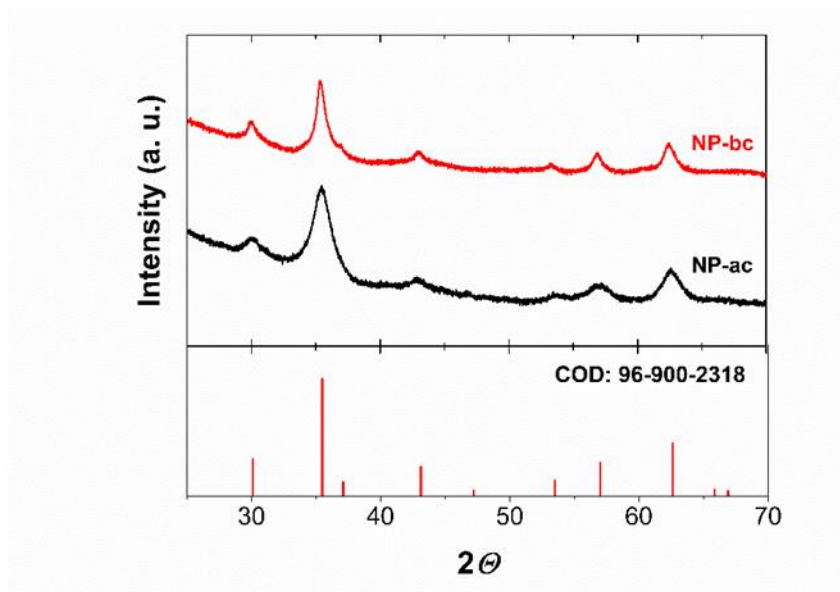


Figure 18: XRD pattern of NP-bc (top, red) and NP-ac (top, black). Position and relative intensity (bottom) of the XRD reflections of a Fe_3O_4 single phase with inverse spinel structure from the crystallographic open database (COD), pattern code 96-900-2318. No additional peaks were found as secondary phases or impurities.

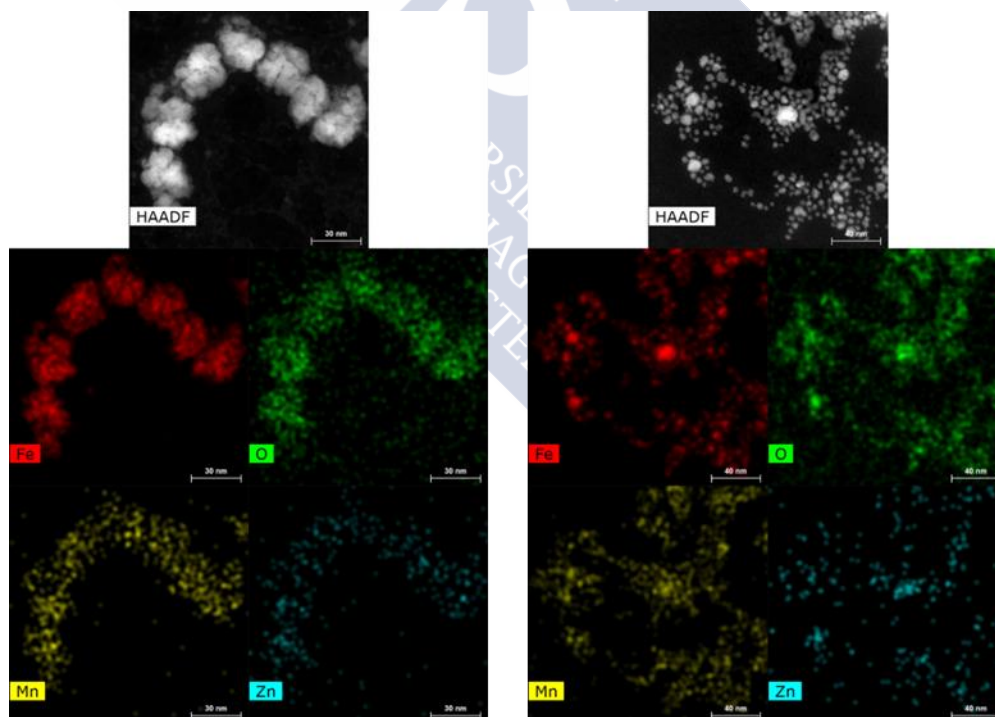


Figure 19: HAADF–STEM images and EDX elemental analysis maps (Fe, O, Mn, and Zn) of NP-bc (left) and NP-ac (right).

The magnetic core was further characterized by transmission electron microscopy (TEM). The acquired images showed **NP-bc** with higher polydispersity, while **NP-ac** appeared with a narrower size distribution (Figure 20). This was also confirmed by

scanning transmission electron microscopy (STEM) images, where **NP-bc** is seen as large aggregates, while **NP-ac** appears as individual, more monodisperse NPs (Figure 21). The mean diameter of the particles measured from the TEM images, however, is very similar in both cases (Figure 22). This can be attributed to the fact that only the clearly defined particles were taken into consideration for the counting. Notably, the TEM images of **NP-ac** taken after a storage time of 10 months in water at 4 °C confirm that the sample remains comparable to the freshly prepared one.

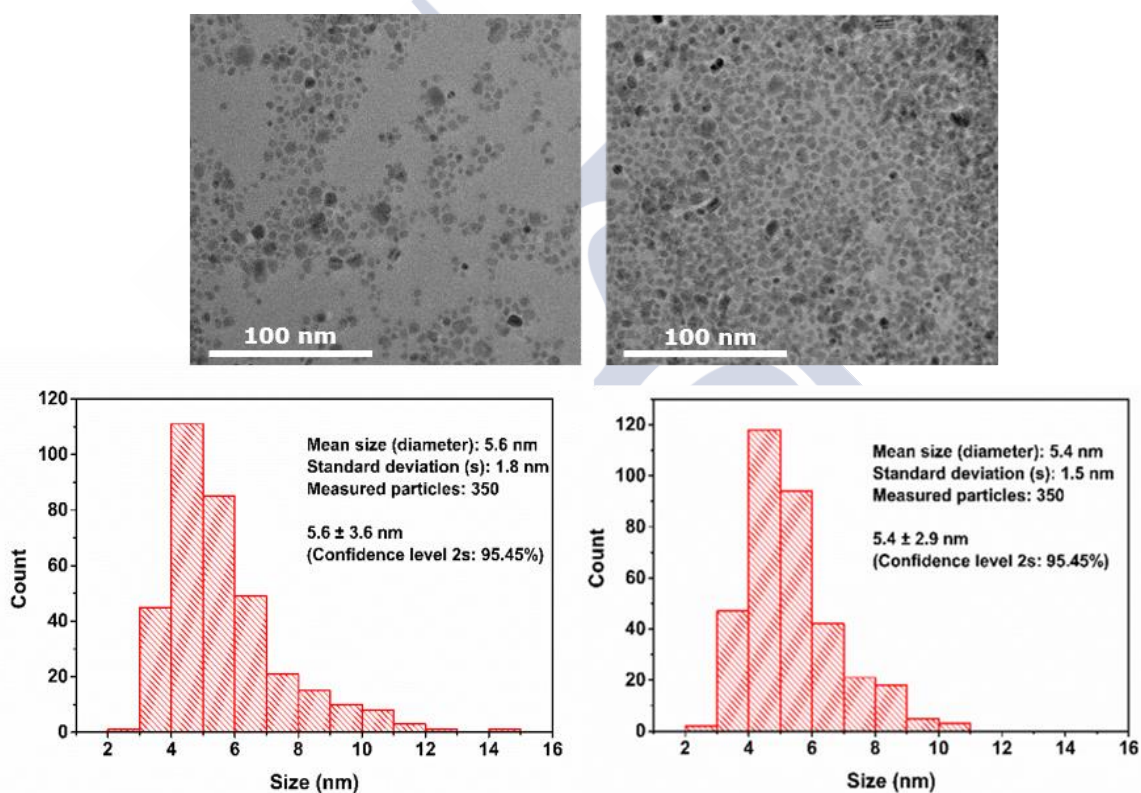


Figure 20: TEM images acquired of NP-bc (left) and NP-ac (right) from freshly prepared samples, reflecting the greater polydispersity in NP-bc and the existence of populations with larger diameters than 11 nm.

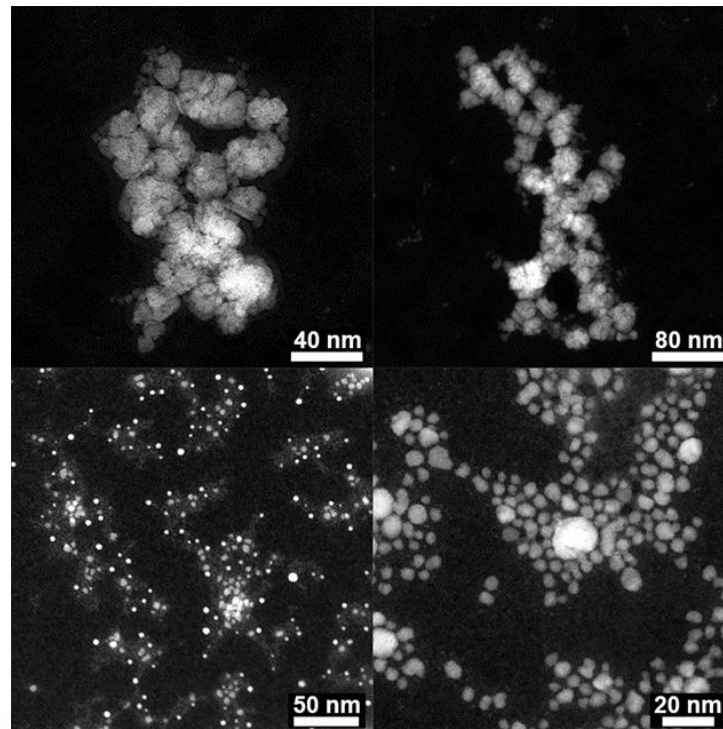


Figure 21: HAADF-STEM images of NP-bc (top) and NP-ac (bottom).

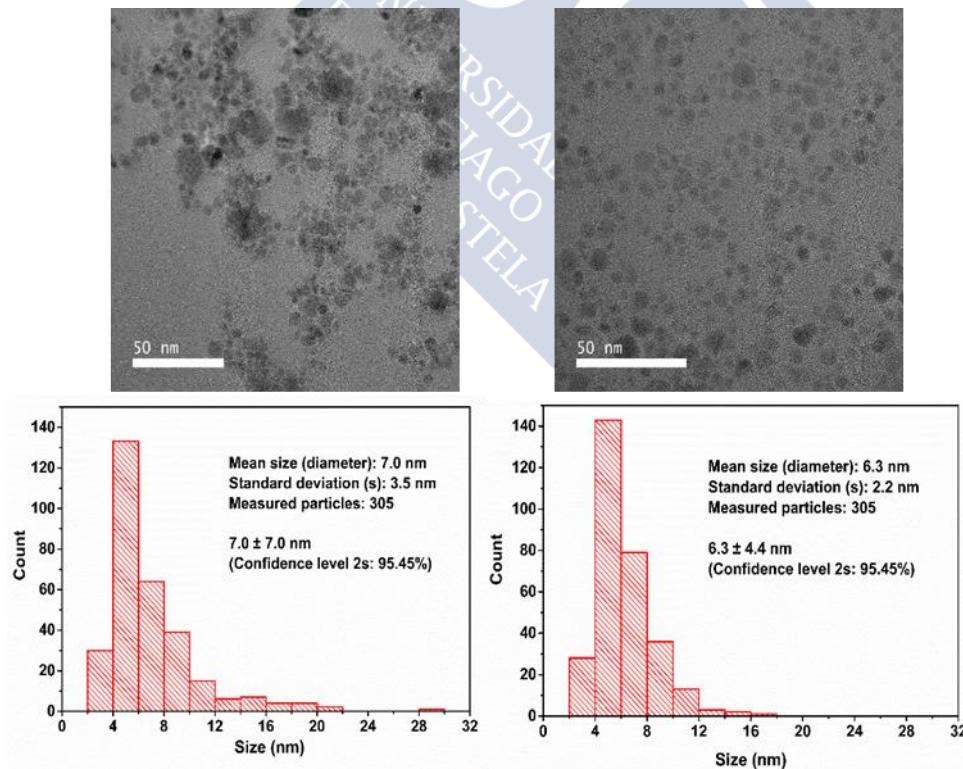


Figure 22: TEM images acquired from NP-bc (left) and NP-ac (right) with samples stored over 10 months in water at 4 °C, reflecting the greater polydispersity of NP-bc as compared to NP-ac, with the latter remaining unchanged and monodisperse.

The hydrodynamic diameter (D_h), which takes into account the diameter of the hydrated particle, gave sizes of 35 and 18 nm for **NP-bc** and **NP-ac**, respectively (Table 5). The polydispersity indices of the samples were 0.35 and 0.20 for **NP-bc** and **NP-ac**, respectively, showing that the centrifugation step leads to NPs with lower hydrodynamic radius and higher monodispersity. The average crystallite size (D_{hkl}), which is related with the core diameter in the superparamagnetic range, was derived from the XRD pattern. For sample **NP-bc**, D_{hkl} was found to be approximately twice as large as that of **NP-ac**, 10 and 5.8 nm, respectively (Table 5).

Table 5: Results of the characterization of USPIOs by DLS, XRD, VSM, and TGA.

Sample	D_h (nm)	D_{hkl} (nm)	M_s (emu/g)	H_c (Oe)	Organic coating (%)
NP-bc	35 ± 17 PI = 0.346	10 ± 3	42.3	4.8	20
NP-ac	18 ± 6 PI = 0.204	5.8 ± 1.6	38.9	0.19	39

Saturation magnetization (M_s) and coercive forces (H_c) were measured by vibrating sample magnetometer (VSM). M_s showed similar values for both samples, while H_c was found to decrease from 4.8 Oe for **NP-bc** to 0.19 Oe for **NP-ac**, most likely due to the decrease in the size of the NPs (Figure 23).

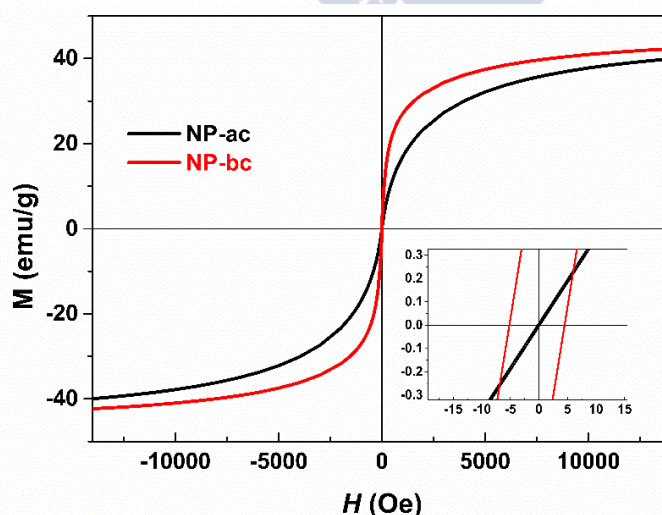


Figure 23: Hysteresis loops for samples NP-bc (red) and NP-ac (black) with an inset of the low magnetic field area.

Thermogravimetric assay (TGA) of the samples showed 20% of organic coating for **NP-bc** and 39% for **NP-ac** (Figure 24), showing that, as expected, the fraction of the NPs remaining stable in the supernatant after the additional centrifugation step bears more organic coating. The thermal profile of the samples show three main weight loss contributions, which were attributed to desorption of physically absorbed water (≤ 400 °C), partial decomposition of PAA (400–650 °C), and further degradation of the carbonic residues (≥ 650 °C).¹⁹⁸ Notably, for **NP-bc** the weight loss curve at 650 °C is much smoother as compared to **NP-ac**, presumably due to the lower amount of polymeric coating.

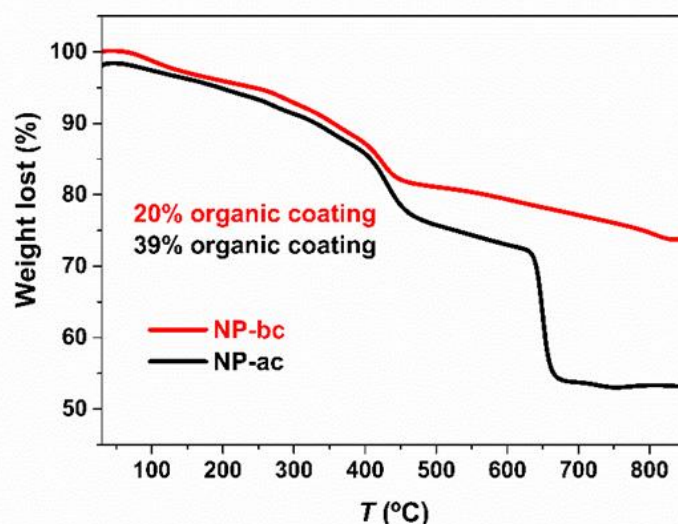


Figure 24: TGA revealing the percentage of organic content of **NP-bc** (red) and **NP-ac** (black).

The composition of the organic coating was analyzed by Fourier transform infrared spectroscopy (FT-IR), which confirmed the presence of carboxylic acid moieties in both samples, as demonstrated by the vibrational bands at 1650 cm^{-1} attributed to $\text{C}=\text{O}$, 1540 and 1400 cm^{-1} ($-\text{CO}_2^-$), 1100 cm^{-1} ($-\text{CO}_2\text{H}$), (Figure 25).

The carboxylic acid moieties of the PAA coating offer an opportunity for further functionalization, for example using peptide coupling. In order to probe the reactivity of the carboxylic acids, the coupling reaction between **NP-ac** was tested with the fluorophore $\text{Cy}3\text{-NH}_2$ as a model system with 100, 300, and 500 equivalent (eq) per 1 mmol of NPs (Scheme 5). The functionalized NPs were purified by centrifugation, and

the amount of unreacted Cy3-NH₂ was quantified by comparing against a calibration curve of the fluorophore in water (Figure 26). The unreacted amount of Cy3-NH₂ was subtracted from the amount placed in the reaction mixture, and assumed to be covalently attached to the PAA in **NP-ac**. The results obtained showed the success of the peptide coupling in 98% yield when 100 eq of Cy3-NH₂ per NP were employed (Table 6), showing that the PAA coating can be employed for NP functionalization with e.g. biomolecules for targeting or drug delivery.

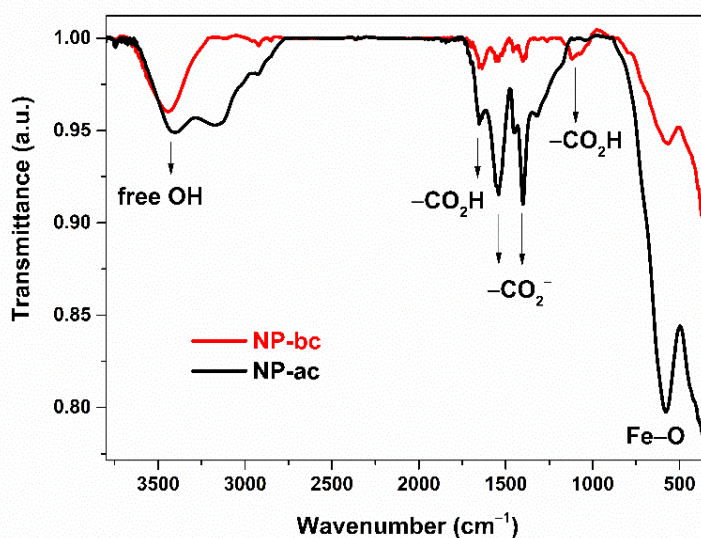
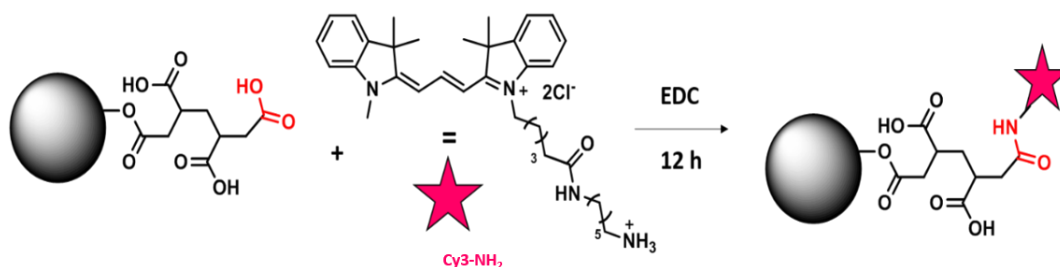


Figure 25: FT-IR of NP-bc (red) and NP-ac (black) with the characteristic bands of carboxylic acid moieties stemming from the polyacrylic acid coating: 1650 cm^{-1} for C=O, 1540 and 1400 cm^{-1} for $-\text{CO}_2^-$, 1100 cm^{-1} for $-\text{CO}_2\text{H}$, and 578 cm^{-1} for Fe-O of the magnetic core.

Table 6: Various conditions employed for the coupling of Cy3-NH₂, and the yield of functionalized NPs after purification

Cy3-NH ₂ eq	μg added	μg recovered	Yield (%)
100	19	0.33	98
300	57	2.82	95
500	90	13.2	85



Scheme 5: Peptide coupling between carboxylic acid moieties of the PAA coating and Cy3-NH₂.

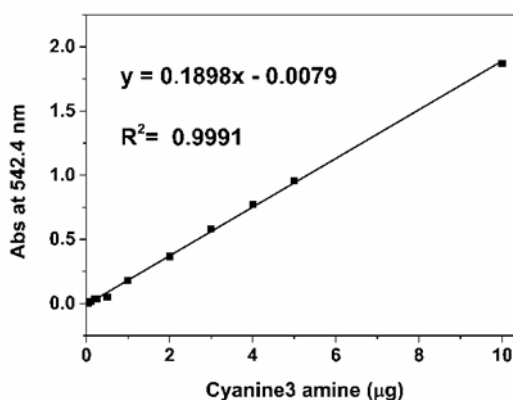


Figure 26: Calibration curve with Cy3-NH₂.

2.3 USPIO STABILITY

2.3.1 Chemical Stability

One of the requirements for nanomaterials to be successfully applied in the biomedical field is the preservation of their chemical integrity over time and under biological conditions.²⁰³ Metal leaching from NPs, for example, has been shown to promote toxicity in some cases.²⁰³ Thus, chemical stability of metal nanoparticles implies that no metal ions are released into the solution, and this should not only be evaluated when NPs are stored over time, but also in the presence of biomolecules, such as proteins, vitamins, and lipids.

The chemical integrity of **NP-bc** and **NP-ac** was evaluated by quantifying free Fe and Mn ions released from the samples during storage in water at 4 °C during 10 months. The results showed negligible metal leaching after 10 months of storage, with 0.03 and

0.02% of Fe ions and 0.14 and 0.09% of Mn ions released into the storage solution for **NP-bc** and **NP-ac**, respectively (Figure 27), showing that these NPs are chemically stable for storage periods of at least 10 months.

Additionally, in order to quantify the chemical leaching of **NP-bc** and **NP-ac** in a biological context, NPs were incubated for 1 h at 37 °C with rat mesenchymal stem cell (rMSC) culture medium, which has a highly protein-rich composition to hinder stem cell differentiation into other types of cells.²⁰⁴ When NPs are incubated in this biological medium, the release of Fe and Mn ions is increased as compared to the sample stored in water at 4 °C. However, the leached quantities remain small, with 0.42% of Fe ions and 0.53% of Mn ions for **NP-bc**, and 0.73% of Fe ions and 0.56% of Mn ions for **NP-ac** (Figure 27). Although comparison with literature-reported materials is difficult due to differences in conditions and types of materials, the values obtained for **NP-bc** and **NP-ac** are very low: for example, Wang and coworkers²⁰⁵ recently showed 9% Mn ion leaching for hydrogels loaded with iron and manganese oxides after incubation with phosphate buffer saline (PBS) at pH = 7.4 for 4 h, whereas Yeh and coworkers²⁰⁶ reported 1.3% of Mn ion loss for Mn_3O_4 nanoplates after 48 h in PBS and 37 °C. As the chemical stability of **NP-bc** and **NP-ac** is high, toxic effects attributed to metal ions leaching seem to be of less concern.

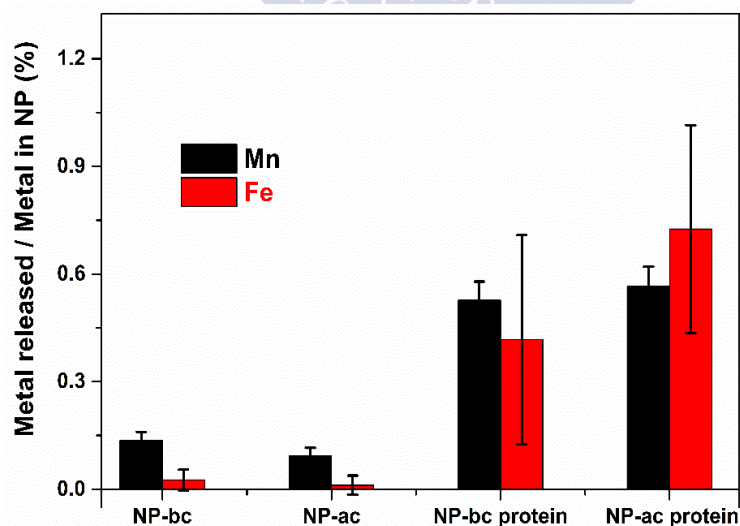


Figure 27: Percentage of Fe and Mn ions released from **NP-bc** and **NP-ac** to storage solution after 10 months of storage in water at 4 °C (**NP-bc**, **NP-ac**) and after 1 h incubation in rMSC culture medium at 37 °C (**NP-bc protein**, **NP-ac protein**).

2.3.2 USPIOs Protein Adsorption

Although iron oxide NPs are expected to be biocompatible because iron ions are intrinsic in the human body, once they are in contact with a complex medium, such as blood, interactions between the NP surface and proteins may occur.^{207,208} This phenomenon can affect the biodistribution of the NPs, promote particle aggregation, and result in toxicity.^{147,209} The physicochemical properties of NPs, such as size and surface charge, have a large impact on protein adsorption.^{210–213} Therefore, the characterization of NPs in contact with biological medium is of fundamental importance to verify their suitability for biomedical applications.

In order to characterize the physicochemical behavior of **NP-bc** and **NP-ac** under biological conditions, both samples were incubated with rMSC culture medium. **NP-bc** and **NP-ac** were incubated at 200 $\mu\text{g}/\text{mL}$ of Fe in the medium for 1 h at 37 °C. The samples were then recovered by centrifugation at 30000 rpm for 30 min, and the pellet was redispersed in phosphate buffer at pH = 7.4. Then, ζ -potential and D_h of the samples were measured by dynamic light scattering (DLS) and compared to the data obtained prior to incubation. There were no significant changes in the ζ -potential of neither sample after incubation (Figure 28A). However, the D_h of **NP-bc** had increased from 35 to 50 nm, presumably due to adsorption of proteins onto the NP surface (Figure 28B). In contrast, the D_h of **NP-ac** remains unchanged after the incubation period, indicating that no aggregation between **NP-ac** and the proteins of the medium took place.

In order to quantify the protein adsorption, a bicinchoninic acid (BCA) assay was performed in rMSC culture medium (Figure 29). BCA assay quantifies the total amount of protein in a given sample by absorbance due to the formation of a purple complex of Cu^+ . The results of BCA assay showed that the quantity of proteins adsorbed onto **NP-bc** was five times larger compared to **NP-ac**. This can be attributed to the different physicochemical properties of **NP-bc** and **NP-ac**, most likely the hydrodynamic radius and the coating coverage. **NP-bc** with a large hydrodynamic radius (35 nm) has lower curvature on the surface as compared to the smaller **NP-ac**, which may facilitate the binding of the mainly bulky proteins of the medium.²¹⁴ Additionally, the higher amount

of polymeric coating around **NP-ac** (39%) compared to **NP-bc** (20%) could shield the smaller NP from interactions with biomolecules

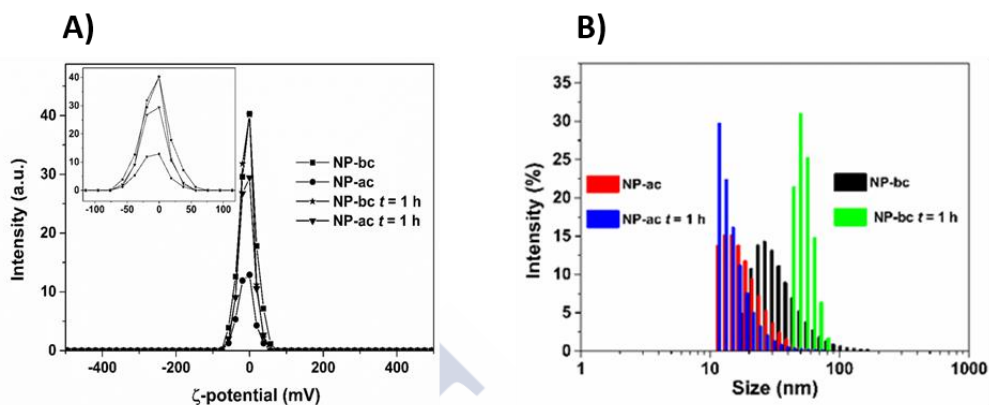


Figure 28: A) ζ -potential of NP-bc and NP-ac before and after incubation with rMSC culture medium at 37 °C for 1 h; B) D_h of NP-bc and NP-ac at 200 $\mu\text{g/mL}$ before and after incubation with rMSC culture medium at 37 °C for 1 h.

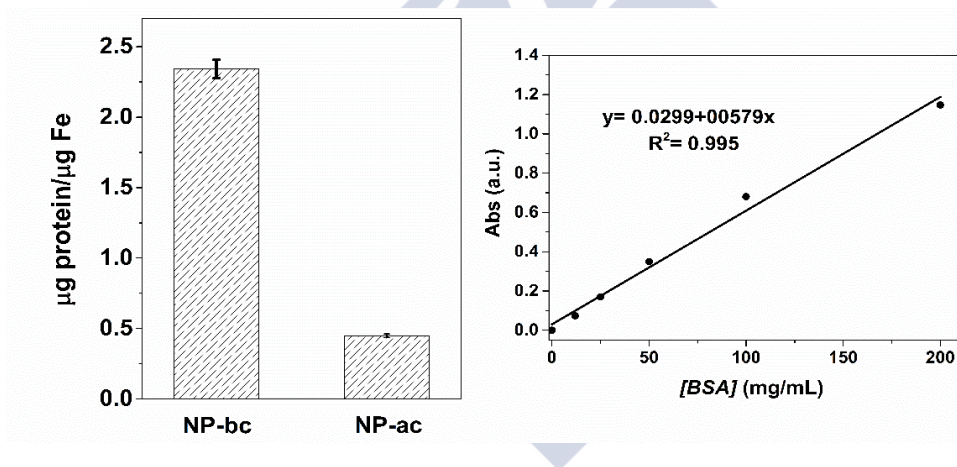


Figure 29: Micrograms of proteins adsorbed onto NP-bc and NP-ac (left) after 1 h incubation in rMSC culture medium. Calibration curve (right) with bovine serum albumin (BSA) protein for the BCA quantification assay.

2.3.3 In vitro Studies

When NPs come into contact with a more complex medium, such as blood, protein adsorption is known to lead to NP aggregation.²¹⁵ In order to study the behavior of **NP-bc** and **NP-ac** samples in contact with cells, *in vitro* studies were carried out using rMSCs (Figure 30, left). Sample **NP-bc** formed large aggregates already after 1 h of incubation (Figure 30, middle), whereas **NP-ac** remained stable even after 16 h

(Figure 30, right), rendering **NP-ac** suitable candidates for cell detection by MRI.²¹⁶ Clearly, the additional centrifugation step affords NPs that are much more stable in biological medium, showing promise for the use of **NP-ac** for biomedical applications. In order to test the biocompatibility of **NP-ac**, lactate dehydrogenase (LDH) and cell count assays were carried out with rMSCs. LDH assay measures the release of the cytosolic enzyme lactate dehydrogenase, which is an indicator of plasma membrane damage. Cell count assay quantifies are used to verify the normal growth of rMSCs. Briefly, rMSCs were exposed to a concentration of **NP-ac** as high as 200 μg of Fe/mL for a long incubation time of 24 h, subjecting the rMSCs to demanding conditions (Figure 31). Both cell count and LDH viability assays showed no differences between the control rMSCs and those exposed to **NP-ac**, highlighting the good biocompatibility of the sample.

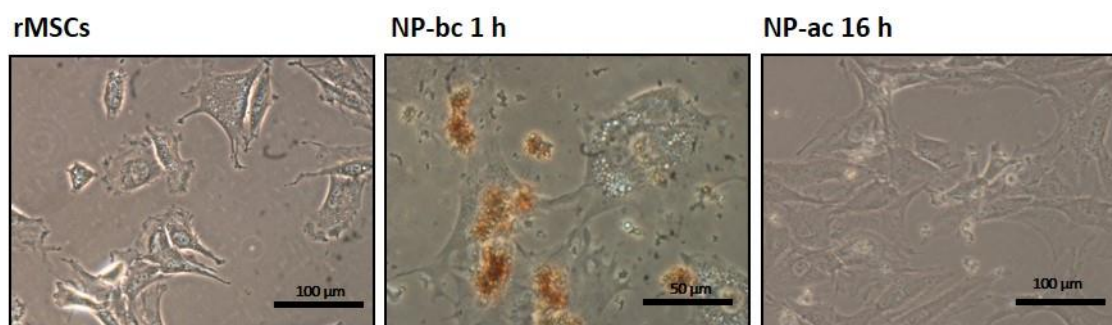


Figure 30: Optical microscopy images of rMSCs (left), after incubation with NP-bc for 1 h (middle), and with NP-ac for 16 h (right).

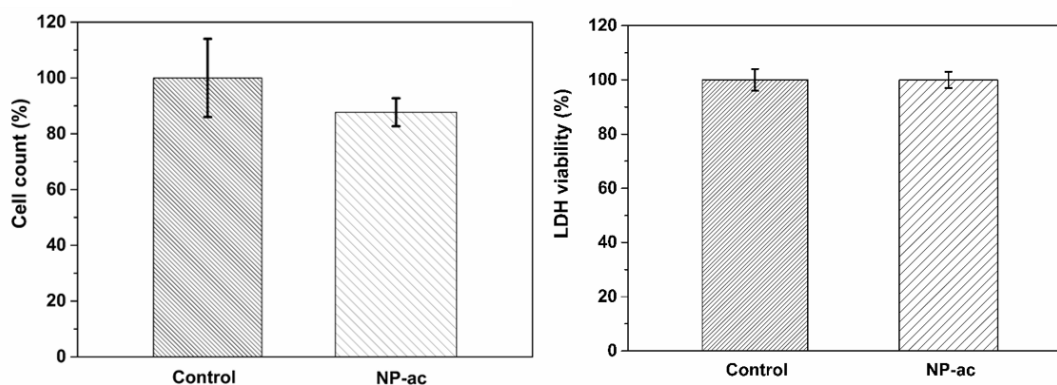


Figure 31: A) Cell count of rMSCs after incubation with NP-ac for 24 h at 200 μg /mL of Fe. B) LDH viability assay of rMSCs after incubation with NP-ac for 24 h at 200 μg /mL of Fe.

2.4 MRI MEASUREMENTS

The ratio between the longitudinal and transversal relaxation is an important parameter defining CA performance: a high r_1 value and a r_2/r_1 ratio near 1 results in bright contrast in T_1 -weighted imaging mode. On the other hand, when r_2 is the predominant value with a high r_2/r_1 ratio, the dark contrast is enhanced in a T_2 -weighted imaging mode. If an intermediate r_2/r_1 ratio is reached, a dual T_1 – T_2 reduction can be accomplished.²¹⁷ In order to evaluate the efficiency of the nanoparticles as CAs for MRI applications, both transversal and longitudinal r of samples **NP-bc** and **NP-ac** were measured at a magnetic field of 1.4 T and 37 °C, giving r_2 values of 178 $\text{mM}^{-1}\text{s}^{-1}$ for **NP-bc** (Figure 32A), and 58.8 $\text{mM}^{-1}\text{s}^{-1}$ for **NP-ac** (Figure 32B), both higher than that of Feridex and similar to Resovist, with r_2 of 41 $\text{mM}^{-1}\text{s}^{-1}$ and 61 $\text{mM}^{-1}\text{s}^{-1}$, respectively, both superparamagnetic iron oxide NPs approved by FDA as negative CAs (Table 7).⁶⁵ The r_1 values of **NP-bc** and **NP-ac** are very similar, 13.1 $\text{mM}^{-1}\text{s}^{-1}$ and 13.4 $\text{mM}^{-1}\text{s}^{-1}$, respectively, resulting in very different r_2/r_1 ratios: 14 for **NP-bc** and 4.4 for **NP-ac**, the latter an intermediate value indicating possible dual behavior.

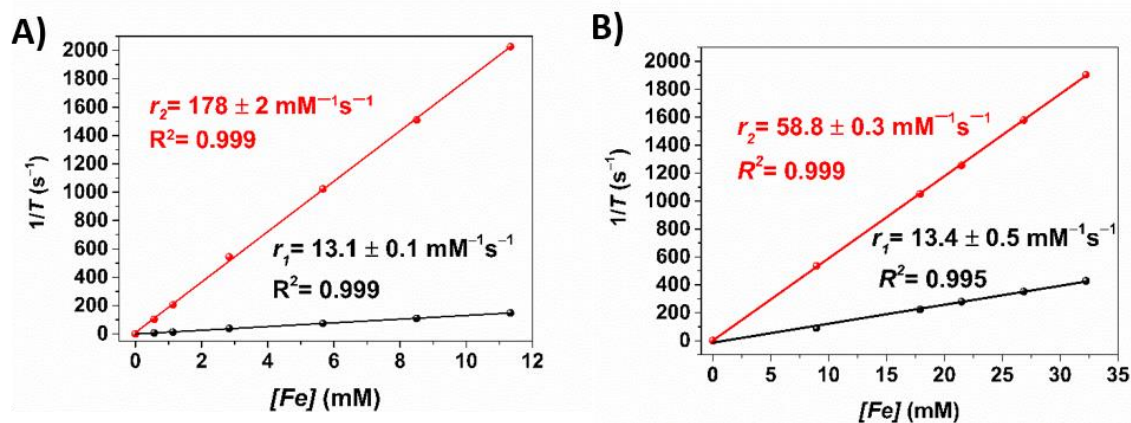


Figure 32: A) r_1 and r_2 of NP-bc at 1.4 T and 37 °C; B) r_1 and r_2 of NP-ac at 1.4 T and 37 °C.

Table 7: Comparison of r between Feridex, Supravist, Resovist, Dotarem, and NP-ac. NP-ac was measured at 1.4 T and 37 °C. ^aMeasured at 1.5 T and 37 °C. ^bCA in clinical trials.

	D_h (nm)	Coating agent	r ($\text{mM}^{-1}\text{s}^{-1}$)		r_2/r_1	Contrast
Feridex, Endorem	120	Carboxydextran	^a $r_1= 4.7$	^a $r_2= 41$	8.7	Negative
^b Supravist, SHU-555C	20	Carboxydextran	^a $r_1= 13.2$	^a $r_2= 44$	3.3	Positive
Resovist, SHU-555A	60	Carboxydextran	^a $r_1= 8.7$	^a $r_2= 61$	7.0	Negative
Dotarem	-	-	^a $r_1= 2.9$	^a $r_2= 3.2$	1.1	Positive
NP-ac	18	Polyacrylic acid	$r_1= 13.4$	$r_2= 58.8$	4.4	Dual

The r of the samples after 10 months of storage in water at 4 °C was re-evaluated, as it is crucial for drug formulations that the properties remain unchanged during storing. The r of stored **NP-bc** measured at 1.4 T and 37 °C displayed a reduction in both r_1 , from 13.1 to 8.17 $\text{mM}^{-1}\text{s}^{-1}$, and r_2 , from 178 to 118 $\text{mM}^{-1}\text{s}^{-1}$, showing that the properties of this sample were significantly deteriorated during storage. On the contrary, **NP-ac** showed good reproducibility in both r_1 , displaying values of 13.4 when fresh and 12.0 $\text{mM}^{-1}\text{s}^{-1}$ after storage, and r_2 , merely changing from 58.8 to 61.8 $\text{mM}^{-1}\text{s}^{-1}$.

The $r_{1,2}$ of **NP-ac** were not only promising for a dual CA in MRI, but also featured good reproducibility over time, and therefore **NP-ac** was the sample of choice for further studies on relaxivity (Table 8). Relaxivity measurements of **NP-ac** were performed at different magnetic fields in order to probe its efficiency as a CA, in both water and 1.6% agar, the latter to mimic tissue density.

The r_1 obtained for **NP-ac** is reduced when increasing the magnetic field from 1.4 to 9.4 T, as expected due to the slower electronic relaxation relative to rotational motion at high fields.²¹⁸ The values are above 10 $\text{mM}^{-1}\text{s}^{-1}$ at clinical fields (3 T or lower) in both water and agar, which are great values to efficiently shorten the T_1 . Moreover, the r_2/r_1 ratios are between 4 and 5.5, intermediate ratios that suggest good performance of **NP-ac** as dual CA in clinical fields. However, at the ultra-high magnetic field of 9.4 T (Figure 33), r_1 was significantly reduced to 0.49 $\text{mM}^{-1}\text{s}^{-1}$, limiting the use of **NP-ac** in T_1 mode.

The r_1 values are slightly higher in agar when compared to water at the same field, because the rate of spin exchange may increase with slowing molecular motion.²¹⁹ The r_2 is also higher in agar when compared to the results in water in the same field, again due to limited molecular motion, but also because solid environments promote local static field disturbances that shorten the T_2 .

Table 8: $r_{1,2}$ of NP-ac at 1.4 and 3 T in water and 1.6% agar gel, and at 9.4 T in agar. ^aSample measured after 10 months of storage in aq solution at 4 °C.

	1.4 T		3 T		9.4 T
	Water	Agar	Water	Agar	Agar
r_1 ($\text{mM}^{-1}\text{s}^{-1}$)	13.4	^a 14.2	^a 10.2	^a 12.5	0.49
r_2 ($\text{mM}^{-1}\text{s}^{-1}$)	58.8	^a 81.6	^a 50.2	^a 68.5	43
r_2/r_1	4.4	5.7	4.9	5.5	87

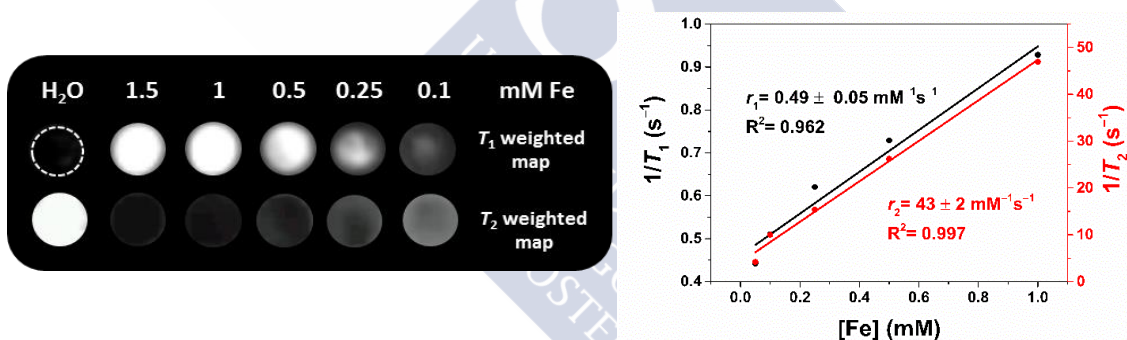


Figure 33: T_1 and T_2 weighted map in 1.6% agar of NP-ac at 9.4 T (left). $r_{1,2}$ of NP-ac in 1.6% of agar at 9.4 T (right).

Phantom images were taken to verify the shown contrast of **NP-bc** and **NP-ac** in MRI. The images acquired at a magnetic field of 3 T showed **NP-bc** serving as a negative CA (Figure 34A). Similarly, when applying a T_2 -weighted sequence, **NP-ac** produced a reduction in signal, resulting in dark contrast (Figure 34B). On the other hand, when applying a T_1 -weighted sequence, the contrast given by the two samples was very different: while **NP-bc** did not show much difference when compared to water, **NP-ac** produced a notable increase in signal resulting in bright contrast (Figure 34B), revealing **NP-ac** as T_1 – T_2 contrast agent. This dual enhancement along with high stability in biological medium are desirable features for advanced CAs, and they were

only displayed by **NP-ac** after the centrifugation step. Therefore, sample **NP-ac** is suitable for dual T_1 – T_2 image acquisition at clinical fields, 3 T or lower, but also as a negative CA at a higher field.

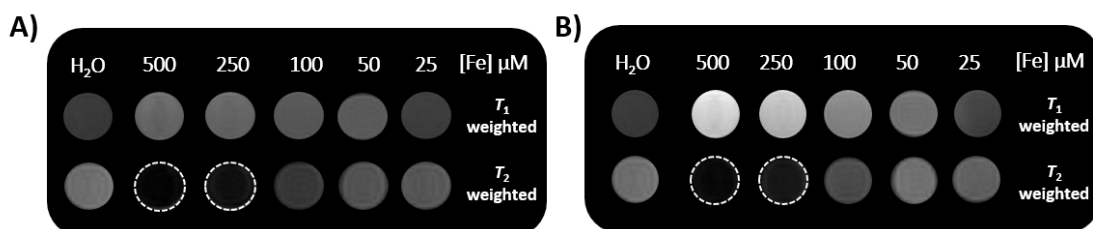


Figure 34: A) MRI image at 3 T of a NP-bc phantom; B) MRI image at 3 T of a NP-ac phantom. White dashed circles are used in T_2 -weighted sequences for clarity.

In order to evaluate the efficiency of **NP-ac** as a dual CA, its properties were compared with those of ferrites proposed as dual CAs in the literature, since there is currently no dual CAs commercially available for use in the clinic (Table 9). Although direct comparison is difficult due to differences in the conditions of the measurements, such as magnetic field and the medium, reported dual CAs have similar r_2/r_1 ratios between 4.4 and 5.4. A comparison of the $r_{1,2}$ values and the r_2/r_1 ratios shows that **NP-ac** displays similar performance as the previously reported dual CAs. However, the advantage of **NP-ac** is that the synthesis method offers an organic solvent-free alternative to obtaining a dual MRI CA in gram-scale quantity.

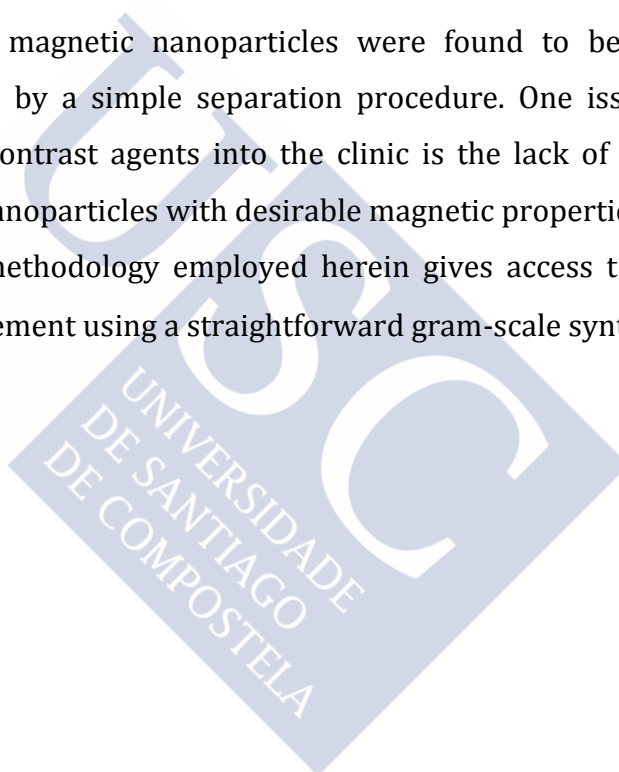
Table 9: Comparison of r between Feridex, Supravist, Resovist, Dotarem, and NP-ac. NP-ac was measured at 1.4 T and 37 °C. ^aMeasured at 1.5 T and 37 °C. ³² ^bCA in clinical trials.

Ref.	Field	Coating	Synthesis method	r_1	r_2	r_2/r_1
199	1.5	Polyethylene glycol	Seed-mediated growth	13.3	65	4.9
200	0.5	Sodium tartrate	Thermal decomposition	27.2	146	5.4
201	4.7	Poly(methacrylic acid)	Coprecipitation	6.6	35.9	5.4
NP-ac	1.5	Poly(acrylic acid)	Hydrothermal	13.5	58.8	4.4

2.5 CONCLUSIONS

Ultrasmall superparamagnetic iron oxide nanoparticles were synthesized by hydrothermal method on a gram scale with hydrophilic polyacrylic acid as coating and Mn^{2+} as the main doping ion, using a procedure that refrains from the use of both organic solvents and phase-transfer procedures. The carboxylate moieties of the coating offer the possibility of functionalization by peptide coupling, which was successfully demonstrated with a fluorophore as a model system.

The properties of the magnetic nanoparticles were found to be optimized for biomedical applications by a simple separation procedure. One issue limiting the progress of new dual contrast agents into the clinic is the lack of facile synthesis methods that provide nanoparticles with desirable magnetic properties, stability, and biocompatibility. The methodology employed herein gives access to nanoparticles with dual T_1 – T_2 enhancement using a straightforward gram-scale synthesis.



2.6 EXPERIMENTAL

2.6.1 Chemicals

Agar, $\text{FeCl}_3 \cdot 6\text{H}_2\text{O}$, ZnCl_2 , $\text{MnCl}_2 \cdot 4\text{H}_2\text{O}$, NH_4OH , polyacrylic acid sodium salt (MW 5100 Da), and 1-ethyl-3-(3-dimethylaminopropyl)carbodiimide were purchased from Sigma-Aldrich and used without further purification. Potassium bromide (99% for spectroscopy, IR grade) was purchased from Acros Organics. Cyanine3 amine ($\text{Cy}3\text{-NH}_2$) was purchased from Lumiprobe. Ultrapure water produced by Milli-Q Advantage A10 system (Millipore). BCA protein assay was purchased from Life Technologies. Rat mesenchymal stem cells (Cultrex, Trevigen, Gaithersburg, MD, USA) were cultured in IMDM (78%), fetal bovine serum (10%), horse serum (10%), penicillin-streptomycin (1%) (Gibco, Invitrogen, Paisley, UK), and amphotericin B (1%) (Sigma-Aldrich, St. Louis, MO, USA).

2.6.2 USPIOs Synthesis Procedure

NPs were synthesized using a modification of a previously reported hydrothermal method.¹⁹⁸ Briefly, 14 mmol of $\text{FeCl}_3 \cdot 6\text{H}_2\text{O}$, 5.6 mmol of $\text{MnCl}_2 \cdot 4\text{H}_2\text{O}$, and 1.4 mmol of ZnCl_2 were dissolved in 10 mL of water (deoxygenated via bubbling N_2 through the solution for 30 min prior to use) in a 40 mL poly(tetrafluoroethylene) (PTFE) vessel. Next, 15 mL of aq 25–30% NH_4OH were added, and subsequently 0.4 mmol of poly(acrylic acid) sodium salt in 5 mL of water were rapidly added to the reaction mixture. The PTFE vessel with the resultant black suspension was capped and placed into a stainless steel autoclave. The autoclave was sealed and kept at 200 °C for 24 h under autogenous pressure. NPs were isolated using a magnet, the solution was removed, and NPs were redispersed in 200 mL of water and isolated magnetically again. Redispersion was repeated twice in total. The resultant NPs were centrifuged at 3000 rpm for 10 min, the supernatant was kept and stored to yield sample **NP-bc** (1.8 g). **NP-bc** was subjected to an additional centrifugation of 4000 rpm for 12 h and the supernatant was kept to yield sample **NP-ac** (1.0 g).

2.6.3 Characterization

TEM, HAADF-STEM, and STEM-EDX studies were performed using Titan ChemiSTEM (FEI, 0.08 nm STEM resolution) electron microscope, operated at 200 KV and equipped with a Super-X detector. The samples were prepared by dropping 10 μ L of a diluted dispersion of the nanoparticles onto a Cu-grid coated by ultrathin carbon film on lacey carbon support film followed by evaporation of the solvent in vacuum at room temperature.

DLS experiments were carried out in a SZ-100 nanoparticle analyzer (Horiba) at 173° detection angle. Results were represented in the histograms as volume scattered light. Hydrodynamic diameter and standard deviation of both samples were calculated as an average of 5 successive measurements.

TGA was performed in a TGA/DSC 1 STARE system, Mettler-Toledo, fitted with OmniStar GSD320 gas analysis system (Pfeiffer Vacuum), with 10 K/min gradient from 30 to 900 °C under 30 mL/min of Ar flow.

FT-IR spectra were acquired on a Bruker VERTEX 80v FT-IR spectrometer in absorbance mode. A spatula tip of the sample was mixed with 200 mg of KBr and the powder was pressed at 10 tons for 2 min to obtain a transparent pellet. Spectra were recorded at 1.66 hPa with 32 scans and 4 cm^{-1} resolution with deuterated triglycine sulfate detector. The empty holder at 1.66 hPa was used as background and baseline correction was applied to the spectra.

Hysteresis loops were measured in a VSM (EV9, Lot-Oriel) in the applied magnetic field range from -14 kOe to +14 kOe at RT.

ICP-OES studies were carried out in an ICPE-9000 Multitype ICP Emission Spectrometer from Shimadzu equipped with a nebulizing system and using optical emission spectroscopy for detection. Samples were prepared by dissolving 100 μ L of nanoparticle solutions in 1 mL of HCl/HNO₃ (3:1) and diluted with Milli-Q water up to 100 mL. Measurements were repeated three times and the results are the mean value with RSD.

XRD was performed in a PanAnalytical X Pert PRO MRD system working at 45 kV/40 mA and using a Cu X-ray radiation with wavelengths $K\alpha_1 = 1.5405980 \text{ \AA}$, $K\alpha_2 = 1.5444260 \text{ \AA}$ and $K\alpha_1/K\alpha_2$ intensity ratio = 0.5. In the incident beam path geometry a soller slit of 0.04 rad and a divergence and an anti-scatter slit of $1/2^\circ$ and 1° , respectively, were used. On the other hand, a soller slit of 0.04 rad and Ni large beta-filter were used in the diffracted beam path. The detector used was a Pixcell 3D area detector with 255 channels and an active length of 2.511° . Measurements were performed in a zero-background signal sample holder in the range 25° – 70° (2θ), with a step size of 0.0098° and time per step of 1500 s in scanning line detector mode.

Absorbance for BCA assay was measured with BioTek, Synergy H1 hybrid reader at 562 nm. Standard calibration curve was done with BSA standard solution in phosphate buffer (0 to 200 mg/mL).

Optical microscopy images were taken with Olympus IX51.

2.6.4 Nanoparticle Functionalization

Reaction between the carboxylic acid moieties on the NP surface and Cy3-NH₂ was performed overnight with water as solvent. **NP-ac** was dispersed in water at 23 mg/mL concentration of nanoparticles. Calculation of MW of nanoparticle was done assuming it is the sum of the MW of the core and that of the ligand. The MW of the core was calculated taking into account the core size estimated from a STEM image and the density of magnetite. The MW of the ligand was calculated by taking into account the percentage of organic coating from TGA and MW of PAA.

For the coupling reaction, 22 μL of aq. **NP-ac** solution (23 mg/mL) was diluted to a final volume of 300 μL . Three different quantities of Cy3-NH₂ were tested to evaluate the quantity of carboxylic acids available for the coupling reaction, corresponding to 100, 300, and 500 equivalents to 1 mmol of nanoparticles: 194, 580, and 960 μL of Cy3-NH₂ solution (0.5 mg/mL in water) were added to the **NP-ac** solution.

Then, 50 μL of freshly prepared aq EDC solution (5 mg/mL) was added, and the reaction mixture was stirred at rt overnight. Purification was carried out by centrifugation at 7500 rpm during 10 min with Amicon Ultra-0.5 Centrifugal Filter

Devices. Three washing cycles were performed with water, one with aq 0.1 NaOH solution, and two more with water, to recover functionalized **NP-ac**. The supernatants of all centrifugal purifications were combined and analyzed by UV-Vis at 542.4 nm. By comparing against a calibration curve of Cy3-NH₂ in water, the amount of free fluorophore was quantified. The amount of Cy3-NH₂ not recovered was assumed to be covalently attached to the PAA-coating of the NP.

2.6.5 Chemical Stability

Metal leaching from **NP-bc** and **NP-ac** was investigated after 10 months of storage in Milli-Q water at 4 °C. The NPs were removed from the supernatant by centrifugation at 4000 rpm during 10 min with an Amicon Ultra 10K Centrifugal Filter. The collected supernatant was analyzed by ICP for the presence of free Fe and Mn ions.

2.6.6 USPIO Stability in Biological Medium

Chemical stability in biological medium: **NP-bc** and **NP-ac** were incubated at a concentration of 200 µg/mL of Fe with rMSC culture medium at 37 °C during 1 h. Then, the nanoparticles were removed from the supernatant by centrifugation at 4000 rpm during 10 min with an Amicon Ultra 10K Centrifugal Filter. The collected supernatant was analyzed by ICP for the presence of free Fe and Mn ions.

DLS studies: NPs were measured in 100 mM PBS (pH = 7.4) at 200 µg/mL of Fe. Incubation with **NP-bc** and **NP-ac** in rMSC culture medium was carried out at 37 °C during 1 h. After the incubation time, the sample was centrifuged at 30000 rpm for 30 min, and the pellet was collected and redispersed by sonication in 100 mM of PBS at pH = 7.4 prior to analysis.

BCA assay: **NP-bc** and **NP-ac** were incubated for 1 h with rMSC culture medium at 37 °C at 200 µg/mL of Fe. The samples were then subjected to centrifugation (30000 rpm, 30 min) and the supernatant was kept and diluted 100 times with PBS to remove interferences in the colorimetric assay. A standard calibration curve was measured with BSA protein at 1, 12, 25, 50, 100, and 200 µg/mL. Absorbance was measured at 562 nm.

2.6.7 Viability Assay

Cell viability was determined by means of the LDH (Assay Kit, Sigma-Aldrich, St Louis, USA) following the manufacturer protocol. Supernatants of lysed cells were included as a negative control. In brief, rMSCs were incubated with 200 $\mu\text{g}/\text{mL}$ of Fe for 24 h. Then, the medium was removed and the cells were washed three times with PBS. Afterwards, fresh medium was added to the cells and they were left overnight. Then, the supernatants were collected and centrifuged at 1000 rpm for 5 minutes and further incubated with LDH reagents for 20 minutes. Finally, absorbance was read with Synergy2 plate reader (Biotek Instruments, Vermont, USA) at 490 nm and viability rate (in percentage) was calculated in respect to control and lysed values.

2.6.8 Cell Count

Total cell count was performed to determine the influence of nanoparticles on rMSCs. Staining was done using Trypan blue (STEMCELL Technologies, Grenoble, France) and a Neubauer counting chamber (Blaubrand, Sigma-Aldrich, St. Louis, MO, USA) was employed. rMSCs after 24 h incubation with **NP-ac** and subsequent 12 h incubation in fresh medium were diluted 1:5 with PBS and 1:2 with Trypan blue. Cell count was performed using an inverted microscope (Olympus IX51, Shinjuku, Tokyo, Japan) and referred to control rMSCs.

2.6.9 MRI Measurements

Relaxivity measurements at a magnetic field of 1.4 T were performed in a minispec mq60 contrast agent analyzer from Bruker at 37 °C with a standard inversion recovery sequence for T_1 and Carr Purcell Meiboom Gill (CPMG) for T_2 calculations. The relaxivity constants (r_1 and r_2) were calculated from the slope of the curve obtained by fitting the T_1^{-1} or T_2^{-1} values *versus* the total Fe concentration in mM. Repetition of relaxivity measurements after 10 months of storage were carried out at the same Fe concentration of the samples and with the same sequence parameters.

Relaxivity measurements at 3 T were performed with a MR Solutions Benchtop (Guildford, UK) at 37 °C with matrix 256 x 252, field of view (FOV) 60 x 60 mm, 3 slices

with a slice thickness of 1 mm and 1 mm slice gap. An inversion recovery sequence was used for T_1 , with $T_R = 24000$ ms and $T_1 = 150, 450, 800, 1200, 2400, 4800, 9600, 16000, \text{ and } 23500$ ms. Then, r_1 was calculated from the slope of the curve obtained by fitting the T_1^{-1} values versus the total Fe concentration in mM.

For r_2 in water, a T_2 map was acquired with a multi-echo-multi-sliced (MEMS) sequence of 50 ms echo time, repetition time of 4800 ms and 10 echoes. For r_2 in agar, a T_2 map was acquired with MEMS sequence of 15 ms echo time, repetition time of 3100 ms and 10 echoes. Post-processing was performed using ImageJ software (Rasband, W. NIH) for the construction of T_2 maps, and r_2 was calculated from the slope of the curve obtained by fitting the T_2^{-1} values versus the total Fe concentration in mM.

MR imaging: was performed in a 3 T horizontal bore MR Solutions Benchtop (Guildford, UK) equipped with 48 G cm⁻¹ actively-shielded gradients. For imaging the sample, a 56 mm diameter quadrature bird-cage coil was used in transmit/receive mode. For the phantom measurements, the samples at different concentrations (between 25 and 500 μM in Fe) were dissolved in 200 μL of Milli-Q water in 300 μL tubes. All MR images of the phantoms were acquired with an image matrix 256 x 252, FOV 60 x 60 mm, 3 slices with a slice thickness of 1 mm and 1 mm slice gap. For T_2 -weighted imaging a fast spin echo (FSE) sequence with the following parameters was used: $T_E = 68$ ms, $T_R = 4800$ ms, $N_A = 50$. For T_1 -weighted imaging a FSE sequence with $T_E = 11$ ms, $T_R = 400$ ms, and $N_A = 50$ was used. MRI studies at high magnetic field were conducted on a 9.4 T MR system (Bruker Biospin, Ettlingen, Germany) with 440 mT/m gradients. A quadrature radio-frequency transmit-receive resonator was used for data acquisition. T_2 -weighted images were acquired using a multi slice multi echo sequence of 7.32 ms echo time, 5.389 s repetition time, 16 echoes, 14 slices, 1 average, FOV of 7.5 cm x 7.5 cm and matrix size of 100 x 100. T_1 -weighted images were acquired using a RARE-VTR sequence of 8.81 ms echo time, 17.62 ms echo spacing, rare factor 4, repetition times of 900 s, 1500 s, 3000 s, 4500 s, 7000 s, 8500 s, 14 slices, 1 average, FOV of 7.5 cm x 7.5 cm and a matrix size of 200 x 200. Post-processing was performed using ImageJ software (Rasband, W. NIH).

CHAPTER 3

3 Magnetite Nanoparticles for Stem Cell Labeling



3.1 INTRODUCTION

Stem cells show promise for the treatment of various diseases, such as glioma, ischemic brain injury, Alzheimer's and Parkinson's diseases,²²⁰ and cardiovascular disease,⁷¹⁻⁷³ as demonstrated by their involvement in more than 360 clinical trials.⁷⁴ Cell therapy is based on the administration of stem cells, relying on their ability to self-renew and differentiate into most cell types of the adult body. Therefore, the understanding of the needed dose, administration route, and biodistribution of these transplanted stem cells is of fundamental importance in order to develop safe therapies. Non-invasive cell tracking and specific imaging of labeled stem cells *in vivo* is an ideal methodology to follow the migration and grafting of transplanted cells and to evaluate their fate and therapeutic effect.⁷⁵ IONs together with MRI constitute a common approach for cell tracking due to the biocompatibility and effectiveness of IONs, and the high spatial resolution, penetration depth, and the lack of ionizing radiations provided by MRI.⁷⁶ As explained in the Introduction, IONs shorten the transverse relaxation time or T_2 in MRI, and therefore create dark contrast in T_2 -weighted MR images.

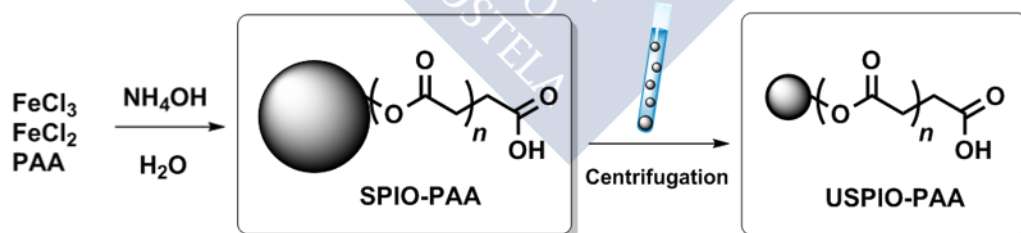
Clinically approved IONs, such as Feridex or Ferumoxytol, provide low labeling efficiency.²²¹ Although in their natural niches mesenchymal stem cells (MSCs) are phagocytic in nature, during *ex vivo* cell culture and expansion they lose their phagocytic ability, rendering their efficient labeling a challenge.^{71,222} A low labeling efficiency limits the use of IONs as magnetic labels to short-term detection, usually referred to as 0–72 h after cell transplantation.²²³ Thus, significant efforts have been devoted to developing new ION formulations with different organic coatings to enhance cellular uptake and enable mid- to long-term tracking.^{77,81,224,225} IONs can be classified as superparamagnetic iron oxide nanoparticles (SPIOs), if the hydrodynamic diameter (D_h) is above 50 nm, or as ultrasmall iron oxide nanoparticles (USPIOs), if it is below. USPIOs have often been studied as CAs because of their enhanced blood half-life when compared to SPIOs, but low cell uptake has hampered their use for cell tracking applications.^{226,227} The smaller size of USPIOs as compared to SPIOs could result in advantageous properties for cell tracking, such as higher stability in biological

fluids, reproducible cell labeling procedures, and homogeneous labeling of the entire cell population.²²⁸

In this chapter, the cell labeling performance of SPIOs and USPIOs was studied with MSCs for cell tracking applications. The IONs were studied in regard to their internalization by MSCs and to the contrast achieved in MRI images.

3.2 SYNTHESIS OF IONS

In order to apply IONs as magnetic labeling agents in cell tracking, they were synthesized by a hydrothermal method¹⁹⁸ using PAA as coating because of the high yield and magnetic response of the NPs, high stability in aqueous medium, and the possibilities the coating offers for further functionalization. Two sets of IONs were synthesized following the same synthetic procedure by hydrothermal method,¹⁹⁸ but differing in the purification protocols (Scheme 6).²²⁹ The synthesized IONs were purified twice by magnetic separation using water as solvent to render sample **SPIO-PAA**, classified as superparamagnetic iron oxide nanoparticles. The collected supernatant of an extra centrifugation step with **SPIO-PAA** gave sample **USPIO-PAA**, classified as ultrasmall iron oxide nanoparticles.



Scheme 6: Synthesis route used to produce the two different IONs: after hydrothermal synthesis, SPIO-PAA was obtained. Its purification by centrifugation gave access to USPIO-PAA.

SPIO-PAA sample was fully characterized in a previous work by Kolen'ko and coworkers,¹⁹⁸ and the data used in this work to compare with **USPIO-PAA**. The inorganic core composition was confirmed to be magnetite, Fe₃O₄, by XRD. The diffractogram showed one single phase corresponding to an inverse spinel structure for **USPIO-PAA** (Figure 35, left). The nature of PAA in the organic coating of **SPIO-PAA** was confirmed by X-ray photoelectron spectroscopy (XPS). On the other hand, the

presence of PAA on **USPIO-PAA** was confirmed by IR spectroscopy, as identified by the vibrational bands at 1633 cm^{-1} attributed to $-\text{CO}_2\text{H}$, 1551 cm^{-1} for $-\text{CO}_2^-$, and 558 cm^{-1} for Fe–O (Figure 35, right).

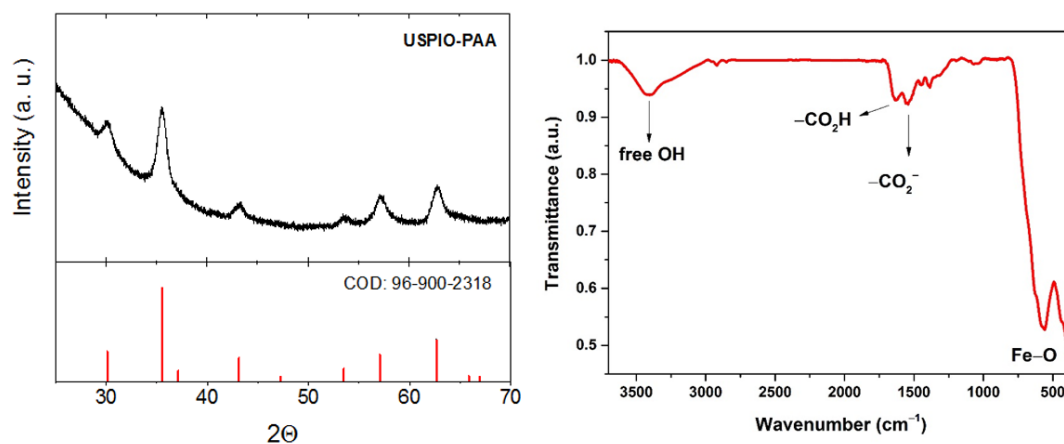


Figure 35: Left: XRD pattern of **USPIO-PAA**, position and relative intensity (bottom) of the XRD reflections of a Fe_3O_4 single phase with inverse spinel structure from the COD, pattern code 96-900-2318. Right: IR of **USPIO-PAA** with the characteristic bands of carboxylic acid moieties stemming from the PAA coating of 1633 cm^{-1} attributed to $-\text{CO}_2\text{H}$ and 1551 cm^{-1} for $-\text{CO}_2^-$, and 558 cm^{-1} for Fe–O.

The difference between **SPIO-PAA** and **USPIO-PAA** is related with the NP size and the content of organic matter. On one hand, core size measured from TEM images showed values around double for **SPIO-PAA** compared to **USPIO-PAA**, 18 and 8.5 nm, respectively (Table 10, see also Figure 36).

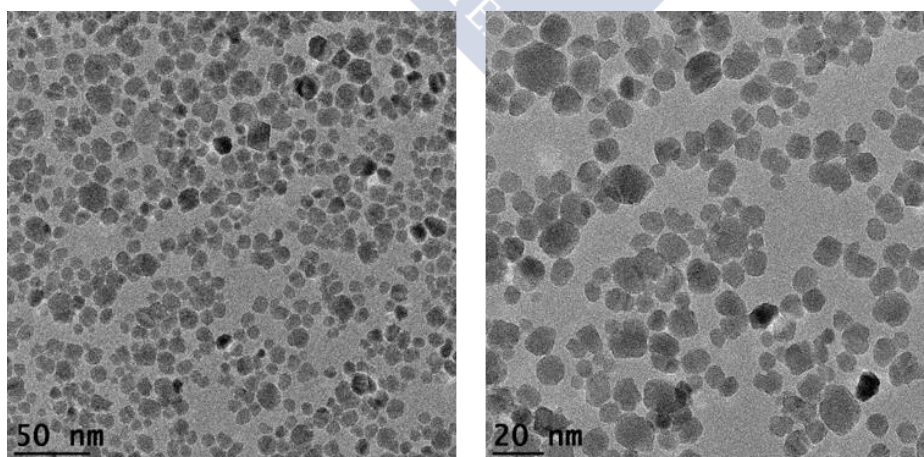


Figure 36: TEM images of **USPIO-PAA**.

Table 10: Core size from TEM images, D_h , percentage of organic coating calculated from TGA, and M_s , and H_c obtained by VSM for SPIO-PAA and USPIO-PAA. ^aData for SPIO-PAA are from ref 198.

	Core size (nm)	D_h (nm)	Coating (wt%)	M_s (emu g ⁻¹)	H_c (Oe)
^aSPIO-PAA	18	95	9.3	81	20
USPIO-PAA	8.5	24	23	65	0.12

The same trend was observed with the hydrodynamic diameter (D_h) measured by DLS, where **SPIO-PAA** presented a size of 95 nm, nearly four times that of **USPIO-PAA**, 24 nm, the latter corresponding to an ultrasmall NP size (Table 10).²³⁰ PAA content, calculated by TGA, was found to be 9.3 and 23 wt% for **SPIO-PAA** and **USPIO-PAA**, respectively (Table 10, Figure 37 left). As discussed in Chapter 2,²²⁹ D_h and the amount of organic coating of IONs play an important role in the colloidal stability of the NPs and their interactions with biomolecules, both important features governing cell uptake. Regarding the magnetic properties, **USPIO-PAA** featured M_s of 65 emu g⁻¹ and H_c of 0.12 Oe by VSM measurements (Figure 37, right). As expected, these values are significantly below those of **SPIO-PAA** that featured M_s of 81 emu g⁻¹ and H_c of 20 Oe,¹⁹⁸ as a result of the larger core size.

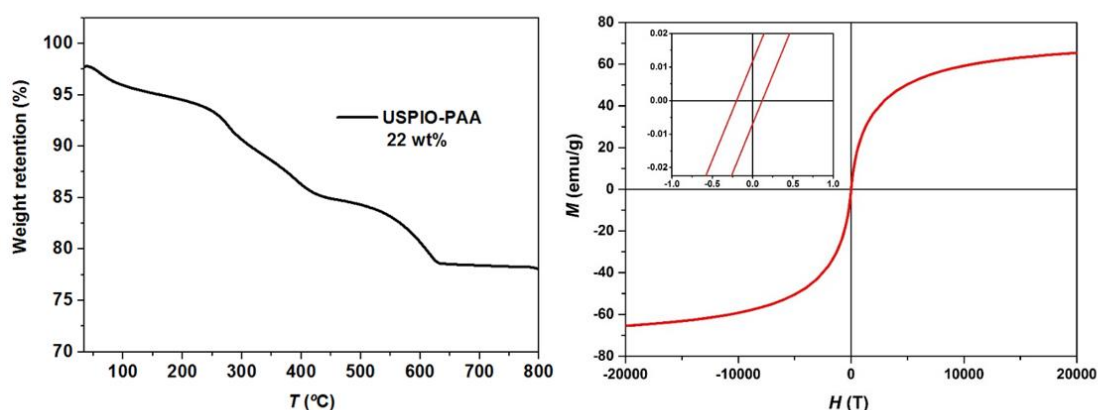


Figure 37: Left: TGA revealing the percentage of organic content in wt% of USPIO-PAA. Right: Hysteresis loop of USPIO-PAA with an inset of the low magnetic field area.

MRI performance of **USPIO-PAA** was then evaluated. Transverse r_2 , of **USPIO-PAA** was found to be $127 \text{ mM}^{-1}\text{s}^{-1}$ and longitudinal r_1 , $17.7 \text{ mM}^{-1} \text{ s}^{-1}$ at 1.4 T and 37°C (Figure 38), indicating **USPIO-PAA** as a three times more efficient CA than the clinically approved SPIO Feridex, which has an r_2 of $41 \text{ mM}^{-1} \text{ s}^{-1}$ under the same conditions.⁶⁵ On the other hand, **SPIO-PAA** featured values of 202 and $19.3 \text{ mM}^{-1} \text{ s}^{-1}$ for r_2 and r_1 , respectively. The higher r in comparison with **USPIO-PAA** is in agreement with the larger M_s as a consequence of the larger core size. However, the performance of IONs in cell labeling depends much more on their uptake than on their magnetic properties, since the latter are affected/modified by the cell internalization.¹⁴³

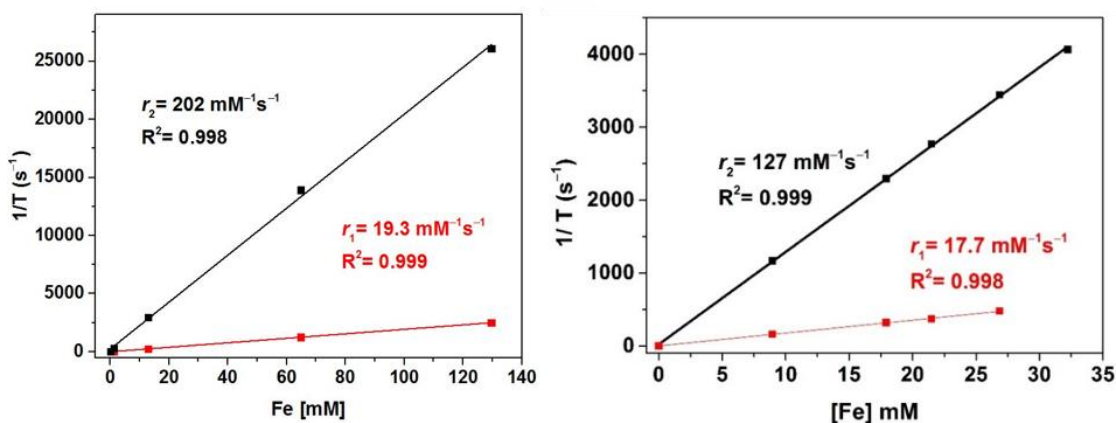
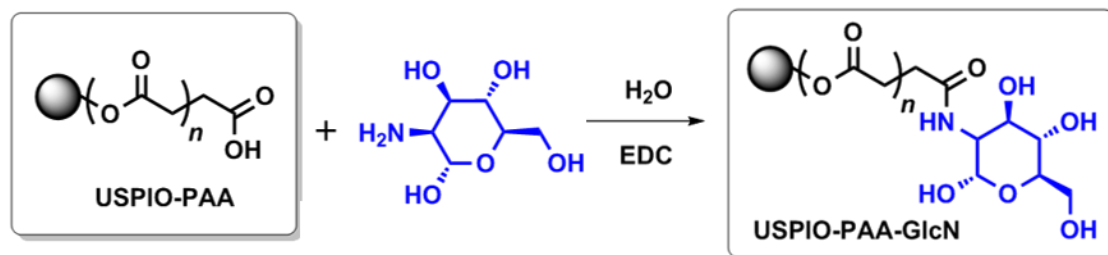


Figure 38: r_1 and r_2 of SPIO-PAA (left) and USPIO-PAA (right) at 1.4 T and 37°C .

3.3 COATING MODIFICATION

In general, USPIOs have been reported to be internalized through fluid-phase endocytosis, which results in poor cell uptake.²³¹ As an example, negligible amounts of commercial Ferumoxytol are internalized by MSCs *in vitro* even when incubated in the presence of protamine. To increase MSCs' Ferumoxytol loading, the CA has to be used in combination with protamine and heparine, known as the heparin-protamine-Ferumoxytol (HPF) nanocomplex methodology,²³² and even then, MSCs only show an iron content of $2.12 \pm 0.11 \text{ pg Fe/cell}$. Consequently, in an attempt to achieve receptor-mediated endocytosis, **USPIO-PAA** was functionalized with targeting molecules. D-Glucosamine (GlcN) was selected for the modification because glucose is

known to be biocompatible and has been shown to enhance cellular uptake in other systems (Scheme 7).^{233,234}



Scheme 7: Functionalization through peptide coupling of USPIO-PAA with GlcN molecules in water to yield USPIO-PAA-GlcN.

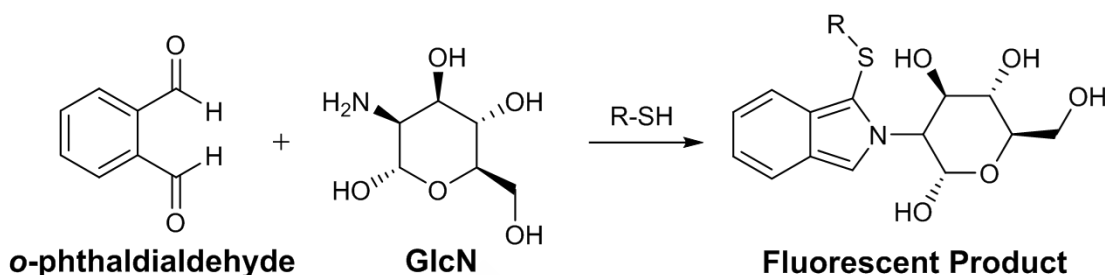
In order to calculate the carboxylic acid moieties available for GlcN functionalization, **USPIO-PAA** was reacted with the dye Cy3-NH₂, following the same procedure as described in Chapter 2.²²⁹ Three different quantities of Cy3-NH₂ were tested corresponding to 100, 300, and 500 eq to 1 mmol of NPs. By comparing against a calibration curve of Cy3-NH₂ in water, the amount of free fluorophore (Cy3-NH₂ recovered after purification) was quantified, and found to be 0.33, 2.8 and 13 μg , respectively for 100, 300 and 500 eq (Table 11). The remaining quantity of Cy3-NH₂ was assumed to be covalently attached to the PAA coating of the NP. These results suggest that **USPIO-PAA** has 100 eq of carboxylic acids per mmol of NP available for the reaction by peptide coupling with a 98% yield.

Table 11: Carboxylic acid quantification of USPIO-PAA by reaction with Cy3-NH₂, Amounts of different equivalents of fluorophore added with the corresponding recovered amounts for each condition. The reaction yield was calculated with respect to added amounts of Cy3-NH₂.

Equivalents	Amount added [μG]	Amount recovered [μG]	Yield [%]
100	19	0.33	98
300	57	2.8	95
500	90	13	85

After evaluation of carboxylic acids available in **USPIO-PAA**, GlcN was employed for the reaction with an excess of 1000 eq for the functionalization of **USPIO-PAA**, following the same synthetic procedure as for Cy3-NH₂. The quantification of GlcN in **USPIO-PAA-GlcN** was performed with the *o*-phthaldialdehyde (OPA) method (Scheme 8) by comparing the results against a calibration curve (Figure 39).²³⁵ The

coupling reaction showed high reproducibility in terms of the amount of glucosamine attached to the NP between different batches, with an average of 143 μg GlcN/mg NP (Table 12).



Scheme 8: Reaction between unbound GlcN and o-phthaldialdehyde in water at rt that yields to a fluorescent product.

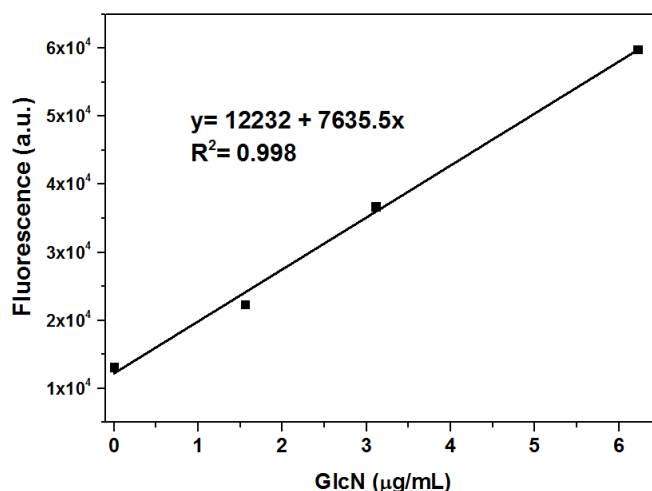


Figure 39: Calibration curve between GlcN and o-phthaldialdehyde in water.

Table 12: Amount of GlcN attached to USPIO-PAA in three different reactions.

	μg GlcN/mg NP
Batch 1	139 ± 17
Batch 2	146 ± 24
Batch 3	145 ± 11

DLS measurements were performed with **USPIO-PAA-GlcN** to evaluate the surface charge of the NPs. At basic pH, the ζ -potential was -114 ± 14 mV, which after glucosamine modification shifted to -86 ± 7 mV (Figure 40). While **USPIO-PAA-GlcN** reaches its isoelectric point at around pH 6.0 (-0.4 ± 0.1 mV), **USPIO-PAA** still presents

a highly negative ζ -potential at that pH (-22.2 ± 0.8 mV), the neutralization confirming that a significant part of the carboxylic acid moieties has reacted with GlcN molecules.

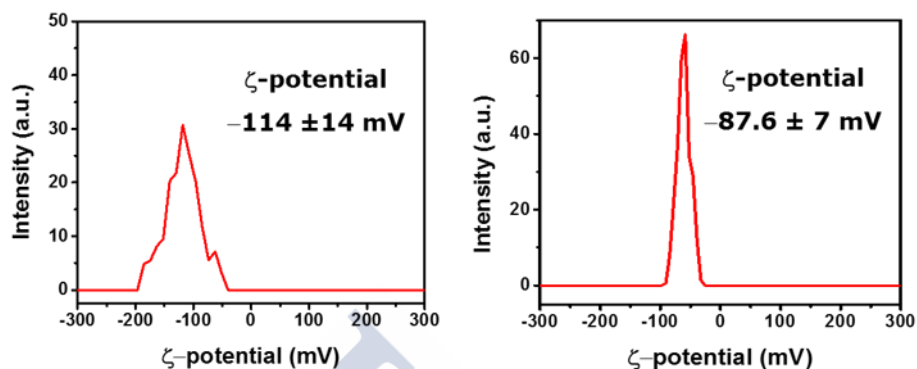


Figure 40: ζ -Potential of USPIO-PAA (left) and USPIO-PAA-GlcN (right) at pH = 9.

TEM images were acquired after glucosamine modification to ensure that no morphological changes took place after the functionalization procedure (Figure 41), and the core size did not show noticeable changes after the modification. D_h as measured by DLS showed an increase from the original 24 nm to 40 nm after GlcN coupling, with no signs of NP aggregation. Due to the small amount of GlcN molecules attached per NP, the organic content by TGA did not show any significant changes between USPIO-PAA-GlcN and USPIO-PAA, as expected.

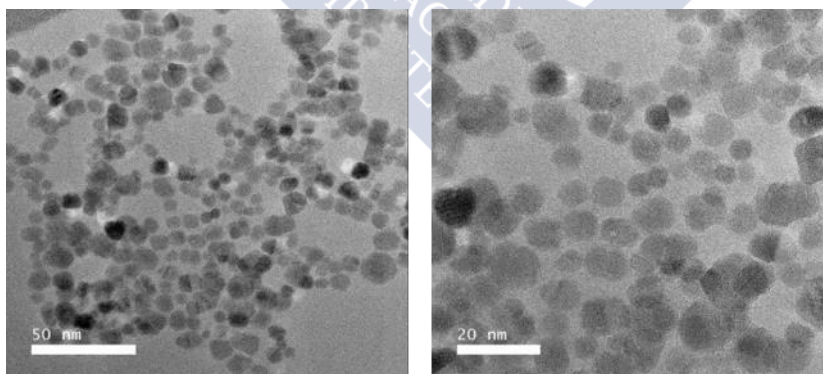


Figure 41: TEM images of USPIO-PAA-GlcN.

3.4 FE CONTENT IN MSCS

In order to foresee the *in vivo* detection window by MRI, *in vitro* experiments were performed over time to follow the decrease of internalized Fe as MSCs proliferate

(Figure 42). Even though *in vitro* experiments do not represent an accurate scenario to extract *in vivo* conclusions due to an enhanced growth rate with the associated underestimation in Fe loading, they can provide a first rough estimation of the timeframe available for *in vivo* imaging. The Fe content of a constant number of cells, 10^5 MSCs, was analyzed at different time points in culture after the labeling procedure (Figure 42).

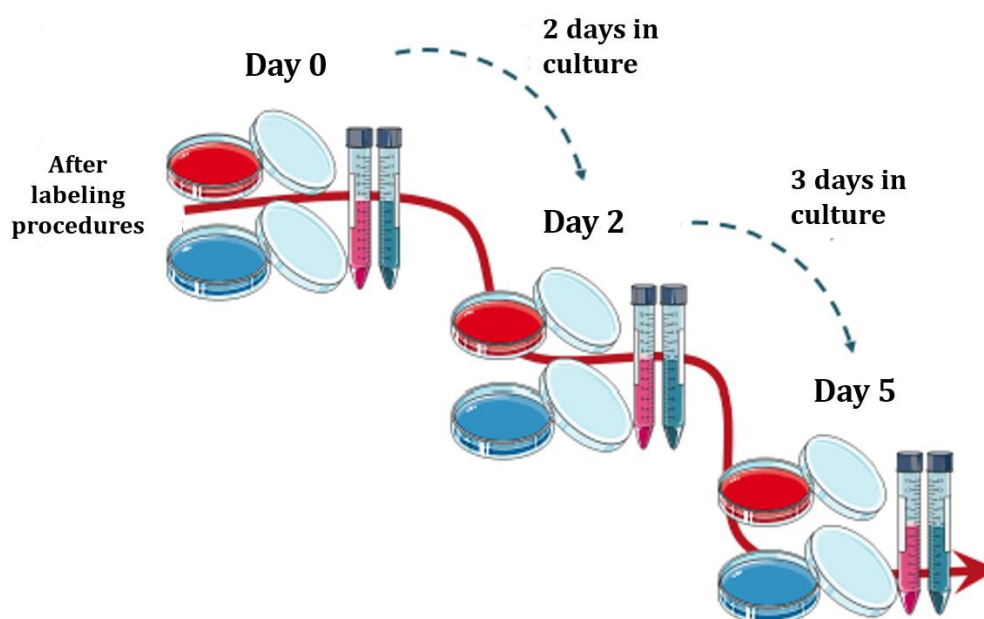


Figure 42: MSCs in culture after incubation with USPIO-PAA-GlcN.

At day 0 post-incubation, 56.5 pg Fe/cell were found in MSC cultures. From this value, an exponential decrease in Fe concentration was observed (Figure 43). This is consistent with the exponential growth of the MSCs that undergo two cell divisions each 24 h. Fe loss may come from a combination of MSCs proliferation with NPs degradation/dissolution in endosomes/lysosomes.²³⁶ After 8 days in culture, MSCs were found to still contain around 3% of initial Fe, 1.63 pg Fe/cell, and after 12 days no differences in Fe content were found when the treated cells were compared to the control. This result verifies the long-term detection of labeled MSCs by MRI. The same trend was observed in PB staining images (Figure 44), where the cells were followed for 12 days at regular intervals. A clear labeling was observed up to 8 days post-incubation. These results guarantee that the values from the ICP measurements come from internalized Fe rather than from extracellular NP aggregates. From day 5 on, an

inhomogeneous cell labeling can be observed in the PB images. This is the result of the asymmetric cargo distribution after cell division as previously reported in several works.^{237,238} Compared to **SPIO-PAA**, the use of **USPIO-PAA-GlcN** delays the emergence of effects derived from asymmetric cell division *in vitro* until day 5, which brings added value to **USPIO-PAA-GlcN** as an MR cell tracking probe.

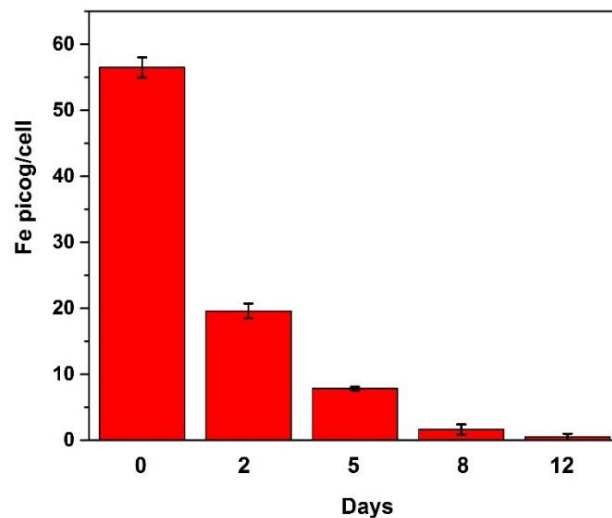


Figure 43: ICP results for Fe quantification in MSCs after labeling procedure.

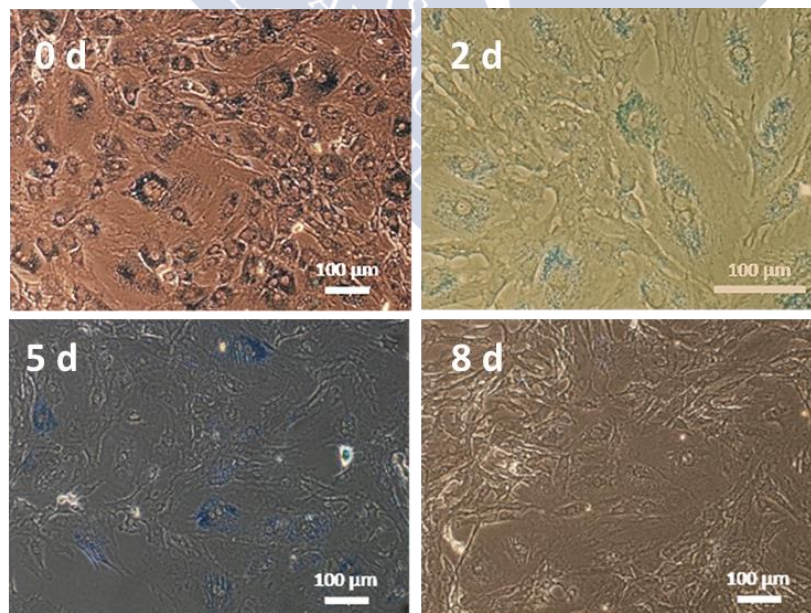


Figure 44: PB staining images of MSCs after incubation with USPIO-PAA-GlcN after 0, 2, 5, and 8 days in culture.

To correlate the amount of Fe per cell with detectability by MRI, T_2^* values were calculated from MR phantom images of MSCs incubated with **USPIO-PAA-GlcN**. MR imaging results are in good agreement with the cellular Fe content measured by ICP spectroscopy. MSCs incubated with **USPIO-PAA-GlcN** showed an initial reduction in T_2^* of 57% after the labeling procedure, and even after 8 days in culture a 23% reduction in T_2^* was observed (Figure 45), following an exponential signal recovery until day 12 post-incubation. This suggests that **USPIO-PAA-GlcN** offer long-term detectability of MSCs by MRI, enabling longitudinal *in vivo* studies on the stem cell fate.

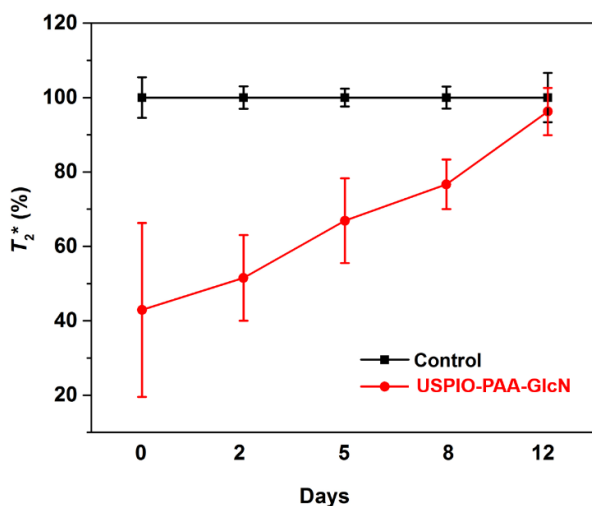


Figure 45: Signal reduction in T_2^* of MSCs labeled with **USPIO-PAA-GlcN**.

3.5 CELL HEALTH

The cell proliferation and viability of MSCs labeled with **USPIO-PAA-GlcN** were studied by means of cell count assays and LDH, respectively, at different time points after the labeling procedure (Figure 46). A slight reduction in cell number is observed at day 5 after incubation with **USPIO-PAA-GlcN** when compared to the control (Figure 46A). However, the number of cells does not statistically differ from the control, and before and after this point no diminishment of cell number was detected. The results of LDH assay showed no differences in viability detected between the control and **USPIO-PAA-GlcN** labeled cells at any time point investigated (Figure 46B),

confirming that these NPs do not affect the viability of the cells. This, together with the cell count data, confirms the lack of toxicity of **USPIO-PAA-GlcN**, and therefore, its use as safe labeling agents for MSC tracking.

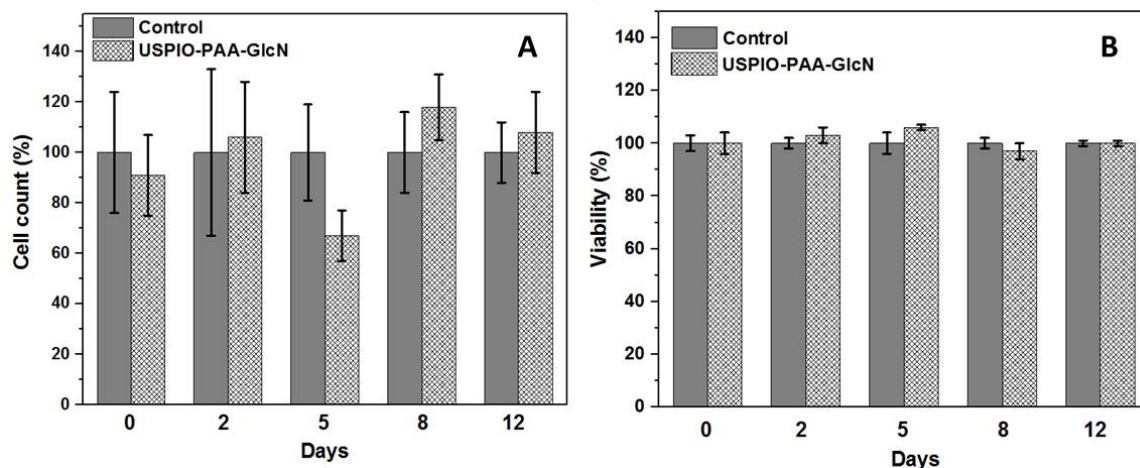


Figure 46: A) Cell count assay after incubation with USPIO-PAA-GlcN; B) LDH viability assay after incubation with USPIO-PAA-GlcN.

3.6 IN VIVO STUDIES

After the promising performance of **USPIO-PAA-GlcN** in *in vitro* experiments, cell tracking studies were conducted with labeled MSCs in order to evaluate their *in vivo* ability to reach the brain, and engraft and decrease the MR signal for sustained periods of time. Many studies have reported good stem cell therapy results using the intra-arterial delivery route in experimental animal models of neurological diseases.²³⁹ The most common method of intra-arterial administration is the use of catheterization to guide the cells into the carotid artery, which enables the delivery of large numbers of cells directly to the brain.²⁴⁰ On the other hand, intravenous cell delivery has been also proven preclinically to be an effective route for cell therapy against neurological diseases, while being less invasive than intra-arterial administration. However, using intravenous route, a part of the administered cells accumulates in peripheral organs, leading to low cell concentrations in the brain.²⁴⁰ Thus, in order to validate **USPIO-PAA-GlcN** for cerebral cell tracking, the labeled cells were transplanted in healthy rats via intra-arterial perfusion to deliver them in large numbers to the brain.

In this study, labeled MSCs were administered at day 0 and MR imaging was performed right after cell administration (1 h) and after 1, 5, and 8 days. Right after the cell administration, labeled MSCs were easily detected in every animal as strong hypointense signals in T_2^* -weighted images (Figure 47). Dark signal voids were found over a wide area in the ipsilateral hemisphere (IH, with respect to the carotid administration), with a prevalence for the area directly fed by the external carotid artery, while only a few dark spots were visible in the contralateral hemisphere (CH). T_2 -weighted images were also taken to discard cerebral lesions, and no significant hyperintensity areas were observed, confirming that no severe damage of the brain had occurred.

From the MR images, the reduction of T_2^* -weighted signal in the IH was estimated over a broad area delimited in red boxes with respect to the CH (Figure 48). The values of MRI signal were calculated as $[100 \times (IH/CH)]$ and as an average of the MRI signal in 7 brain slices with labeled MSCs. Right after the cell administration, labeled MSCs were easily detected in every animal as strong hypointense signals corresponding to a 55% signal reduction in T_2^* -weighted images (Figure 47 and Figure 48).

At day 1, the strong dark signals were still clearly visible with a 32% of signal reduction in T_2^* -weighted images, predominantly in the ipsilateral hemisphere, confirming the engraftment of MSCs mainly during the initial pass without systemic circulation.²⁴¹ From day 1 to day 8, the brain signal was partially recovered from an average signal reduction of 27% (day 2), to 16% (day 5), to 10% (day 8) in T_2^* -weighted images (Figure 48), but well-defined hypointense spots were still visible even after 8 days of the administration. These results highlight the potential of **USPIO-PAA-GlcN** as an efficient and long-term labeling agent of MSCs in MRI. As opposed to the results obtained *in vitro*, where 8 days after the labeling the differences in signal intensity between the control and labeled cells were small, *in vivo* MR images showed that labeled cells can be easily followed in a wide area of the right hemisphere of the animals beyond the 8 days mark.

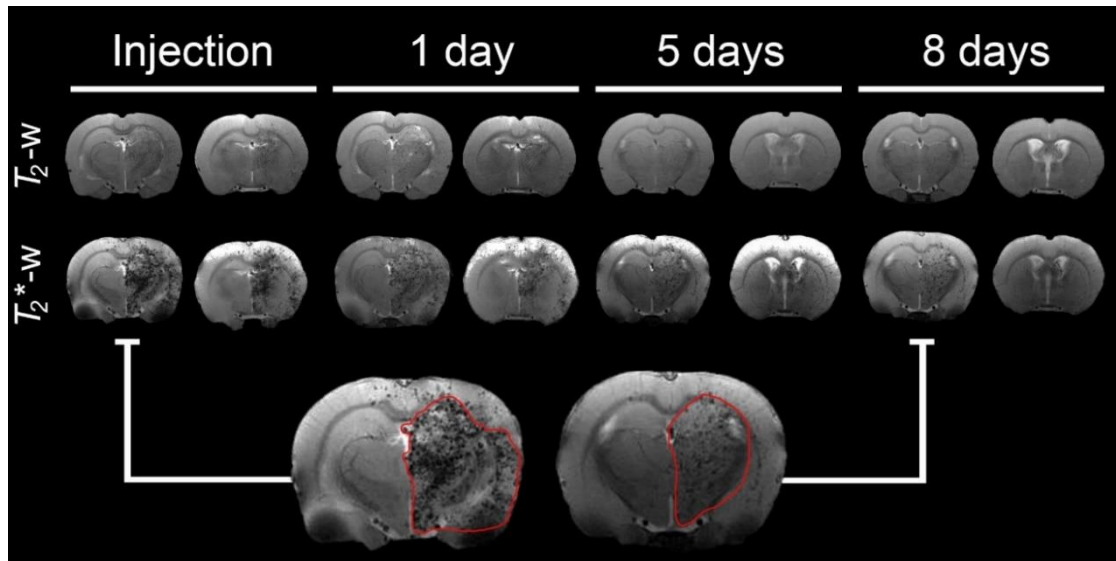


Figure 47: Representative T_2 - and T_2^* -weighted MR images of a healthy rat injected intra-arterially with USPIO-PAA-GlcN-labeled MSCs at different time points at 9.4 T. Inset: red regions highlight the labeled cells in same slice of T_2^* -weighted images after injection and after 8 days.

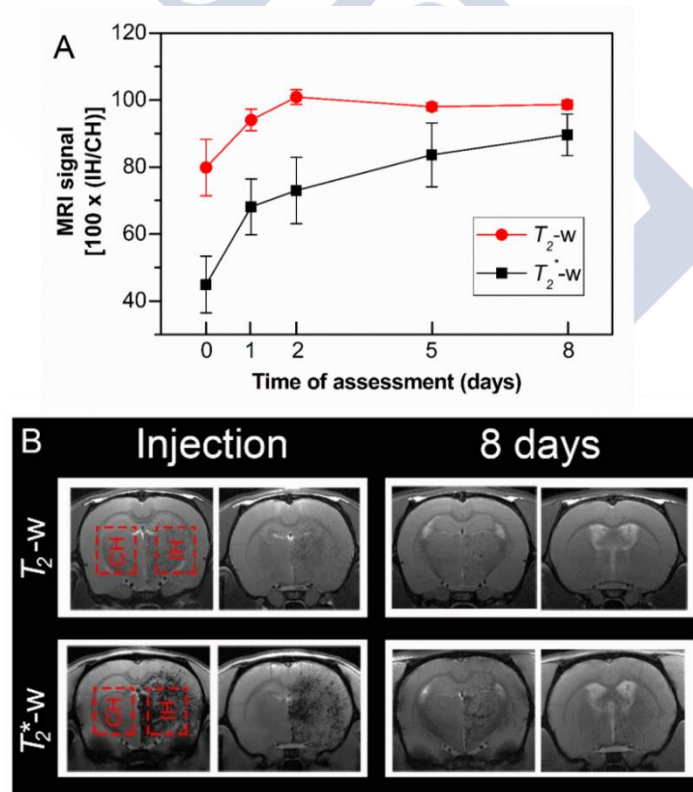
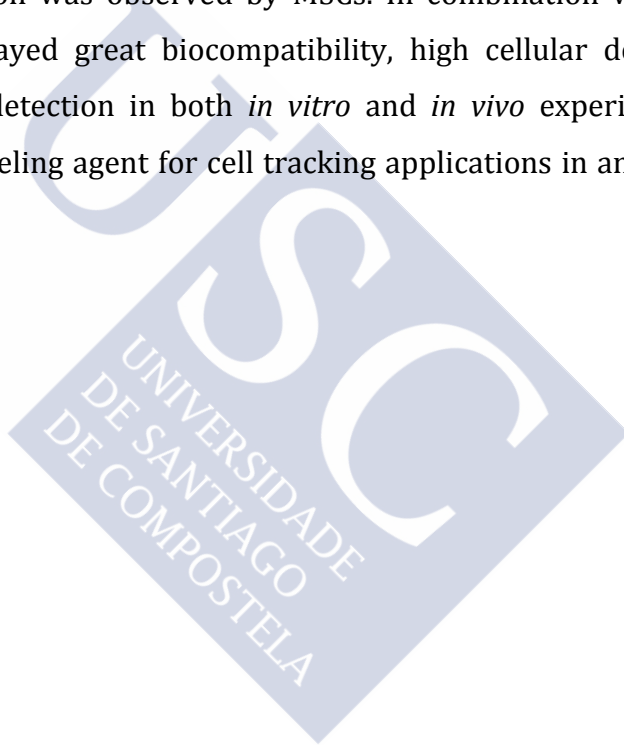


Figure 48: A) Signal reduction in T_2^* -w and T_2 -w in the IH compared to the CH, calculated as $[100 \times (IH/CH)]$. Each point is the average of the MRI signal of 7 slices expressed as mean \pm SD. B) Representative slice highlighting the selected area where the MRI signal was determined in both hemispheres just after injection and after 8 days.

3.7 CONCLUSIONS

SPIOs (**SPIO-PAA**) and USPIOs (**USPIO-PAA**) coated with polyacrylic acid, as well as USPIOs functionalized with glucosamine (**USPIO-PAA-GlcN**), were studied as labeling agents for MSCs. Dramatic differences were found in the cell-labeling performance of these magnetic NPs. **SPIO-PAA** showed signs of aggregation in cell culture medium and as a result the uptake was localized and non-homogeneous within the cell population. On the other hand, **USPIO-PAA** showed good stability *in vitro* but no significant internalization was observed by MSCs. In combination with polylysine, **USPIO-PAA-GlcN** displayed great biocompatibility, high cellular dose of 56.5 pg Fe/cell, and sensitive detection in both *in vitro* and *in vivo* experiments by MRI, showing promise as labeling agent for cell tracking applications in animal models of cerebral ischemia.



3.8 EXPERIMENTAL

3.8.1 Materials and Methods

$\text{FeCl}_3 \cdot 6\text{H}_2\text{O}$, NH_4OH , polyacrylic acid sodium salt (MW 5100 Da), D-glucosamine hydrochloride, poly-L-lysine (PLL, $1.5 - 3.0 \times 10^5$ molecular weight), potassium ferrocyanide trihydrate ($\text{KFe}(\text{CN})_6 \cdot 3\text{H}_2\text{O}$), 1-ethyl-3-(3-dimethylaminopropyl)carbodiimide, 1,8-diazabicyclo[5.4.0]undec-7-ene (DBU), OPA, and LDH kit were purchased from Sigma-Aldrich and used without further purification. Potassium bromide (99% for spectroscopy, IR grade) was purchased from Acros Organics. Cy3-NH₂ was purchased from Lumiprobe. Trypan blue staining was purchased from STEMCELL Technologies. Ultrapure water was produced by Milli-Q Advantage A10 system (Millipore) and used always when not mentioned otherwise. MSCs were purchased from Cultrex, Trevigen, (Gaithersburg, MD, USA), and were cultured in IMDM (78%), fetal bovine serum (10%), horse serum (10%), penicillin-streptomycin (1%) (Gibco, Invitrogen, Paisley, UK), and amphotericin B (1%) (Sigma-Aldrich, St. Louis, MO, USA). EDTA-trypsin and phosphate buffer saline without Mg^{2+} and Ca^{2+} was purchase from Gibco (Invitrogen, Paisley, UK).

XRD was performed with a PanAnalytical X Pert PRO MRD system working at 45 kV/40 mA and using a Cu X-ray radiation with wavelengths $K\alpha_1 = 1.5405980 \text{ \AA}$, $K\alpha_2 = 1.5444260 \text{ \AA}$ and $K\alpha_1/K\alpha_2$ intensity ratio = 0.5. In the incident beam path geometry, a Soller slit of 0.04 rad and a divergence and an anti-scatter slit of $1/2^\circ$ and 1° , respectively, were used. On the other hand, a Soller slit of 0.04 rad and Ni large beta-filter were used in the diffracted beam path. The detector used was a Pixcell 3D area detector with 255 channels and an active length of 2.511° . Measurements were performed in a zero-background signal sample holder in the range $25^\circ - 70^\circ$ (2θ), with a step size of 0.0098° and time per step of 1500 s in scanning line detector mode.

TEM studies were performed using a Titan ChemiSTEM electron microscope and a JEOL JEM-2100 electron microscope, both operated at 200 kV. The samples were prepared by dropping 10 μL of a diluted dispersion of the nanoparticles onto a lacey

carbon-coated Cu grid (400 mesh) followed by evaporation of the solvent under vacuum at room temperature. Image processing was performed using Digital Micrograph software (Gatan) and the size distribution of the particles was calculated using ImageJ software.

TGA was performed in a TGA/DSC 1 STARe system, Mettler-Toledo, fitted with OmniStar GSD320 gas analysis system (Pfeiffer Vacuum), with 10 K/min gradient from 30 to 900 °C under 30 mL/min of Ar flow.

FT-IR spectra were acquired on a Bruker VERTEX 80v FT-IR spectrometer in absorbance mode. A spatula tip of the sample was mixed with 200 mg of KBr and the powder was pressed at 10 tons for 2 min to obtain a transparent pellet. Spectra were recorded at 1.66 hPa with 32 scans and 4 cm⁻¹ resolution with deuterated triglycine sulfate detector. The empty holder at 1.66 hPa was used as background and baseline correction was applied to the spectra.

Hysteresis loops were measured with a VSM (EV9, Lot-Oriel) in the applied magnetic field range from -14 kOe to +14 kOe at RT.

Relaxivity measurements: were performed in a minispec mq60 contrast agent analyzer from Bruker at 37 °C and under 1.4 T magnetic field, with standard inversion recovery sequence for T_1 and CPMG for T_2 calculations. The r_1 and r_2 were calculated as the slope of the curve obtained by fitting the T_1^{-1} or T_2^{-1} values *versus* the Fe concentration in mM.

OPA reaction was measured with BioTek, Synergy H1 hybrid reader at 562 nm. A standard calibration curve was done with BSA standard solution in phosphate buffer (0 to 200 mg/mL).

Optical microscopy images were taken with Olympus IX51.

LDH assays were performed by measuring the absorbance with Synergy2 Biotek Instruments, Vermont, USA.

MRI studies were conducted using a 9.4 T MR system (Bruker BioSpin, Billerica, MA, USA) with 440 mT/m gradients and a combination of a linear birdcage resonator (7 cm in diameter) for signal transmission and a 2 × 2 surface coil array for signal detection.

A quadrature volume coil (7 cm in diameter) was also used in phantom studies. MRI post-processing was performed using ImageJ software (W. Rasband, NIH, USA).

DLS measurements were performed with SZ-100 nanoparticle analyzer (Horiba). The results of ζ -potential are shown as the average of seven consecutive measurements. The results of D_h are represented in the histograms as intensity scattered light of three consecutive measurements.

3.8.2 IONs Synthesis Procedure

SPIO-PAA was synthesized using our previously reported hydrothermal methodology.¹⁹⁸ **USPIO-PAA** was synthesized following a slightly modified procedure. Briefly, 8 mmol of $\text{FeCl}_2 \cdot 6\text{H}_2\text{O}$ and 14 mmol of $\text{FeCl}_3 \cdot 6\text{H}_2\text{O}$ were dissolved in 10 mL of ultrapure water in a 40 mL PTFE vessel. Next, 15 mL of aq 25–30% NH_4OH and 0.4 mmol of poly(acrylic acid) sodium salt in 5 mL of water were added to the reaction mixture. The PTFE vessel was placed in a stainless steel autoclave and kept at 200 °C for 24 h under autogenous pressure. NPs were isolated by magnetic separation and redispersed in water by sonication (two times). The resultant NPs were centrifuged at 3000 rpm for 10 min, the supernatant was subjected to an additional centrifugation at 4000 rpm for 12 h, and the supernatant was kept to yield sample **USPIO-PAA** (1.5 g).

3.8.3 Glucosamine Modification

The quantification of free carboxylic acids in PAA coating of **USPIO-PAA** was performed with Cy3-NH₂. For the coupling with GlcN, **USPIO-PAA** was dispersed in water at a NP concentration of 18.6 mg mL⁻¹, and GlcN (2.8 mg, 1000 eq per nanoparticle) was added. Subsequently, DBU (2.5 μL) was added to ensure a basic pH during the reaction, and last, 100 μL of freshly prepared aq. EDC solution (5 mg mL⁻¹) were added. The reaction was stirred overnight at room temperature, and then purification was carried out by centrifugation at 7500 rpm during 10 min with Amicon Ultra-0.5 Centrifugal Filter Devices to obtain **USPIO-PAA-GlcN** (11 mg mL⁻¹, 500 μL). Three washing cycles were performed with water, one with aq. 0.1 M NaOH solution, and three more with water, to recover functionalized NPs. The supernatants of all

centrifugal purifications were combined and analyzed by the OPA method²³⁵ to determine the quantity of unreacted GlcN. A calibration curve of GlcN was performed in triplicate at 12, 10, 8, 6, 4, 2 $\mu\text{g mL}^{-1}$, and the fluorescence was measured at $\lambda_{\text{excitation}} = 340 \text{ nm}$ and $\lambda_{\text{emission}} = 450 \text{ nm}$. Three different batches of **USPIO-PAA-GlcN** were quantified in order to ensure the reproducibility of the coupling reaction.

3.8.4 *In vitro* Experiments

MSC lines were cultured in IMDM (78%), fetal bovine serum (10%), horse serum (10%), penicillin-streptomycin (1%), and amphotericin-B (1%). Cell passage numbers between 19 and 25 were used.

Cells were plated in 6 well-plates, 1.5×10^5 cells/plate and labeled with $100 \mu\text{g mL}^{-1}$ of IONs for 24 h ($n = 6$) following the protocol described elsewhere²⁴² with slight modifications. Briefly, MSCs were incubated for 24 h in the presence of IONs ($100 \mu\text{g mL}^{-1}$) or IONs ($100 \mu\text{g mL}^{-1}$) premixed with PLL ($1.5 \mu\text{g mL}^{-1}$, vigorously shaken at 1300 rpm for 1 h). After the cell incubation period, the medium was removed and cells were washed three times with 1.5 mL of PBS (without Mg^{2+} and Ca^{2+}). After washing, the cells were left for 12 h in 1 mL of fresh label-free medium. Next, the cells were washed once with 1.5 mL of PBS, and 0.5 mL of EDTA-trypsin was added to detach the cells from the well. The detached cells were collected, and after a centrifugation (1000 rpm for 5 min) the supernatant was discarded and the cells were resuspended in fresh medium. Labeled and non-labeled MSCs were plated sequentially to evaluate the possible cellular toxicity and labeling clearance. Characterization of MSCs after labeling was performed at different cellular points: 12 h, and 2, 5, 8 and 12 days after labeling.

3.8.5 Incubation between PLL and USPIO-PAA-GlcN

The incubation between PLL (1.5 mg mL^{-1}) and **USPIO-PAA-GlcN** (100 mg mL^{-1}) was performed in phosphate buffer at $37 \text{ }^\circ\text{C}$ for 24 h. The purification of the NPs from unbound PLL was performed by centrifugation (30000 rpm for 30 min), and the pellet

was redispersed in water and purified again by centrifugation. NPs from the pellet were dried and analyzed by IR spectroscopy.

3.8.6 ICP of Labeled MSC

A total of 1×10^5 cells were dissolved in 1 mL of 37% HCl solution and 4 mL of water was added. The Fe concentration was determined by ICP using an ICPE-9000 Multitype ICP Emission Spectrometer from Shimadzu. Measurements were performed in triplicate and the results are shown as the mean value with the standard deviation.

3.8.7 PB Staining

PB staining was performed to demonstrate the uptake of the IONs by the cells. Labeled cells were plated and after 8 h washed with PBS and incubated for 20 min with a mix of equal parts of aqueous solution of HCl (20%) and aqueous solution of potassium ferrocyanide trihydrate (10%). After incubation, cells were washed three times with PBS and images were taken using an inverted microscope.

3.8.8 LDH Assay

For assessing the viability of the cells after labeling, supernatants from the incubation between **USPIO-PAA-GlcN** and MSCs were collected, including a negative control of lysed cells. Cell viability was determined by means of LDH following the manufacturer's protocol. In brief, supernatants were subjected to centrifugation at 1000 rpm for 5 min and further incubated with LDH reagents for 20 min. Next, the absorbance of the plate was read at 490 nm and the viability rate was calculated with respect to control and lysed values.

3.8.9 Cell Count

Total cell count was performed with Trypan blue staining and a Neubauer counting chamber. Samples were diluted 1:5 with PBS and 1:2 with Trypan blue. Cell count was performed using an inverted microscope.

3.8.10 *In vivo* Experiments

Experimental animals: all procedures involving the use of research animals were approved by the Research Committee of the University Clinical Hospital of Santiago de Compostela (Spain) and were performed according to the “Principles of Laboratory Animal Care” (NIH publication No. 86-23, revised 1985), as well as specific Spanish (RD 1201/2005 and RD 53/2013) and European Union (Directives 86/609/CEE, 2003/65/CE, 2010/63/EU) regulations.

Male Wistar rats (Harlan Laboratories, Barcelona, Spain) weighing 290 ± 10 g were kept in a controlled environment at 22 ± 1 °C and $60 \pm 5\%$ humidity, with 12:12 h light:darkness cycles and were fed ad libitum with standard diet pellets and tap water. All surgical procedures and MRI studies were conducted under Sevoflurane anesthesia (3–4%) using a carrier 65:35 gas mixture of N₂O: O₂.

Healthy animals ($n = 3$) were anesthetized and 2.5×10^5 **USPIO-GlcN** labeled MSCs suspended in 300 μ L of PBS were administered into the brain intra-arterially (perfusion rate: 20 μ L/min) through one of the external carotid and with the common carotid opened.

3.8.11 MRI Studies

All MRI studies were conducted using a 9.4 T MR system with 440 mT/m gradients and a combination of a linear birdcage resonator (7 cm in diameter) for signal transmission and a 2×2 surface coil array for signal detection. A quadrature volume coil (7 cm in diameter) was also used in phantom studies.

MRI post-processing was performed using ImageJ software.

3.8.12 Agar Phantoms

Agar phantoms were made following a previously described procedure²⁴² with 1×10^5 cells per condition. T_2^* -weighted and T_2 -weighted images were acquired 0, 2, 5, 8 and 12 days after the cell plantation.

T_2^* -weighted images were acquired using a multi-gradient echo (MGE) sequence with 4.44 ms echo time, 1.8 s repetition time, 16 echoes with 6.75 ms echo spacing, implemented with a flip angle (FA) of 30° , 14 slices, 2 averages, field of view (FOV) of $7.5 \times 7.5 \text{ cm}^2$, and a matrix size of 256×256 . T_2 -weighted images were acquired using a multi-slice multi-spin-echo sequence (MSME) with 10.44 ms echo time, 3 s repetition time, 16 echoes with 10.4 ms echo spacing, implemented with a FA of 108° , 14 slices, 1 average, FOV of $7.5 \times 7.5 \text{ cm}^2$, and a matrix size of 256×256 .

3.8.13 *In vivo* MRI

In order to assess **USPIO-GlcN** labeled MSCs *in vivo*, animals were scanned following T_2 -weighted and T_2^* -weighted sequences in MRI to evaluate the presence and the distribution of injected cells at 1 h, and 1, 5 and 8 days after the injection.

T_2^* -weighted images were acquired using a MGE sequence with a 2.9 ms echo time, 1.5 s repetition time, 16 echoes with 3.28 ms echo spacing, implemented with a FA of 30° , 14 slices, 2 averages and with a $19.2 \times 19.2 \text{ mm}^2$ FOV, a 192×192 image matrix (isotropic in-plane resolution of $100 \mu\text{m}/\text{pixel} \times 100 \mu\text{m}/\text{pixel}$). T_2 -weighted images were acquired using a MSME sequence with a 9 ms echo time, 3 s repetition time, 16 echoes with 9 ms echo spacing, implemented with a FA of 180° , 2 averages, 14 slices of 1 mm and $19.2 \times 19.2 \text{ mm}^2$ FOV, a 192×192 image matrix (isotropic in-plane resolution of $100 \mu\text{m}/\text{pixel} \times 100 \mu\text{m}/\text{pixel}$).



CHAPTER 4

4 Clickable Iron Oxide Nanoparticle: Towards Responsive Controlled Release and Targeting



4.1 INTRODUCTION

The low-cost production, high biocompatibility, and great magnetic response of iron oxide NPs are desired properties for their application in biomedicine. These properties depend on the composition, morphology, size of the inorganic core, and on the nature and the degree of coverage of the organic coating.³¹ Strategies for the functionalization of inorganic cores have been developed over the past years,²⁶ and efforts have been devoted to engineering NPs with multifunctional ligands on the surface to enable active tumor targeting, detection through different imaging modalities, and stimulus-driven cargo release.²⁴³

Despite of the potential of nanoparticles for biomedical applications, the biointerface between the synthetic nanomaterials and biological entities, such as macromolecules, cells, and tissues, remains unpredictable.¹⁴¹ Thus, NPs have faced several drawbacks for their application in medicine. First, their stability in biological fluids is not self-evident while being of fundamental importance to guarantee safe and successful therapies. Second, the interaction between nanoparticles and biomolecules governs the fate of the nanoparticles *in vivo*, and therefore limits the targeting performance of the engineered nanoparticles. Third, drug loading efficiencies should be higher than found to date to ensure effective drug delivery therapies.

New chemistry strategies for the functionalization and stabilization of iron oxide NPs are needed to move forward to the next generation of functionalized magnetic NPs with optimal drug loading, high colloidal stability in biological medium, and predictable interactions with biomolecules. Orthogonal reactions known as 'click chemistry' have outstanding characteristics such as broad scope, high yields, no need of chromatographic purifications, and they give access to stereospecific products.⁴³

NPs display distinctive characteristics from small molecules and bulk materials, such as the size, magnetic properties, solubility, etc. that complicate their physicochemical characterization. Due to the limitations in the characterization and purification of NPs, click reactions constitute an ideal scenario for their functionalization towards biomedical applications.

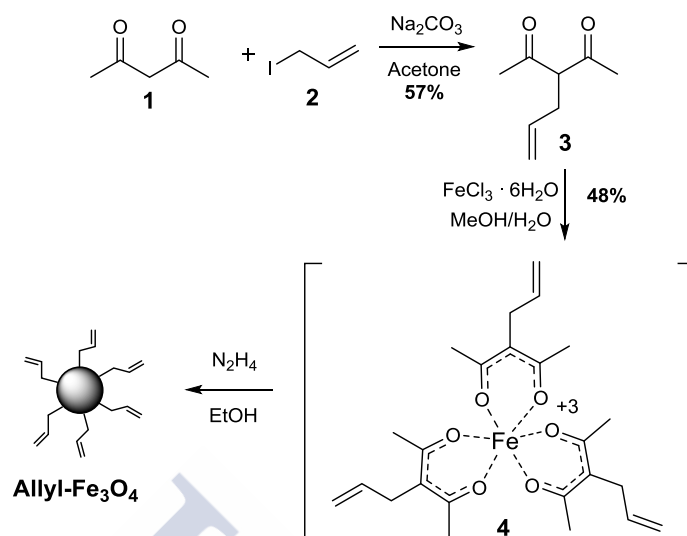
The objective of the work described in this Chapter was to gain access to multifunctional systems based on iron oxide NPs by decorating their surface with organic moieties that can undergo reactions with a wide range of substances through orthogonal procedures. The final goal was to produce NPs bearing both targeting molecules and moieties with thermosensitive bonds that release their cargo with increased temperature.

4.2 ALLYL-FUNCTIONALIZED IONS

In order to obtain multifunctional systems, the surface of IONs was to be decorated with organic moieties. The first approach for the attachment of functional groups to the surface of IONs relied on the modification of the Fe precursor followed by the formation of IONs by the co-precipitation method.²⁴⁴ In this approach, the ION precursor iron acetylacetonate complex was modified with an allylic group in order to take advantage of the well-known thiol-ene chemistry at a later stage.²⁴⁵

For that purpose, acetylacetonone (**1**), a common bidentate chelating ligand, was substituted with an allylic group (Scheme 9). In the first step, the α -position between the two carbonyls in **1** ($pK_a \sim 10$) was deprotonated using sodium carbonate followed by nucleophilic substitution of allyl iodide (**2**) to yield 3-allylacetylacetonate (**3**).²⁴⁶ The reaction proceeded with a fair yield of 57% due to the emergence of a side product identified as 3,3 di(allyl) acetylacetonone. Then, iron(III) 3-allylacetylacetonate (**4**) was obtained by heating Fe (III) chloride salt at 80 °C in the presence of ligand **3**.²⁴⁷ The formation of **Allyl-Fe₃O₄** occurred by reducing the Fe (III) complex **4** with hydrazine.²⁴⁴

The inorganic core of **Allyl-Fe₃O₄** was characterized by TEM, showing NPs with core sizes of 7 ± 5 nm and a spherical shape (Figure 49). The size distribution and the morphology of the NPs are not well controlled in co-precipitation synthesis, but this method is the simplest and cheapest option for the synthesis of IONs.



Scheme 9: Synthetic procedure for Allyl-Fe₃O₄.

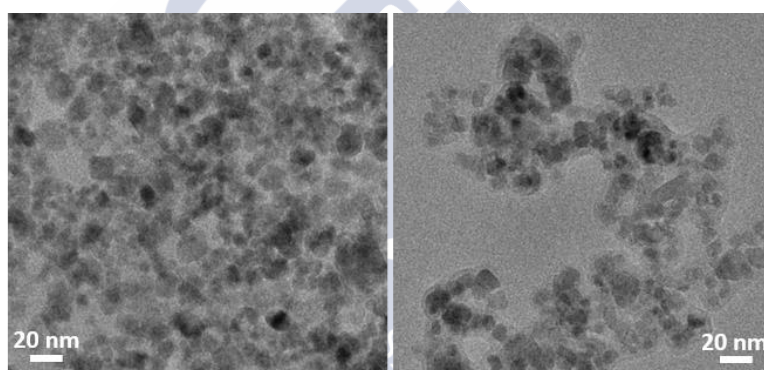


Figure 49: TEM images of Allyl-Fe₃O₄.

The organic coating was characterized by IR, TGA, and elemental analysis to verify the existence of the allylic groups. The IR spectrum (Figure 50) showed a strong band at 587 cm^{-1} attributed to the vibration of Fe–O in the spinel structure of the IONs, but no bands were found for the allyl groups. This suggested the non-preservation of the allyl group after the formation of the NPs from iron (III) 3-allylacetylacetonate (**4**), possibly due to the loss of the chelating ligand during the reduction to Fe²⁺. This result was confirmed by the quantification of the organic coating by TGA and elemental analysis (Figure 51). TGA showed an organic coating coverage of less than 10 wt%, and elemental analysis showed a carbon content of around 2% (Table 13). Consequently, it was concluded that NP functionalization using a functionalized Fe precursor failed, and therefore a new strategy was chosen based on the functionalization of already prepared IONs.

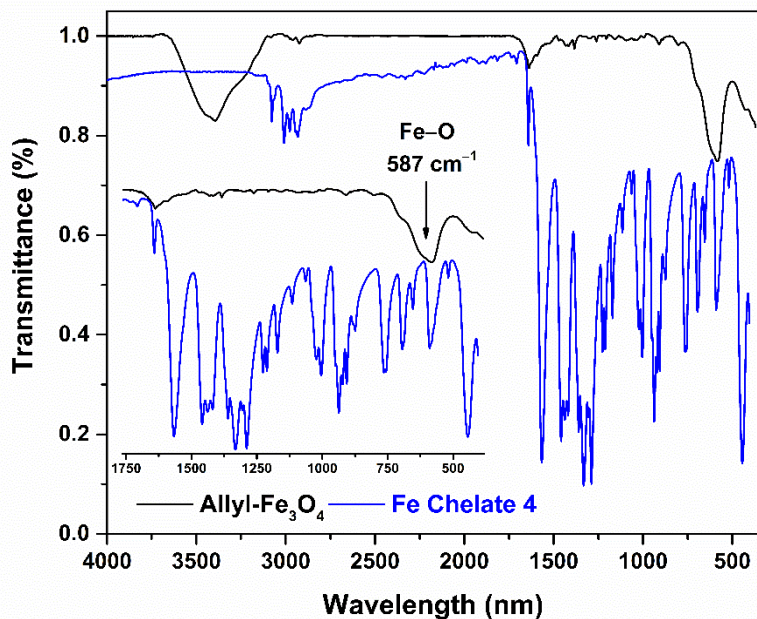


Figure 50: IR spectrum of $\text{Allyl-Fe}_3\text{O}_4$ (black) compared to Fe chelate 4 (blue). Inset with a zoom in the region of vibrations from the organic moieties.

Table 13: Elemental analysis of $\text{Allyl-Fe}_3\text{O}_4$.

	%N	%C	%H
$\text{Allyl-Fe}_3\text{O}_4$	0.26	1.93	0.45

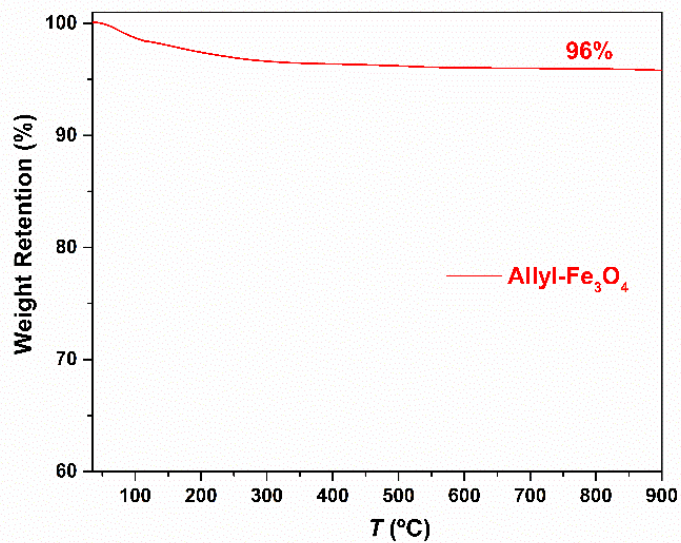


Figure 51: TGA of $\text{Allyl-Fe}_3\text{O}_4$.

4.3 NAKED ION SYNTHESIS

The next approach for NP functionalization relied on the modification of the surface of already formed ION. Licandro and coworkers²⁴⁸ recently reported a new strategy for the functionalization of nanoparticles based on the formation of carbamates upon reaction between the hydroxyl groups on the NP surface and isocyanate ligands. The advantage of this strategy is in its versatility because the isocyanate moiety can react with different types of NPs bearing moieties with nucleophilic character on the surface. Therefore, these functional groups can be attached to different kind of NPs.

In order to prepare naked magnetite NPs bearing hydroxyl groups on the surface, the synthesis was performed without surfactants in water with the method of Stroeve and coworkers.²⁴⁹ Chloride salts of Fe (II) and Fe (III) were treated with an aqueous solution of sodium hydroxide at pH 11. Purification was simply performed by magnetic separation and replacing the reaction mixture with fresh water.

TEM images of naked IONs showed a spherical core morphology with an average size of 6 ± 3 nm, which is a core size within the superparamagnetic region (Figure 52).

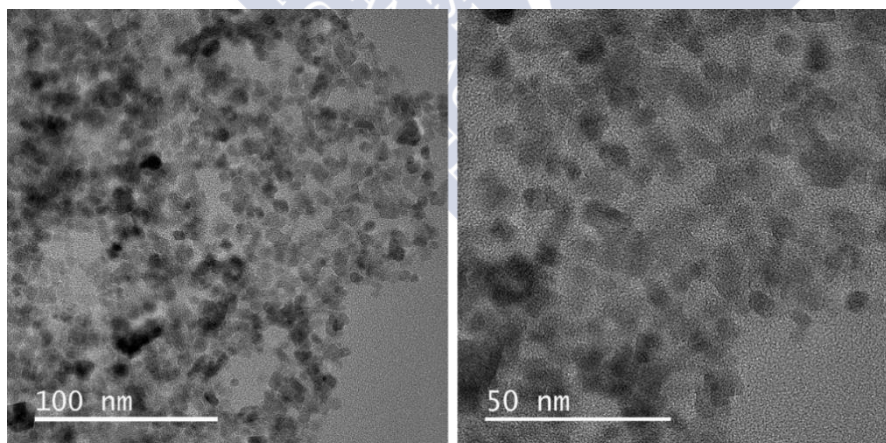


Figure 52: TEM images of naked IONs synthesized through the co-precipitation method.

When IONs are in water, their surface is covered with hydroxyl groups because iron atoms act as Lewis acids and coordinate water molecules on the surface.²² The protonation state of the hydroxyl groups on the surface of IONs is affected by the pH of the water-containing solution. The nucleophilic character of the hydroxyl groups governs the reactivity with isocyanates ligands. Therefore, the ζ -potential of IONs,

which is related with the surface charge of the NPs, was evaluated at different pH values to foresee the reactivity of hydroxyls as nucleophiles. The solution of IONs in water was set to different pH values by adding different amounts of 1 M solution of either NaOH or HCl. The measurement of ζ -potential was performed by DLS after the stabilization of the pH (Figure 53). The IONs set to pH around 7 showed instantaneous agglomeration that hampered the measurement of ζ -potential, and NPs with ζ -potential in the neutral range, i.e. pH set from 6.5 to 8, showed massive agglomeration after storage overnight at those pH values; indicating that naked IONs are mainly stabilized by electrostatic repulsions. As expected,²¹ the ζ -potential results showed that IONs at acidic pH are positively charged with values of +20 mV at pH 2; and at basic pH are negatively charged with values of -90 mV at pH 12. Therefore, the protonated hydroxyl groups on IONs at acidic pH are less reactive against isocyanates as there are non-nucleophilic, as oppose to the deprotonated hydroxyl moieties at basic pH. This information is important to foresee the reactivity of hydroxyl groups and it will be further discussed in this Chapter in the section *ION Functionalization with Isocyanates*.

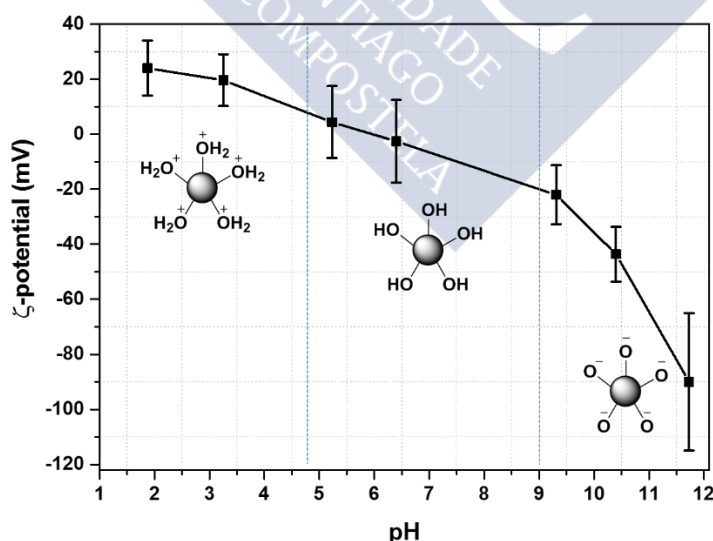


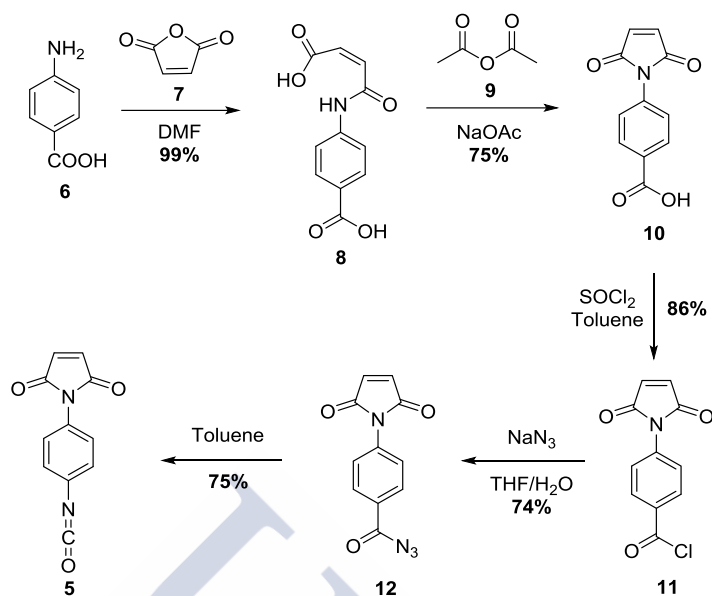
Figure 53: ζ -Potential measurements of naked IONs at varying pH. Results are represented as the mean value of five consecutive measurements with their SD.

4.4 ISOCYANATES FOR ION FUNCTIONALIZATION

4.4.1 Synthesis of Isocyanate Ligands

Two different moieties were chosen to decorate the surface of IONs in order to have two possibilities for the functionalization: maleimide and alkyne. The maleimide moiety offers reactivity in the thermally reversible Diels–Alder cycloaddition which opens the possibility to induce the release of molecules of interest by heating,⁵⁵ while also being a substrate for thiol–yne click reactions.²⁴⁵ On the other hand, the alkyne moiety enables functionalization with copper-catalyzed alkyne–azide cycloaddition (CuAAC), which offers an easy and reproducible way of functionalization with a wide variety of commercially available azides.²⁵⁰

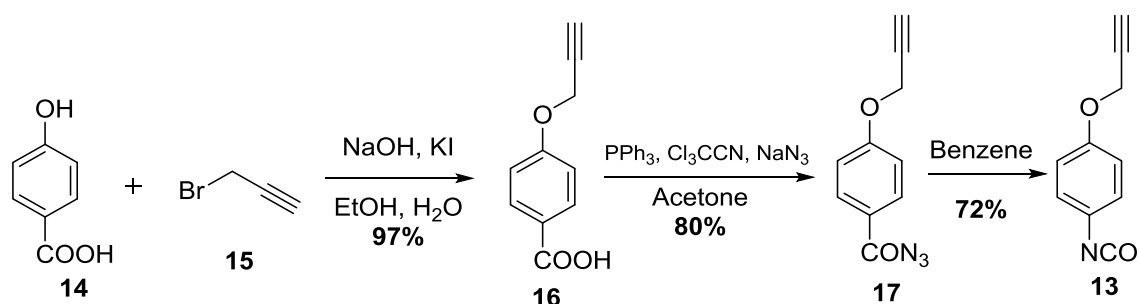
The synthesis of literature-known 4-maleimidophenyl isocyanate²⁵¹ (**5**) started with the reaction of 4-aminobenzoic acid (**6**) and maleic anhydride (**7**) (Scheme 10). Then, carboxylic acid **8** was dehydrated to form a five-membered ring upon treatment with acetic anhydride (**9**) under basic conditions. The carboxylic acid in **10** was transformed into acyl chloride **11** using thionyl chloride, and purified by crystallization in a solvent mixture of dried hexane/acetone (1:3). Acyl azide **12** was obtained by the subsequent nucleophilic substitution of the chloride in **11** with sodium azide. In the final step, Curtius rearrangement of acyl azide **12** gave maleimidophenyl isocyanate **5**. In summary, 4-maleimidophenyl isocyanate (**5**) was obtained in five steps with an overall yield of 35%, and all intermediates were obtained without the need of chromatographic purifications. Maleimidophenyl isocyanate **5** was kept under N₂ to avoid hydrolysis by atmospheric water.



Scheme 10: Synthetic route for 4-maleimidophenyl isocyanate (5).

Alkyne isocyanate **13** was obtained in three steps starting from 4-hydroxybenzoic acid (**14**) that was reacted with propargyl bromide (**15**) to give carboxylic acid **16** (Scheme 11). The conversion of the carboxylic acid in **16** was possible in only one step by the *in situ* transformation to acyl chloride and the following substitution with sodium azide which afforded the acyl azide **17** in 80% yield.²⁵²

The transformation of **17** to alkyne isocyanate **13** was performed by Curtius rearrangement in benzene as a solvent to lower the temperature of the transformation to 80 °C due to the side reactions observed at 110 °C with toluene as solvent. Alkyne isocyanate **13** was successfully synthesized in three steps with an overall yield of 55% and stored under N₂ due to its sensitivity against water.



Scheme 11: Synthetic route for the alkyne isocyanate 13.

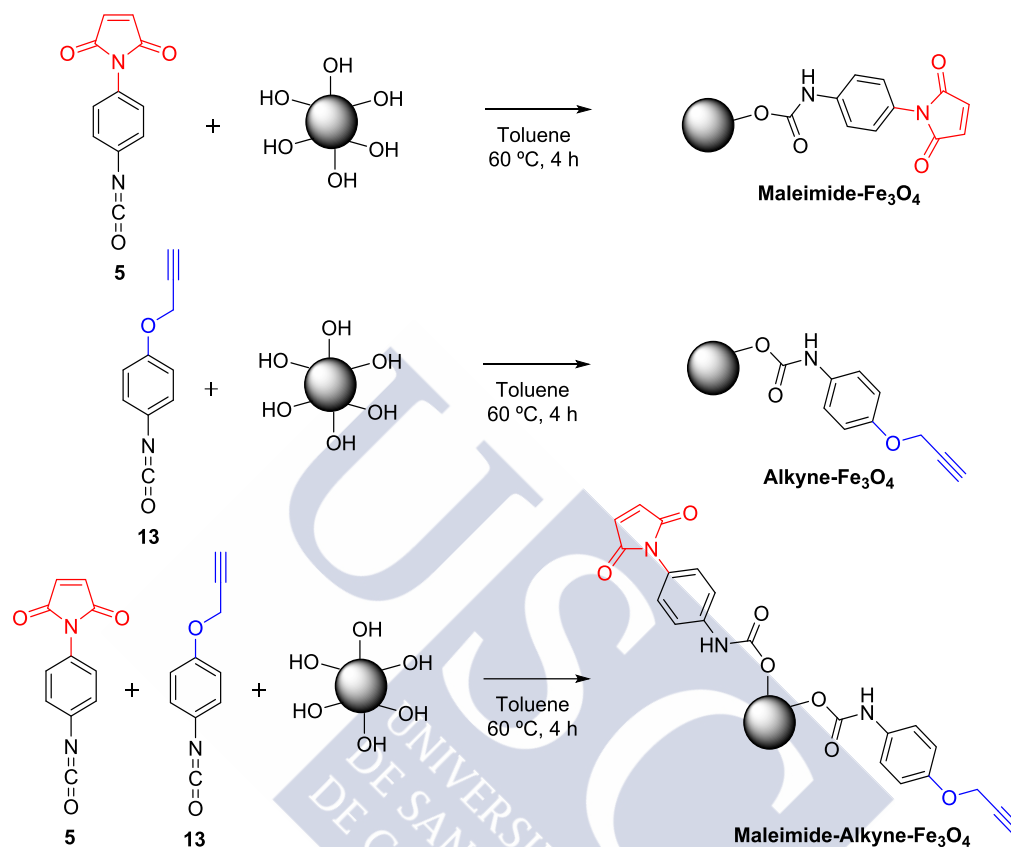
4.4.2 ION Functionalization with Isocyanates

With the ligands in hand, the functionalization of naked IONs was performed with maleimide isocyanate **5**, alkyne isocyanate **13**, and with an equimolar mixture of isocyanates maleimide **5** and alkyne **13** in order to obtain nanoparticles with two orthogonal groups allowing for the attachment of both drugs and targeting molecules. The first functionalization of IONs with isocyanates was described by Licandro and coworkers,²⁴⁸ and they performed the reaction in toluene at 60 °C under sonication to ensure the dispersion of naked IONs. Therefore, we first investigated the reactions under these conditions (Scheme 12). We found two key factors influencing the success of the nanoparticle functionalization with the isocyanate ligands. First, prior to the functionalization reaction, IONs were dispersed in water and the pH of the solution set to a specific value to determine the degree of protonation of the hydroxyl groups on the IONs, as showed by the ζ -potential measurements discussed earlier (Figure 53). For the reaction with the isocyanate containing molecules to work the most efficiently, it was found that the pH of the solution containing the nanoparticles must be set around 7 before evaporation of the solvent, to avoid free hydroxide ions and to ensure nucleophilicity of the surface.

The second key factor is the selection of solvent for the reaction between the NPs and the isocyanate ligands. The reaction between the NPs and the isocyanate ligands was attempted in DMSO. The TGA results showed no increment in the organic material and no bands from the isocyanate ligand were found by IR spectroscopy. A possible explanation for the failure of the reaction could be the Lewis basic character of DMSO. The solvent molecules can coordinate to the ION surface, thus impeding the reaction. For the reaction to work, the NPs were transferred to a solvent with non-Lewis basic character. Therefore, toluene was maintained as the solvent of choice to perform the functionalization.

In all cases, the functionalized nanoparticles were purified by centrifugation washing three times with toluene and three times with diethyl ether, and characterized by IR spectroscopy, thermogravimetric assay, elemental analysis, and nuclear magnetic resonance. The characterization of conjugates in the nanoscale is not straightforward;

therefore, the characterization of **Maleimide-Fe₃O₄** and **Alkyne-Fe₃O₄** was performed first to ensure the success of the functionalization.



Scheme 12: Functionalization of naked iron oxide nanoparticles with maleimide isocyanate **5**, with alkyne isocyanate **13**, and with a 1:1 mixture of maleimide and alkyne isocyanate ligands.

The IR spectrum of **Maleimide-Fe₃O₄** (Figure 54) featured vibrational bands at 3300, 1602, and 1240 cm^{-1} corresponding to the stretching peaks of N–H, C=O, and C–O of the carbamate moiety, respectively. Additionally, the band at 2306 cm^{-1} , corresponding to the N=C=O stretching of ligand **5**, disappeared after the reaction with the NPs. This suggests the successful reaction between the isocyanate maleimide **5** and the hydroxyl groups on the surface of the IONs. **Alkyne-Fe₃O₄** (Figure 55) showed the characteristics bands at 2900, 1520, 1239, and 571 cm^{-1} , corresponding to the stretching of $\text{C}\equiv\text{C}$ -, C=O, C–O, and Fe–O, respectively. At the same time the vibrational band at 2278 cm^{-1} , corresponding to the functional group NCO, disappeared after reaction between NPs and ligand **13**. This result again suggests the success of the reaction between the hydroxyl groups on IONs and isocyanate **13**.

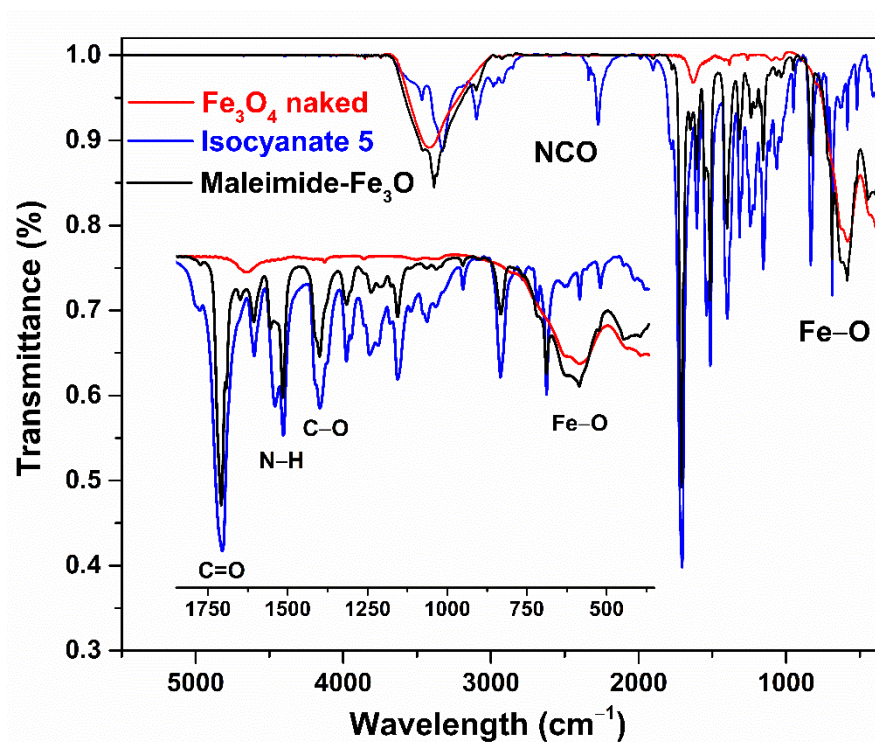


Figure 54: IR spectrum of maleimide isocyanate 5 (blue), naked Fe_3O_4 (red), and Maleimide- Fe_3O_4 (black).

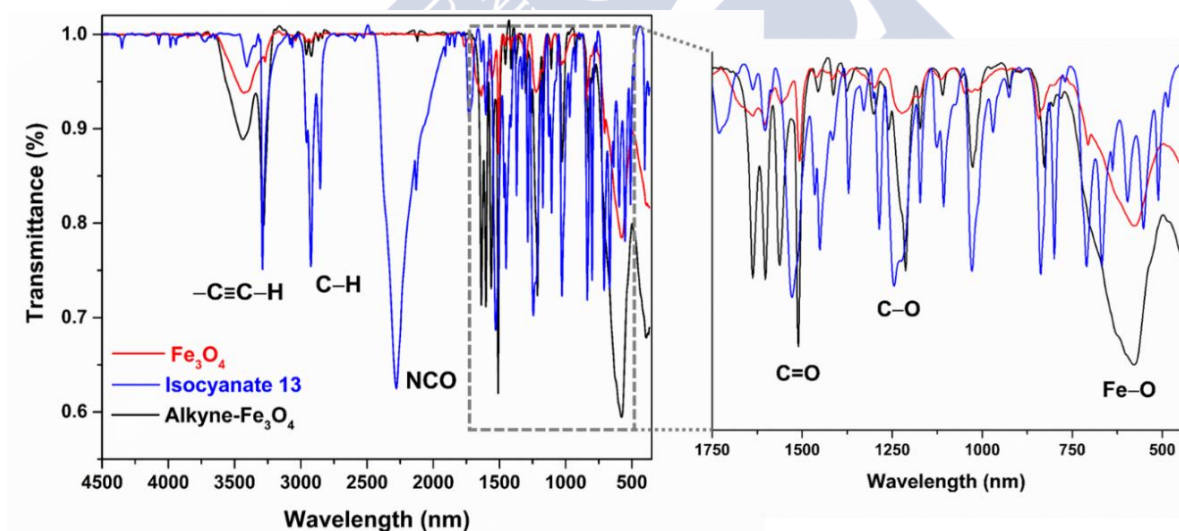


Figure 55: IR spectrum of alkyne isocyanate 13 (blue), naked Fe_3O_4 (red), and Alkyne- Fe_3O_4 (black).

Maleimide-Alkyne- Fe_3O_4 featured mixed bands from both maleimide and alkyne ligands that were difficult to assign to one particular moiety, with the exception of the strong vibration band at 2900 cm^{-1} due to the stretching of the alkyne moiety (Figure 56).

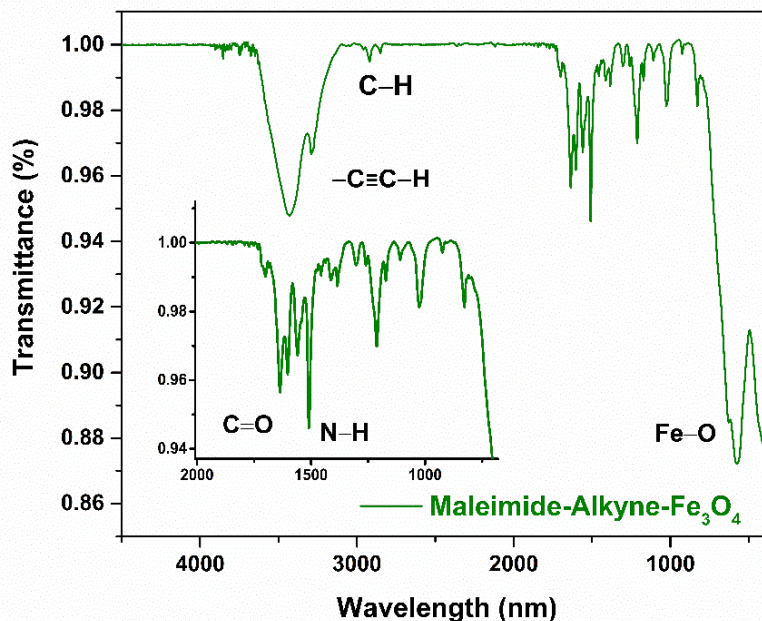


Figure 56: IR spectrum of Maleimide-Alkyne-Fe₃O₄ (green).

TGA measurements were performed in order to quantify the amount of organic content in **Maleimide-Fe₃O₄**, **Alkyne-Fe₃O₄**, and **Maleimide-Alkyne-Fe₃O₄**. The results (Figure 57) showed naked Fe₃O₄ with the lowest organic content as expected, featuring a weight retention of 97 wt%. **Maleimide-Fe₃O₄** showed a weight retention of 51 wt% and **Alkyne-Fe₃O₄** of 63 wt%. On the other hand, **Maleimide-Alkyne-Fe₃O₄** featured the highest organic content with 36 wt%, which may be due to placing the double molar amount of ligands for the reaction mixture. This result is in agreement with the findings of Licandro and coworkers,²⁵³ who found the relation of a higher loading of organic material with a higher amount of reacting isocyanate. Both **Maleimide-Fe₃O₄** and **Alkyne-Fe₃O₄** featured two strong weight losses, at 200 and 600 °C for **Alkyne-Fe₃O₄** and at 350 and 700 °C for **Maleimide-Fe₃O₄**. Interestingly, **Maleimide-Alkyne-Fe₃O₄** showed at least three strong weight losses at 200, 350, and 700 °C, suggesting the presence of both maleimide and alkyne moieties on the NPs.

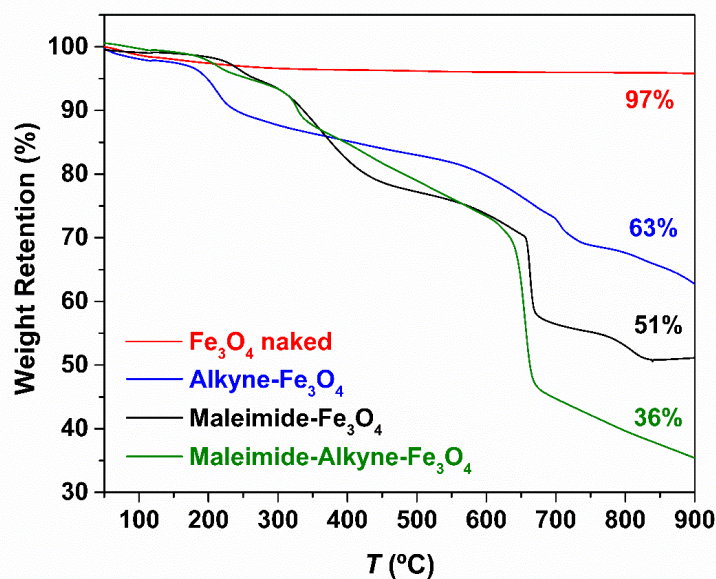


Figure 57: TGA of naked Fe_3O_4 (red), Alkyne- Fe_3O_4 (blue), Maleimide- Fe_3O_4 (black), and Maleimide-Alkyne- Fe_3O_4 (green).

Elemental analysis measurements of the samples (Table 14) were found to be in agreement with the TGA results. **Maleimide-Alkyne- Fe_3O_4** contains the most organic material, followed by **Maleimide- Fe_3O_4** and **Alkyne- Fe_3O_4** . Notably, the N% is higher in **Maleimide- Fe_3O_4** when compared to **Alkyne- Fe_3O_4** , in agreement with the chemical structure of the maleimide group that contains one additional N atom. The total molar organic content of **Maleimide- Fe_3O_4** is 37.3%, which corresponds to 1.73 mmol of maleimide ligand per g of NP, and is in good agreement with the results of Licandro and coworkers.²⁵³ For **Alkyne- Fe_3O_4** the total molar organic content was 31.6%, corresponding to 1.81 mmol of ligand per g of NP. **Maleimide-Alkyne- Fe_3O_4** has two ligands on the surface and it is therefore not possible to calculate the percentage of each ligand by elemental analysis.

Table 14: Elemental analysis measurements for naked Fe_3O_4 , Maleimide- Fe_3O_4 , Alkyne- Fe_3O_4 , Maleimide-Alkyne- Fe_3O_4 , and the theoretical values for the Maleimide and Alkyne ligands attached to the NPs.

Sample	% C	% H	% N
Fe_3O_4	0.054	0.460	-
Maleimide-Fe_3O_4	23.10	1.27	4.28
Maleimide ligand	61.4	3.28	13.02
Alkyne-Fe_3O_4	18.90	1.86	2.38
Alkyne ligand	68.96	4.63	8.04
Maleimide-Alkyne-Fe_3O_4	36.06	2.23	6.47

NMR measurements were performed with the three samples to confirm the integrity of the ligands on the nanoparticle. For **Maleimide- Fe_3O_4** , the spectrum (Figure 58) featured a singlet at 8.88 ppm corresponding to the N–H proton, a pair of doublets in the aromatic region at 7.55 and 7.23 corresponding to the phenyl protons, and a singlet at 7.15 ppm corresponding to the protons of the double bond in the maleimide moiety. These data are in agreement with the work of Licandro and coworkers.²⁵³

On the other hand, the proton spectrum of **Alkyne- Fe_3O_4** (Figure 59) featured a peak at 8.45 ppm corresponding to the N–H proton, a pair of broad signals at 7.37 and 6.91 ppm corresponding to the phenyl protons, and a singlet at 4.74 corresponding to the CH_2 in α -position to the alkyne. Notably, for both samples, the presence of the N–H proton indicates the formation of the carbamate on the NP surface.

The ^1H NMR spectrum of **Maleimide-Alkyne- Fe_3O_4** (Figure 60) featured the proton signals with the same chemical shifts as those for pure **Maleimide-** and **Alkyne- Fe_3O_4** samples, but the signals corresponding to N–H were found as duplicate. This could be the result of the formation of dimers on the NP surface: homodimers would contribute one N–H signal each, whereas heterodimers would result in two additional N–H signals. However, more studies would be necessary to prove the dimer formation.

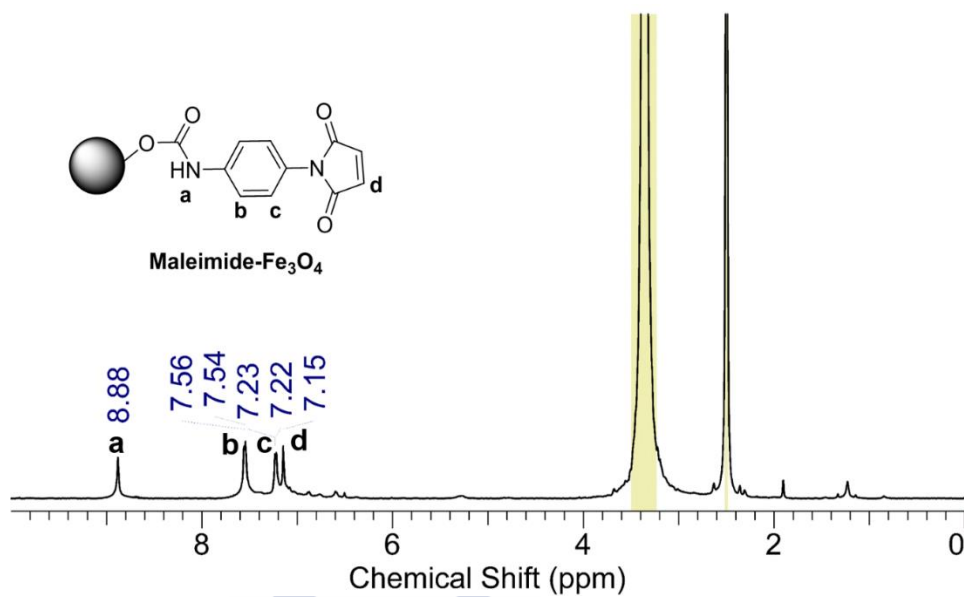


Figure 58: ¹H NMR spectrum (500 MHz, DMSO) of Maleimide-Fe₃O₄.

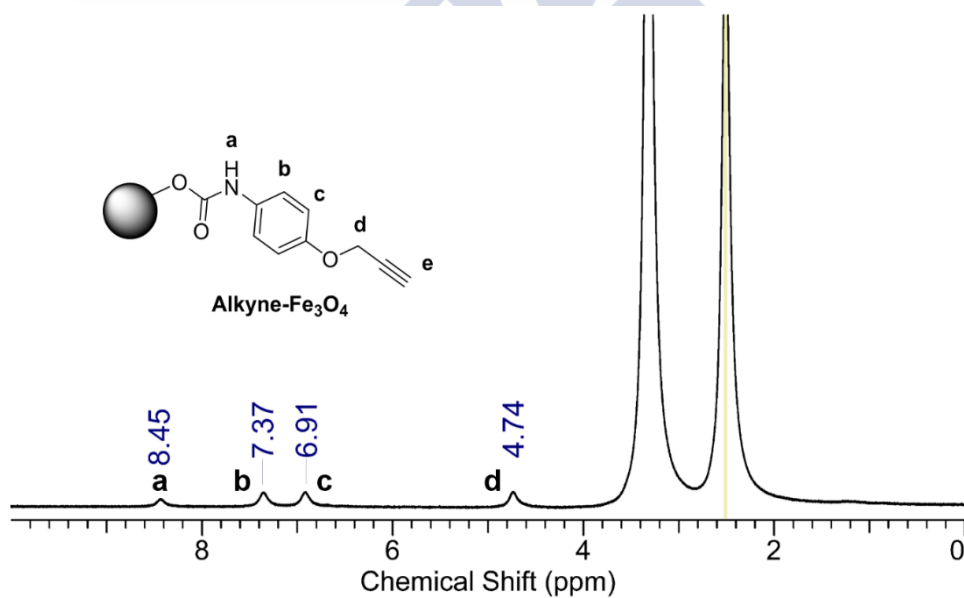


Figure 59: ¹H NMR spectrum (500 MHz, DMSO) of Alkyne-Fe₃O₄.

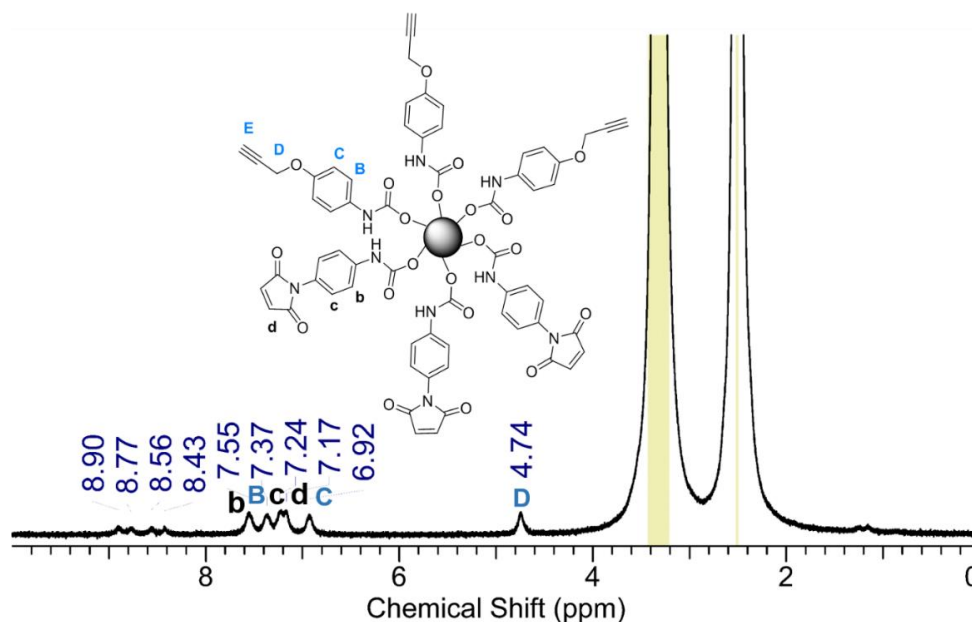


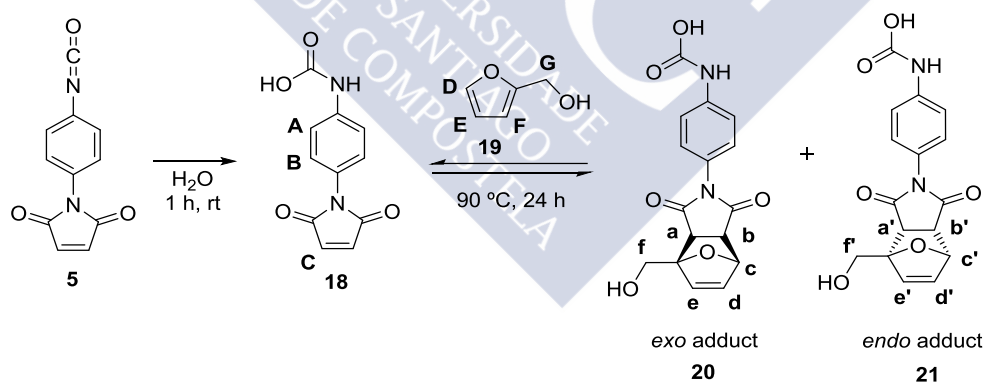
Figure 60: ^1H NMR spectrum (500 MHz, DMSO) of Maleimide-Alkyne- Fe_3O_4 .

In summary, the reaction between the NPs and maleimide isocyanate **5**, alkyne isocyanate **13**, and their molar mixture took place, as confirmed by IR spectroscopy, TGA, elemental analysis, and NMR. The efficiency of the reaction could not be calculated, as it was not possible to quantify the hydroxyl groups available in the surface of naked IONs.

4.4.3 Model Reactions

In order to find appropriate reaction conditions for the functionalization of the maleimide and alkyne moieties on the surface of IONs, both Diels–Alder and CuAAC reactions were studied first in the absence of magnetic nanoparticles to facilitate characterization procedures. The Diels–Alder reaction has been known for over 50 years in the literature.²⁵⁴ The diene and dienophile can be tuned to form a cyclized product able to undergo a retrocyclization, which results in a reversible reaction.⁵⁶ Diels–Alder reaction has the desirable characteristic to be self-contained, i.e. all the atoms present in the diene and dienophile are kept in the resulting products, meaning that the displacement of the equilibrium is governed by temperature, solvent, or reactant concentration, but not by outsider molecules such as water, metal catalyst, or base/acid.⁵⁶

The reversibility of the Diels–Alder reaction is key to achieve a temperature-controlled release with IONs. Due to the difficulties in the characterization of IONs, the reactivity was first studied on a carbamate mimic rather than the functionalized IONs. For that purpose, maleimide isocyanate **5** was hydrolyzed in water to give access to maleimide carbamic acid **18** (Scheme 13). Then, the reactivity of the maleimide moiety of carbamate **18** was investigated with 2-furfuryl alcohol (**19**) as diene (Scheme 13). The Diels–Alder reaction in pure furfuryl alcohol as solvent was found to take place after 24 h at 90 °C, resulting in the *exo* and *endo* adducts **20** and **21** in an estimated ratio of 1:1. The reversibility of the reaction was tested by heating the mixture to 90 and 120 °C to induce the retro-Diels–Alder reaction. The adducts **20** and **21** showed instantaneous temperature-sensitive behavior as shown by the disappearance of their signals while the signals for furfuryl alcohol and maleimide carbamate were recovered in NMR measurements (Figure 61). This confirms the thermal response of adducts based on the carbamic acid **18** and furfuryl alcohol **19**, and shows promise for IONs functionalized through Diels–Alder reaction to display properties of thermo-controlled release.



Scheme 13: Maleimide isocyanate **5** hydrolyzed with water to give access to carbamic acid **18**. Model Diels–Alder reaction with carbamic acid **18** and furfuryl alcohol **19** to yield thermo-sensitive adducts **20** and **21**.

Jegat and Mignard²⁵⁵ studied the Diels–Alder reaction of *N*-phenylmaleimide and furfuryl alcohol, and found that the *exo* adduct is the thermodynamic product and the *endo* adduct is the kinetic one, therefore, the *endo* adduct needed lower temperature to proceed in the retro-Diels–Alder reaction than the *exo* adduct. However, for the aim

of this project the adducts were employed as a mixture due to the expected difficulties in controlling the synthesis and the purification to obtain pure *endo* and *exo* adducts.

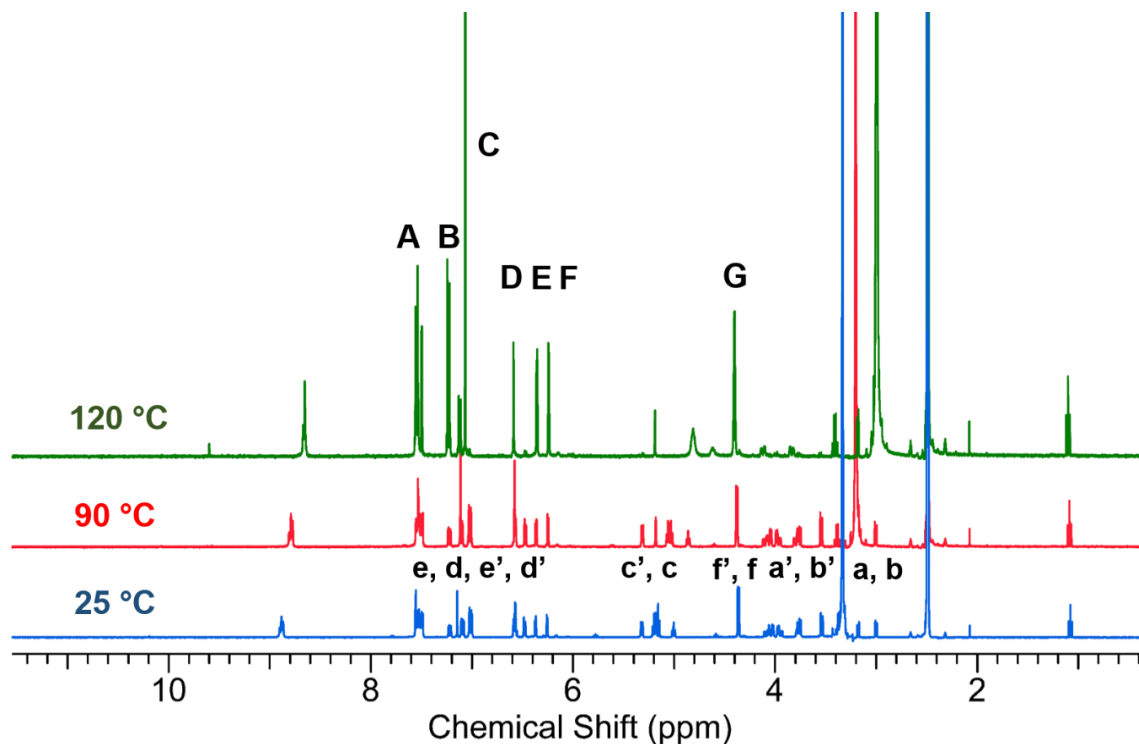
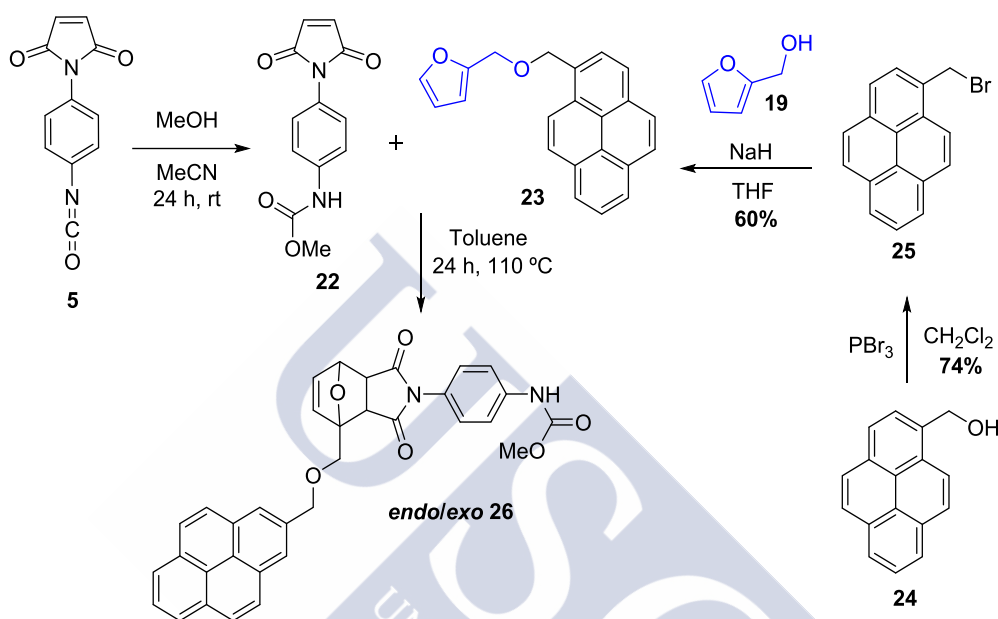


Figure 61: ^1H NMR spectra (400 MHz, DMSO) of Diels–Alder adducts acquired at different temperatures (25, 90, and 120 °C). The disappearance of the signals from the *exo* (a–f) and *endo* (a'–f') adducts and the appearance of the signals from carbamate **18** (A–C) and furfuryl **19** (D–G) indicates that the retro-Diels–Alder reaction took place in the NMR tube. For the assignment of the proton signals, see Scheme 5.

The second parameter studied was the solvent for the Diels–Alder transformation. Apart from pure furfuryl alcohol, the reaction between carbamic acid **18** and furfuryl alcohol **19** was proven to happen in dichloromethane, but in solvents such as toluene and DMSO, carbamic acid **18** was not soluble. In order to determine if the reaction could also run in toluene, maleimide isocyanate **5** was hydrolyzed with methanol to yield methoxy carbamate **22**, where the methyl group was expected to improve the solubility. To quantify the amount of released molecules with fluorescence, pyrene was selected to be attached to a furan moiety. The novel furan pyrene **23** was synthesized in two steps with an overall yield of 44% (Scheme 14). First, commercially available pyrenemethanol **24** was reacted with phosphorus tribromide under anhydrous conditions to yield pyrene bromide **25**. In the second step, the substitution of bromide with furfuryl alcohol (**19**) was performed with sodium hydride as a base to yield furan

pyrene **23**. Next, the Diels–Alder reaction between furfuryl pyrene **23** and methoxy carbamate **22** was studied with toluene as a solvent (Scheme 14). The NMR spectrum indicated the formation of both *endo* and *exo* adducts **26** after heating reflux the reaction mixture to in toluene for 24 h.



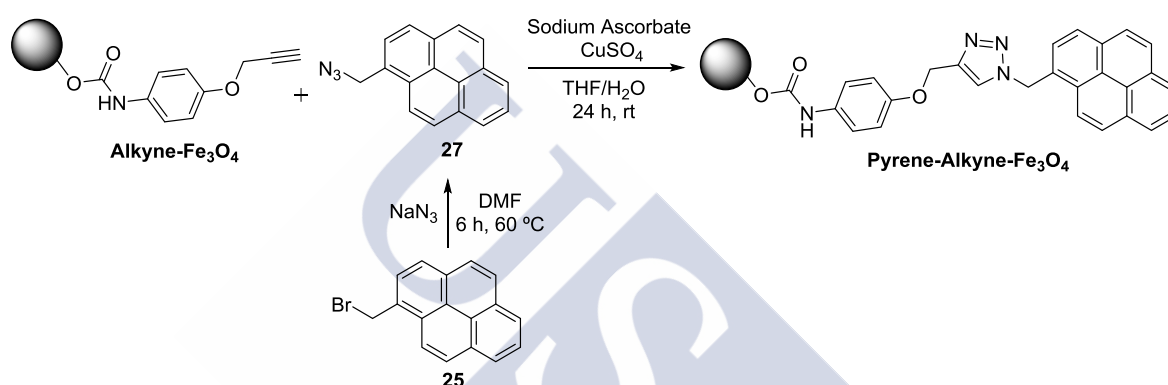
Scheme 14: Diels–Alder reaction between methoxy carbamate **22** and furan pyrene **23** in toluene. The synthetic route to yield furan pyrene **23** in two steps.

After the study of the Diels–Alder reaction with a model system, the retro-cycloaddition between 2-substituted furan pyrene **23** and maleimide carbamate **22** was shown to take place in the NMR tube after heating at 90°C , as suggested by the appearance of proton signals from furan pyrene **23** and maleimide **22**. Therefore, toluene was selected as the solvent for the corresponding reactions with the maleimide moieties on the surface of the IONs.

4.5 CLICK REACTIONS ON THE NP SURFACE

In order to optimize the reaction conditions for the double click reactions on **Maleimide-Alkyne-Fe₃O₄**, they were first tested with pure **Maleimide-Fe₃O₄** and **Alkyne-Fe₃O₄** using pyrene derivatives as the test system. **Alkyne-Fe₃O₄** was reacted with azide pyrene **27** in a mixture of THF and water (1:0.73) and with copper sulfate

and sodium ascorbate as catalysts (Scheme 15). The obtained **Pyrene-Alkyne-Fe₃O₄** was washed four times with the solvent mixture and the nanoparticles were subsequently collected by magnetic separation. **Pyrene-Alkyne-Fe₃O₄** dispersed in THF showed absorption bands in UV-Vis characteristic of the pyrene moiety (Figure 62). Additionally, TGA measurements showed an increase of 7 wt% in organic content after the functionalization of **Alkyne-Fe₃O₄** (Figure 63).



Scheme 15: CuAAC between **Alkyne-Fe₃O₄** and azide pyrene **27** in THF/H₂O with sodium ascorbate and copper sulfate as catalysts to yield **Pyrene-Alkyne-Fe₃O₄**.

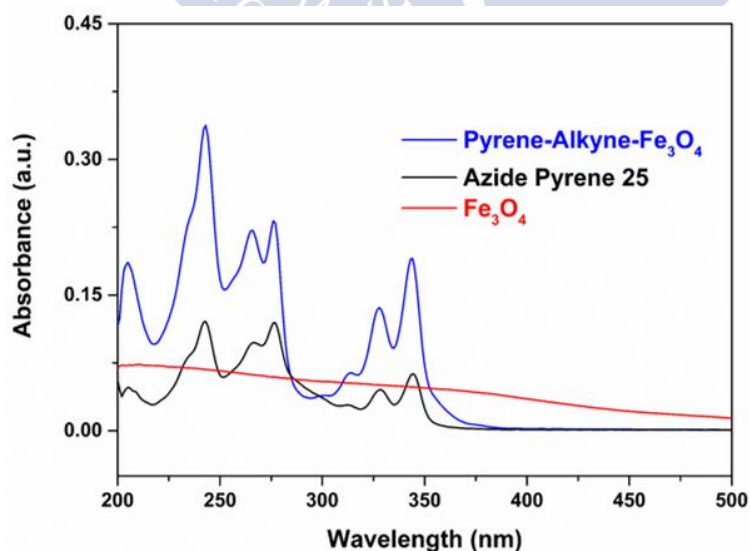


Figure 62: UV-Vis spectra of a solution of naked **Fe₃O₄**, azide pyrene **25** and **Pyrene-Alkyne-Fe₃O₄** in THF.

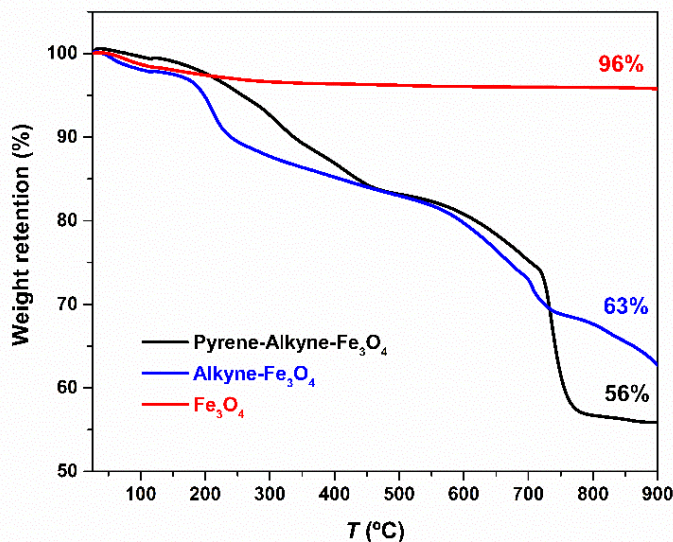
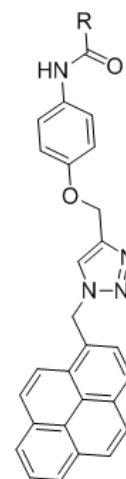


Figure 63: TGA measurements of naked Fe₃O₄ (red), Alkyne-Fe₃O₄ (blue) and Pyrene-Alkyne-Fe₃O₄ (black).

The analysis of the organic content was also performed by elemental analysis measurements (Table 15), and the data are in agreement with the TGA results. Pyrene-Alkyne-Fe₃O₄ showed a 3.7% molar increment in organic coating by elemental analysis.

Table 15: Elemental analysis of naked Fe₃O₄, Alkyne-Fe₃O₄, and Pyrene-Alkyne-Fe₃O₄. ^aTheoretical values for the pyrene clicked to the ION.

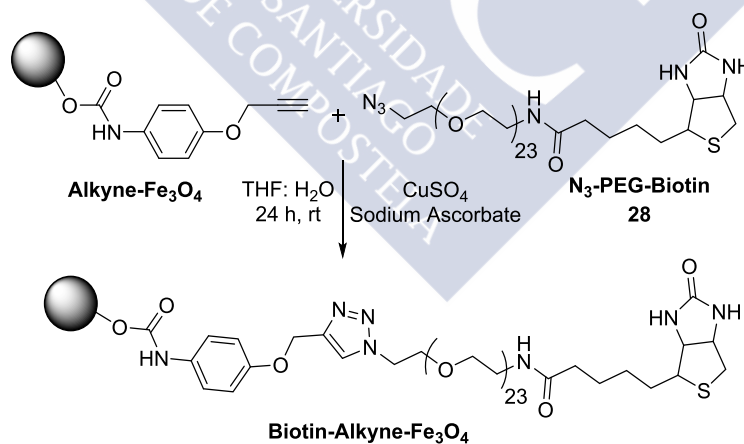
%	Fe ₃ O ₄	Alkyne-Fe ₃ O ₄	Pyrene-Alkyne-Fe ₃ O ₄	Pyrene ligand ^a
C	0.054	18.90	25.8	74.81
H	0.460	1.86	2.20	4.88
N	-	2.38	3.98	12.92



After the CuAAC reaction with the fluorophore, a further ligand, N₃-PEG-Biotin, was selected to functionalize Alkyne-Fe₃O₄ (Scheme 16). The biotin moiety was chosen due to its proven ability to target several tumors cells,² and 23 units of polyethylene

glycol was expected to enhance the solubility of the nanoparticles in water. The reaction between N₃-PEG-Biotin and **Alkyne-Fe₃O₄** was performed under the same conditions as chosen for azide pyrene **27**. After the reaction, TGA measurements showed an increase of 29 wt.% in organic content and two additional weight losses at 100 and 350 °C as compared with **Alkyne-Fe₃O₄** (Figure 64), indicating that the functionalization took place.

Biotinylation of proteins is a standard procedure and there are several commercially available kits to quantify the amount of attached biotin. In order to quantify the amount of biotin attached to **Alkyne-Fe₃O₄**, a commercial kit (Sigma Aldrich) was used based on the formation of a complex composed of 4-hydroxyazobenzene-2-carboxylic acid (HABA) and avidin, which possesses a strong absorbance at 500 nm. In the presence of biotin, HABA is displaced from the complex and the absorbance decreases. There is a linear relationship between the biotin concentration and the concentration of the HABA/avidin complex that can be quantified by UV-Vis spectroscopy (Figure 65). **Biotin-Alkyne-Fe₃O₄** was found to bear 88 μmol of N₃-PEG-Biotin ligand per g of NP.



Scheme 16: CuAAC between **Alkyne-Fe₃O₄** and **N₃-PEG-Biotin 28** in H₂O/THF to yield **Biotin-Alkyne-Fe₃O₄**.

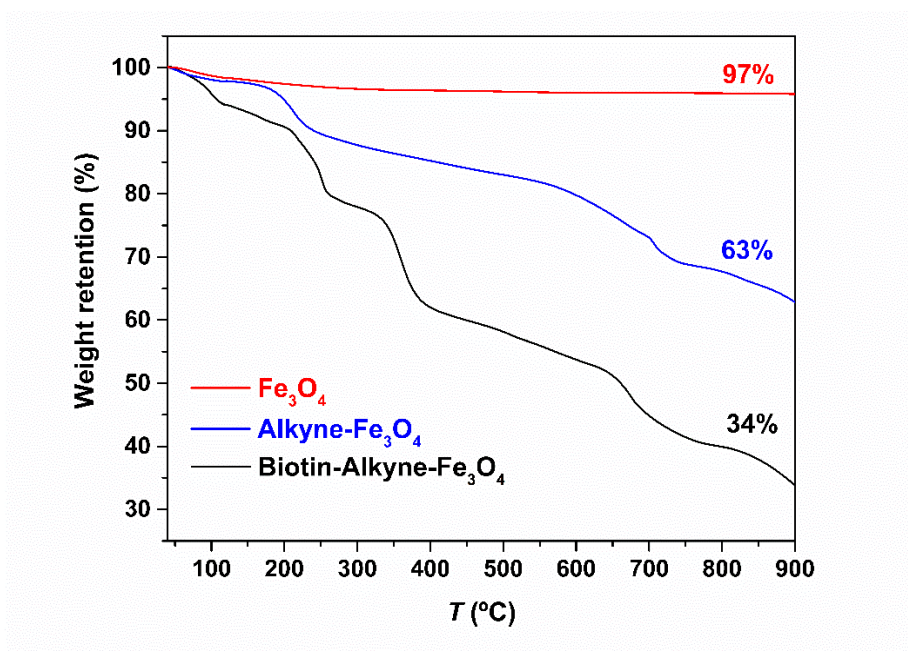


Figure 64: TGA measurements of naked Fe₃O₄ (red), Alkyne-Fe₃O₄ (blue) and Biotin-Alkyne-Fe₃O₄ (black).

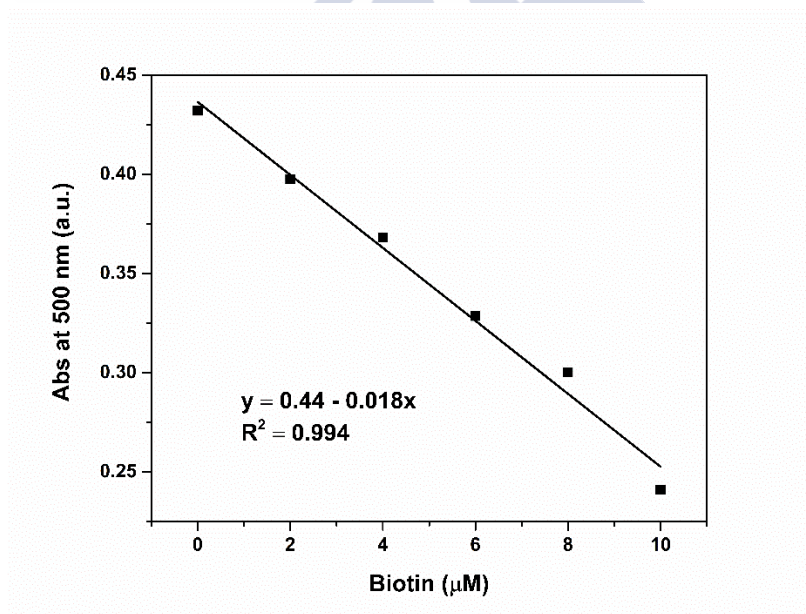
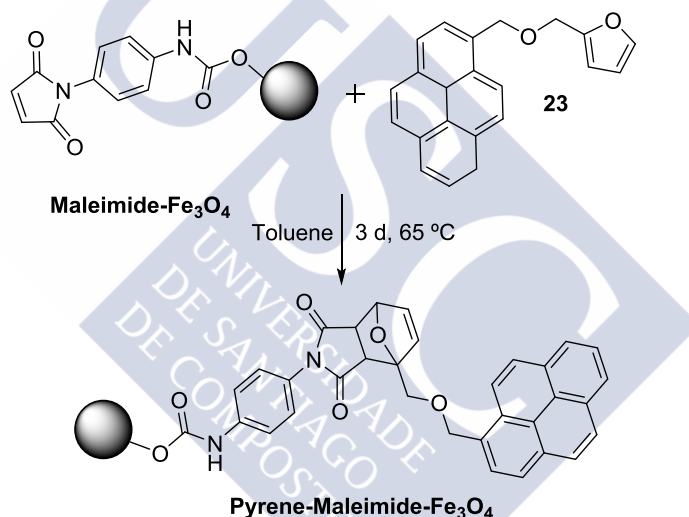


Figure 65: Calibration curve of Biotin with HABA-Avidin commercial kit.

The Diels–Alder reaction was also studied with pure **Maleimide-Fe₃O₄**. The reaction conditions selected to functionalize the IONs employed the lower temperature of 65 °C instead of 110 °C used in the model reactions in order to avoid a detachment of the alkyne carbamates from the ION surface. A reaction time of 24 h at 65 °C did not lead to an increase in the organic content of the resulting IONs compared to

Maleimide-Fe₃O₄ as shown by TGA, suggesting that Diels–Alder reaction did not take place. Therefore, a longer reaction time of 3 days was employed. In this case, TGA measurements showed an increase in the organic content of 9 wt% (Figure 66), indicating that **Pyrene-Maleimide-Fe₃O₄** was obtained successfully (Scheme 17). The UV-Vis spectrum of the resulting IONs in ethanol featured the bands characteristic of furfuryl pyrene **23** at 342, 326, and 267 nm (Figure 67). The thermal release of furfuryl pyrene **23** from **Pyrene-Maleimide-Fe₃O₄** was not tested because the NPs were only dispersible in organic solvents such as THF or ethanol, and thus the testing conditions would not mimic the scenario of physiological conditions.



Scheme 17: Diels–Alder reaction between Maleimide-Fe₃O₄ and furfuryl pyrene **23** in toluene at 65 °C for 3 days to yield Pyrene-Maleimide-Fe₃O₄.

After the optimization of the individual reactions with maleimide and alkyne moieties, the doubly functionalized NPs **Maleimide-Alkyne-Fe₃O₄** were tested. The Diels–Alder reaction was selected to be the first to ensure the steric availability of the maleimide moieties.

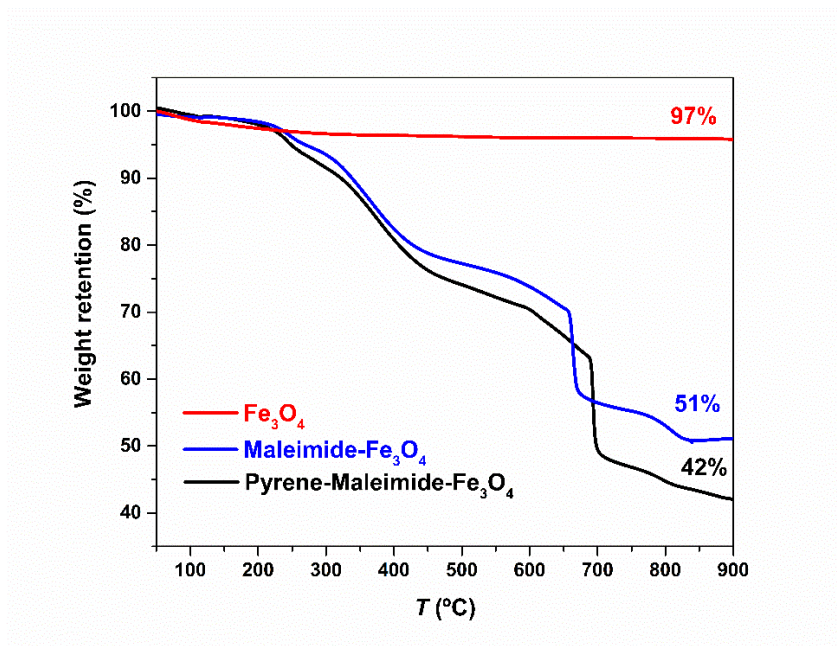


Figure 66: TGA measurements of naked Fe₃O₄ (red), Maleimide-Fe₃O₄ (blue) and Pyrene-Maleimide-Fe₃O₄ (black).

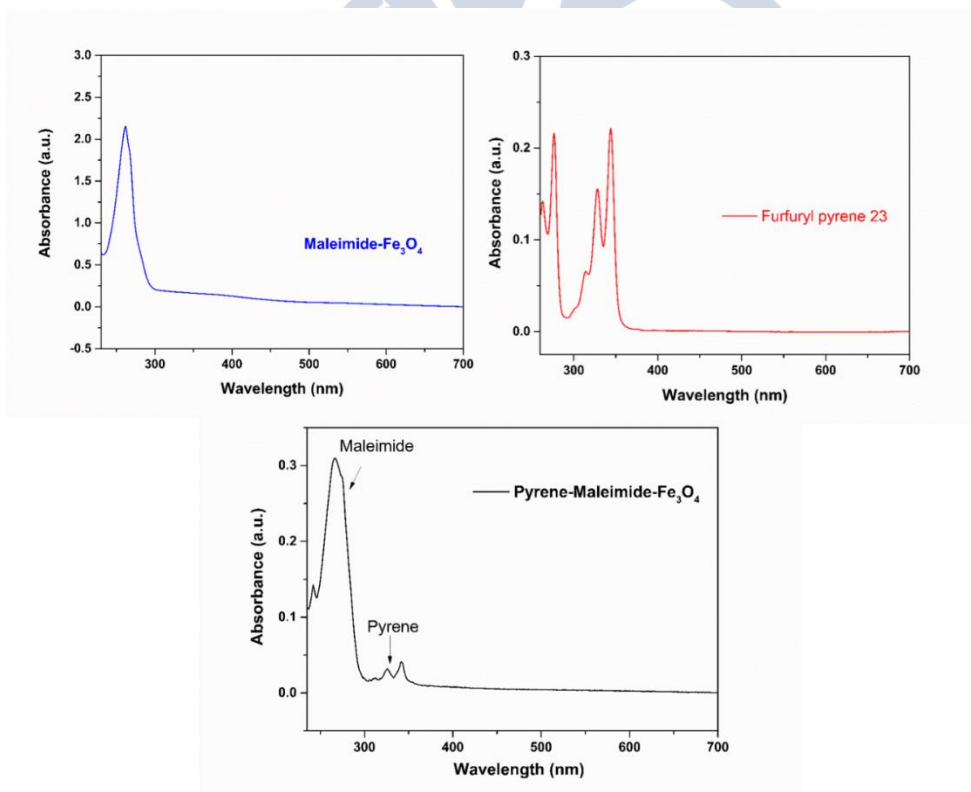
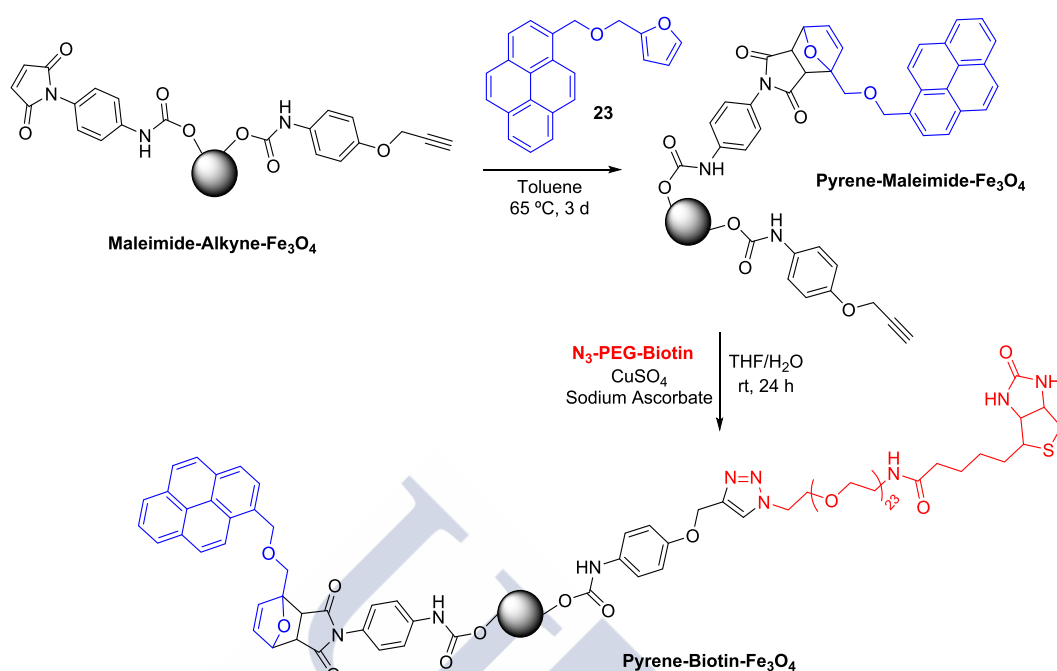


Figure 67: UV-Vis spectrum of Maleimide-Fe₃O₄, furfuryl pyrene 23, and Pyrene-Maleimide-Fe₃O₄ in ethanol.

Diels–Alder reaction between the maleimide moiety of **Maleimide-Alkyne-Fe₃O₄** and furfuryl pyrene **23** was conducted over three days at 65 °C in toluene to yield nanoparticles **Pyrene-Alkyne-Fe₃O₄** (Scheme 18). After purification of the nanoparticles by magnetic separation, the CuAAC between the alkyne moiety of the nanoparticles and the commercially available **N₃-PEG-Biotin** was performed under the same conditions as for **Alkyne-Fe₃O₄**. The purification of **Pyrene-Biotin-Fe₃O₄** was performed by dialysis since the NPs showed good solubility in water after the addition of the PEG linker, as desired for biomedical applications.

The characterization of **Pyrene-Biotin-Fe₃O₄** was performed by fluorescence, and the presence of pyrene **23** was verified by the characteristic emission bands of pyrene furfuryl at 416, 394, and 375 nm (Figure 68). Additionally, the presence of the biotin moiety was verified by the HABA-Avidin assay, and **Pyrene-Biotin-Fe₃O₄** was found to bear 7.54 μM of the biotin ligand per g of NP. Characterization by TGA was not possible because of the low quantities of **Pyrene-Biotin-Fe₃O₄** obtained.

With the IONs bearing biotin moieties for targeting, pyrene units as model system for drug release, and PEG linkers for water solubility, the thermally controlled release was tested by hyperthermia. **Pyrene-Biotin-Fe₃O₄** was treated for 1 h in water at 200 G in a hyperthermia experiment, then the NPs were collected and washed by centrifugation. The collected washes were analyzed by fluorescence and did not show the characteristics bands of furfuryl pyrene **23**, suggesting that the release of the fluorophore did not occur. The reason may be related with a small heat production on the surface of the NPs, probably due to their small core size, which is too low to promote the retro-Diels–Alder reaction. The future work will be to employ naked iron oxide NPs with a larger core size (15–20 nm) for the functionalization in order to increase the heat production to allow for the release to happen during hyperthermia treatment.



Scheme 18: Double functionalization of Maleimide-Alkyne-Fe₃O₄ nanoparticles first with furfuryl pyrene 23 and then N₃-PEG-Biotin.

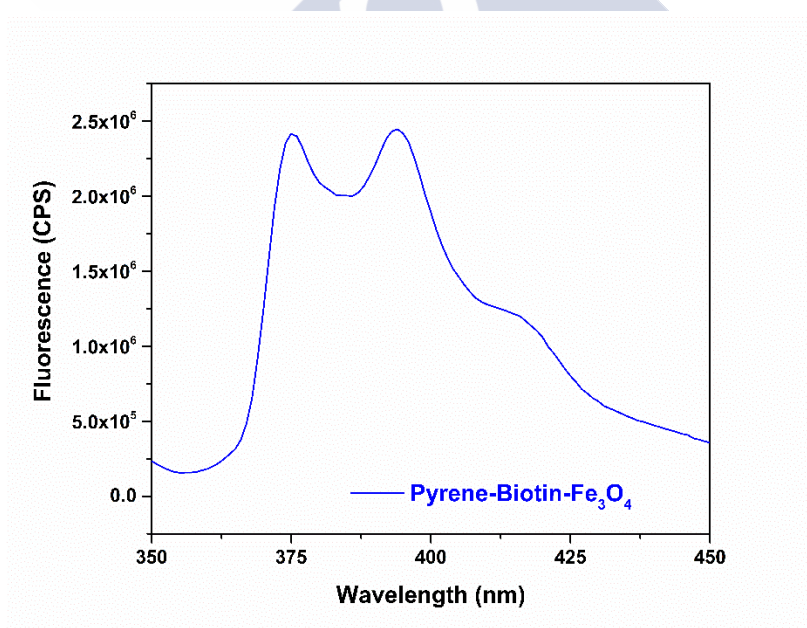


Figure 68: Fluorescence spectrum of Pyrene-Alkyne-Fe₃O₄ in H₂O with λ_{exc} at 300 nm.

On the contrary, preliminary results regarding the thermally controlled release of furfuryl pyrene 23 from Pyrene-Biotin-Fe₃O₄ were obtained by heating the sample in water for 1 h in an oil bath at 60 °C. After heating, nanoparticles were purified by centrifugation and the supernatant analyzed by fluorescence spectroscopy to evaluate

the release of pyrene furfuryl **23**. The fluorescence results were subtracted from control (non-heated **Pyrene-Biotin-Fe₃O₄** in water). The obtained spectrum (Figure 69) showed the characteristic bands of furfuryl pyrene **23**, indicating that the release of the fluorophore by heating was successful.

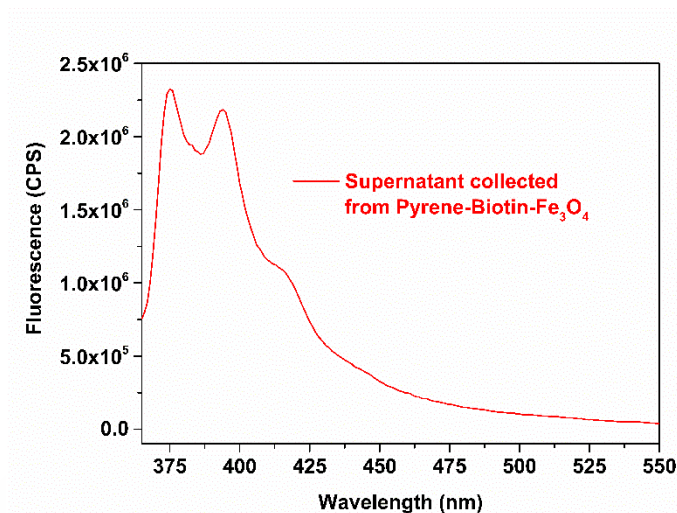


Figure 69: Fluorescence spectrum of the supernatant of Pyrene-Biotin-Fe₃O₄ after oil bath heating for 1 h at 60 °C in water.

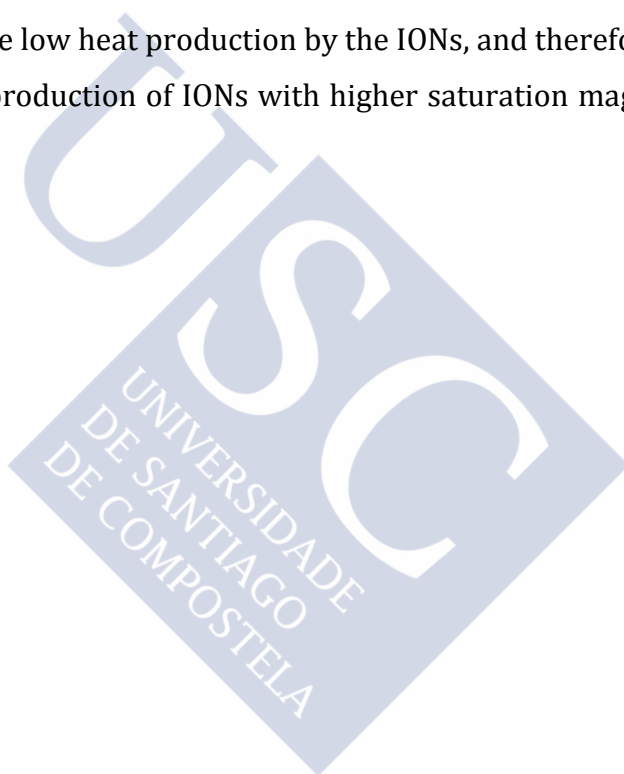
4.6 CONCLUSIONS

The functionalization of IONs was tested with two approaches: the functionalization of the Fe precursor, and the functionalization of the synthesized IONs. The first approach failed at the preservation of the organic functional groups on the NP surface after the formation of the nanoparticles. On the other hand, the functionalization of the surface of IONs was possible upon reaction between the hydroxyl groups on the NP surface and isocyanate ligands. The integrity of the functional groups on the IONs was confirmed by infrared spectroscopy, thermogravimetric assay, and nuclear magnetic resonance.

Two isocyanate molecules were synthesized bearing alkyne and maleimide moieties. Alkyne functional groups were selected in order to obtain IONs susceptible to react through the well-known copper-catalyzed alkyne–azide cycloaddition. The maleimide functional group was selected because it is a substrate of 1,3-Diels–Alder reaction,

which is known to be thermally reversible. The reactivity of IONs functionalized with alkyne and maleimide moieties was confirmed for both in the copper-catalyzed alkyne-azide and the Diels–Alder cycloadditions. This strategy gave access to IONs functionalized with biotin moieties for targeting, polyethylene glycol linkers for water solubility, and with fluorophore molecules as a model system for a drug.

The thermally controlled release was tested with the fluorophore molecules bound to the IONs by the Diels–Alder reaction. The liberation of the fluorophore molecules failed by magnetic hyperthermia, while being successful by heating in an oil bath. These results suggest the low heat production by the IONs, and therefore future work will be focused on the production of IONs with higher saturation magnetization and coercivity forces.



4.7 EXPERIMENTAL

Commercially available chemicals were used without further purification.

Column chromatography (CC) was carried out with SiO₂ (60 Å, 40–63 µm, 230–400 mesh, Macherey Nagel). Thin-layer chromatography (TLC) was conducted using ALUGRAM Xtra SIL G UV254 aluminium sheets from Macherey Nagel, and visualized by exposure to ultraviolet light.

Dried solvents (DMF, DMA, toluene, acetone, MeCN, and MeOH) for reaction and crystallization procedures were purchased from Acros Organics in Extra Dry over 4 Å molecular sieves quality with less than 0.5% of H₂O.

Mass spectrometry (MS) experiments were performed on a Bruker APEX® III FTMS (ESI) and Waters Micromass GC-TOF (EI) instruments at Centro de Apoio Científico e Tecnológico á Investigación (C.A.C.T.I.) at the University of Vigo, Spain.

Proton nuclear magnetic resonance (¹H NMR) spectra of organic compounds were recorded on a 400 MHz Bruker Avance II spectrometer at the NMR service of University of Minho in Braga, Portugal. For iron oxide nanoparticles spectra was recorded on a 500 MHz Bruker DRX-500 and 300 MHz Varian Mercury 300 Robot at the NMR service of Universidade de Santiago de Compostela, Spain. Proton chemical shifts are expressed in parts per million (δ scale) and are calibrated using residual undeuterated solvent peaks as an internal reference (CDCl₃: δ 7.26; (CD₃)₂SO: 2.50). Data for ¹H NMR spectra are reported as follows: chemical shift (δ ppm) (multiplicity, coupling constant (Hz), integration). Multiplicities are reported as follows: s = singlet, d = doublet, t = triplet, q = quartet, m = multiplet, br = broad. Carbon nuclear magnetic resonance (¹³C NMR) spectra were recorded on a 400 MHz Bruker Avance II spectrometer. Carbon chemical shifts are expressed in parts per million (δ scale) and are referenced to the carbon resonances of the solvent (CDCl₃: δ 77.16; (CD₃)₂SO: δ 39.52).

Fourier transform infrared spectroscopy (IR) spectra were acquired on a Bruker VERTEX 80v FT-IR spectrometer in absorbance mode. A spatula tip of the sample was

mixed with 200 mg of KBr and the powder was pressed at 10 tons for 2 min to obtain a transparent pellet. Spectra were recorded at 1.66 hPa with 32 scans and 4 cm^{-1} resolution with deuterated triglycine sulfate detector. The empty holder at 1.66 hPa was used as background and baseline correction was applied to the spectra.

TGA was performed in a TGA/DSC 1 STARE system, Mettler-Toledo, fitted with OmniStar GSD320 gas analysis system (Pfeiffer Vacuum), with 10 K min^{-1} gradient from 30 to 900 $^{\circ}\text{C}$ under 30 mL min^{-1} of Ar flow.

UV-Vis and fluorescence spectroscopy were carried out at room temperature with 1 cm path-length Hellma quartz 111-QS cuvettes. UV-vis spectra were recorded with a Shimadzu UV-2550 spectrophotometer. Fluorescence spectra were recorded with Horiba Fluoromax-4 spectrofluorometer.

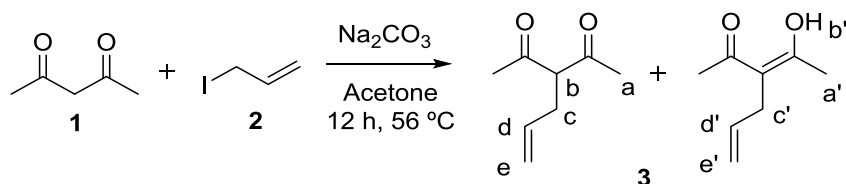
Elemental analysis were performed on Elemental Carlo Erba 1108/Combustion chromatography system at the service of C.A.C.T.I. at the University of Vigo, Spain.

Absorbance for HABA/avidin bioassay was measured with BioTek, Synergy H1 hybrid reader at 500 nm. Standard calibration curve was done with HABA/avidin and biotin standard solution in buffer from Sigma Aldrich (0 to 12 μM).

TEM studies were performed using Titan ChemiSTEM (FEI, 0.08 nm STEM resolution) electron microscope, operated at 200 kV and equipped with a Super-X detector.

4.7.1 Synthetic Procedures

3-Allylacetylacetonate²⁴⁶ (**1**)



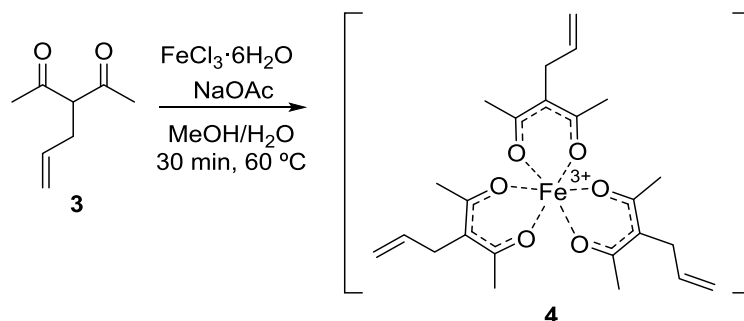
Na₂CO₃ (3.3 g, 24 mmol) was added to a 1 M solution of acetyl acetone (**1**) (2.0 g, 20 mmol) in anhydrous acetone under N₂, and left to stir for 30 min at rt. Allyl iodine (**2**) (2.2 mL, 24 mmol) was added dropwise, and the mixture was stirred 12 h at 56 °C. The reaction mixture was filtrated, and the filtrate was evaporated in vacuo. Purification by CC (SiO₂; hexane/EtOAc 40:1) gave **3** (1.6 g, 48%) as yellow oil and a mixture of tautomers.

¹H NMR (400 MHz, CDCl₃): 16.62 (s, 1H_{b'}), 5.80–5.70 (m, 1H_{d'}), 5.65–5.56 (m, 1H_d), 5.02–4.88 (m, 4H_{e,e'}), 3.65 (t, *J* = 6.4 Hz, 1H_b), 2.91–2.89 (m, 2H_{c'}), 2.51–2.47 (m, 2H_c), 2.09 (s, 6H_a), 2.07 (s, 6H_{a'}).

¹³C NMR (100 MHz, CDCl₃): 203.3, 191.2, 135.5, 133.9, 117.1, 114.5, 106.8, 67.4, 31.9, 30.8, 29.0, 22.5.

EI-MS: *m/z* (%): 140.08 (12, [*M*]⁺, calcd for C₈H₁₂O₂⁺ = 140.0837), 97.06 (100, calcd for C₆H₉O⁺ = 97.0654), 83.05 (48), 98.07 (42).

Iron(III) 3-Allylacetylacetonate²⁴⁷ (**4**)



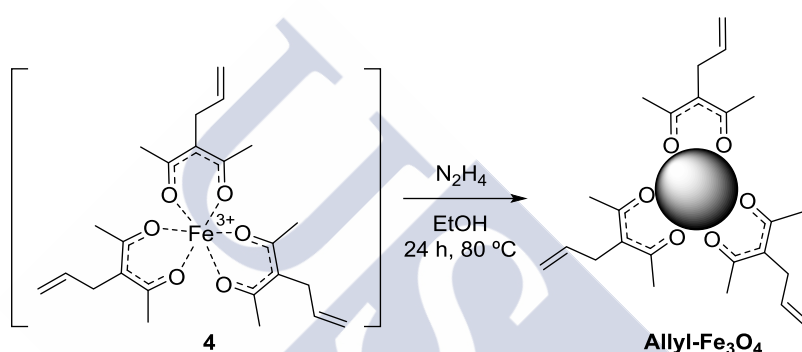
A solution of **3** (1.7 g, 12.5 mmol) in MeOH (2.5 mL, 5 M) was added dropwise to 0.1 M aq solution of FeCl₃ • 6H₂O (1.3 g, 4.7 mmol). The color of the reaction mixture changed from yellow to black, and then an aq. solution of sodium acetate (NaOAc) (3.8 mL,

3.75 M) was added. The mixture was heated to 60 °C for 30 min, and filtration yielded **4** (1.0 g, 48%) as dark red solid after drying in high vacuum.

IR (KBr; cm^{-1}): 3076, 2997, 2923, 1560, 1454, 1437, 1410, 1357, 1327, 1280, 1220, 1200, 1163, 1014, 997, 930, 901, 754, 685, 557, 435.

Elemental analysis calc. for $\text{C}_{24}\text{H}_{36}\text{O}_6\text{Fe}$ (476.38): C 60.90, H 7.03 ; found C 60.34, H 7.45.

Allyl- Fe_3O_4 ²⁴⁴



An aq solution of N_2H_4 (1.9 mL, 50 wt%) and EtOH (5.3 mL) were added to a solution of complex **4** (500 mg, 1.1 mmol) in EtOH (21 mL) at 80 °C. Then, the reaction mixture was left at 80 °C for 24 h, and after cooling, gave **Allyl- Fe_3O_4** NPs dispersed in EtOH.

IR (KBr cm^{-1}): 1642, 1421, 1381, 907, 587.

TGA: weight retention 89%

Elemental analysis found C 1.85, H 0.26.

Fe_3O_4 ²⁴⁹

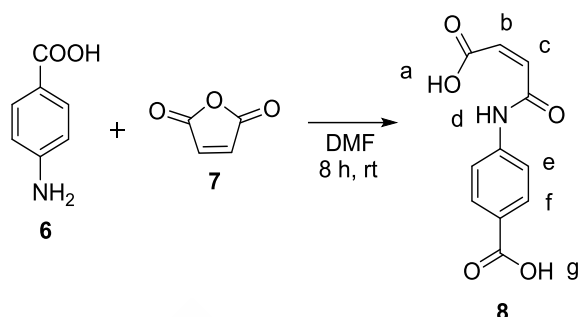
FeCl_3 (5.2 g, 32 mmol) and FeCl_2 (2.0 g, 15.8 mmol) were dissolved in H_2O (25 mL) and 12.1 N solution of HCl (0.85 mL). Then, this solution was added dropwise under mechanical stirring to 1.5 M NaOH solution (250 mL). The reaction mixture was stirred at rt 15 min, after which naked Fe_3O_4 were purified by centrifugation at 4000 rpm for 10 min, and washed with water three times.

Size from TEM images: 6 ± 3 nm.

TGA: weight retention 97%

Elemental analysis found C 0.054, H 0.460.

(Z)-4-(3-Carboxyacrylamido)benzoic Acid (8)



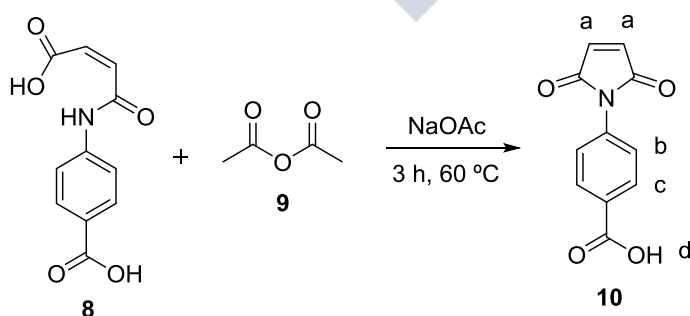
A 1 M solution of maleic anhydride (**7**) (10 g, 73 mmol) in DMF was gradually added to a well-stirred 1 M DMF solution of 4-aminobenzoic acid (**6**) (7.3 g, 74 mmol). Then, the mixture was stirred for 8 h at rt. The reaction mixture was then cooled to 0 °C and the precipitated solid was filtered and dried under vacuum to yield compound **8** (17 g, 99%) as white solid.

$^1\text{H NMR}$ (400 MHz, DMSO- d_6): 12.82 (br. s, 2H_{ag}), 10.59 (s, 1H_d), 7.90 (d, $J = 8.6$ Hz, 2H_e), 7.72 (d, $J = 8.6$ Hz, 2H_f), 6.48 (d, $J = 11.8$ Hz, 1H_b), 6.31 (d, $J = 11.8$ Hz, 1H_c).

$^{13}\text{C NMR}$ (100 MHz, DMSO- d_6): 166.9, 166.8, 163.6, 142.7, 131.6, 130.4, 130.2, 125.5, 118.7.

ESI-MS m/z (%): 234.08 (100, $[M]^-$ calcd. for C₁₁H₈NO₅ = 234.04).

4-Maleimidobenzoic Acid²⁵⁶ (10)



A mixture of **8** (1.0 g, 4.2 mmol), NaOAc (0.7 g, 8.5 mmol), and acetic anhydride (**9**) (5.1 mL) was stirred at 60 °C for 3 h. The cooled reaction mixture was poured onto a large amount of crushed ice, and pale yellow solid **10** (0.69 g, 75%) was isolated by filtration and dried under high vacuum.

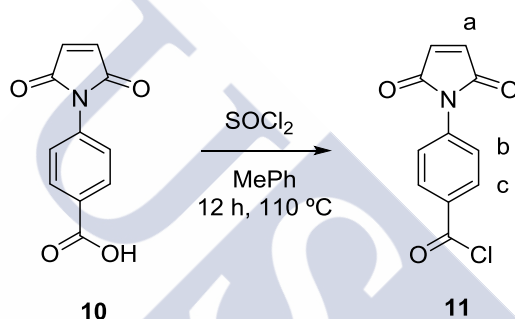
^1H NMR (400 MHz, $\text{DMSO-}d_6$): 8.03 (d, $J = 8.6$ Hz, 2H_b), 7.49 (d, $J = 8.6$ Hz, 2H_c), 7.21 (s, 2H_a).

^{13}C NMR (100 MHz, $\text{DMSO-}d_6$): 169.5, 166.7, 135.5, 135.0, 134.8, 129.9, 126.1.

IR (KBr; cm^{-1}): 3152, 1710, 1604, 1515, 1421, 1401, 1381, 1313, 1301, 1174, 1143, 1063, 1034, 857, 827, 700.

ESI-MS: 216.00 (100, $[M]^-$ calcd. for $\text{C}_{11}\text{H}_6\text{NO}_4 = 216.039$).

4-(2,5-Dioxazoliny)benzoyl Chloride (**11**)

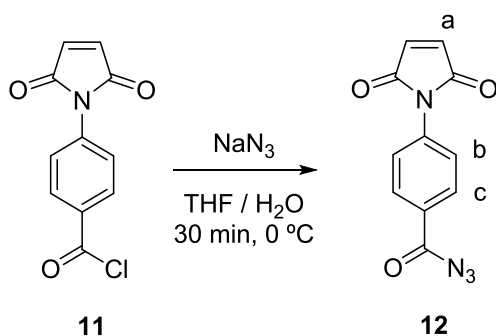


A mixture of **10** (250 mg, 1.15 mmol), SOCl_2 (0.334 ml, 4.60 mmol), and DMF (35.4 μL , 0.460 mmol) in dried toluene (11.5 mL) was heated to 110 $^\circ\text{C}$ for 12 h. The solvent was evaporated in vacuo, and recrystallization from dried hexane:acetone (1:3) gave **11** (233 mg, 86%) as yellow crystals.

IR (KBr; cm^{-1}): 1710, 1604, 1515, 1421, 1401, 1381, 1313, 1301, 1174, 1143, 1063, 1034, 879, 840, 826, 762, 722, 691, 643.

It was not possible to obtain NMR data due to instantaneous hydrolysis of the compound in deuterated solvent.

4-(2,5-Dioxazoliny)benzoyl Azide (**12**)



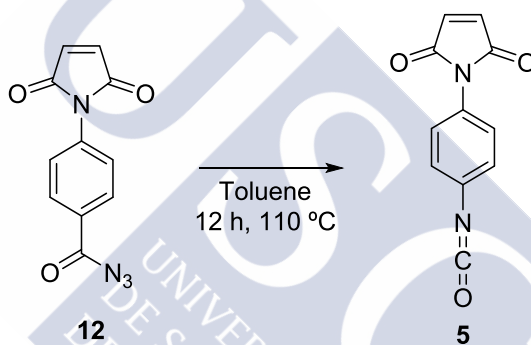
A 1 M solution of compound **11** (100 mg, 0.42 mmol) in THF was added dropwise to a 0.5 M aq solution of NaN₃ (33 mg, 0.5 mmol) at 0 °C. After 30 min, the mixture was poured onto ice, and compound **12** (76 mg, 74%) was isolated as yellow solid after filtration and dried in vacuo.

¹H NMR (400 MHz, DMSO-*d*₆): 8.08 (d, *J* = 8.5 Hz, 2H_b), 7.58 (d, *J* = 8.5 Hz, 2H_c), 7.23 (s, 2H_a).

¹³C NMR (100 MHz, DMSO-*d*₆): 171.3, 169.4, 137.1, 135.0, 129.7, 128.6, 126.2.

EI-MS: 215.0406 (100, [*M*]⁻ calcd. for C₁₀H₇N₃O₂ = 216.0538).

4-Maleimidophenyl Isocyanate²⁵¹ (**5**)

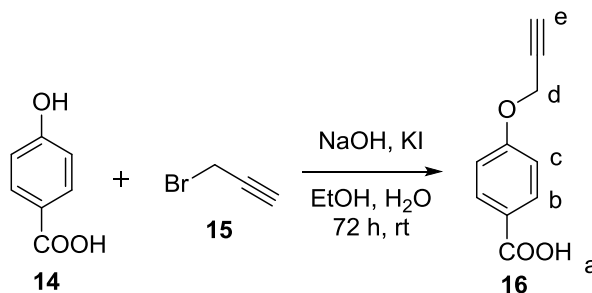


A suspension of compound **12** (200 mg, 0.83 mmol) in dry toluene (8.25 mL) was heated to 110 °C for 12 h under N₂. Then, the solvent was evaporated to give **5** (133 mg, 75%) as a yellow solid.

IR (KBr, cm⁻¹): 2275, 1705, 1602, 1534, 1514, 1397, 1316, 1240, 1151, 1062, 836, 692.

It was not possible to obtain NMR data due to instantaneous hydrolysis of the compound in deuterated solvent.

4-(Prop-2-yn-1-yloxy)benzoic Acid (**16**)



A 0.4 M aq. solution of NaOH (100 mL) with KI (3.6 g, 22 mmol) was added to 4-hydroxybenzoic acid (**14**) (2.6 g, 22 mmol) in EtOH (100 mL) at 50 °C. Then, propargyl bromide (**15**) (3.3 g, 27 mmol) was added dropwise, and the reaction mixture was stirred 72 h at rt. A 1 M solution of HCl (43 mL) was added to neutralize the reaction mixture, and a white solid precipitated that was washed with H₂O and dried under vacuum to yield **16** (3.74 g, 97%).

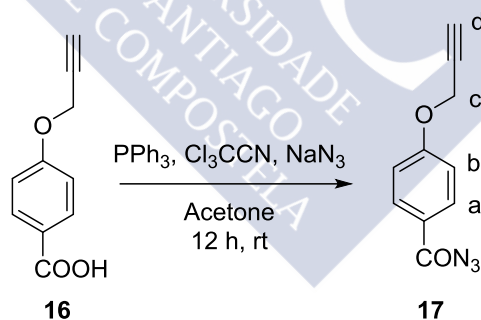
¹H NMR (400 MHz, DMSO-*d*₆): 7.89 (d, *J* = 8.8 Hz, 2H_b), 7.05 (d, *J* = 8.8 Hz, 2H_c), 4.87 (d, *J* = 2.2 Hz, 2H_d), 3.60 (t, *J* = 2.2 Hz, 1H_e).

¹³C NMR (100 MHz, DMSO-*d*₆): 166.9, 160.7, 131.2, 123.6, 114.6, 78.7, 78.6, 55.6.

EI-MS *m/z* (%): 176.05 (38, [*M*]⁺ calcd for C₁₀H₈O₃ = 176.4734), 103.05 (100, calcd for C₇H₃O = 103.0262), 63.02 (37).

IR (KBr, cm⁻¹): 3270, 2970, 2926, 2822, 2668, 2556, 2129, 1683, 1604, 1579, 1510, 1427, 1380, 1330, 1301, 1248, 1176, 1118, 1021, 974, 934, 844, 769, 722, 676, 654, 546, 503.

4-(Prop-2-yn-1-yloxy)benzoyl Azide²⁵² (**17**)



Dry acetone (11 mL) was added to **16** (200 mg, 1.13 mmol) to form a suspension. After the addition of CCl₃CN (328 mg, 2.27 mmol) and PPh₃ (600 mg, 2.27 mmol), alkyne **16** dissolved to form a yellow solution. Then, NaN₃ (88.6 mg, 1.36 mmol) was added and the solution turned dark. The reaction mixture was stirred at rt for 12 h. The reaction mixture was filtrated and the filtrate evaporated to dryness, dissolved in CH₂Cl₂ and extracted with H₂O. The organic phase was dried over Na₂SO₄, filtrated, and the solvent evaporated under vacuum to yield **17** (182 mg, 80%) as yellow pale solid.

^1H NMR (400 MHz, $\text{DMSO-}d_6$): 7.94 (d, $J = 9.0$ Hz, 2H_a), 7.13 (d, $J = 9.0$ Hz, 2H_b), 4.92 (d, $J = 2.0$ Hz, 2H_c), 3.64 (t, $J = 2.0$ Hz, 1H_d).

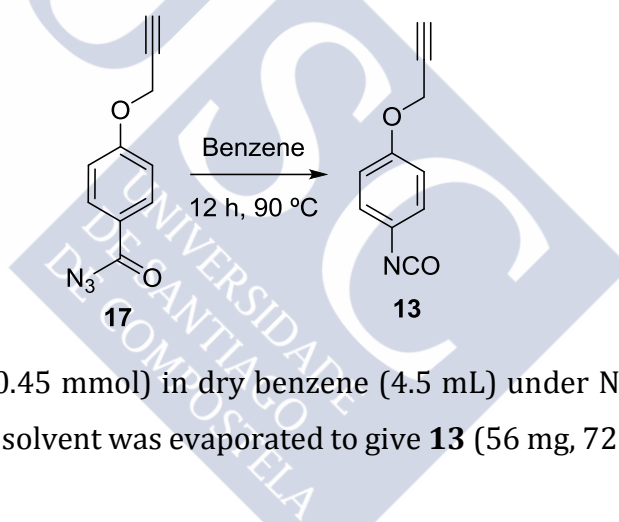
^{13}C NMR (100 MHz, $\text{DMSO-}d_6$): 170.9, 162.3, 131.3, 123.1, 115.2, 78.9, 78.5, 55.9.

EI-MS m/z (%): 201.06 (2.3, $[M]^+$ calcd for $\text{C}_{10}\text{H}_7\text{N}_3\text{O}_2 = 201.0538$), 134.02 (100), 103.06 (54), 78.08 (29).

EI-MS-HR m/z (%): 201.0534 (100, $[M]^+$ calcd for $\text{C}_{10}\text{H}_7\text{N}_3\text{O}_2 = 201.0538$), 202.0572 (26).

IR (KBr, cm^{-1}): 3362, 3113, 3092, 2344, 2139 ($-\text{N}=\text{N}=\text{N}$), 1722, 1691, 1604, 1514, 1401, 1382, 1310, 1255, 1215, 1188, 1149, 1071, 1031, 990, 948, 848, 833, 691.

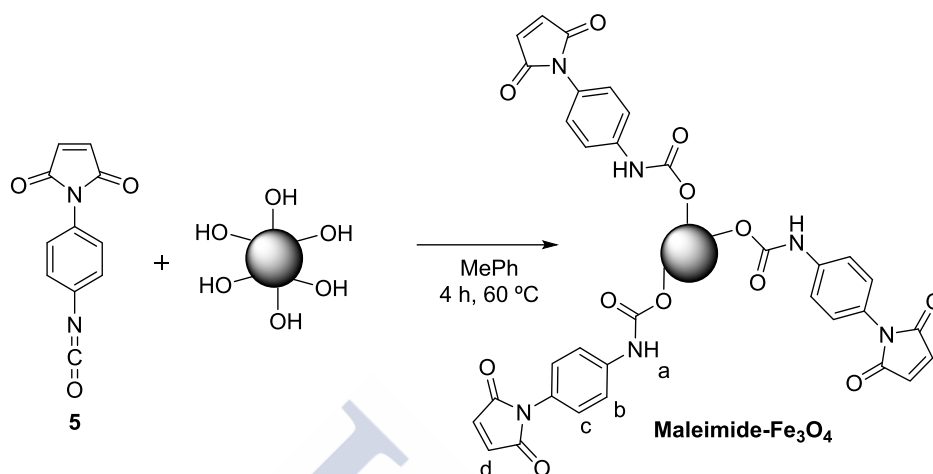
4-(Prop-2-yn-1-yloxy)benzoyl Isocyanate (**13**)



Compound **17** (90 mg, 0.45 mmol) in dry benzene (4.5 mL) under N_2 was heated to 90 °C for 12 h. Then, the solvent was evaporated to give **13** (56 mg, 72%) as an orange solid.

IR (KBr; cm^{-1}): 3285 ($\text{C}\equiv\text{C}-\text{H}$), 2964, 2924, 2854 ($\text{C}-\text{H}$ stretch), 2281 (NCO), 1730, 1603, 1529, 1450, 1371, 1288, 1244, 1169, 1104, 1025, 835, 800, 712, 666, 597, 551, 508, 401.

It was not possible to obtain NMR data due to instantaneous hydrolysis of the compound in deuterated solvent.

Maleimide-Fe₃O₄²⁴⁸

Naked iron oxide NPs (20 mg) were suspended in dry toluene (1 mL) and subjected to 5 min of sonication. Isocyanate **5** (25 mg, 0.12 mmol) was added to the suspension and the mixture was kept under sonication for 4 h at 60 °C. Then, the reaction mixture was subjected to centrifugation at 5000 rpm for 10 min, and the supernatant was discarded. The brown residue was washed 3 times with toluene and 3 times with Et₂O. Functionalized NPs were dried under vacuum to afford **Maleimide-Fe₃O₄** (13 mg) as brown powder.

IR (KBr; cm⁻¹): 1705, 1602, 1534, 1514, 1397, 1316, 1240, 1151, 1062, 836, 692, 630, 587.

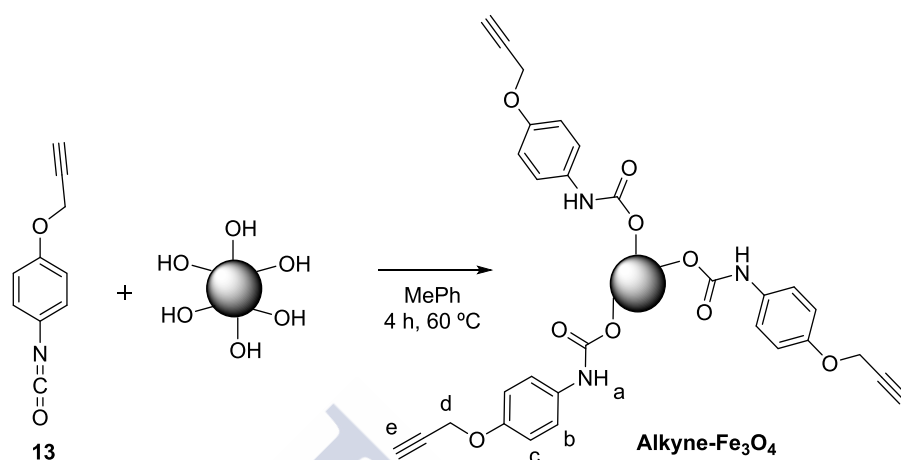
TGA: weight retention 51%

Elemental analysis found C 23.10, H 1.27, N 4.28.

UV-Vis spectrum in EtOH (nm): 260, 213.

¹H NMR (500 MHz, DMSO-*d*₆): 8.88 (s, 1H_a), 7.55 (d, *J* = 7.6 Hz, 2 H_b), 7.23 (d, *J* = 7.6 Hz, 2H_c), 7.15 (s, 1H_d).

¹³C NMR (500 MHz, DMSO-*d*₆): 170, 139, 135, 125, 119, 115. Data obtained from an HSQC experiment.

Alkyne-Fe₃O₄

Naked iron oxide NPs (74 mg) were suspended in dry toluene (10 mL) and subjected to 5 min of sonication. Isocyanate **13** (102 mg, 0.8 mmol) was added to the suspension and the mixture was kept under sonication for 4 h at 60 °C. Then, the reaction mixture was subjected to centrifugation at 5000 rpm for 10 min, and the supernatant was discarded. The solid residue was washed 3 times with toluene and 3 times with Et₂O. Functionalized NPs were dried under vacuum to afford **Alkyne-Fe₃O₄** (64.2 mg) as brown powder.

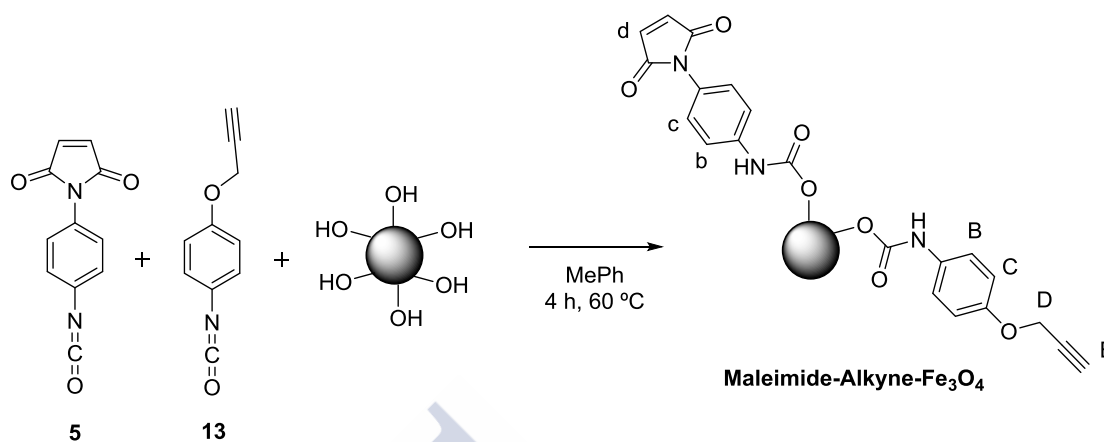
IR (KBr; cm⁻¹): 3290, (C≡C-H), 2959, 2928, 2864 (C-H), 2123 (-C≡C-), 1636, 1603, 1558, 1509, 1454, 1411, 1369, 1298, 1210, 1027, 923, 826, 643, 525.

Elemental analysis: found C 18.9, H 1.86, N 2.38, calculated to correspond to the molecular formula of C₁₀H₁N_{1.27}O_{8.48}, equivalent to 1.81 mmol ligand alkyne/g NP.

TGA: weight retention 63%

¹H NMR (500 MHz, DMSO-*d*₆): 8.44 (s, 1H_a), 7.36 (d, *J*=8.9 Hz, 2H_b), 6.92 (d, *J*=8.9 Hz, 2H_c), 4.74 (br. s, 2H_d), 3.46 (br. s, 1H_e).

¹³C NMR (125 DMSO-*d*₆): 119.8, 115.2, 55.7, 39.9. Data obtained from an HSQC experiment, three carbon signals were not seen due to an overlap with signals from deuterated solvent

Maleimide-Alkyne-Fe₃O₄

Naked iron oxide NPs (27 mg) were suspended in dry toluene (1.4 mL) and subjected to sonication for 5 min. Maleimide isocyanate **5** (8.6 mg, 0.04 mmol) and alkyne isocyanate **13** (6.9 mg, 0.04 mmol) were added to the suspension and the mixture was subjected to sonication at 60 °C for 4 h. Then, the NPs were isolated by magnetic separation and washed with toluene (4 times) to yield **Maleimide-Alkyne-Fe₃O₄** (20 mg).

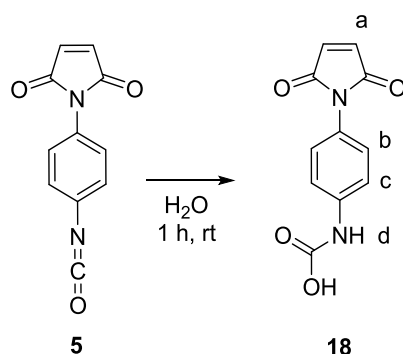
Elemental analysis found C 36.06, H 2.23, N 6.47.

UV-Vis in EtOH (nm): 264.

TGA: weight retention 36%.

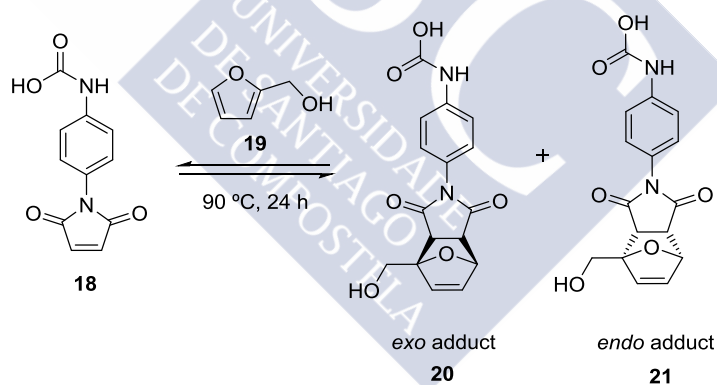
¹H NMR (500 MHz, DMSO-*d*₆): 8.90 (s), 8.77 (s), 8.56 (s), 8.43 (s), 7.55 (br. s, 2H_B), 7.37 (br. s, 2H_B), 7.24 (br. s, 2H_C), 7.17 (br. s, 2H_D), 6.92 (br. s, 2H_C), 4.74 (br. s, 2H_D). Signal from H_E was hidden under the water signal of the deuterated solvent.

¹³C NMR (125 DMSO-*d*₆): 134.5, 127.5, 119.8, 118.2, 115.3, 55.55. Data obtained from an HSQC experiment.

(4-Maleimidophenyl)carbamic Acid (18)

Isocyanate **5** (20 mg, 93.4 μmol) was suspended in H_2O (2 mL) and stirred at rt for 1 h. After evaporation, orange solid **18** (15 mg, 69%) was obtained.

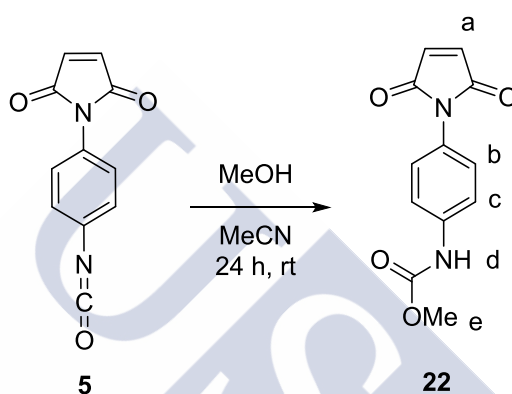
^1H NMR (400 MHz, $\text{DMSO-}d_6$): 8.89 (br. s, 1H), 7.55 (d, $J = 8.7$ Hz, 2H_c), 7.22 (d, $J = 8.7$ Hz, 2H_b), 7.15 (s, 2H_a).

(4-(4-(Hydroxymethyl)-1,3-dioxo-1,3,4,7-hexahydro-2H-4,7-epoxyisindol-2-yl)phenyl)carbamic Acid²⁵⁵

Carbamic acid **18** (45 mg, 0.19 mmol) was dissolved in furfuryl alcohol **19** (0.5 mL, 5.8 mmol) and stirred at 90 °C for 24 h. The excess furfuryl alcohol **19** was evaporated in vacuo by adding 80 wt% of water to form an azeotrope with a boiling point of ~ 100 °C. Diethyl ether was then added to precipitate the adducts. A pale yellow solid was obtained as a mixture of *exo* and *endo* adducts **20** and **21** (66.9 mg) with an excess of furfuryl alcohol **19**.

^1H NMR (400 MHz, $\text{DMSO-}d_6$): 8.90–8.86, 7.57–7.48, 7.24–7.20, 7.15, 7.10–7.08, 7.03–7.00, 6.59–6.55, 6.49–6.47, 6.38–6.37, 6.26–6.25, 5.33–5.31, 5.21–5.14, 5.02–4.99, 4.37–4.36, 4.11–3.93, 3.80–3.75, 3.55–3.53, 3.38, 3.36, 3.19–3.17, 3.00–2.99. No interpretation of the signals was carried out due to superposition of *endo* and *exo* protons.

Methyl(4-maleimidophenyl) Carbamate (**22**)



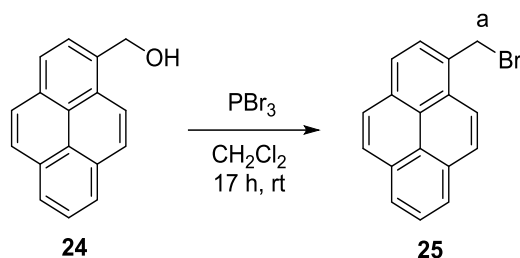
MeOH (16 μL) was added to isocyanate **5** (41 mg, 190 μmol) in dried MeCN (1.90 mL). The mixture was stirred at rt for 24 h. After evaporation in vacuo, **22** was isolated (45 mg, 96%) as yellow solid.

^1H NMR (400 MHz, CDCl_3): 9.92 (br. s, 1H_d), 7.65 (d, $J = 6.2$ Hz, 2H_c), 7.34 (d, $J = 6.2$ Hz, 2H_b), 7.15 (s, 2H_a), 3.80 (s, 3H_e).

^{13}C NMR (100 MHz, CDCl_3): 170.1, 154.0, 138.7, 134.6, 127.5, 125.7, 118.3, 51.7.

EI-MS m/z (%): 246.07 (100, $[M]^+$ calcd for $\text{C}_{12}\text{H}_{10}\text{N}_2\text{O}_4 = 246.0641$), 214.04 (65, $[M-\text{OCH}_3]^+$ calcd for $\text{C}_{11}\text{H}_6\text{N}_2\text{O}_3 = 214.0456$), 187.05 (22).

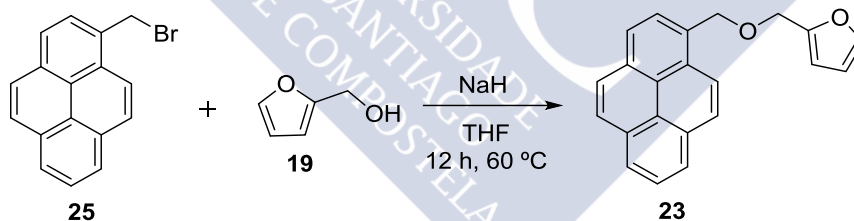
EI-MS-HR m/z (%): 246.0645 (100, $[M]^+$ calcd for $\text{C}_{12}\text{H}_{10}\text{N}_2\text{O}_4 = 246.0641$), 247.0683 (10, $[M]^+$ calcd for $\text{C}_{12}\text{H}_{10}\text{N}_2\text{O}_4 = 246.0674$).

1-(Bromomethyl)pyrene (25)

A 1 M of PBr_3 (3.65 mL, 3.65 mmol) in CH_2Cl_2 was added dropwise to a solution of 1-pyrenemethanol (500 mg, 2.15 mmol) in dry CH_2Cl_2 (14 mL) under N_2 . The reaction mixture was stirred at rt for 17 h. The mixture was then poured over ice and extracted with CH_2Cl_2 . Organic extracts were dried over Na_2SO_4 , filtrated and concentrated to afford **25** (471 mg, 74%) as green solid.

^1H NMR (400 MHz, CDCl_3): 8.31–8.16 (m, 5H), 8.12–7.96 (m, 4H), 5.05 (s, 2H_a).

^{13}C NMR (100 MHz, CDCl_3): 132.0, 131.2, 130.8, 130.6, 129.1, 128.2, 128.0, 127.7, 127.3, 126.3, 125.63, 125.61, 125.1, 124.9, 124.6, 122.8, 32.2.

2-((Pyren-1-ylmethoxy)methyl)furan (23)

Compound **25** (100 mg, 0.339 mmol) and furfuryl alcohol **19** (90 μL , 1.0 mmol) were dissolved in dry THF (800 μL). Then, NaH (68 mg, 2.8 mmol) was added to the mixture, and it was stirred overnight at 40 $^\circ\text{C}$. The reaction mixture was poured onto ice and extracted with CH_2Cl_2 . Combined organic extracts were dried over Na_2SO_4 , filtrated, and concentrated in vacuo. Purification by CC (SiO_2 ; hexane/ CH_2Cl_2 3:1) gave **23** (64 mg, 60%) as yellow-green solid.

^1H -NMR (400 MHz, CDCl_3): 8.36–8.14 (m, 5H), 8.10–8.00 (m, 4H), 7.49 (m, 1H), 6.40 (m, 2H), 5.27 (s, 2H), 4.62 (s, 2H).

^{13}C NMR (100 MHz, CDCl_3): 151.8, 142.9, 131.4, 131.2, 131.0, 130.8, 129.5, 127.8, 127.5, 127.4, 127.2, 125.9, 125.24, 125.22, 125.0, 124.7, 124.5, 123.4, 110.3, 109.6, 70.3, 63.8.

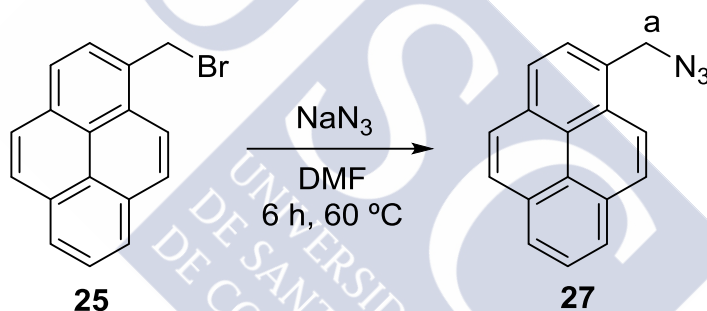
ESI-MS m/z (%): 311.11 (100, $[M-H]^+$ calcd. for $\text{C}_{22}\text{H}_{15}\text{O}_2 = 311.11$).

Elemental analysis calc. for $\text{C}_{22}\text{H}_{18}\text{O}_2$ (314.38): C 84.05, H 5.77, O 10.18; found C 84.19, H 5.61, O 10.20.

IR (KBr, cm^{-1}): 2959, 2924, 2854, 1591, 1501, 1471, 1457, 1410, 1351, 1261, 1147, 1065, 1053, 1011, 919, 848, 810, 739, 701, 600.

UV-Vis spectra at 70 mg L^{-1} in DMF (nm): 343, 328, 314, 278, 263.

1-(Azidomethyl)pyrene²⁵⁷ (**27**)



NaN_3 (250 mg, 3.90 mmol) was added to a solution of **25** (500 mg, 1.70 mmol) in dry DMF (5.2 mL), under N_2 . The reaction mixture was heated at 60°C for 6 h, poured onto water (100 mL), and extracted with CH_2Cl_2 . Combined organic extracts were dried over Na_2SO_4 and concentrated in vacuo. Recrystallization from hexane/acetone (1:1) gave azide pyrene **27** (283 mg, 65%) as light orange solid.

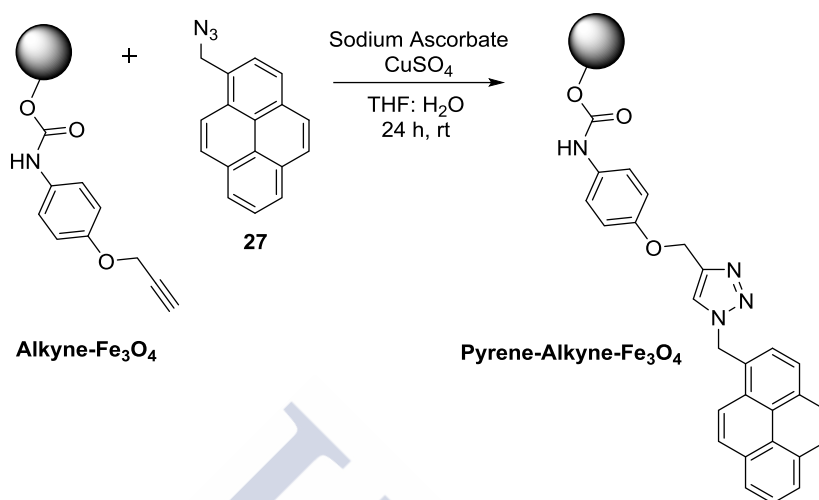
^1H NMR (400 MHz, CDCl_3): 8.32–8.18 (m, 5H), 8.13–8.00 (m, 4H), 5.07 (s, 2H_a).

^{13}C NMR (100 MHz, CDCl_3): 131.8, 131.2, 130.7, 129.3, 128.4, 128.3, 127.9, 127.5, 127.3, 126.2, 125.63, 125.56, 125.1, 124.6, 122.7, 77.21, 53.1.

IR (KBr, cm^{-1}): 3270, 2102, 1679, 1601, 1429, 1304, 1244, 1178, 1023, 893, 839, 696.

EI-MS m/z (%): 257.10 (6, $[M]^+$ calcd for $\text{C}_{17}\text{H}_{11}\text{N}_3 = 257.0953$), 228.06 (100, $[M-\text{N}_2]^+$ calcd for $\text{C}_{17}\text{H}_{11}\text{N} = 229.09$), 201.6 (91, $[M-\text{CH}_2\text{N}_3]^+$ calcd for $\text{C}_{16}\text{H}_9 = 201.07$).

UV-Vis spectra at 20 mg L^{-1} in THF (nm): 344, 329, 314, 276, 266.

Pyrene-Alkyne-Fe₃O₄

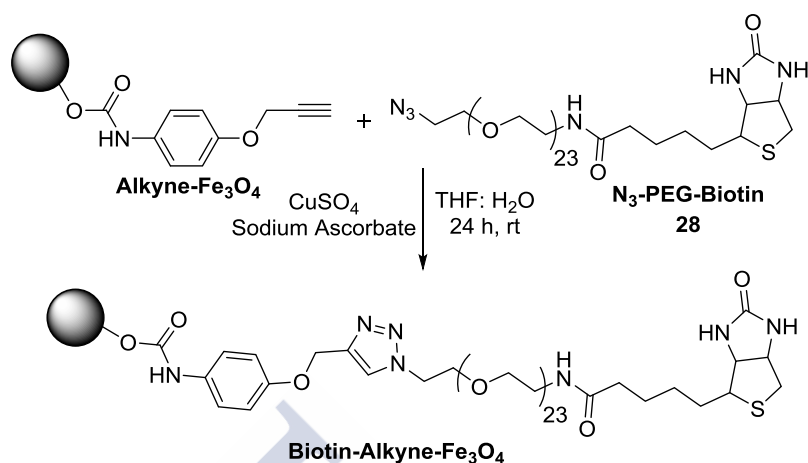
Alkyne-Fe₃O₄ (40 mg) was suspended in THF (1 mL) and subjected to sonication for 5 min. Azide pyrene **27** (18 mg, 69 μ mol), H₂O (0.73 mL), and 0.3 M aq solution of CuSO₄•5H₂O (13 μ L) and 0.6 M aq solution of sodium ascorbate (13 μ L) were added to the suspension and the reaction was kept away from light and stirred for 24 h at rt. Then, the reaction mixture was washed 4 times with a solvent mixture of THF:H₂O (1:0.73) and isolated by magnetic separation. **Pyrene-Alkyne-Fe₃O₄** (30 mg) was dried under vacuum and storage as brown powder.

Elemental analysis: found C 26.41, H 2.145, N 4.134.

UV-Vis spectroscopy in THF (nm): 344, 328, 276, 265, 243, 205.

TGA: weight retention 56%.

Quantification of pyrene azide in the combined washing solution of purified **Pyrene-Alkyne-Fe₃O₄** was performed by UV-Vis spectroscopy against a calibration curve. The amount of pyrene azide found in the washing solution was subtracted from the quantity of the starting material placed into the reaction mixture, and the result was treated as pyrene azide covalently attached to **Pyrene-Alkyne-Fe₃O₄**: 0.139 mmol of pyrene azide/mg of NP

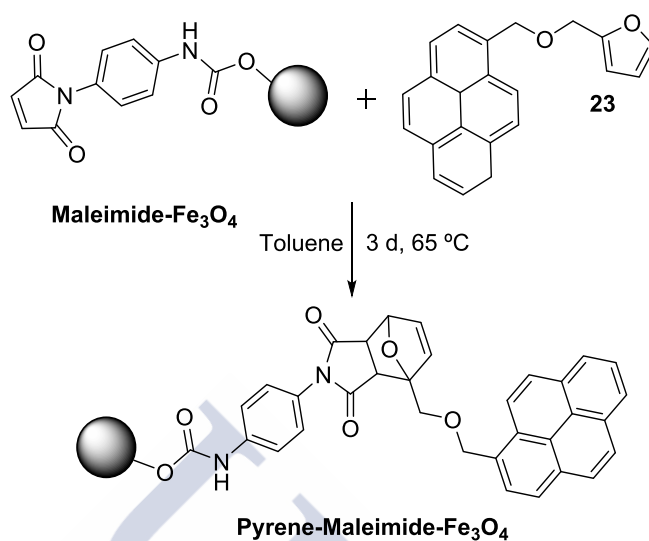
Biotin-Alkyne-Fe₃O₄

Alkyne-Fe₃O₄ (30 mg) was suspended in THF (0.75 mL) and sonicated for 5 min. **N₃-PEG-Biotin 28** (30 mg, 23 μmol), H₂O (0.55 mL), 0.3 M aq solution of CuSO₄•5H₂O (18 μL), and 0.6 M aq solution of sodium ascorbate (18 μL) were added to the suspension and the reaction was kept away from light. 0.3 M aq solution of CuSO₄•5H₂O (18 μL) and 0.6 M aq solution of sodium ascorbate (18 μL) were added two more times with the time interval of 8 h. After 24 h, NPs were purified by dialysis with a cellulose membrane (cut off 2000 Da, MilliPore), during 48 h with 4 water replacements (500 mL). **Biotin-Alkyne-Fe₃O₄** was recovered in aq. solution.

UV-Vis in H₂O (nm): 256.

TGA: weight retention 34%.

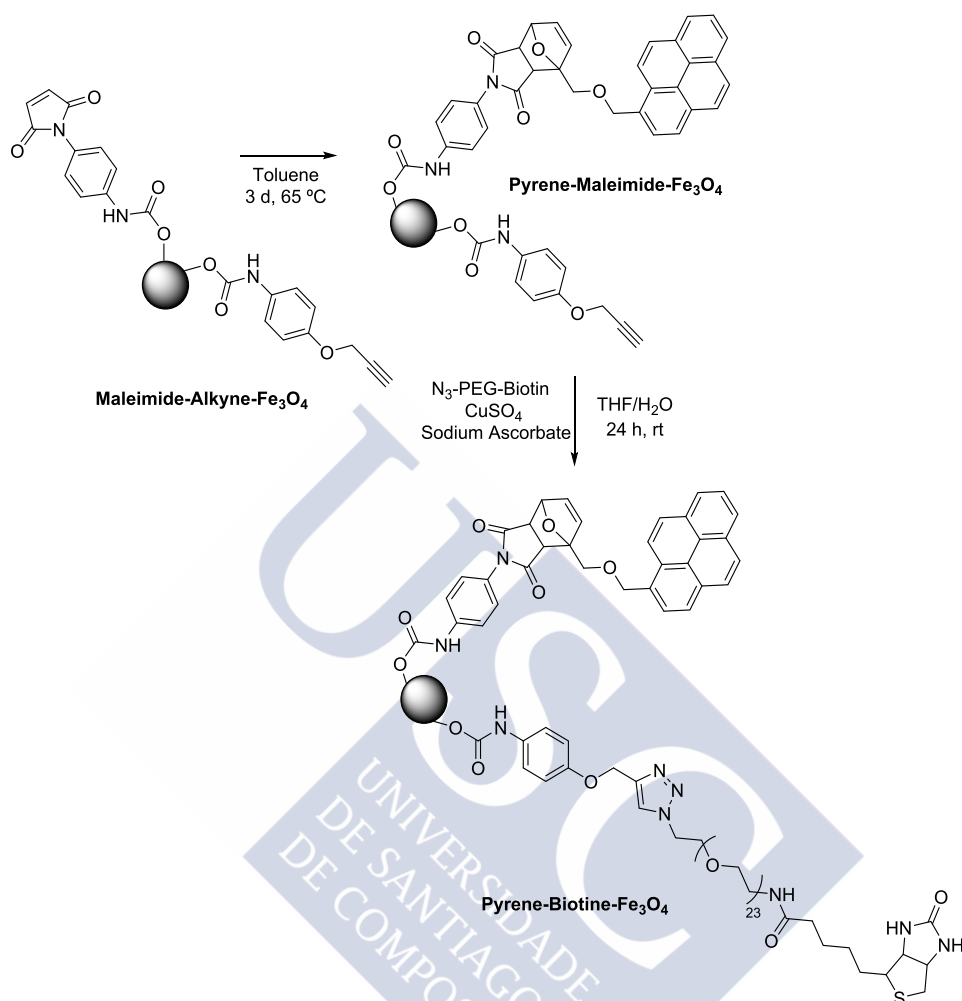
Quantification of biotin in **Biotin-Alkyne-Fe₃O₄** was performed by HABA/avidin bioassay. Calibration curve between HABA/avidin reagent and biotin from 0 to 20 μM was done in buffer solution at pH 7.3 by monitoring the absorbance at 500 nm. **Biotin-Alkyne-Fe₃O₄** sample was diluted 50 times to adjust the absorbance value to the calibration curve, and **Biotin-Alkyne-Fe₃O₄** bore 88 μmol of N₃-PEG-Biotin per g of NP.

Pyrene-Maleimide-Fe₃O₄

Maleimide-Fe₃O₄ (10 mg) was suspended in toluene (0.5 mL) and subjected to sonication for 5 min. Then, furfuryl pyrene (5.4 mg, 23 μmol) was added and the reaction mixture was stirred for 3 d at 65 °C. Then, the reaction mixture was washed 4 times with toluene, and NPs were isolated by magnetic separation to yield **Pyrene-Maleimide-Fe₃O₄** as a brown powder.

UV-Vis in EtOH (nm): 342, 326, 267, 202.

TGA: weight retention 42%.

Pyrene-Biotin-Fe₃O₄

Maleimide-Alkyne-Fe₃O₄ (10 mg) was suspended in toluene (0.5 mL) and subjected to sonication for 5 min. Then, furfuryl pyrene **23** (5.4 mg, 23 μmol) was added and the reaction mixture was stirred for 3 d at 65 °C. Then, NPs were washed 4 times with toluene, and isolated by magnetic separation to yield **Pyrene-Maleimide-Fe₃O₄**. THF (250 μL) was added to **Pyrene-Maleimide-Fe₃O₄** and NPs were subjected to sonication for 5 min. N₃-PEG-Biotin (10 mg, 767 μmol), H₂O (185 μL), 0.3 M aq solution of CuSO₄•5H₂O (6 μL), and 0.6 M aq solution of sodium ascorbate (6 μL) were added to the suspension and the reaction was kept away from light. A 0.3 M aq solution of CuSO₄•5H₂O (6 μL) and a 0.6 M aq solution of sodium ascorbate (6 μL) were added two more times with a time interval of 8 h. After 24 h, NPs were purified by dialysis with cellulose membrane (cut off 2000 Da) over 48 h with four water replacements (500 mL), then **Pyrene-Biotin-Fe₃O₄** was recovered in aq. solution.

Fluorescence (nm) in water and λ_{exc} 300 nm = 416, 394 and 375 nm.

In biotin quantification by HABA-Avidin assay, it was found 7.54 μM of biotin ligand per g of NP.





CHAPTER 5

5 General Conclusions



A synthesis method based on hydrothermal methodology was developed in order to produce iron oxide nanoparticles doped with manganese that featured dual T_1 – T_2 contrast in MRI. The development of doped magnetite was sustainable, i.e. refraining from the use of organic solvents and phase-transfer procedures, showing also scalability and reproducibility. Additionally, nanoparticles with larger sizes were found to adsorb higher amount of proteins and lead to aggregation in biological medium. These findings shed light on the design of iron oxide nanoparticles to regulate the protein corona formation.

Due to the contrast generated in MRI, iron oxide nanoparticles are used as magnetic labels for cell tracking applications. Magnetite nanoparticles of two different core sizes and with different coatings were studied for the labeling of mesenchymal stem cells. The results showed that nanoparticles with low colloidal stability in cell culture medium were internalized into stem cells due to a sedimentation process. This process led to a non-homogeneous distribution of magnetite nanoparticles across the cell population, resulting in stem cells with no label while others were heavily labeled. On the other hand, nanoparticles that remained stable in the cell culture medium did not effectively interact with cells failing to promote nanoparticle internalization. A modification of the polyacrylic acid coating with glucosamine moieties was shown to boost the internalization of the nanoparticles with record values of Fe internalized in stem cells. Due to this efficient labeling of stem cells, the long-term study of cell migration was possible *in vivo* after 8 days of cell transplantation.

The third aspect of iron oxide nanoparticles studied in this work relied on the functionalization of the surface of magnetite nanoparticles to gain access to multifunctional nanoparticles. The attachment of ligands of interest was possible by the formation of carbamates upon reaction between the hydroxyl groups on the nanoparticle surface and isocyanate ligands. Two isocyanate-bearing molecules were synthesized in order to place maleimide and alkyne functionalities at the nanoparticles' surface with high organic loadings, susceptible to undergoing click chemistry reactions. In the case of the maleimide functional group, it offered the possibility of undergoing Diels–Alder cycloaddition that is thermally reversible. The cargo release of the nanoparticles functionalized with the Diels–Alder reaction and a

fluorophore derivative took place after 1 h heating in an oil bath. Additionally, the nanoparticles bearing an alkyne group underwent the functionalization by copper-catalyzed alkyne–azide cycloaddition with a biotin-ligand for targeting purposes. In summary, multifunctional water-soluble nanoparticles were obtained with the ability to release cargo by thermal control, and with biotin ligands for targeting.





6 Bibliography

- 1 K. Riehemann, S. W. Schneider, T. A. Luger, B. Godin, M. Ferrari and H. Fuchs, *Angew. Chem. Int. Ed.*, 2009, **48**, 872–897.
- 2 K. Ulbrich, K. Holá, V. Šubr, A. Bakandritsos, J. Tuček and R. Zbořil, *Chem. Rev.*, 2016, **116**, 5338–5431.
- 3 A. Hervault and N. T. K. Thanh, *Int. J. Mol. Sci.*, 2013, **2**, 11553–73.
- 4 N. Lee, D. Yoo, D. Ling, M. H. Cho, T. Hyeon and J. Cheon, *Chem. Rev.*, 2015, **115**, 10637–10689.
- 5 L. K. Bogart, G. Pourroy, C. J. Murphy, V. Puentes, T. Pellegrino, D. Rosenblum, D. Peer and R. Lévy, *ACS Nano*, 2014, **8**, 3107–3122.
- 6 K. Turcheniuk, A. V Tarasevych, V. P. Kukhar, R. Boukherroub and S. Szunerits, *Nanoscale*, 2013, **5**, 10729–52.
- 7 W. Wu, Z. Wu, T. Yu, C. Jiang and W.-S. Kim, *Sci. Technol. Adv. Mater.*, 2015, **16**, 23501.
- 8 L. H. Reddy, J. L. Arias, J. Nicolas and P. Couvreur, *Chem. Rev.*, 2012, **112**, 5818–5878.
- 9 R. M. Cornell and U. Schwertmann, *The Iron Oxides: Structures, Properties, Reactions, Occurrences and Uses*, Weinheim: Wiley, 2nd ed., 2003.
- 10 G. S. Parkinson, *Surf. Sci. Rep.*, 2016, **71**, 272–365.
- 11 J. Guo, W. Yang and C. Wang, *Adv. Mater.*, 2013, **25**, 5196–5214.
- 12 J. Jang, H. Nah, J.-H. Lee, S. H. Moon, M. G. Kim and J. Cheon, *Angew. Chem. Int. Ed.*, 2009, **48**, 1234–1238.
- 13 A.-H. Lu, E. L. Salabas and F. Schüth, *Angew. Chem. Int. Ed.*, 2007, **46**, 1222–1244.
- 14 S. Laurent, D. Forge, M. Port, A. Roch, C. Robic, L. Vander Elst and R. N. Muller, *Chem. Rev.*, 2008, **108**, 2064–2110.
- 15 R. Boistelle and J. P. Astier, *J. Cryst. Growth*, 1988, **90**, 14–30.
- 16 L. Babes, B. Denizot, G. Tanguy, J. J. Le Jeune and P. Jallet, *J. Colloid Interface Sci.*, 1999, **212**, 474–482.
- 17 Y. El Mendili, F. Grasset, N. Randrianantoandro, N. Nerambourg, J.-M. Greneche and J. F. Bardeau, *J. Phys. Chem. C*, 2015, **119**, 10662–10668.
- 18 X. Wang, J. Zhuang, Q. Peng and Y. Li, *Nature*, 2005, **437**, 121–124.
- 19 M. A. López-Quintela, C. Tojo, M. C. Blanco, L. García Rio and J. R. Leis, *Curr. Opin. Colloid Interface Sci.*, 2004, **9**, 264–278.
- 20 W. R. Sanhai, J. H. Sakamoto, R. Canady and M. Ferrari, *Nat. Nanotechnol.*, 2008, **3**, 242–244.

- 21 G. W. Simmons and B. C. Beard, *J. Phys. Chem.*, 1987, **91**, 1143–1148.
- 22 E. McCafferty and J. P. Wightman, *Surf. Interface Anal.*, 1998, **26**, 549–564.
- 23 R. A. Bohara, N. D. Thorat and S. H. Pawar, *RSC Adv.*, 2016, **6**, 43989–44012.
- 24 N. T. K. Thanh and L. A. W. Green, *Nano Today*, 2010, **5**, 213–230.
- 25 L. Zhou, J. Yuan and Y. Wei, *J. Mater. Chem.*, 2011, **21**, 2823.
- 26 N. Erathodiyil and J. Y. Ying, *Acc. Chem. Res.*, 2011, **44**, 925–935.
- 27 W. Stöber, A. Fink and E. Bohn, *J. Colloid Interface Sci.*, 1968, **26**, 62–69.
- 28 Z. Xu, Y. Hou and S. Sun, *J. Am. Chem. Soc.*, 2007, **129**, 8698–8699.
- 29 J.-H. Lee, J. Jang, J. Choi, S. H. Moon, S. Noh, J. Kim, J.-G. Kim, I.-S. Kim, K. I. Park and J. Cheon, *Nat. Nanotechnol.*, 2011, **6**, 418–422.
- 30 Y. W. Jun, J. S. Choi and J. Cheon, *Chem. Commun.*, 2007, 1203–1214.
- 31 A. K. Gupta and M. Gupta, *Biomaterials*, 2005, **26**, 3995–4021.
- 32 M. Sairam, B. V. K. Naidu, S. K. Nataraj, B. Sreedhar and T. M. Aminabhavi, *J. Membr. Sci.*, 2006, **283**, 65–73.
- 33 M. H. Stewart, K. Susumu, B. C. Mei, I. L. Medintz, J. B. Delehanty, J. B. Blanco-Canosa, P. E. Dawson and H. Mattoussi, *J. Am. Chem. Soc.*, 2010, **132**, 9804–9813.
- 34 L. Li, K. Y. Mak, C. W. Leung, K. Y. Chan, W. K. Chan, W. Zhong and P. W. T. Pong, *Microelectron. Eng.*, 2013, **110**, 329–334.
- 35 N. Fauconnier, J. N. Pons, J. Roger and A. Bee, *J. Colloid Interface Sci.*, 1997, **194**, 427–433.
- 36 C. Xu, K. Xu, H. Gu, R. Zheng, H. Liu, X. Zhang, Z. Guo and B. Xu, *J. Am. Chem. Soc.*, 2004, **126**, 9938–9939.
- 37 J. V Jokerst, T. Lobovkina, R. N. Zare and S. S. Gambhir, *Nanomedicine*, 2011, **6**, 715–28.
- 38 W. Wu, Q. He and C. Jiang, *Nanoscale Res. Lett.*, 2008, **3**, 397–415.
- 39 S. Meier, G. Pütz, U. Massing, C. E. Hagemeyer, D. von Elverfeldt, M. Meißner, K. Ardipradja, S. Barnert, K. Peter, C. Bode, R. Schubert and C. von zur Muhlen, *Biomaterials*, 2015, **53**, 137–148.
- 40 W. R. Algar, D. E. Prasuhn, M. H. Stewart, T. L. Jennings, J. B. Blanco-Canosa, P. E. Dawson and I. L. Medintz, *Bioconjugate Chem.*, 2011, **22**, 825–858.
- 41 E. K. Lim, T. Kim, S. Paik, S. Haam, Y. M. Huh and K. Lee, *Chem. Rev.*, 2015, **115**, 327–394.
- 42 K. E. Sapsford, W. R. Algar, L. Berti, K. B. Gemmill, B. J. Casey, E. Oh, M. H. Stewart and I. L. Medintz, *Chem. Rev.*, 2013, **113**, 1904–2074.
- 43 H. C. Kolb, M. G. Finn and K. B. Sharpless, *Angew. Chem. Int. Ed.*, 2001, **40**, 2004–2021.
- 44 V. V. Rostovtsev, L. G. Green, V. V. Fokin and K. B. Sharpless, *Angew. Chem. Int.*

- Ed.*, 2002, **41**, 2596–2599.
- 45 H. C. Kolb and K. B. Sharpless, *Drug Discovery Today*, 2003, **8**, 1128–1137.
- 46 E. M. Sletten and C. R. Bertozzi, *Angew. Chem. Int. Ed.*, 2009, **48**, 6974–6998.
- 47 Y. Chen, Y. Xianyu, J. Wu, B. Yin and X. Jiang, *Theranostics*, 2016, **6**, 969–985.
- 48 S. Liu, K. T. Dicker and X. Jia, *Chem. Commun.*, 2015, **51**, 5218–5237.
- 49 E. Lallana, A. Sousa-Herves, F. Fernandez-Trillo, R. Riguera and E. Fernandez-Megia, *Pharm. Res.*, 2012, **29**, 1–34.
- 50 S. Ilyas, M. Ilyas, R. a L. Van Der Hoorn and S. Mathur, *ACS Nano*, 2013, **7**, 9655–9663.
- 51 T. Borase, T. Ninjbadgar, A. Kapetanakis, S. Roche, R. O'Connor, C. Kerskens, A. Heise and D. F. Brougham, *Angew. Chem. Int. Ed.*, 2013, **52**, 3164–3167.
- 52 L. Hansen, E. K. U. Larsen, E. H. Nielsen, F. Iversen, Z. Liu, K. Thomsen, M. Pedersen, T. Skrydstrup, N. C. Nielsen, M. Ploug and J. Kjems, *Nanoscale*, 2013, **5**, 8192–201.
- 53 O. Diels and K. Alder, *Justus Liebigs Ann. Chem.*, 1928, **460**, 98–122.
- 54 F. Fringuelli and A. Taticchi, *The Diels-Alder Reaction: Selected Practical Methods*, John Wiley & Sons, Baffins Lane, vol. 3, Chichester, England, 2002.
- 55 A. Gandini, *Prog. Polym. Sci.*, 2013, **38**, 1–29.
- 56 R. C. Boutelle and B. H. Northrop, *J. Org. Chem.*, 2011, **76**, 7994–8002.
- 57 M. A. Tasdelen, *Polym. Chem.*, 2011, **2**, 2133–2145.
- 58 A. Sanyal, *Macromol. Chem. Phys.*, 2010, **211**, 1417–1425.
- 59 G. Hizal, U. Tunca and A. Sanyal, *J. Polym. Sci., Part A: Polym. Chem.*, 2011, **49**, 4103–4120.
- 60 T. T. T. N'Guyen, H. T. T. Duong, J. Basuki, V. Montembault, S. Pascual, C. Guibert, J. Fresnais, C. Boyer, M. R. Whittaker, T. P. Davis and L. Fontaine, *Angew. Chem. Int. Ed.*, 2013, **52**, 14152–14156.
- 61 L. Mancuso, T. Knobloch, J. Buchholz, J. Hartwig, L. Mçller, L. Möller, K. Seidel, W. Collisi, F. Sasse and A. Kirschning, *Chem. Eur. J.*, 2014, **20**, 17541–17551.
- 62 R. Weissleder, D. D. Stark, B. L. Engelstad, B. R. Bacon, C. C. Compton, D. L. White, P. Jacobs and J. Lewis, *Am. J. Roentgenol.*, 1989, **152**, 167–173.
- 63 N. Lee and T. Hyeon, *Chem. Soc. Rev.*, 2012, **41**, 2575–2589.
- 64 L. Josephson, J. Lewis, P. Jacobs, P. F. Hahn and D. D. Stark, *Magn. Reson. Imaging*, 1988, **6**, 647–653.
- 65 M. Rohrer, H. Bauer, J. Mintonovitch, M. Requardt and H.-J. Weinmann, *Invest. Radiol.*, 2005, **40**, 715–724.
- 66 D. Yoo, J.-H. Lee, T.-H. Shin and J. Cheon, *Acc. Chem. Res.*, 2011, **44**, 863–874.
- 67 N. A. Keasberry, M. Bañobre-López, C. Wood, G. J. Stasiuk, J. Gallo and N. J. Long,

- Nanoscale*, 2015, **7**, 16119–16128.
- 68 K. Cheng, M. Yang, R. Zhang, C. Qin, X. Su and Z. Cheng, *ACS Nano*, 2014, **8**, 9884–9896.
- 69 H. Chen, D. Sulejmanovic, T. Moore, D. C. Colvin, B. Qi, O. T. Mefford, J. C. Gore, F. Alexis, S.-J. Hwu and J. N. Anker, *Chem. Mater.*, 2014, **26**, 2105–2112.
- 70 P. McColgan, P. Sharma and P. Bentley, *Stem Cell Rev.*, 2011, **7**, 1031–40.
- 71 H. Liu, J. Zhang, X. Chen, X.-S. Du, J.-L. Zhang, G. Liu and W.-G. Zhang, *Nanoscale*, 2016, **8**, 7808–7826.
- 72 T. C. Burns, C. M. Verfaillie and W. C. Low, *J. Comp. Neurol.*, 2009, **515**, 125–144.
- 73 J. V. Frangioni and R. J. Hajjar, *Circulation*, 2004, **110**, 3378–3383.
- 74 P. Bianco, *Annu. Rev. Cell Dev. Biol.*, 2014, **30**, 677–704.
- 75 J. W. M. Bulte, *AJR*, 2009, **193**, 314–325.
- 76 L. Li, W. Jiang, K. Luo, H. Song, F. Lan, Y. Wu and Z. Gu, *Theranostics*, 2013, **3**, 595–615.
- 77 M. Barrow, A. Taylor, P. Murray, M. J. Rosseinsky and D. J. Adams, *Chem. Soc. Rev.*, 2015, **44**, 6733–6748.
- 78 T. L. Moore, L. Rodriguez-Lorenzo, V. Hirsch, S. Balog, D. Urban, C. Jud, B. Rothen-Rutishauser, M. Lattuada and A. Petri-Fink, *Chem. Soc. Rev.*, 2015, **44**, 6287–6305.
- 79 A. M. Reddy, B. K. Kwak, H. J. Shim, C. Ahn, H. S. Lee, Y. J. Suh and E. S. Park, *J. Korean Med. Sci.*, 2010, **25**, 211–219.
- 80 J. Jo, I. Aoki and Y. Tabata, *J. Controlled Release*, 2010, **142**, 465–473.
- 81 S. Ju, G. Teng, Y. Zhang, M. Ma, F. Chen and Y. Ni, *Magn. Reson. Imaging*, 2006, **24**, 611–617.
- 82 K. von der Haar, A. Lavrentieva, F. Stahl, T. Scheper and C. Blume, *Appl. Microbiol. Biotechnol.*, 2015, **99**, 9907–9922.
- 83 H. R. Moyer and K. A. Delman, *Int. J. Hyperthermia*, 2008, **24**, 251–261.
- 84 F. Westermarck, *Zbl. Gynak.*, 1898, 1335–1339.
- 85 W. L. Tittsworth, G. J. A. Murad, B. L. Hoh and M. Rahman, *Anticancer Res.*, 2014, **34**, 565–574.
- 86 M. Hurwitz and P. Stauffer, *Semin. Oncol.*, 2014, **41**, 714–729.
- 87 J. R. Lepock, *Int. J. Hyperthermia*, 2003, **19**, 252–266.
- 88 J. F. Kerr, C. M. Winterford and B. V Harmon, *Cancer*, 1994, **73**, 2013–2026.
- 89 N. Bloy, J. Pol, G. Manic, I. Vitale, A. Eggermont, J. Galon, E. Tartour, L. Zitvogel, G. Kroemer and L. Galluzzi, *Oncoimmunology*, 2014, **3**, e954929.
- 90 P. S. Steeg, *Nat. Rev. Cancer*, 2016, **16**, 201–18.

- 91 B. Hildebrandt, *Crit. Rev. Oncol. Hematol.*, 2002, **43**, 33–56.
- 92 J. van der Zee, *Ann. Oncol.*, 2002, **13**, 1173–1184.
- 93 N. R. Datta, S. G. Ordóñez, U. S. Gaipal, M. M. Paulides, H. Crezee, J. Gellermann, D. Marder, E. Puric and S. Bodis, *Cancer Treat. Rev.*, 2015, **41**, 742–753.
- 94 X. Liu, H. J. Chen, X. Chen, Y. Alfadhl, J. Yu and D. Wen, *Appl. Phys. Rev.*, 2015, **2**, 11103–1.
- 95 E. A. Périgo, G. Hemery, O. Sandre, D. Ortega, E. Garaio, F. Plazaola and F. J. Teran, *Appl. Phys. Rev.*, 2015, **2**, 41302.
- 96 M. Bañobre-López, A. Teijeiro and J. Rivas, *Rep. Pract. Oncol. Radiother.*, 2013, **18**, 397–400.
- 97 A. J. Giustini, A. A. Petryk, S. M. Cassim, J. A. Tate, I. Baker and P. J. Hoopes, *Nano Life*, 2010, **1**, 17–32.
- 98 M. Kallumadil, M. Tada, T. Nakagawa, M. Abe, P. Southern and Q. A. Pankhurst, *J. Magn. Magn. Mater.*, 2009, **321**, 1509–1513.
- 99 M. Suto, Y. Hirota, H. Mamiya, A. Fujita, R. Kasuya, K. Tohji and B. Jeyadevan, *J. Magn. Magn. Mater.*, 2009, **321**, 1493–1496.
- 100 V. Marnett, A. Musinu, A. Ardu, G. Ennas, D. Peddis, D. Niznansky, C. Sangregorio, C. Innocenti, N. T. K. Thanh and C. Cannas, *Nanoscale*, 2016, 10124–10137.
- 101 X. Lasheras, M. Insausti, I. Gil de Muro, E. Garaio, F. Plazaola, M. Moros, L. De Matteis, J. M. de la Fuente and L. Lezama, *J. Phys. Chem. C*, 2016, acs.jpcc.5b10216.
- 102 I. Sharifi, H. Shokrollahi and S. Amiri, *J. Magn. Magn. Mater.*, 2012, **324**, 903–915.
- 103 H. Zhao, Z. Chen, L. Tao, X. Zhu, M. Lan and Z. Li, *RSC Adv.*, 2015, **5**, 68454–68460.
- 104 C. S. S. R. Kumar and F. Mohammad, *Adv. Drug Delivery Rev.*, 2011, **63**, 789–808.
- 105 G. Salas, J. Camarero, D. Cabrera, H. Takacs, M. Varela, R. Ludwig, H. D??hring, I. Hilger, R. Miranda, M. D. P. Morales and F. J. Teran, *J. Phys. Chem. C*, 2014, **118**, 19985–19994.
- 106 R. Hergt, R. Hiergeist, M. Zeisberger, G. Glöckl, W. Weitschies, L. P. Ramirez, I. Hilger and W. A. Kaiser, *J. Magn. Magn. Mater.*, 2004, **280**, 358–368.
- 107 Z. Nemati, J. Alonso, L. M. Martinez, H. Khurshid, E. Garaio, J. A. Garcia, M. H. Phan and H. Srikanth, *J. Phys. Chem. C*, 2016, **120**, 8370–8379.
- 108 P. Guardia, R. Di Corato, L. Lartigue, C. Wilhelm, A. Espinosa, M. Garcia-Hernandez, F. Gazeau, L. Manna and T. Pellegrino, *ACS Nano*, 2012, **6**, 3080–3091.
- 109 D. Rodrigues, M. Bañobre-López, B. Espiña, J. Rivas and J. Azeredo, *Biofouling*, 2013, **29**, 1225–1232.
- 110 A. Riedinger, P. Guardia, A. Curcio, M. A. Garcia, R. Cingolani, L. Manna and T. Pellegrino, *Nano Lett.*, 2013, **13**, 2399–2406.
- 111 Y. Min, J. M. Caster, M. J. Eblan and A. Z. Wang, *Chem. Rev.*, 2015, **115**, 11147–

- 11190.
- 112 S. Behrens and I. Appel, *Curr. Opin. Biotechnol.*, 2016, **39**, 89–96.
- 113 H. Kettiger, A. Schipanski, P. Wick and J. Huwyler, *Int. J. Nanomedicine*, 2013, **8**, 3255–3269.
- 114 J. Gautier, E. Allard-Vannier, J. Burlaud-Gaillard, J. Domenech and I. Chourpa, *J. Biomed. Nanotechnol.*, 2014, **10**, 1–13.
- 115 Y. Tian, X. Jiang, X. Chen, Z. Shao and W. Yang, *Adv. Mater.*, 2014, **26**, 7393–7398.
- 116 M. Peng, H. Li, Z. Luo, J. Kong, Y. Wan, L. Zheng, Q. Zhang, H. Niu, A. Vermorken, W. Van de Ven, C. Chen, X. Zhang, F. Li, L. Guo and Y. Cui, *Nanoscale*, 2015, **7**, 11155–11162.
- 117 S. Carregal-Romero, P. Guardia, X. Yu, R. Hartmann, T. Pellegrino and W. J. Parak, *Nanoscale*, 2015, **7**, 570–576.
- 118 J. Fang, Y. Yang, W. Xiao, B. Zheng, Y.-B. Lv, X.-L. Liu and J. Ding, *Nanoscale*, 2016, **8**, 3259–3263.
- 119 N. Griffete, J. Fresnais, A. Espinosa, C. Wilhelm, A. Bée and C. Ménager, *Nanoscale*, 2015, **7**, 18891–6.
- 120 J. H. Lee, K. J. Chen, S. H. Noh, M. A. Garcia, H. Wang, W. Y. Lin, H. Jeong, B. J. Kong, D. B. Stout, J. Cheon and H. R. Tseng, *Angew. Chem. Int. Ed.*, 2013, **52**, 4384–4388.
- 121 J. Cheon, S.-H. Noh, H.-R. Tseng and K.-J. Chen, 2014, Supramolecular Magnetic Nanoparticles, WO201412735.
- 122 M. Kanamala, W. R. Wilson, M. Yang, B. D. Palmer and Z. Wu, *Biomaterials*, 2016, **85**, 152–167.
- 123 G. Helmlinger, F. Yuan, M. Dellian and R. K. Jain, *Nat. Med.*, 1997, **3**, 177–182.
- 124 M. P. Stewart, A. Lorenz, J. Dahlman and G. Sahay, *WIREs Nanomed Nanobiotechnol*, 2016, **8**, 465–478.
- 125 L. Zhu, D. Wang, X. Wei, X. Zhu, J. Li, C. Tu, Y. Su, J. Wu, B. Zhu and D. Yan, *J. Controlled Release*, 2013, **169**, 228–238.
- 126 X. Ding, Y. Liu, J. Li, Z. Luo, Y. Hu, B. Zhang, J. Liu, J. Zhou and K. Cai, *ACS Appl. Mater. Interfaces*, 2014, **6**, 7395–7407.
- 127 C. Gialeli, A. D. Theocharis and N. K. Karamanos, *FEBS J.*, 2011, **278**, 16–27.
- 128 G. Y. Lee, W. P. Qian, L. Wang, Y. A. Wang, C. A. Staley, M. Satpathy, S. Nie, H. Mao and L. Yang, *ACS Nano*, 2013, 2078–2089.
- 129 M. Nantz and R. Knipp, 2015, *Nanoparticles Drug Deliv. U.S. 2012/0302516*.
- 130 P. Saint-Cricq, S. Deshayes, J. I. Zink and A. M. Kasko, *Nanoscale*, 2015, **7**, 13168–72.
- 131 B. Rühle, S. Datz, C. Argyo, T. Bein and J. I. Zink, *Chem. Commun.*, 2015, **52**, 1843–1846.
- 132 S. Friberg and A. M. Nyström, *J. Nanobiotechnol.*, 2016, **14**, 17.

- 133 Y. Min, J. M. Caster, M. J. Eblan and A. Z. Wang, *Chem. Rev.*, 2015, **115**, 11147–11190.
- 134 E. Seneterre, R. Weissleder, P. Jaramillo, P. Reimer, A. Lee, T. J. Brady and J. Wittenberg, *Radiology*, 1991, **179**.
- 135 H. Bernd, E. De Kerviler, S. Gaillard and B. Bonnemain, *Invest. Radiol.*, 2009, **44**, 336–342.
- 136 A. E. Nel, L. Mädler, D. Velegol, T. Xia, E. M. V Hoek, P. Somasundaran, F. Klaessig, V. Castranova and M. Thompson, *Nat. Mater.*, 2009, **8**, 543–557.
- 137 N. Feliu, D. Docter, M. Heine, P. del Pino, S. Ashraf, J. Kolosnjaj-Tabi, P. Macchiarini, P. Nielsen, D. Alloyeau, F. Gazeau, R. H. Stauber and W. J. Parak, *Chem. Soc. Rev.*, 2016, **5**, 33–37.
- 138 P. Rivera-Gil, D. Jimenez De Aberasturi, V. Wulf, B. Pelaz, P. Del Pino, Y. Zhao, J. M. De La Fuente, I. Ruiz De Larramendi, T. Rojo, X. J. Liang and W. J. Parak, *Acc. Chem. Res.*, 2013, **46**, 743–749.
- 139 T. Cedervall, I. Lynch, S. Lindman, T. Berggård, E. Thulin, H. Nilsson, K. a Dawson and S. Linse, *Proc. Natl. Acad. Sci. U. S. A.*, 2007, **104**, 2050–2055.
- 140 B. Fadeel, N. Feliu, C. Vogt, A. M. Abdelmonem and W. J. Parak, *Wiley Interdiscip. Rev.: Nanomed. Nanobiotechnol.*, 2013, **5**, 111–129.
- 141 D. Docter, D. Westmeier, M. Markiewicz, S. Stolte, S. K. Knauer and R. H. Stauber, *Chem. Soc. Rev.*, 2015, **44**, 6094–6121.
- 142 G. Hu, B. Jiao, X. Shi, R. P. Valle, Q. Fan and Y. Y. Zuo, *ACS Nano*, 2013, **7**, 10525–105.
- 143 A. Taylor, A. Herrmann, D. Moss, V. Sée, K. Davies, S. R. Williams and P. Murray, *PLoS One*, 2014, **9**, e100259.
- 144 C. D. Walkey, J. B. Olsen, F. Song, R. Liu, H. Guo, W. Olsen, Y. Cohen, A. Emili and W. C. W. Chan, *ACS Nano*, 2014, **8**, 2439–2455.
- 145 A. Lesniak, F. Fenaroli, M. P. Monopoli, C. Åberg, K. A. Dawson and A. Salvati, *ACS Nano*, 2012, **6**, 5845–5857.
- 146 B. Kang, P. Okwieka, S. Schöttler, S. Winzen, J. Langhanki, K. Mohr, T. Opatz, V. Mailänder, K. Landfester and F. R. Wurm, *Angew. Chem. Int. Ed.*, 2015, **54**, 1–6.
- 147 M. M. Yallapu, N. Chauhan, S. F. Othman, V. Khalilzad-Sharghi, M. C. Ebeling, S. Khan, M. Jaggi and S. C. Chauhan, *Biomaterials*, 2015, **46**, 1–12.
- 148 Y. Y. Tyurina, E. R. Kisin, A. Murray, V. A. Tyurin, V. I. Kapralova, L. J. Sparvero, A. A. Amoscato, A. K. Samhan-Arias, L. Swedin, R. Lahesmaa, B. Fadeel, A. A. Shvedova and V. E. Kagan, *ACS Nano*, 2011, **5**, 7342–7353.
- 149 M. Mahmoudi, A. M. Abdelmonem, S. Behzadi, J. H. Clement, S. Dutz, M. R. Ejtehadi, R. Hartmann, K. Kantner, U. Linne, P. Maffre, S. Metzler, M. K. Moghadam, C. Pfeiffer, M. Rezaei, P. Ruiz-Lozano, V. Serpooshan, M. A. Shokrgozar, G. U. Nienhaus and W. J. Parak, *ACS Nano*, 2013, **7**, 6555–6562.

- 150 S. Tenzer, D. Docter, J. Kuharev, A. Musyanovych, V. Fetz, R. Hecht, F. Schlenk, D. Fischer, K. Kiouptsi, C. Reinhardt, K. Landfester, H. Schild, M. Maskos, S. K. Knauer and R. H. Stauber, *Nat. Nanotechnol.*, 2013, **8**, 772–781.
- 151 K. Saha, M. Rahimi, M. Yazdani, S. T. Kim, D. F. Moyano, S. Hou, R. Das, R. Mout, F. Rezaee, M. Mahmoudi and V. M. Rotello, *ACS Nano*, 2016, **10**, 4421–4430.
- 152 M. S. Ehrenberg, A. E. Friedman, J. N. Finkelstein, G. Oberdörster and J. L. McGrath, *Biomaterials*, 2009, **30**, 603–610.
- 153 M. Lundqvist, J. Stigler, G. Elia, I. Lynch, T. Cedervall and K. A. Dawson, *Proc. Natl. Acad. Sci. U. S. A.*, 2008, **105**, 14265–14270.
- 154 M. A. Dobrovolskaia, B. W. Neun, S. Man, X. Ye, M. Hansen, A. K. Patri, R. M. Crist and S. E. McNeil, *Nanomedicine*, 2014, **10**, 1453–1463.
- 155 M. P. Monopoli, D. Walczyk, A. Campbell, G. Elia, I. Lynch, F. Baldelli Bombelli and K. A. Dawson, *J. Am. Chem. Soc.*, 2011, **133**, 2525–2534.
- 156 A. Salvati, A. S. Pitek, M. P. Monopoli, K. Prapainop, F. B. Bombelli, D. R. Hristov, P. M. Kelly, C. Åberg, E. Mahon and K. A. Dawson, *Nat. Nanotechnol.*, 2013, **8**, 137–143.
- 157 V. Mirshafiee, M. Mahmoudi, K. Lou, J. Cheng and M. L. Kraft, *Chem. Commun.*, 2013, **49**, 2557–2559.
- 158 M. P. Monopoli, C. Åberg, A. Salvati and K. A. Dawson, *Nat. Nanotechnol.*, 2012, **7**, 779–786.
- 159 Y. Hoshino, H. Koide, T. Urakami, H. Kanazawa, T. Kodama, N. Oku and K. J. Shea, *J. Am. Chem. Soc.*, 2010, **132**, 6644–6645.
- 160 K. Prapainop, D. P. Witter and P. Wentworth, *J. Am. Chem. Soc.*, 2012, **134**, 4100–4103.
- 161 A. Albanese, P. S. Tang and W. C. W. Chan, *Annu. Rev. Biomed. Eng.*, 2012, **14**, 1–16.
- 162 A. Verma and F. Stellacci, *Small*, 2010, **6**, 12–21.
- 163 L. Shang, K. Nienhaus and G. U. Nienhaus, *J. Nanobiotechnol.*, 2014, **12**, 5.
- 164 R. A. Petros and J. M. DeSimone, *Nat. Rev. Drug Discovery*, 2010, **9**, 615–627.
- 165 E. Gonzalez Solveyra and I. Szleifer, *WIREs Nanomed Nanobiotechnol*, 2016, **8**, 334–354.
- 166 J. L. S. Au, B. Z. Yeung, M. G. Wientjes, Z. Lu and M. G. Wientjes, *Adv. Drug Delivery Rev.*, 2016, **97**, 280–301.
- 167 J. A. Champion and S. Mitragotri, *Proc. Natl. Acad. Sci. U. S. A.*, 2006, **103**, 4930–4934.
- 168 B. D. Chithrani, A. A. Ghazani and W. C. W. Chan, *Nano Lett.*, 2006, **6**, 662–668.
- 169 F. Lu, S. H. Wu, Y. Hung and C. Y. Mou, *Small*, 2009, **5**, 1408–1413.
- 170 H. Jin, D. A. Heller, R. Sharma and M. S. Strano, *ACS Nano*, 2009, **3**, 149–158.

- 171 M. P. Calatayud, B. Sanz, V. Raffa, C. Riggio, M. R. Ibarra and G. F. Goya, *Biomaterials*, 2014, **35**, 6389–6399.
- 172 G. Y. Tonga, K. Saha and V. M. Rotello, *Adv. Mater.*, 2014, **26**, 359–370.
- 173 R. Weissleder, *Science*, 2006, **312**, 1168–1171.
- 174 Z. Cheng, A. Al Zaki, J. Z. Hui, V. R. Muzykantov and A. Tsourkas, *Science*, 2012, **338**, 903–910.
- 175 C. Liao, Q. Sun, B. Liang, J. Shen and X. Shuai, *Eur. J. Radiol.*, 2011, **80**, 699–705.
- 176 H. Lee, H. Fonge, B. Hoang, R. M. Reilly and C. Allen, *Mol. Pharmaceutics*, 2010, **7**, 1195–1208.
- 177 P. S. Low, W. A. Henne and D. D. Doorneweerd, *Acc. Chem. Res.*, 2008, **41**, 120–129.
- 178 F. Zhang, X. Huang, L. Zhu, N. Guo, G. Niu, M. Swierczewska, S. Lee, H. Xu, A. Y. Wang, K. A. Mohamedali, M. G. Rosenblum, G. Lu and X. Chen, *Biomaterials*, 2012, **33**, 5414–5422.
- 179 D. Bhattacharya, M. Das, D. Mishra, I. Banerjee, S. K. Sahu, T. K. Maiti and P. Pramanik, *Nanoscale*, 2011, **3**, 1653–1662.
- 180 S. Mohapatra, S. K. Mallick, T. K. Maiti, S. K. Ghosh and P. Pramanik, *Nanotechnology*, 2007, **18**, 1–9.
- 181 C. Fan, W. Gao, Z. Chen, H. Fan, M. Li, F. Deng and Z. Chen, *Int. J. Pharm.*, 2011, **404**, 180–190.
- 182 D. Li, S. Song and C. Fan, *Acc. Chem. Res.*, 2010, **43**, 631–641.
- 183 A. Z. Wang, V. Bagalkot, C. C. Vasilliou, F. Gu, F. Alexis, L. Zhang, M. Shaikh, K. Yuet, M. J. Cima, R. Langer, P. W. Kantoff, N. H. Bander, S. Jon and O. C. Farokhzad, *ChemMedChem*, 2008, **3**, 1311–1315.
- 184 F. Gu, L. Zhang, B. A. Teply, N. Mann, A. Wang, A. F. Radovic-Moreno, R. Langer and O. C. Farokhzad, *Proc. Natl. Acad. Sci.*, 2008, **105**, 2586–2591.
- 185 W. Jiang, B. Y. S. Kim, J. T. Rutka and W. C. W. Chan, *Nat. Nanotechnol.*, 2008, **3**, 145–150.
- 186 T. Lammers, F. Kiessling, W. E. Hennink and G. Storm, *J. Controlled Release*, 2012, **161**, 175–187.
- 187 K. Riviere, Z. Huang, K. Jerger, N. Macaraeg and F. C. Szoka, *J. Drug Targeting*, 2011, **19**, 14–24.
- 188 T. M. Allen and P. R. Cullis, *Adv. Drug Delivery Rev.*, 2013, **65**, 36–48.
- 189 T.-H. Shin, Y. Choi, S. Kim and J. Cheon, *Chem. Soc. Rev.*, 2015, **44**, 4501–4516.
- 190 H. Bin Na and T. Hyeon, *J. Mater. Chem.*, 2009, **19**, 6267–6273.
- 191 T.-H. Shin, J. Choi, S. Yun, I.-S. Kim, H.-T. Song, Y. Kim, K. I. Park and J. Cheon, *ACS Nano*, 2014, **8**, 3393–3401.
- 192 Z. Zhou, D. Huang, J. Bao, Q. Chen, G. Liu, Z. Chen, X. Chen and J. Gao, *Adv. Mater.*,

- 2012, **24**, 6223–6228.
- 193 J. Choi, J.-H. Lee, T.-H. Shin, H.-T. Song, E. Y. Kim and J. Cheon, *J. Am. Chem. Soc.*, 2010, **132**, 11015–11017.
- 194 F. Hu and Y. S. Zhao, *Nanoscale*, 2012, **4**, 6235–6243.
- 195 J. Huang, L. Wang, X. Zhong, Y. Li, L. Yang and H. Mao, *J. Mater. Chem. B*, 2014, **2**, 5311–5482.
- 196 F. Hu, Q. Jia, Y. Li and M. Gao, *Nanotechnology*, 2011, **22**, 245604–245611.
- 197 H. Johnston, D. Brown, A. Kermanizadeh, E. Gubbins and V. Stone, *J. Controlled Release*, 2012, **164**, 307–313.
- 198 Y. V Kolen'ko, M. Bañobre-López, C. Rodríguez-Abreu, E. Carbó-Argibay, A. Sailsman, Y. Piñeiro-Redondo, M. F. Cerquiera, D. Y. Petrovykh, K. Kovnir, O. I. Lebedev and J. Rivas, *J. Phys. Chem. C*, 2014, **118**, 8691–8701.
- 199 M. Pernia Leal, S. Rivera-Fernández, J. M. Franco, D. Pozo, J. M. de la Fuente and M. L. García-Martín, *Nanoscale*, 2015, **7**, 2050–2059.
- 200 G. Huang, H. Li, J. Chen, Z. Zhao, L. Yang, X. Chi, Z. Chen, X. Wang and J. Gao, *Nanoscale*, 2014, **6**, 10404.
- 201 Z. Li, S. X. Wang, Q. Sun, H. L. Zhao, H. Lei, M. B. Lan, Z. X. Cheng, X. L. Wang, S. X. Dou and G. Q. Max Lu, *Adv. Healthcare Mater.*, 2013, **2**, 958–964.
- 202 V. Vallet, U. Wahlgren and I. Grenthe, *J. Am. Chem. Soc.*, 2003, **125**, 14941–14950.
- 203 D. W. Grainger and D. G. Castner, *Adv. Mater.*, 2008, **20**, 867–877.
- 204 Z. Gong, G. Calkins, E. Cheng, D. Krause and L. E. Niklason, *Tissue Eng. Part A*, 2009, **15**, 319–30.
- 205 X. Wang, D. Niu, Q. Wu, S. Bao, T. Su, X. Liu, S. Zhang and Q. Wang, *Biomaterials*, 2015, **53**, 349–357.
- 206 C. C. Huang, N. H. Khu and C. S. Yeh, *Biomaterials*, 2010, **31**, 4073–4078.
- 207 D. Walczyk, F. Baldelli Bombelli, M. P. Monopoli, I. Lynch and K. A. Dawson, *J. Am. Chem. Soc.*, 2010, **132**, 5761–5768.
- 208 I. Lynch and K. A. Dawson, *Nano Today*, 2008, **3**, 40–47.
- 209 T. L. Moore, L. Rodriguez-Lorenzo, V. Hirsch, S. Balog, D. Urban, C. Jud, B. Rothen-Rutishauser, M. Lattuada and A. Petri-Fink, *Chem. Soc. Rev.*, 2015, **44**, 6287–6305.
- 210 S. Khoei, H. Shagholani and N. Abedini, *Polymer*, 2015, **56**, 207–217.
- 211 H. Amiri, L. Bordonali, A. Lascialfari, S. Wan, M. P. Monopoli, I. Lynch, S. Laurent and M. Mahmoudi, *Nanoscale*, 2013, **5**, 8656–65.
- 212 V. Hirsch, C. Kinnear, M. Moniatte, B. Rothen-Rutishauser, M. J. D. Clift and A. Fink, *Nanoscale*, 2013, **5**, 3723–32.
- 213 A. Petri-Fink, B. Steitz, A. Finka, J. Salaklang and H. Hofmann, *Eur. J. Pharm.*

- Biopharm.*, 2008, **68**, 129–137.
- 214 J. Klein and J. Klein, *Proc. Natl. Acad. Sci. U. S. A.*, 2007, **104**, 2029–2030.
- 215 C. D. Walkey, J. B. Olsen, H. Guo, A. Emili and W. C. W. Chan, *J. Am. Chem. Soc.*, 2012, **134**, 2139–2147.
- 216 L. Li, W. Jiang, K. Luo, H. Song, F. Lan, Y. Wu and Z. Gu, *Theranostics*, 2013, **3**, 595–615.
- 217 N. Lee and T. Hyeon, *Chem. Soc. Rev.*, 2012, **41**, 2575–2589.
- 218 P. Caravan, C. T. Farrar, L. Frullano and R. Uppal, *Contrast Media Mol. Imaging*, 2009, **4**, 89–100.
- 219 N. Bloembergen, E. M. Purcell and R. V. Pound, *Phys. Rev.*, 1948, **73**, 679–712.
- 220 G. Upadhyay, S. Shankar and R. K. Srivastava, *Mol. Neurobiol.*, 2015, **52**, 610–625.
- 221 M. Barrow, A. Taylor, D. J. Nieves, L. K. Bogart, P. Mandal, C. M. Collins, L. R. Moore, J. J. Chalmers, R. Lévy, S. R. Williams, P. Murray, M. J. Rosseinsky and D. J. Adams, *Biomater. Sci.*, 2015, **3**, 608–616.
- 222 A. Khurana, F. Chapelin, G. Beck, O. D. Lenkov, J. Donig, H. Nejadnik, S. Messing, N. Derugin, R. C.-F. Chan, B. Sennino, D. M. McDonald, P. J. Kempen, G. A. Tikhomirov, J. Rao and H. E. Daldrup-Link, *Radiology*, 2013, **269**, 186–197.
- 223 J. T. Rosenberg, K. L. Sellgren, A. Sachi-Kocher, F. C. Bejarano, M. A. Baird, M. W. Davidson, T. Ma and S. C. Grant, *Cytotherapy*, 2013, **15**, 307–322.
- 224 B. Argibay, J. Trekker, U. Himmelreich, A. Beiras, A. Topete, P. Taboada, M. Pérez-Mato, T. Sobrino, J. Rivas, F. Campos and J. Castillo, *Cell Transplant.*, 2016, doi:10.3727/096368916X691303.
- 225 S. Shrestha, P. Jiang, M. H. Sousa, P. C. Morais, Z. Mao and C. Gao, *J. Mater. Chem. B*, 2016, **4**, 245–256.
- 226 D. L. J. Thorek and A. Tsourkas, *Biomaterials*, 2008, **29**, 3583–3590.
- 227 R. D. Oude Engberink, S. M. A. van der Pol, E. A. Döpp, H. E. de Vries and E. L. A. Blezer, *Radiology*, 2007, **243**, 467–474.
- 228 L. Hansen, A. B. Hansen, A. B. Mathiasen, M. Ng, K. Bhakoo, A. Ekblond, J. Kastrup and T. Friis, *Scand. J. Clin. Lab. Invest.*, 2014, **74**, 437–446.
- 229 N. Guldris, B. Argibay, Y. V Kolen 'ko, E. Carbó-Argibay, T. Sobrino, F. Campos, L. M. Salonen, M. Bañobre-López, J. Castillo and J. Rivas, *J. Colloid Interface Sci.*, 2016, **472**, 229–236.
- 230 M. Di Marco, C. Sadun, M. Port, I. Guilbert, P. Couvreur and C. Dubernet, *Int. J. Nanomedicine*, 2007, **2**, 609–622.
- 231 Y. Zhang, N. Kohler and M. Zhang, *Biomaterials*, 2002, **23**, 1553–1561.
- 232 M. S. Thu, L. H. Bryant, T. Coppola, E. K. Jordan, M. D. Budde, B. K. Lewis, A. Chaudhry, J. Ren, N. R. S. Varma, A. S. Arbab and J. A. Frank, *Nat. Med.*, 2012, **18**, 463–467.

- 233 L. Venturelli, S. Nappini, M. Bulfoni, G. Gianfranceschi, S. Dal Zilio, G. Coceano, F. Del Ben, M. Turetta, G. Scoles, L. Vaccari, D. Cesselli and D. Cojoc, *Sci. Rep.*, 2016, **6**, 21629.
- 234 O. Betzer, R. Meir, T. Dreifuss, K. Shamalov, M. Motiei, A. Shwartz, K. Baranes, C. J. Cohen, N. Shraga-Heled, R. Ofir, G. Yadid and R. Popovtzer, *Sci. Rep.*, 2015, **5**, 15400.
- 235 J. R. Benson and P. E. Hare, *Proc. Nat. Acad. Sci. USA*, 1975, **72**, 619–622.
- 236 S. J. Soenen, W. J. Parak, J. Rejman and B. Manshian, *Chem. Rev.*, 2015, **115**, 2109–2135.
- 237 H. D. Summers, P. Rees, M. D. Holton, M. R. Brown, S. C. Chappell, P. J. Smith and R. J. Errington, *Nat. Nanotechnol.*, 2011, **6**, 170–174.
- 238 P. Walczak, D. A. Kedziorek, A. A. Gilad, B. P. Barnett and J. W. M. Bulte, *Magn. Reson. Med.*, 2007, **58**, 261–269.
- 239 B. Argibay, J. Trekker, U. Himmelreich, A. Beiras, A. Topete, P. Taboada, M. Pérez-Mato, A. Vieites-Prado, R. Iglesias-Rey, J. Rivas, A. M. Planas, T. Sobrino, J. Castillo and F. Campos, *Sci. Rep.*, 2017, **7**, 10.1038/srep40758.
- 240 B. Rodríguez-Frutos, L. Otero-Ortega, M. Gutiérrez-Fernández, B. Fuentes, J. Ramos-Cejudo and E. Díez-Tejedor, *Transl. Stroke Res.*, 2016, 10.1007/s12975-016-0482-6.
- 241 P. Walczak, J. Zhang, A. A. Gilad, D. A. Kedziorek, J. Ruiz-Cabello, R. G. Young, M. F. Pittenger, P. C. M. Van Zijl, J. Huang and J. W. M. Bulte, *Stroke*, 2008, **39**, 1569–1574.
- 242 J. Trekker, C. Leten, T. Struys, V. V Lazenka, B. Argibay, L. Micholt, I. Lambrichts, W. Van Roy, L. Lagae and U. Himmelreich, *Biomaterials*, 2014, **35**, 1627–1635.
- 243 S. Laurent, A. A. Saei, S. Behzadi, A. Panahifar and M. Mahmoudi, *Expert Opin. Drug Deliv.*, 2014, **11**, 1449–1470.
- 244 K. Hayashi, T. Shimizu, H. Asano, W. Sakamoto and T. Yogo, *J. Mater. Res.*, 2008, **23**, 3415–3424.
- 245 C. E. Hoyle, A. B. Lowe and C. N. Bowman, *Chem. Soc. Rev.*, 2010, **39**, 1355–1387.
- 246 D. Kalaitzakis, J. D. Rozzell, I. Smonou and S. Kambourakis, *Adv. Synth. Catal.*, 2006, **348**, 1958–1969.
- 247 H. A. Tayim and M. Sabri, *Inorg. Nucl. Chem. Lett.*, 1973, **9**, 753–757.
- 248 C. Carrara, M. C. Sala, E. Caneva, S. Cauteruccio and E. Licandro, *Org. Lett.*, 2014, **16**, 460–463.
- 249 Y. S. Kang, S. Risbud, J. F. Rabolt and P. Stroeve, *Chem. Mater.*, 1996, **8**, 2209–2211.
- 250 J. E. Hein and V. V Fokin, *Chem. Soc. Rev.*, 2010, **39**, 1302–1315.
- 251 M. E. Annunziato, U. S. Patel, M. Ranade and P. S. Palumbo, *Bioconjugate Chem.*, 1993, **4**, 212–218.

- 252 J. G. Kim and D. O. Jang, *Synlett*, 2008, 2072–2074.
- 253 C. Carrara, M. C. Sala, E. Caneva, S. Cauteruccio and E. Licandro, *Org. Lett.*, 2014, **16**, 460–463.
- 254 J. Sauer and R. Sustmann, *Angew. Chem. Int. Ed.*, 1980, **19**, 779–807.
- 255 C. Jegat and N. Mignard, *Polym. Bull.*, 2008, **60**, 799–808.
- 256 B. L. Hiran, J. Chadhary, S. N. Paliwal, S. Meena and P. R. Chaudhary, *E-J. Chem.*, 2007, **4**, 222–231.
- 257 J. L. Bartels, P. Lu, A. Walker, K. Maurer and K. D. Moeller, *Chem. Commun.*, 2009, 5573–5575.





RESUMEN EN ESPAÑOL

La nanotecnología estudia materiales con tamaños en el rango nanométrico, de 1 a 100 nm. La nanomedicina es una nueva área de conocimiento que utiliza las herramientas de la nanotecnología para aplicaciones biomédicas. Los materiales nanoestructurados tienen un tamaño intermedio entre las pequeñas moléculas y los materiales macroscópicos, y por tanto, ofrecen la posibilidad de interactuar con procesos biológicos en la misma escala. Además, los nanomateriales poseen características físico-químicas diferentes a los materiales convencionales en estado masivo, como por ejemplo superparamagnetismo, resonancia plasmónica, o una elevada área superficial. Las nanopartículas ofrecen propiedades prometedoras para lograr la 'medicina personalizada', gracias a la posibilidad de modificar su superficie con moléculas de interés biológico, como proteínas, ligandos receptores, o sondas de imagen, que permiten, en la teoría, el reconocimiento selectivo por parte de tejidos y células en un organismo vivo.

Las nanopartículas compuestas por óxidos de hierro son particularmente prometedoras por poseer excelente biocompatibilidad, bajos costes de producción, y buena respuesta magnética. El comportamiento de las nanopartículas de óxidos de hierro depende de su composición y morfología, de su tamaño, del recubrimiento orgánico o inorgánico, etc. En los últimos años se han desarrollado nuevas estrategias para la modificación superficial de nanopartículas de óxidos de hierro. El objetivo es intentar diseñar nanoestructuras que se acumulen selectivamente en tumores, que puedan ser detectadas mediante varias técnicas de imagen y que permitan la liberación de un fármaco acoplado, bien remotamente o de forma espontánea bajo ciertas condiciones fisiológicas.

A pesar del potencial de las nanopartículas de óxidos de hierro, la interfaz entre los materiales producidos y elementos biológicos como macromoléculas, células, o tejidos, todavía se mantiene impredecible. Las nanopartículas afrontan varios impedimentos en su camino hacia la aplicación en medicina. Primero, garantizar la estabilidad de las nanopartículas en fluidos biológicos para asegurar terapias seguras y efectivas. Segundo, la interacción entre nanopartículas y biomoléculas es la

responsable de dictar la biodistribución de las nanopartículas *in vivo*, y por tanto, es un factor limitante para el reconocimiento de nanomateriales con ligandos de reconocimiento. Y tercero, la eficiencia de la síntesis de nanopartículas con propiedades deseadas debe ser elevada y reproducible para poder asegurar terapias rentables a gran escala.

En esta tesis doctoral se han evaluado tres aspectos fundamentales alrededor de las nanopartículas de óxidos de hierro que condicionan su aplicación en biomedicina. Primero, se ha estudiado el proceso de síntesis y de purificación de nanopartículas de óxido de hierro, así como su interacción con biomoléculas. Segundo, se ha evaluado las diferencias en internalización en células madre de nanopartículas de óxidos de hierro de diferentes tamaños y con diferentes recubrimientos orgánicos. Y tercero, se han explorado nuevos métodos de funcionalización de nanopartículas mediante química 'click' que ofrece ventajas como simplicidad, altos rendimientos, y buena reproducibilidad. Estos estudios han estado enmarcados hacia el uso de estas nanopartículas en tres áreas de gran relevancia dentro del ámbito diagnóstico y terapéutico: 1) como agentes de contraste en resonancia magnética de imagen; 2) como agentes de marcaje magnético de células madre para terapia celular; y 3) como agentes de transporte y liberación de fármacos.

En el segundo Capítulo de esta tesis se presenta la síntesis y la purificación de nanopartículas de óxidos de hierro dopadas con metales de transición. En la actualidad, existen varios métodos de síntesis para la obtención de óxidos de hierro nanométricos que ofrecen ventajas y desventajas dependiendo de las propiedades físico-químicas deseadas para el material. Sin embargo, en ocasiones la búsqueda de nuevas propiedades origina métodos de síntesis que no son compatibles con el uso de los nanomateriales obtenidos en aplicaciones médicas, y que impiden su avance hacia la práctica clínica. En este Capítulo, se describe la síntesis de nanopartículas de óxido de hierro dopadas con iones de metales de transición mediante reacción hidrotermal. El procedimiento de síntesis llevado a cabo permitió obtener nanopartículas en escala de gramo con un solo paso sintético y empleando agua como disolvente. Estas características suponen alta simplicidad y garantizan la posibilidad del escalado.

Una vez obtenidas las nanopartículas se observó que un paso de purificación extra mediante una centrifugación en unas condiciones de gravedad y tiempo determinadas, origina diferencias no sólo en el tamaño medio de las nanopartículas sino también en la cantidad de recubrimiento orgánico, lo que determina muchas de las propiedades químico-físicas estudiadas, como por ejemplo su estabilidad coloidal, su interacción con biomoléculas y células en medios fisiológicos, y su comportamiento como agentes de contraste en resonancia magnética de imagen. Se comprobó, que aquellas nanopartículas de 35 nm de diámetro hidrodinámico actuaban exclusivamente como agentes de contraste oscuro, mientras que las nanopartículas de semejante composición pero con diámetros hidrodinámicos de 18 nm, actuaban como agentes duales en resonancia magnética de imagen. Este efecto se debe principalmente a las diferencias en el ratio área superficial/volumen, que se incrementa al disminuir el tamaño de partícula. El ion dopante en este caso, el Mn^{2+} , es un ion paramagnético con 5 electrones desapareados. En nanopartículas de 18 nm existe un mayor número de estos iones en la superficie en comparación con los que existen en el núcleo, que pueden interaccionar directamente con los protones del agua, y por tanto, producir de una manera efectiva una aceleración de la relajación longitudinal que origina el contraste positivo.

La obtención de agentes de contraste duales en resonancia magnética de imagen supone un avance significativo en el análisis del contraste de las imágenes adquiridas, ya que permiten identificar falsos positivos y facilitan un diagnóstico más certero y preciso. Los agentes de contraste oscuro presentan interferencias de imagen con zonas hemorrágicas, burbujas de aire o depósitos de metales, y por tanto puede llevar a un diagnóstico erróneo. Por otra parte, los agentes de contraste brillante, que reducen el tiempo de relajación T_1 , o tiempo de relajación longitudinal, poseen también interferencias con acumulaciones de grasa corporal. Además, los agentes T_1 convencionales están formados por complejos de Gd, que generan serios problemas de toxicidad, hasta el punto de no poder ser administrados en pacientes con disfunciones renales. Por tanto, el desarrollo de nuevos agentes de contraste duales y biocompatibles, como el presentado en este trabajo, es de alto interés para la práctica clínica.

Por otra parte, el comportamiento de las nanopartículas en contacto con biomoléculas fue también evaluado para garantizar su biocompatibilidad como agentes de contraste. Para ello se realizó la incubación de las nanopartículas en medio de cultivo celular, que contiene biomoléculas como azúcares, vitaminas y proteínas. Las nanopartículas de mayor tamaño adsorbieron cinco veces más cantidad de proteínas que sus análogas de menor tamaño. Además, también se comprobó que el diámetro hidrodinámico de las nanopartículas de 35 nm se doblaba en este medio, lo que sugiere la aparición de fenómenos de agregación y de adsorción de proteínas, que no son deseables en aplicaciones biomédicas. En cambio, las nanopartículas de 18 nm no presentaron ningún aumento de diámetro hidrodinámico al estar en contacto con proteínas, de lo que se deduce que tamaños de partícula reducidos originan una mayor curvatura en la superficie que impide la adsorción de biomoléculas de gran tamaño.

Análogamente, se realizaron también experimentos *in vitro* para estudiar el comportamiento de las nanopartículas en contacto con líneas celulares. En nuestro estudio, se encontró que las nanopartículas de óxido de hierro de mayor tamaño y con una adsorción de proteínas alta, formaban grandes agregados cuando se incubaron con las células. La formación de estos agregados es desaconsejable en sistemas biológicos, ya que es fenómeno altamente incontrolable que origina problemas de toxicidad y reproducibilidad.

Por otro lado, la estabilidad coloidal de las nanopartículas fue evaluada en función del tiempo, observándose que en aquellas de mayor tamaño la estabilidad química se vio afectada al cabo de un almacenamiento de diez meses en agua en condiciones de temperatura de 4 °C, mientras que en las nanopartículas más pequeñas, ésta se mantuvo completamente inalterable. Es importante remarcar que tanto la estabilidad química de las nanopartículas como su estabilidad coloidal como dispersión acuosa a 4 °C son de gran importancia para el desarrollo de formulaciones con potencial aplicación clínica.

En el tercer Capítulo de esta tesis doctoral se presenta el empleo de nanopartículas de magnetita puras para el etiquetado magnético de células madre mesenquimales, con el objetivo de habilitar su visualización por una técnica de imagen no invasiva, en

particular resonancia magnética de imagen, una vez inyectadas en un organismo vivo. En los últimos años ha existido un creciente interés en el conocimiento de las propiedades y comportamiento biológico de células madre debido a su prometedor potencial en terapia celular, el cual se encuentra en un estadio muy preliminar en muchas de las aplicaciones médicas de interés que se están explorando actualmente.

Para el etiquetado de las células madre se siguió un procedimiento de incubación *in vitro* entre las células y las nanopartículas, como paso previo a su administración *in vivo*. Para el seguimiento de las células mediante resonancia magnética de imagen es imprescindible que las nanopartículas hayan sido internalizadas por las células, y que por tanto, creen un contraste negativo en la imagen, haciéndolas distinguibles de las células intrínsecas del organismo vivo. El proceso de internalización en células madre es complejo, ya que a diferencia de otros tipos celulares se trata de células de naturaleza no fagocítica.

En este apartado, se estudió el etiquetado de células madre con nanopartículas de magnetita de dos tamaños diferentes, por un lado nanopartículas de más de 50 nm de diámetro hidrodinámico (todavía en el rango superparamagnético), y por otro, nanopartículas de magnetita ultrafinas, es decir, con diámetros hidrodinámicos de menos de 50 nm. El efecto en la internalización en células madre mesenquimales fue radicalmente diferente en las dos muestras. Por un lado, las nanopartículas con tamaños mayores mostraron agregados de nanopartículas de tamaños de micras cuando fueron incubadas con las células, observándose una internalización poco homogénea en la población celular gobernada por procesos de sedimentación. En cambio, las nanopartículas ultrafinas no formaron agregados en cultivo con las células mesenquimales, pero no fueron incorporadas por las células. Por tanto, una modificación del recubrimiento orgánico se llevó a cabo para intentar mediar el proceso de endocitosis. La estrategia consistió en funcionalizar el recubrimiento de ácido poliacrílico con moléculas de glucosamina mediante acoplamiento peptídico. La glucosamina es un compuesto biocompatible que presenta afinidad por los receptores de azúcares en la membrana celular, y por eso fue la molécula de elección para la funcionalización del recubrimiento polimérico.

La incubación de las nanopartículas ultrafinas modificadas con moléculas de glucosamina dio lugar a una internalización celular record de 56.5 picogramos de Fe por célula. Este es el valor de carga magnética más alto reportado en la literatura para células mesenquimales con nanopartículas ultrafinas de magnetita. El incremento de la carga del etiquetado magnético en las células madre es importante para el posterior seguimiento de dichas células *in vivo* durante tiempos prolongados. Sin embargo, es importante asegurar que el etiquetado no interfiere con la capacidad terapéutica de las células madre. Con este objetivo, se realizaron estudios de toxicidad y proliferación que garantizaron que las nanopartículas de magnetita modificadas superficialmente con glucosamina constituyen un etiquetado inocuo para las células madre mesenquimales.

Por último, se realizó la validación *in vivo* de las células etiquetadas en un modelo animal de rata dirigiendo las células marcadas al cerebro por vía intra-arterial. Una vez administradas, las células madre marcadas magnéticamente pudieron ser detectadas *in vivo* durante más de 8 días mediante resonancia magnética de imagen. Esto supone una ventana temporal amplia que permite evaluar la localización y la migración de las células *in vivo* a largo plazo, permitiendo correlacionar su migración en los tejidos de interés con su potencial efecto terapéutico.

En el cuarto Capítulo de esta tesis se ha estudiado nuevos métodos para la funcionalización superficial de nanopartículas, en particular aquellas formadas por magnetita, con grupos funcionales susceptibles de reaccionar mediante química de tipo 'click'. La funcionalización de magnetita es importante para conseguir sistemas nanométricos multifuncionales. Las técnicas de caracterización actuales son limitadas y en ocasiones la determinación estructural de los híbridos orgánicos/inorgánicos no se puede llevar a cabo por los métodos tradicionales. En este aspecto, las reacciones tipo 'click' presentan ventajas muy significativas para la funcionalización de nanomateriales, como reacciones cuantitativas y reproducibles, y procesos de purificación simples.

El acceso a nanomateriales multifuncionales es muy prometedor para lograr la conocida como 'medicina personalizada', que supondría una reducción en la toxicidad

sistémica y una mayor especificidad en los tratamientos. Para ello es imprescindible producir nanopartículas con diversas funcionalidades que permitan al mismo tiempo, por ejemplo, la unión de moléculas para el reconocimiento de tejidos, como tumores, y también ofrezcan la liberación de fármacos para su tratamiento. En particular, la decoración de las nanopartículas con grupos funcionales termosensibles es muy atractiva debido a la capacidad de las nanopartículas magnéticas de generar calor cuando se colocan bajo un campo magnético oscilante, fenómeno conocido como hipertermia magnética. De esta manera, el objetivo de este trabajo consistió en la obtención de sistemas nanométricos basados en nanopartículas de magnetita modificados mediante química 'click' para exhibir alta solubilidad en agua, un reconocimiento específico de tejidos mediado por el diseño de ligandos diana personalizados, y liberación controlada de fármacos acoplados mediante estímulos térmicos generados externa y remotamente.

La obtención de nanopartículas de magnetita multifuncionales se llevó a cabo en dos etapas. Primero, la modificación de las nanopartículas de magnetita desnudas se realizó con ligandos que contenían un grupo funcional isocianato. La configuración electrónica de los átomos de hierro en la superficie de la magnetita hacen que éste actúe como un ácido de Lewis, y por eso, cuando estas nanopartículas se encuentran dispersas en agua, el hierro coordina los grupos hidroxilo. En este caso, los grupos hidroxilo de la superficie de las nanopartículas puede reaccionar en una reacción típicamente nucleofílica con los grupos isocianato para generar grupos funcionales conocidos como carbamatos.

Por tanto, se sintetizaron dos ligandos bifuncionales diferentes, ambos presentando un grupo isocianato, para reaccionar con la nanopartículas, y otro grupo orgánico funcional de interés, para posteriores funcionalizaciones. Como grupos de funcionales de interés se escogieron, para uno de ellos, la maleimida, por actuar como sustrato de la reacción de Diels–Alder y originar un enlace termosensible; y para el otro, el alquino, que reacciona en la cicloadición alquino–azida catalizada por cobre (I) (CuAAC), conocida como la reacción click por excelencia y que posee una gran librería de compuestos comerciales disponibles para su funcionalización. Paralelamente, se modificó químicamente un fluoróforo comercial (pireno) con el objetivo de incorporar

un grupo furano en su estructura molecular, y así actuar como un sistema modelo de fármaco. Este grupo furano habilitará el acoplamiento del fluoróforo a la nanopartícula a través de la reacción Diels–Alder con el grupo funcional maleimida.

Después de la modificación de las nanopartículas de magnetita con grupos maleimida y alquino se procedió a la segunda funcionalización de dichos grupos. Para la reacción con el grupo maleimida se llevó a cabo la reacción de Diels–Alder con el fluoróforo sintetizado como sistema modelo. La caracterización del producto híbrido orgánico/inorgánico concluyó que después de la reacción de Diels–Alder los nanomateriales poseían una mayor cantidad de material orgánico y exhibían propiedades de fluorescencia. Por otro lado, para la reacción con el grupo alquino, se escogió un ligando compuesto por una cadena de polietilenoglicol de veintitrés unidades, para aportar solubilidad en agua, y también con un grupo biotina terminal. Las unidades de biotina han sido utilizadas para el reconocimiento de ciertos receptores en células tumorales, y por tanto fueron escogidas como ligando.

Una vez se obtuvieron las nanopartículas de magnetita con estabilidad coloidal en agua y funcionalizadas con ligandos diana de biotina y un fluoróforo como sistema modelo de fármaco, se comprobó la liberación del fluoróforo mediante hipertermia magnética. La liberación no fue posible mediante hipertermia magnética en las condiciones experimentales empleadas, posiblemente por tratarse de nanopartículas de magnetita de pequeño tamaño, y por consiguiente, baja eficiencia térmica. Sin embargo, la situación fue diferente cuando las nanopartículas se calentaron mediante baño tradicional, donde la liberación del fluoróforo fue promovida después de calentar las nanopartículas a 65 °C durante 1 h.

En conclusión, el trabajo desarrollado en esta tesis doctoral supone avances significativos en el conocimiento del comportamiento de las nanopartículas de óxido de hierro hacia su aplicación en biomedicina. En particular, se han estudiado aspectos importantes que rodean el uso de estas nanopartículas como agentes de contraste en resonancia magnética de imagen, como etiquetas magnéticas en estudios de seguimiento de células madre, y también como vehículos para el transporte y liberación controlada de fármacos. Con este objetivo, y en base a los resultados

obtenidos, se ha actuado sobre el diseño racional de estas nanopartículas, desarrollando estrategias originales de síntesis y funcionalización que nos han permitido proveer a las nanopartículas finales con las propiedades físico-químicas requeridas para su funcionamiento en las aplicaciones biomédicas de interés. Así, los principales hallazgos de esta tesis pueden resumirse en los siguientes puntos. Primero, el tamaño hidrodinámico de las nanopartículas de óxido de hierro determina la adsorción de proteínas en la superficie de las nanopartículas, que a su vez está directamente relacionado con fenómenos de agregación, lo que incrementa en varios órdenes de magnitud el tamaño de las nanopartículas y puede ocasionar problemas de toxicidad. Un tamaño menor de las nanopartículas, en cambio, implica una curvatura superficial mayor que impide estéricamente la adsorción de proteínas de gran tamaño. Por otra parte, en aquellas nanopartículas de tamaños menores, el contacto entre los iones de manganeso (metal de transición magnético usado como elemento dopante en las nanopartículas de óxido de hierro) y las moléculas de agua favoreció una reducción simultánea del tiempo de relajación T_1 y T_2 de los protones del agua, originando un contraste dual en resonancia magnética de imagen. Estos hallazgos constituyen un avance importante hacia el desarrollo de nuevos agentes de contraste con propiedades duales en MRI y alta estabilidad en fluidos biológicos.

Segundo, se observó que nanopartículas de magnetita recubiertas con ácido poliacrílico con tamaños en el rango ultrafino (de menos de 50 nm) poseen elevada estabilidad en medio de cultivo celular, pero no promueven la internalización en células mesenquimales. Sin embargo, se encontró que cuando este recubrimiento inicial de ácido poliacrílico fue modificado con moléculas de glucosamina, la internalización celular fue la mayor alcanzada hasta el momento para nanopartículas ultrafinas y células mesenquimales.

Tercero, se consiguió la funcionalización química superficial de nanopartículas de óxido de hierro desnudas mediante reacción simultánea con dos ligandos isocianato diferentes modificados con los grupos funcionales alquino y maleimida, respectivamente. Además, se confirmó la reactividad de estos grupos funcionales en reacciones de Diels–Alder y de CuAAC, dando lugar a nanopartículas funcionalizadas con enlaces termosensibles, solubilidad en agua, y ligandos biotina para el

reconocimiento de tumores. Además, se comprobó la liberación mediante aplicación de calor de moléculas modelo fluorescentes acopladas covalentemente a estos sistemas. Por tanto, tres aspectos fundamentales de nanopartículas de óxidos de hierro han sido estudiados en esta tesis: su estabilidad en fluidos biológicos, su internalización en células madre, su comportamiento como sonda de imagen para MRI y su funcionalización con moléculas de interés bioquímico.



Noelia Guldris

Date of birth: 29th October 1989

Nationality: Spanish

ResearchID: E-6414-2016

E-mail: noelia.guldris@gmail.com

Education

12/13–present	University of Santiago de Compostela (USC), Spain International Iberian Nanotechnology Laboratory (INL), Braga, Portugal
06–09/16	Osaka University, Japan
09/12–11/13	Center for Research in Biological Chemistry and Molecular Materials (CIQUS), University of Santiago de Compostela, Spain
09/10–06/11	University of Leicester, England
09/07–07/13	University of Santiago de Compostela, Spain
06/13	Secondary School, Ames, Spain

Publications

1. **N. Guldris**, B. Argibay, Y. V. Kolen'ko, E. Carbó-Argibay, T. Sobrino, F. Campos, L. M. Salonen, M. Bañobre-López, J. Castillo, J. Rivas, 'Magnetite Nanoparticles for Stem Cell Labeling with High Efficiency and Long-Term in Vivo Tracking', *Bioconjugate Chemistry*, 10.1021/acs.bioconjchem.6b00522.
2. M. Fernandez-Villamarin, A. Sousa-Herves, S. Porto, **N. Guldris**, J. Martínez-Costas, R. Riguera, E. Fernandez-Megia, 'Amplified Stabilization of Polyion Complex Micelles for Drug Delivery: Dendrimer–Hydrophobic Interactions', *submitted*.
3. L. M. Salonen, D. D. Medina, E. Carbo-Argibay, M. G. Goesten, L. Mafra, **N. Guldris**, J. M. Rotter, D. G. Stroppa, C. Rodríguez-Abreu, 'A Supramolecular Strategy Based on Molecular Dipole Moments for High-Quality Covalent Organic Frameworks', *Chem. Commun.* **2016**, 52, 7986–7989.
4. **N. Guldris**, B. Argibay, Y. V. Kolen'ko, E. Carbó-Argibay, T. Sobrino, F. Campos, L. M. Salonen, M. Bañobre-López, J. Castillo, J. Rivas, 'Influence of the Separation Procedure on the Properties of Magnetic Nanoparticles: Gaining *in vitro* Stability and T_1 - T_2 Magnetic Resonance Imaging Performance', *J. Colloid Interface Sci.* **2016**, 472, 229–236.
5. J. L. Lado, X. Wang, E. Paz, E. Carbó-Argibay, **N. Guldris**, C. Rodríguez-Abreu, L. Liu, K. Kovnir, Y. V. Kolen'ko, 'Amorphous Oxygen-rich Molybdenum Oxysulfide

- Decorated *p*-type Silicon Microwire Arrays for Efficient Photoelectrochemical Water Reduction', *ACS Catalysis*, **2015**, *5*, 6503–6508.
6. V. Vilas-Boas, **N. Guldris**, E. Carbó-Argibay, D. G. Stroppa, M. F. Cerqueira, B. Espiña, J. Rivas, C. Rodríguez-Abreu, Yu. V. Kolen'ko, 'Straightforward Phase-transfer Route to Colloidal Iron Oxide Nanoparticles for Protein Immobilization', *RSC Adv.* **2015**, *5*, 47954–47958.
 7. X. Bao, Dmitri Y. Petrovykh, P. Alpuim, D. G. Stroppa, **N. Guldris**, H. Fonseca, M. Costa, J. Gaspar, C. Jin, L. Liu, 'Amorphous Molybdenum Sulfoxide Decorated *p*-Type Silicon Microwire Arrays for Efficient Photoelectrochemical Water Reduction', *Nano Energy*, **2015**, *16*, 130–142.

Courses and Conferences

1. **Oral Presentation:** 'Iron Oxide Nanoparticles with Glucosamine-Modified Coating for Highly Efficient Labelling of Mesenchymal Stem Cells', **N. Guldris**, B. Argibay, Y. V. Kolen'ko, J. Gallo, R. Iglesias, F. Campos, L. M. Salonen, M. Bañobre-López, J. Castillo, José Rivas. *5th Portuguese Young Chemists Meeting*, Guimarães, Portugal, 26-29.04.2016.
2. **Oral Presentation:** 'Ultrasmall Doped Iron Oxide Nanoparticles as Dual T_1 – T_2 Contrast Agents for MRI', **N. Guldris**, B. Argibay, Y. V. Kolen'ko, E. Carbó-Argibay, F. Campos, L. M. Salonen, M. Bañobre-López, J. Castillo, J. Rivas. *nanoPT2016 Conference*, Braga, Portugal, 16-19.02. 2016.
3. **Oral Presentation:** 'Superparamagnetic Iron Oxide Nanoparticles as Multifunctional Systems for Biomedical Applications', **N. Guldris**, B. Argibay, Y. V. Kolen'ko, E. Carbó-Argibay, L. M. Salonen, M. Bañobre-López, J. Rivas, *6th Iberian Meeting on Colloids and Interfaces*, Guimarães, Portugal, 8-10.07.2015.
4. **Oral Presentation:** 'Iron Oxide Nanoparticles as Contrast Agents for MRI-Based Stem Cell Tracking', **N. Guldris**, B. Argibay, Y. V. Kolen'ko, E. Carbó-Argibay, L. M. Salonen, M. Bañobre-López, J. Rivas, *InveNNta meeting*, Braga, Portugal, 31.10.2015.
5. **Oral Presentation** 'Iron Oxide Nanoparticles as Contrast Agents for MRI-Based Stem Cell Tracking', **N. Guldris**, B. Argibay, Y. V. Kolen'ko, E. Carbó-Argibay, R. Iglesias, F. Campos, L. M. Salonen, M. Bañobre-López, J. Castillo, *InveNNta meeting*, Santiago de Compostela, 31.10.2014.
6. **Poster Presentation:** 'Design of More Efficient Contrast Agents for Enhanced MRI Applications', **N. Guldris**, R. Grillo, L. M. Salonen, L. F. Fraceto, N. J. Long, J. Castillo, J. Rivas, J. Gallo and M. Bañobre-López. *Molecular Imaging Workshop 2015*, San Sebastian, Spain, 10-12.11.15.
7. **Poster Presentation:** 'Superparamagnetic Iron Oxide Nanoparticles for Stem Cell Tracking by Magnetic Resonance Imaging', **N. Guldris**, B. Argibay, Y. V.

- Kolen'ko, E. Carbó-Argibay, J. Gallo, R. Iglesias, F. Campos, L. M. Salonen, M. Bañobre-López, J. Castillo, J. Rivas, *Nanotech conference*, Paris, France, 15-17.06.2015.
8. **Poster Presentation** 'Iron Oxide Nanoparticles as Contrast Agents for Magnetic Resonance Imaging Applications', **N. Guldris**, B. Argibay, Y. V. Kolen'ko, E. Carbó-Argibay, R. Iglesias, F. Campos, L. M. Salonen, M. Bañobre-López, J. Castillo, J. Rivas, *nanoPT2015 Conference*, Porto, Portugal, 11-13.02.2015.
 9. **Poster Presentation:** 'Fe₃O₄ Nanocolloids with High Heating Efficiency in Magnetic Hyperthermia', Y. V. Kolen'ko, M. Bañobre-López, **N. Guldris**, D. Y. Petrovykh, J. Rivas, *NANO2014 Conference*, Moscow, Russia, 13-18.07.2014.
 10. **Attended course:** 'Advanced Biomaterials for Bioapplications' University of Vigo, Spain, 24.10.2014
 11. **Attended course:** 'Glycoconjugates: from Chemistry to Biology', Science Faculty Nantes, France, 19–22.03.2013.
 12. **Attended course:** 'Introduction to Microscopy Techniques: Optic and Electronic', 20 hours, Transmitting Science S.L.U. Barcelona, Spain, 01–15.07.2013.

Awards and prizes

- Norleq award for **Best Oral Presentation** at 5th Portuguese Young Chemists Meeting, Guimarães 26-29.05.2016.
- Nanoscale Horizons **Poster Prize** at Nanotech France 2015. 15-17.06.2015.
- '**Barrié de la Maza**' scholarship to accomplish an abroad internship. 04.06.2015.
- **CIQUS scholarship** for research activities, University of Santiago de Compostela, Spain. 04-10-2013.

Languages

Spanish	Native speaker
Galician	Native speaker
English	Fluent
Portuguese	Intermediate
French	Basic



